LOW-DIMENSIONAL FRUSTRATED QUANTUM MAGNETS: A PLAYGROUND FOR NOVEL PHASES

by

Wen Jin

A dissertation submitted to the faculty of
The University of Utah
in partial fulfillment of the requirements for the degree of

Doctor of Philosophy

in

Physics

Department of Physics and Astronomy

The University of Utah

May 2018

The University of Utah Graduate School

STATEMENT OF DISSERTATION APPROVAL

The dissertation of **Wen Jin**

has been approved by the following supervisory committee members:

Oleg A. Starykh ,	Chair(s)	**25 Aug 2017** Date Approved
Stephan Louis Le Bohec ,	Member	**25 Aug 2017** Date Approved
Dmytro Pesin ,	Member	**25 Aug 2017** Date Approved
Vikram V. Deshpande ,	Member	**25 Aug 2017** Date Approved
Firas Rassoul-Agha ,	Member	**25 Aug 2017** Date Approved

by **Benjamin C. Bromley** , Chair/Dean of

the Department/College/School of **Physics and Astronomy**

and by **David B. Kieda** , Dean of The Graduate School.

ABSTRACT

Low-dimensionality, magnetic frustration, and quantum fluctuations are three ingredients that give rise to nontrivial magnetic orders or exotic ground states, such as spin nematics and spin liquids. In this dissertation I discuss some efforts to find novel interesting magnetic phases by cooking up all these ingredients together. First, a large fraction of this dissertation is devoted to the behavior of quantum spin chains in the presence of a uniform Dzyaloshinskii-Moriya (DM) interaction. This problem is analyzed by the bosonization technique. Spin chain is the building block of many materials, such as $K_2CuSO_4(Cl/Br)_2$ which strongly motivates our study. DM interaction originates from spin-orbit coupling, and is widely present in real materials. Theories of these systems are derived and described for both individual chain and weakly coupled ones at zero and finite temperature and in the presence of external magnetic field. A special geometry of DM interactions—staggered between chains, but uniform within a given chain—leads to a peculiar type of frustration that effectively cancels the transverse interchain coupling and strongly reduces the ordering temperature. By taking advantage of this special geometry of DM interaction, one can construct a chiral spin liquid, which shares some basic features of fractional quantum Hall effect, such as gapped bulk and gapless chiral edge states, in arrays of spin chains. The second part of this dissertation describes the investigation of the interplay between frustration, quantum fluctuations, and magnetic field in the phase diagram of quantum antiferromagnets on triangular lattice. For triangular antiferromagnets with spacial and/or exchange anisotropy and near the fully polarized field, the competition between classical degeneracies and quantum fluctuations leads to multiple phase transitions and highly nontrivial intermediate phases. As for a toy model of a zigzag chain, a spin chain with competing nearest and next-nearest exchange interactions, I investigate quantum fluctuations and geometric frustrations establish a 1/3 magnetization plateau and a bond-nematic state, which has a nonzero vector chirality on every lattice bond and circulating spin currents in every elementary triangle.

I dedicate this dissertation to
my parents, Lijie Li and Chenghai Jin,
and my husband, Xiaoyu Sui,
for their constant support and unconditional love.
I love you all dearly.

CONTENTS

LIST OF FIGURES

LIST OF TABLES

ACKNOWLEDGEMENTS

Over the past six years I have spent in University of Utah, I had lots of "interactions" with different people. It is these interactions that shape and model me as a researcher in Physics. Although the list of those I would like to thank is too long to fit here, I will mention some in particular whose imprint cannot go unnoticed by any means.

Firstly, I wish especially thank my advisor Professor Oleg Starykh for his invaluable guidance, patience, support and for sharing with me his vast knowledge of physics. He gave the opportunity to get into quantum many-body physics. Professor Starykh is also a great teacher, and his lecture notes are well organized and written. I benefited a lot from his lectures. He likes to encourage me to heights I think I am not capable of and lets me realize that I can work as a researcher.

I am also grateful to Professor Stephan Lebohec. He is more like my second supervisor. He taught me programming, and showed me how to code from scratch. His enthusiasm in science outreach inspires me. I was a slow learner in the field of computation, and he was very patient. I still remember how he spent two hours looking for one of my silly typos.

I would like to thank my collaborators, Professor Andrey Chubukov, Doctor Yang-Hao Chan, and Professor Hong-Chen Jiang. I appreciate so much your incredible talent and your great collaboration. Thanks for the great help from and enlightened discussions on Diagrammatic Monte Carlo, and many others, with Kun Chen, Yuan Huang, Professor Nikolai Prokof'ev, and Professor Boris Svistunov during my stay at Amherst, Massachusetts. Even though I did not include this part of my work in this dissertation. I am thankful for many helpful and stimulating conversions with Fei Teng, who showed me the connections between high-energy physics and condensed matter physics. Thanks to my group members Ran Tao and Hassan Allami.

A special thanks to my family and friends. A PhD is not just an intellectual exercise, and it requires a certain temperament and stress management. Words cannot express how grateful I am for the caring and support from my mother, my father and my husband. I

want to thank Ting Zhang for being my best friend for more than ten years, and more like a sister to me. Thanks for my fellows while I was in Salt Lake City, Jieying Mao, Jing Ma, Hui Zhou, Yaxin Zhai, Haojie Xu, Jian Lan, and Lei Shan.

Last but not least, I would like to thank my other thesis committee members, Professor Dmytro Pesin, Professor Vikram Deshpande and Professor Firas Rassoul-Agha, for useful suggestions and comments on my research projects and this dissertation.

Wen Jin

University of Utah

October 2017

CHAPTER 1

INTRODUCTION

Magnetic insulators have proved to be a fertile ground for studying novel types of quantum many-body state. The work presented in this dissertation attempts to find these novel states of matter by studying, in the field of quantum magnetism, several experimentally relevant antiferromagnets. By "novel," I mean these phases are nonintuitive under classical consideration, and they emerge when quantum effects play a more or most dominant role. The projects presented here propose realistic scenarios for the realization of novel phases in low-dimensional and/or frustrated antiferromagnets. All the problems embark on well-defined microscopic spin models and are tackled by solving the spin-wave or field theories. In particular, this dissertation focuses on the quantum Heisenberg spin-1/2 chain, which is probably the simplest quantum system, and it serves as an interesting model system to explore strongly correlated quantum order in low-dimensional antiferromagnets, superconductors, and ultracold atoms. This spin chain hosts a quantum critical ground state, and many unconventional magnetic induced states, with the joint influence of spin-orbit coupling or competing exchange interactions with nearest and next-nearest neighbors. The present introduction is designed to explain some basics of these novel phases, and their experimental detections/realizations, followed by the introduction of theoretical methods in the end.

An antiferromagnet is characterized by a negative Curie-Weiss temperature $\theta_{\rm cw}$, which is easily determined experimentally via high-temperature behavior of the spin susceptibility $\chi \propto (T-\theta_{\rm cw})^{-1}$, with T being temperature. Generally, the antiferromagnet leaves the paramagnetic phase and develops a usual Neel order with antiparallel alignments of neighboring spins when it is cooled to the Neel temperature[1] $T_N \propto zS(S+1)J$, which is a product of energy J with the number of nearest neighbors z and the spin length $S(S+1)$. This result is obtained from mean field analysis, a classical consideration that treats spin

as a vector of fixed length. Under mean-field consideration, one assumes each magnetic moment on one sublattice experiences the same effective magnetic field proportional to the magnetization of the other sublattice. In this case, T_N is in the same order of θ_{cw}. However, qualitatively different situations can appear for antiferromagnets that are accompanied by strong quantum fluctuations. The paramagnetic phase extends to temperature $T \ll \theta_{\mathrm{cw}}$. Magnetic ordering (unusual spin structure different form Neel order) or spin freezing (spin ice state) may appear at a much lower temperature T_c, and even the magnetic disorder preserves down to $T = 0$ Kelvin, with the resultant quantum spin liquid. The projects in this dissertation explore behaviors below T_c, where novel states of matter can emerge.

The study of quantum magnetism has seen many of these novel phases, which are summarized by Balents[2] in **Figure 1.1**. The more "quantum-ness" the system experiences, equivalently, the stronger quantum fluctuations are, more and more nontrivial phases emerge. The quantum fluctuations appear as a result of the zero-point motion, from the quantum uncertainty principle, and can persist down to $T = 0$ K. From the perspective of classical consideration, the most surprising feature of quantum fluctuations is that they can be phase coherent, namely the allowance of linear superposition. The concept of superposition makes spins entangled with one another far away. That is the phenomenon called *entanglement*, which is the essence of quantum spin liquid. It turns out that low-dimensionality (1D) and magnetic frustration are the two sources enhancing the quantum

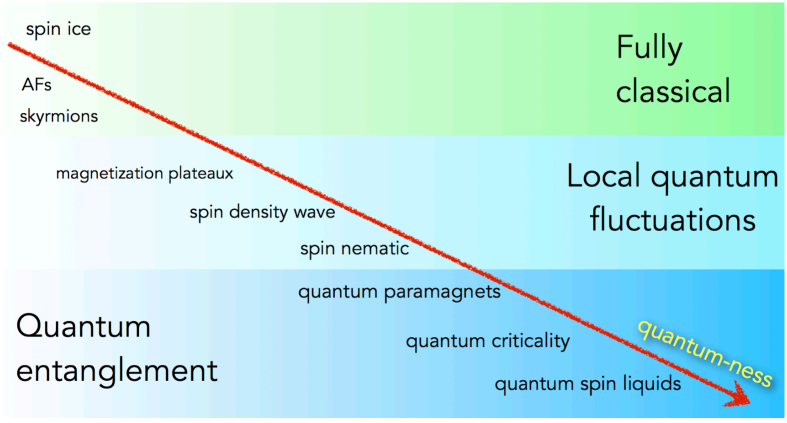

Figure 1.1. Novel phases predicted in the field of quantum magnetism. The more "quantum-ness" the system experiences, the more nontrivial phases emerge. (Adapted from Balents[2])

fluctuations. They share many common features by leading to both exotic excitations and reduced critical temperature T_c.

Magnetic frustration occurs when the interactions between the spins are in close competition with each other. The frustration may originate both from lattice geometry and competition of exchange interactions. Some 2D and 3D geometrically frustrated lattices are depicted in **Figure 1.2**. The example of competing interactions is shown in the right side of **Figure 1.3**. It illustrate spins, on a 1D chain, coupled with their nearest (solid lines) and next-nearest (dashed lines) neighbors through antiferromagnetic interactions. The hallmark of frustration is the large degeneracy of the ground state,[3] rather than a single stable ground-state configuration. This feature leads to magnetic analogues of liquid and ice. The lift of ground state degeneracy can be understood with the help of **Figure 1.4**. For Ising spins, which must point upward or downward, on an elementary triangle couple with antiferromagnetic interactions, all three spins cannot be antiparallel at the same time. As a result, instead of the two ground states mandated by the Ising symmetry (up and down), there are six ground states. Such degeneracies can persist on 2D and 3D lattices. More interestingly, these ground states are generally not related by any symmetry operation, so we say the degeneracies are *accidental*.

The low-dimensionality refers to one- or two-spatial dimensionality. In the 2D case (triangular-based lattices), quantum fluctuations are enhanced by geometrical frustrations. For 1D antiferromagnet, spins array by nearest-neighbour isotropic exchange, forming a Heisenberg spin chain. It is a strongly fluctuating statistical system at all temperatures.

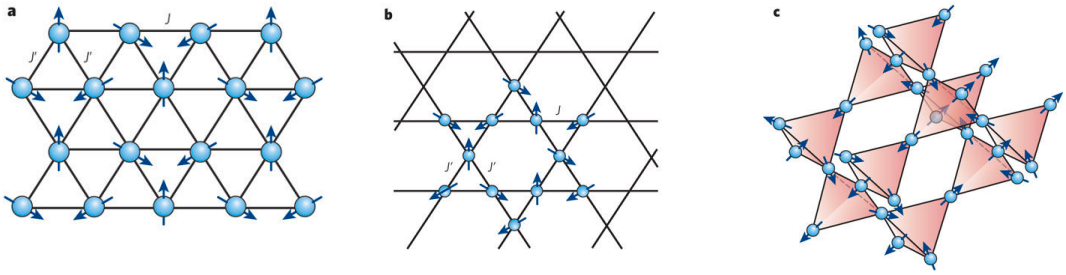

Figure 1.2. Magnetic lattices that are frustrating when occupied by spins with nearest neighbor antiferromagnetic interactions. Two types of 2D lattice are depicted: a triangular lattice (**a**), and a Kagome lattice (**b**). A 3D lattice is a pyrochlore lattice (**c**), and it is in the spin-ice state. (Adapted from Balents[4])

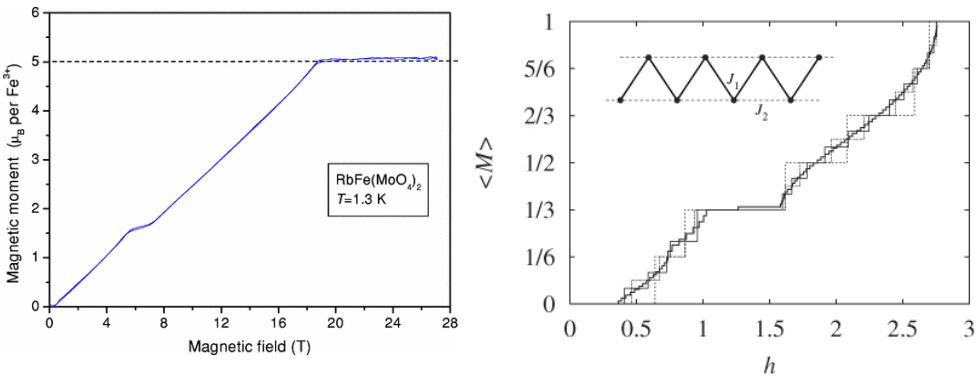

Figure 1.3. Magnetization plateaux. *Left*: The magnetization plateau at 1/3 of saturation observed in $RbFe(MoO_4)_2$, a spin=5/2 triangular lattice. (Adapted from Smirnov et al.[5]); *Right*: Inset: The Heisenberg chain with nearest and next-nearest neighbors coupling J_1 and J_2, respectively. Points denote the locations of S $=$ 1/2 spins. Main panel: the magnetization curve for $J_1 = 1, J_2 = 0.8$. The thin dashed and solid curves were obtained by ED of rings (periodic boundary conditions) with $L = 12$ (dashed), 24 (dotted)[6] and 36 sites (full); the bold solid curve was obtained by DMRG for $L = 192$ sites with open boundary conditions.[7] (Adapted from Honecker et al.[8])

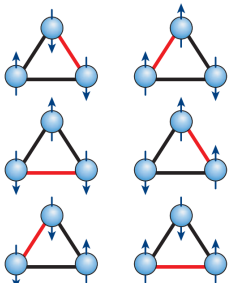

Figure 1.4. Illustrations of accidental degeneracy. A triangle of antiferromagnetically interacting Ising spins, as a example of geometrical frustration. All three spins cannot be antiparallel. As a result, instead of the two ground states mandated by the Ising symmetry (up and down), there are six ground states. (Adapted from Balents[4])

The antiferromagnetic spin chains are expected not to have long-range order in general. Haldane[9] argued for integer, but not half integer spin, that there is a gap to the excited state. The Heisenberg spin-1/2 chain is quantum critical, at $T = 0$ the two-spin correlations decay algebraically, indicating infinitely large correlated antiferromagnetic regions. More interestingly, it has gapless excitation which is fractionalized and known as spinon,[10] depicted in **Figure 1.5**, with spin 1/2 and charge neutral. Spinons in 1D deconfine and

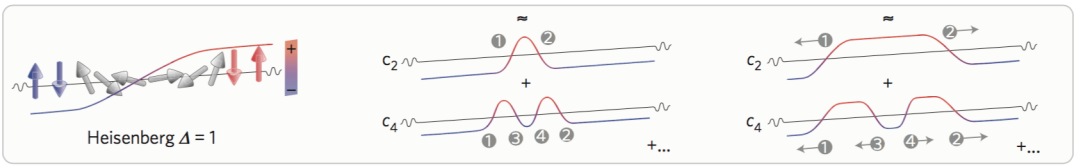

Figure 1.5. Deconfinement of spinons in Heisenberg spin chain. The spatial extent of a spinon on Heisenberg spin$-1/2$ chain, and it decomposes into a rapidly converging series of states containing two, four and higher even numbers of such spinons. (Adapted from Mourigal et al.[11])

become independent elementary excitations. Spinons are created in pairs when probed by neutron scattering. Thus, the excitation spectrum should be continuous, as shown in **Figure 1.6**. For some cases, the phase transitions of quantum spin chains can map onto phase transitions of certain 2D classical models in which the variable parameter is the temperature. Then the role of quantum fluctuations is taken over by thermal fluctuations. Sec. 2.2 falls into this category, and the $h - T$ phase diagram of spin chain material $K_2CuSO_4Br_2$ is shown in **Figure 1.7**. There are many experimental realizations of spin chain, where magnetic atoms residue on the lattice sites of a three-dimensional crystal. The couplings between two of the three crystal axes are negligible, and magnetic atoms only strongly interact along one axis, forming a spin chain. One example is shown in **Figure 1.7**.

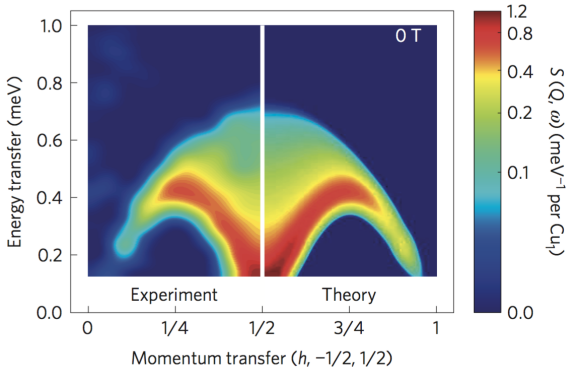

Figure 1.6. Intensity color maps of the experimental inelastic neutron scattering spectrum of $CuSO_4 \cdot 5D_2O$ at zero-field and theoretical two- and four-spinon dynamic structure factor. (Adapted from Mourigal et al.[11])

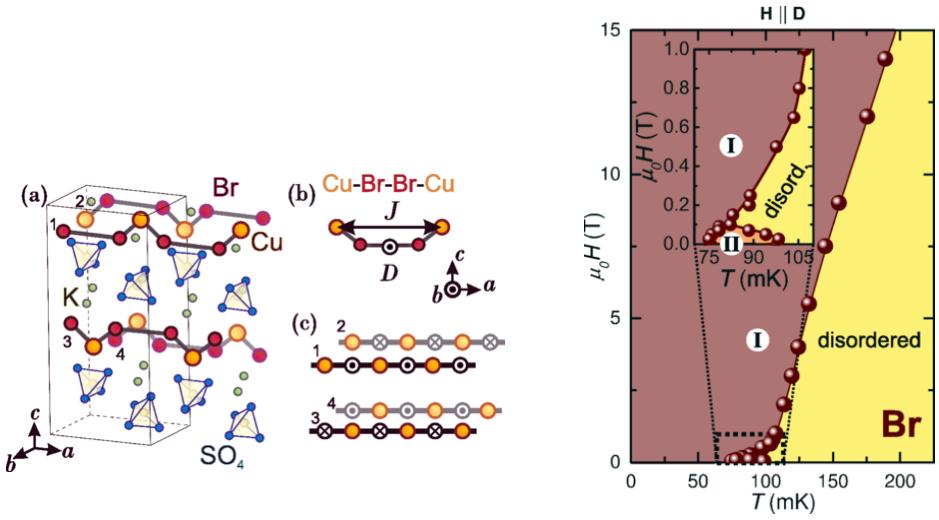

Figure 1.7. Spin chain material $K_2CuSO_4Br_2$ and its magnetic phase diagram. *Left*: Illustration of $K_2CuSO_4Br_2$ lattice, where Cu^{2+} ions form spin chains along the a axis. *Right*: Magnetic phase diagram of $K_2CuSO_4Br_2$ for a magnetic field applied along the b axis, there are two distinct phases. The ordering temperatures are much smaller than exchange energy scale J in order of 1 K. (Adapted from Smirnov et al.[12])

Now let us discuss some novel magnetic phases appearing in low-dimensional frustrated systems. This discussion is ordered by the extent of symmetry breaking of the resultant states. Firstly nontrivial long-ranged orders breaking both spin rotational and time-reversal symmeries are introduced in Sec. 1.1, then bond spin nematic states with partial symmetry breaking is in Sec. 1.2, followed by exotic quantum spin liquid in Sec. 1.3.

1.1 Nontrivial ordered states

Here we introduce two unconventional magnetic ordered states, magnetization plateau and spin density wave, both of which are beyond the classical intuition. These states exhibit long-range orders, and are characterized by a local oder parameter $\langle \boldsymbol{S}_i \rangle \neq 0$ at least in one component.

1.1.1 Magnetization plateau

One of the surprising feature of frustrated antiferromagnets is the occurrence of plateau during the magnetization process. The plateaux are at rational values of the saturation magnetization M_s, namely $m = fM_s$ with f being a fractional number. Two plots in **Figure 1.3** show the $1/3$ magnetization plateaux ($f = 1/3$) observed both by experimen-

tal measurements and numerical simulations. The presence of a magnetization plateau implies some kind of incompressibility,[13] in the sense that in some range of the magnetic field, it is impossible to increase the total spin by increasing the total magnetic field. This phenomenon in turn implies the presence of a gap to magnetic excitations. This gap can be detected by nuclear magnetic resonance (NMR) or inelastic neutron scattering experiments, and indeed it has been detected in a number of systems. For a $m = fM_s$ magnetization plateau, the following relation should be established: $n(S - f)$ must be an integer. Here n is the number of spins in a magnetic cell. When $f = 1/3$, the allowed value of n is multiple of 3, which implies there are 3 sites in a unit cell, and they form a elementary triangle. In this $1/3$-magnetization plateau, two spins on each essential triangle point up and one points down with respect to the direction of the magnetic field. This spin configuration is known as the up-up-down (UUD) state. In this dissertation, I explore an example where the UUD state is induced in a zigzag chain, a spin chain with nearest and next-nearest antiferromagnetic exchange, illustrated in the inset of **Figure 1.3**. The quantum fluctuations and competing interactions stabilize UUD spin arrangement, forming a $1/3$ magnetization plateau as predicted by numerical simulations[7,14] shown in **Figure 1.3**.

Usually the magnetization plateau breaks the spatial symmetry. For example, the UUD state breaks discrete Z_3 symmetry, but it preserves continuous $U(1)$ symmetry of spin rotation on the plane transverse to the magnetic field. In the meantime, the $U(1)$ symmetry is usually broken outside the plateau. According to the Landau theory of symmetry breaking, the phase transition between two phases is generically either of first order, or it involves an intermediate phase where both types of order coexist.[13] For the first case, a magnetization jump should be present at the transition. This jump corresponds to an anomaly in the field dependences of dM/dH measurements, see Figure 3(a) in.[5] As for the second case, the expected intermediate phase should break both the spatial and the rotational spin symmetries.

1.1.2 Spin density wave

Now we consider another unusual magnetic ordered state in magnetic insulators, the spin density wave (SDW). SDW usually exists when considering the magnetism in metals,

for electron gas having nested Fermi surfaces.[1] Here in magnetic insulators, the SDW phase is characterized by the *modulated* expectation value of the local magnetization,[15]

$$\langle S^z_{\boldsymbol{r}} \rangle = M + \Re[\boldsymbol{\phi} e^{i\boldsymbol{k}_{\rm sdw}\cdot\boldsymbol{r}}], \tag{1.1}$$

where $\boldsymbol{\phi}$ is the SDW order parameter and the SDW wave vector $\boldsymbol{k}_{\rm sdw}$ can be both commensurate and incommensurate with the lattice. This SDW is unusual in a sense that the modulated expectation value is contradictory to a classical intuition, where the spin is treated as a vector with fixed length. This collinear SDW preserves U(1) symmetry of rotations about the direction of $\boldsymbol{\phi}$. The SDW is usually induced by external magnetic field, and $\boldsymbol{\phi}$ is along the field. The appearance of such a state in a frustrated system of coupled spin-1/2 chains, as discussed in Secs. 2.1 and 2.2, originates from the equivalence between Heisenberg spin chain and one-dimensional spin-1/2 Dirac fermions, see details in Ref.[15,16] and also Sec. 1.5.1. The spin-1/2 Ising-like antiferromagnet $BaCo_2V_2O_8$ maybe was the first magnetic insulator to realize collinear SDW order. This ordering is confirmed by neutron diffraction measurements in Ref.[17] In Sec. 2.2, it is proposed that several magnetic-field-induced two-dimensional SDW states may also emerge in a system of weakly coupled spin-1/2 chains subject to Dzyaloshinskii-Moriya interactions.

It turns out that the magnetization plateau phase is a commensurate collinear SDW phase. For example, the UUD spin configuration corresponds to $k_{\rm sdw} = 2\pi/3$. This configuration is a "sliding" SDW state, which locks in with the lattice with a period of three lattice spacing and breaks the continuous translational symmetry.

1.2 Spin nematic and bond nematic

A magnetic ordered state breaks both spin rotational symmetry and time-reversal symmetry. One may ask whether there is a possibility that a state breaks spin rotational symmetry, and keeps the time-inversion symmetry intact. The answer is yes, and one example is the spin nematic state. It has no magnetic order, i.e., $\langle S_i \rangle = 0$, but still breaks the spin rotational symmetry, by virtue of a more complicated order parameter.[18] There are many possible nematic states, for example, the onsite quadrupolar order. Here we focus on the bond-nematic order associated with the two-magnon pairing and the establishment of a nonlocal order parameter $\boldsymbol{P}_{12} = \boldsymbol{S}_1 \times \boldsymbol{S}_2$, which is defined on the bond connecting two sites $1, 2$. Because $\boldsymbol{P}_{12}$ is bilinear in the spin operators, it describes a type of order where

time-reversal symmetry is not broken. When $\langle \boldsymbol{P} \rangle \neq 0$, it is called p-nematic, one type of bond nematics.

Figure 1.8 gives an example of the bond nematic, which is named as *spin-current order*,[19] on triangular lattice. This state is characterized by both a chiral vector $\boldsymbol{P}$ and a chiral scalar, namely within a single triangle ABC, $\langle \boldsymbol{S}_A \cdot \boldsymbol{S}_B \times \boldsymbol{S}_C \neq 0 \rangle$ and $\langle \hat{\boldsymbol{z}} \cdot \boldsymbol{S}_A \times \boldsymbol{S}_B \rangle = \langle \hat{\boldsymbol{z}} \cdot \boldsymbol{S}_B \times \boldsymbol{S}_C \rangle = \langle \hat{\boldsymbol{z}} \cdot \boldsymbol{S}_C \times \boldsymbol{S}_A \rangle \neq 0$. This state supports circulating spin currents illustrated by arrows in **Figure 1.8**. This state emerges as a result of the condensation of two-magnon pairs. Different from what is proposed for $LiCuVO_4$, here the magnons repulsively interact. (This material[20,21] $LiCuVO_4$ is a spin-nematic candidate based on the combination of frustrated ferromagnetic interactions, low dimension and high magnetic field.) In Sec. 3.2, the same spin current state is predicted in a zigzag ladder. Recently, such a bond nematic has been predicted as a ground state, instead induced by magnetic field, for a spin-1 XXZ model (XXZ model is defined in Eq. (1.7)) on triangular lattice.[22] The authors of[22] found that an easy-plane single-ion anisotropy term, $D(S^z)^2$ ($D > 0$) is also required to realize this chiral state.

The possible observation of a quantum spin-nematic in a real material is challenging. The widely used probes of magnetic order, including neutron scattering, NMR and μSR, couple to internal magnetic fields in the sample. Since quantum spin nematics do not break time reversal symmetry, such internal fields must vanish, rendering spin-nematic order "invisible." Recent inelastic neutron scattering measurements[23] on $PbCuSO_4(OH)_2$ have seen indirect evidence of a spin nematic resulted by two-magnon bound state by tracking the change of propagation vector with magnetic field and temperature.

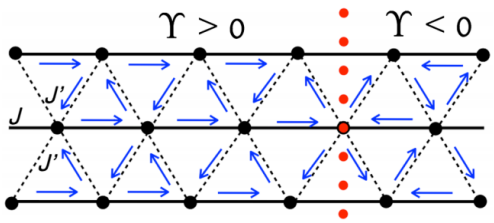

Figure 1.8. The structure of spin currents in the state. The domain wall, denoted by a vertical (red) dotted line, separates domains with opposite chirality γ .(Adapted from Chubukov and Starykh[19]).

1.3 Quantum spin liquids

Quantum spin liquid (QSL) is described as the absence of long range order down to $T = 0$ K. Instead of being defined by what it is not, a more modern definition of QSL, given by Savary and Balents,[24,25] is that a QSL is a state which cannot, in any way, to be connected to a product state. The QSL is an intrinsic ground state, without the induction by external magnetic field, for example, the quantum Hall state.

Quantum spin liquids also play an important role in understanding high T_c superconductors.[26] Due to the fact that spin liquid can lead to a spin-charge separation (the same phenomenon happens for 1D chain), an electron splits into two quasiparticles—a spinon and a holon (spin-0 charge-e). The condensation of holon can lead to high T_c superconductivity.

1.3.1 Valence-bond solids and resonating-valence-bond spin liquids

To start the discussion of QSL, we need to understand the concepts of "valence-bond solids" and "resonating-valence-bond spin liquids" and the differences between these two.

1.3.1.1 Valence-bond solids

The entanglement of two spins, labeled as 1 and 2, separated by any distance enable them talk to each other by forming a state $\phi(1,2) = (|\uparrow_1\downarrow_2\rangle - |\downarrow_1\uparrow_2\rangle)/\sqrt{2}$, named as *valence-bond* state. When this valence bond arranges in a spatially regular pattern, every two spins form a singlet state, as illustrated in on the top of **Figure 1.9**. The system is called a *valence bond solid* (VBS) whose wave function is a product of valence bond sate,

$$\psi_{\text{vbs}}(1,2,\ldots,N) \propto \phi(i_1,i_2)\phi(j_1,j_2)\ldots\phi(k_1,k_2), \tag{1.2}$$

where i, j, and k label different singlet. This a VBS is an ordered state (therefore the use of the word "solid"), which breaks lattice symmetry spontaneously, and persist the spin-rotational symmetry. Such VBS states have been observed in organic compound[27] (C_2H_5)-$(CH_3)_3P[Pd(dmit)_2]_2$.

1.3.1.2 Resonating-valence-bond spin liquids

While the *resonating valence bond* (RVB) state is a superposition of all the possible manifolds of valence-bond configurations (by shuffling all the valence bonds), as depicted in the

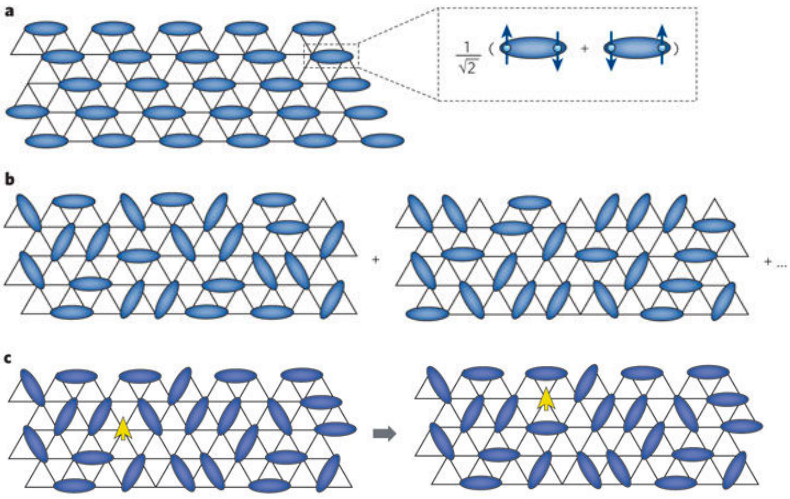

Figure 1.9. Valence-bond (VB) solid and resonating-valence-bond (RVB) spin liquid on triangular lattice. (***a***) Valence bond (VB) solids. (***b***) Resonating valence bond (RVB) state. (***c***) Excitations in a RVB state, where a spinon can move freely by locally adjusting the valence bond. (Adapted from Balents[4])

middle of **Figure 1.9**, such a state has no long range order in any spin, dimer or higher-oder correlation functions. It is a true liquid[28] and restores the translational symmetry of the lattice from VBS. The quantum spin liquids host some exotic emergent properties, for instance the appearance of "fractional excitations," spinons. (On the contrary, excitations in VBS have $\Delta S = \pm 1$). In neutron scattering, the spinons are created in pairs, and they can move from one site to another (nearly) freely, as shown on the bottom of **Figure 1.9**. This is a "deconfinement" analogy to that in the 1D chain shown in **Figure 1.5**. The downside of this property is that, as spin spectral weight can be distributed over a broad range of energy, the spinons are difficult to observe in neutron scattering measurements. There are various types of RVB spin liquids, including Z_2 spin liquids, U(1) spin liquids, and SU(2) spin liquids. The theoretical study of spin liquids usually resorts to gauge field theories, examples of which can be found in Ref.[24]

1.3.2 Chiral spin liquid

In 1987, Kalmeyer and Laughlin[29] introduced a special kind of spin liquids —chiral spin liquid—to explain high temperature superconductivity. Chiral spin liquids (CSLs) are spins counterparts of fractional quantum Hall effect,[30] and are spin liquids that break

time-reversal symmetry and parity. Since the time-reversal symmetry is broken, they are named "chiral." The order parameter is a nonzero scalar spin chirality, $\chi_{ijk} = S_i \cdot S_j \times S_k$ (same as the spin current state), for some triplets of nearby spins i, j, k. The chiral spin liquid have excitations with fractional and non-Abelian statistics. The low energy effective theory of the chiral spin liquids is a U(1) Chern-Simons theory—a topological quantum field theory.[31] The CSL is characterized by a chiral edge and gapped bulk state. To prove a state is exact CSL, one has to study its topological properties, since CSL is a topological order.[32]

Construction of a Hamiltonian, whose ground state is chiral spin liquid, is still challenging. Attempts are made by studying the Kitaev model on the triangle-honeycomb lattice[33] or the Heisenberg model on the Kagome lattice with $J_1 - J_2 - J_3$ coupling,[34,35] as shown in **Figure 1.10**. The CSLs in these two models break the time-reversal symmetry spontaneously. These two Hamiltonians are, however, very complex, and this complexity means difficulties of their experimental realizations. From this point of view, Thomale[36] proposed constructing CSL on a set of coupled quantum wires subject to a Zeeman field and spin-orbit coupling, which is inspired by Kane and collaborators.[37] In a quantum wire, 1D system, the low-energy electron moves around two Fermi points. The mode near $-k_F$ is called left-mover and the one near k_F is right-mover. A simpler and more elegant way

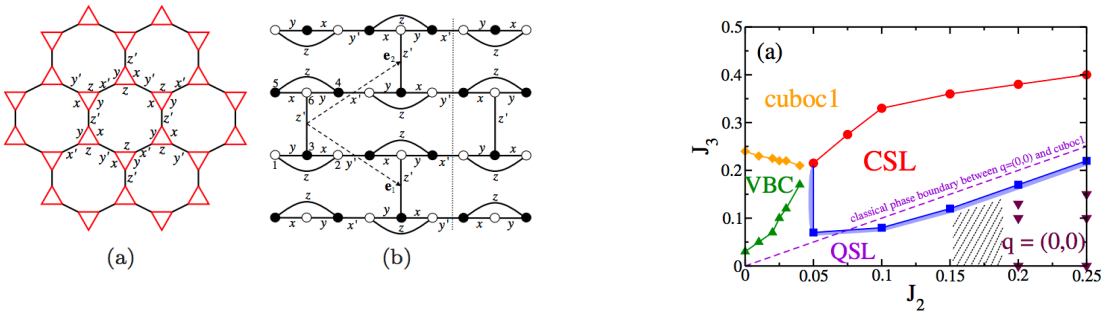

Figure 1.10. Chiral spin liquid with spontaneous time-reversal symmetry. *Left:* (a) The triangle-honeycomb lattice based on a honeycomb lattice by replacing each site with a triangle. (b) Topologically equivalent representation. (Adapted from He and Chen[33]). *Right*: quantum phase diagram of the spin-1/2 $J_1 - J_2 - J_3$ Heisenberg model on Kagome lattice, which is a corner-sharing triangular lattice. (Adapted from Gong et. al[34]) The chiral spin liquid (CSL) in these two models breaks the time-reversal symmetry spontaneously.

to obtain a CSL is to install the desired couplings between right movers in a wire i to left movers of wire $i+1$. The uncoupled left (right) mode residues on the top (bottom) wire thus form a chiral edge state. All the wires in between are gapped through the couplings to neighboring wire. By virtue of the equivalence between Heisenberg spin chain and one-dimensional spin-1/2 fermions, a possible way to construct a CSL on weakly coupled spin chains is presented in this dissertation. However, this chiral spin liquid is not an exact ground state, but induced by external magnetic-field; see details in Sec. 2.3.

1.3.3 Spin ice, quantum spin ice, and pyrochlore lattice

Up to now, we have discussed the novel phases realized in 1D or 2D models. Now we may wonder what happens for 3D lattices, more unusual or less unusual. It turns out that there are unique phases that persist on 3D lattices. Here we focus on the pyrochlore lattice, a network of cornering sharing tetrahedra, see **Figure 1.2**.

1.3.3.1 Spin ice

As discussed at the beginning, geometrical frustration gives rise to huge ground-state degeneracy. One of the most degenerate/frustrated lattices in three dimensions is the pyrochlore lattice pictured in **Figure 1.2**. When this lattice is occupied by Ising-like magnetic rare-earth moments (Ho^{3+}, Dy^{3+}) coupled by an effective ferromagnetic interactions, the large ground-state degeneracy is just equivalent to that of water ice. As a result, the system is in a state called spin ice, where spins on each tetrahedra follow the "ice rule": two spins point into the center of tetrahedra and two point out. **Figure 1.2**-c illustrates this state. The equivalence of spin ice with water ice can be seen in **Figure 1.11**. The center of tetrahedra corresponds to the position of oxygen, and thus Ising spins are located at the middle of oxygen-oxygen bond, and points precisely along the bond in the direction of the oxygen atom closest to the proton. These centers form a diamond lattice. The spins can flip as hexagonal loops in **Figure 1.11**.

The excitations of spin ice is rather surprising, due to the fact that they emerge as magnetic monopoles.[38] This can be understood by the dumbbell model. As shown in **Figure 1.12**, the point-like magnetic dipoles (spins) can be fattened up into a rod with two magnetic charges $\pm q_m$ at the centers of two tetrahedra. The diamond lattice spacing is a_d, and thus the dipole moment recovers as $\mu = q_m a_d$.[39] Then the flip of a single spin can

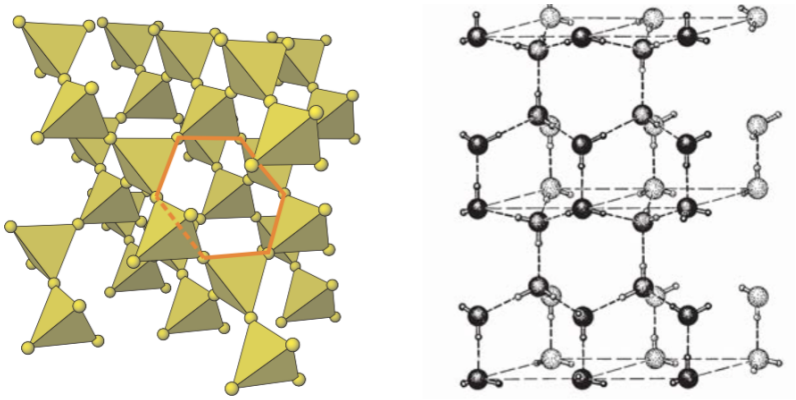

Figure 1.11. Equivalence between pyrochlore lattice and water ice. *Left:* The pyrochlore lattice. The orange hexagonal loop consists of edges of a group of tetrahedra, which can support a zero-energy mode. *Right*: The hexagonal ice consists of protons (small spheres) on the bond connecting two oxygen atoms (large spheres). The oxygens form a diamond lattice. (Adapted from Moessner and Ramirez[3])

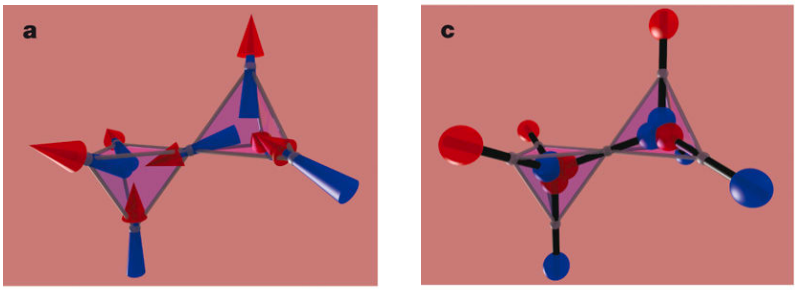

Figure 1.12. Illustration of the dumbbell model for spin ice. (Adapted from Castelnovo, Moessner and Sondhi[38])

be visualized as a change of charge in a tetrahedron by $\pm 2q_m$, then generates a pair of magnetic monopoles. This pair can move along paths on diamond lattice by flipping of spins along the way.

1.3.3.2 Quantum spin ice

The spin ice is a classical state. It is expected that adding some quantum fluctuations to this classical model will lead to the quantum spin ice state, a quantum spin liquid with gapless photon-like excitations (U(1) QSL). The quantum fluctuations are introduced when the spin interactions are described by XXZ model, instead of Ising model.[39] This line of

study is one of the most promising ways to realize spin liquid in 3D model materials, such as $Tb_2Ti_2O_7$, $Pr_2M_2O_7$ (M=Sn,Zr), and $Yb_2Ti_2O_7$.

1.4 Microscopic model

Here we focus on a spin model of magnetic insulators, where we suppose that the charge degrees of freedom are strongly quenched. There are many spin models that have been introduced; here we focus on the Heisenberg model. The Kondo model, $t-J$ model, or Kitaiev model are beyond the scope of this dissertation.

For a magnetic insulator, the magnetic degrees of freedom are spin S unpaired electrons associating with each magnetic atom, such as Cu atom. A spin system is formed by placing a spin $\boldsymbol{S}_i$ on each ion site of the crystal lattice i, and the charge degrees of freedom are quenched. The three components of the spin S^x, S^y, S^z obey the commutation relation,

$$[S^\alpha, S^\beta] = i\xi_{\alpha\beta\gamma}S^\gamma, \tag{1.3}$$

where $\xi_{\alpha\beta\gamma}$ is the totally antisymmetric tensor (that is, equal to zero if two indices are equal and $\xi_{\alpha\beta\gamma} = 1$). The spin operators on different sites commute. It is customary to introduce the ladder operators:

$$S^+ = S^x + iS^y, \quad S^- = S^x - iS^y. \tag{1.4}$$

The S^+ and S^- are raising and lowering operators that raise or lower the magnetic quantum number m of the spin state by 1. Their commutation relations are:

$$[S_i^+, S_j^-] = 2S_i^z\delta_{ij}, \quad [S_i^z, S_j^+] = S_i^+\delta_{ij}, \quad [S_i^z, S_j^-] = -S_i^-\delta_{ij}. \tag{1.5}$$

From these commutators, we see that spins are neither bosons or fermions, and this property makes spin problems difficult to solve. Therefore we need to map the spin problems to those of bosonic or fermionic ones; see discussions in Sec. 1.5.

1.4.1 Heisenberg model

When the dominant magnetic interactions between ions are from superexchange, the quantum Hamiltonian to describe this system would be the Heisenberg model. The Heisenberg Hamiltonian is in the form

$$H = J\sum_{\langle ij\rangle} \boldsymbol{S}_i \cdot \boldsymbol{S}_j. \tag{1.6}$$

Here the sum runs over all neighboring sites on the lattice under consideration, J is the exchange coupling constant between two spins $\boldsymbol{S}_i$ and $\boldsymbol{S}_j$. Here J is the same for any two spins, and the spin system is homogenous; for many practical cases, it is sufficient to consider only nearest neighbor exchange, where $j = i + 1$. If $J > 0$, Eq. (1.6) describes antiferromagnetic coupling. Usually the coupling constant in one direction, say z, is different from those in the other directions. Here comes the anisotropic Heisenberg model (or XXZ model):

$$H = J \sum_{\langle i,j \rangle} \left[\frac{1}{2}(S_i^+ S_j^- + S_i^- S_j^+) + \Delta S_i^z S_j^z \right]. \tag{1.7}$$

S_j^+, S_j^- have been defined in Eq. (1.4), and

$$S_i^+ S_j^- + S_i^- S_j^+ = 2(S_i^x S_j^x + S_i^y S_j^y) = 2(\boldsymbol{S}_i \cdot \boldsymbol{S}_j - S_i^z S_j^z). \tag{1.8}$$

Here Δ is the spin anisotropy parameter, such that $\Delta = 1$ recovers the isotropic Heisenberg limit, $\Delta > 1$ corresponds to uniaxial (Ising-like) anisotropy, and $0 \leq \Delta < 1$ to easy-plane anisotropy. Notice, the Heisenberg Hamiltonian can be only applied to magnetic insulators, when there is no itinerant electron. The theoretical derivation of Heisenberg model is first done by Dirac[40] for $S = 1/2$, and P. W. Anderson[41] proved that this model is also suitable for $S > 1/2$.

1.4.2 Perturbations

While the Heisenberg model in Eq. (1.6) provides a useful basis for understanding the properties of a variety of frustrated magnetic materials, for real, non-ideal systems, inevitable compound-dependent perturbations H' are present. These perturbations usually break some symmetries. These H' include disorders, anisotropies and long-range interactions and lead to a complication of the corresponding phase diagrams. The description of possible types of phases (magnetic structures) is the major subject in this dissertation. Even though the energy scale J' of perturbations is usually smaller than the dominant exchange energy scale J in Eq. (1.6), namely $J' \ll J$, sometimes these perturbations cannot be treated perturbatively.[3] For example, in Chapter 2 the one space-dimensional system is studied by the nonperturbative approach—bosonization, due to the strong correlation effects in the system. As for frustrated magnets, where the frustration leads to large ground state degeneracy, the perturbative method also fails in the spin liquid regime.

1.4.2.1 Dzyaloshinskii-Moriya (DM) interaction

Among the many possible perturbations, we focus on the Dzyaloshinskii-Moriya (DM) interaction,[42,43] an antisymmetric exchange, which originates from spin-orbit coupling, and is widely present in real materials. In a magnetic system, when there is no inversion center between two magnetic sites, there may be present the DM interaction. It is described by a mathematic form of a cross product of two spins:

$$H_{\mathrm{DM}} = \boldsymbol{D}_{ij} \cdot \boldsymbol{S}_i \times \boldsymbol{S}_j. \tag{1.9}$$

This results in a antisymmetric exchange between two spins $\boldsymbol{S}_i$ and $\boldsymbol{S}_j$. We notice that the DM vector $\boldsymbol{D}_{ij}$ tries to pin the two spins in the plane perpendicular to itself,[1] producing a small twist, or canting, of the atomic moments.[44]

The DM interaction is characterized by the DM vector $\boldsymbol{D}_{ij}$, which depends on the relative positions of the magnetic atoms. Mathematically, there is a Moriya rule[43] to determine the orientation of the DM vector from the crystal structure. Take two magnetic ions A and B, and their center is located at point C, for example : when there is a mirror plane which includes A and B, then the DM vector is perpendicular to line AB. On the experimental side, $\boldsymbol{D}$ can be characterized by the electronic spin resonance (ESR) measurements.[12,45,46] In a magnetic field $\boldsymbol{h} \parallel \boldsymbol{D}$, two resonance lines (ESR doublet), shown in **Figure 1.13**, are observed at resonance frequencies $\nu_{\pm}$, with $2\pi\hbar\nu_{\pm} = |g\mu_B h \pm \pi D/2|$. This ESR doublet is only observable for a magnetic field having a component along $\boldsymbol{D}$; thus this property can be used to determine the direction of $\boldsymbol{D}$. In another limiting case $\boldsymbol{h} \perp \boldsymbol{D}$, in contrast, there is only one line shifting with temperature, and the resonance occurs at the "gapped" frequency $2\pi\hbar\nu = \sqrt{(g\mu_B h)^2 + (\pi D/2)^2}$. This gap provides an alternative way to obtain the amplitude D. (The line shape and the temperature dependence of the width of the resonance were studied in Refs.[47] and,[48] correspondingly.) In the case of $K_2CuSO_4Br_2$, several ESR measurements[12,45] have consistently predicted $D_{\mathrm{Br}} \approx 0.28$ K. In $K_2CuSO_4Cl_2$ the DM interaction is smaller. A recent experiment[49] estimates it to be $D_{\mathrm{Cl}} \approx 0.11$ K.

1.5 "Bosonized" and "fermionized" mapping

Working with spin operators is unpleasant since they have funny commutation relations; see Sec. 1.4.1. Hamiltonian with bilinear boson or fermion operators may be solved, in accordance with the specific systems, but one needs to map the spins to either bosons

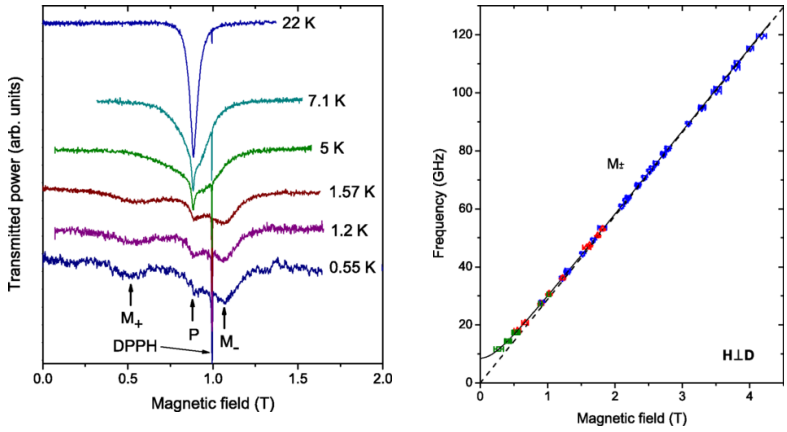

Figure 1.13. Electronic spin resonance measurements of spin chain material $K_2CuSO_4Br_2$. *Left:* ESR lines (doublet) at $\boldsymbol{H} \parallel \boldsymbol{D}$. M_+ and M_- label the doublet. *Right:* Frequency-field diagram for $\boldsymbol{H} \perp \boldsymbol{D}$ in the low-temperature limit. (Adapted from Smirnov et. al[12]).

or fermions. There is no unique way to describe a many-body system, but the mapping is a matter of convenience. In this dissertation we use two types of mapping, either "bosonized" or "fermionized."

1.5.1 Jordan-Wigner transformation and XXZ spin-1/2 chain

First, we introduce a way to "fermionize" the spin-1/2 operator, the Jordan-Wigner transformation, then apply it to the spin chain problem, as we see it establishes the equivalence between Dirac fermions and 1D spin-1/2 problem.

1.5.1.1 Jordan-Wigner transformation

From Eq. (1.8), we notice that for spin-1/2, $\boldsymbol{S}_j \cdot \boldsymbol{S}_j = S(S+1) = 3/4$ and $(S_j^z)^2 = 1/4$, which has a remarkable property:

$$\{S_j^+, S_j^-\} = 1, \tag{1.10}$$

the S_j^+ and S_j^-, on the same site, obey an anticommutation relation, which suggests an analogy with fermions. Also the spin operators on different sites do note anticommute, but commute. So it is not possible to map spin just to a single fermi creation/annihilation operator. However, it turns out that it is possible to produce spin algebra by multiplying a phase factor which is dependent on spin site, thus the Jordan-Wigner transformation:[50–52]

$$
\begin{aligned}
S_j^+ &= \psi_j^\dagger \exp(i\pi \sum_{k<j} \psi_k^\dagger \psi_k), \\
S_j^- &= \exp(-i\pi \sum_{k<j} \psi_k^\dagger \psi_k) \psi_j, \\
S_j^z &= \psi_j^\dagger \psi_j - 1/2,
\end{aligned}
\tag{1.11}
$$

where the Fermi operator ψ satisfies the standard anicommutation relations. This transformation (1.11) is only valid for one dimension, which will be applied to the spin chain problem in Chapter 2.

1.5.1.2 Fermionic Hamiltonian for Heisenberg spin chain

With this transformation (1.11), the spin Hamiltonian (1.7) is equivalent to interacting spinless fermions:

$$
H_F = J \sum_i \left[\frac{1}{2} (\psi_i^+ \psi_{i+1} + \psi_i \psi_{i+1}^+) + \Delta (\psi_i^\dagger \psi_i - \frac{1}{2})(\psi_{i+1}^\dagger \psi_{i+1} - \frac{1}{2}) \right]. \tag{1.12}
$$

The Jordan-Wigner transformation establishes equivalence between the spin-1/2 XXZ spin chain and the model of interacting fermions. For a one-dimensional fermions, the corresponding fermionic problem has Fermi momentum $k_F = \pi/2$, if there is no magnetic field. (Finite magnetic field corresponds to a chemical potential for the fermions). To obtain an effective low-energy continuum fermionic theory, we perform a linearization around the free Fermi points given by k_F, and then express the fermion operators in terms of bosonic ones related to the fermion density fluctuation by using the standard dictionary of Abelian bosonization.[50,52,53] The bosonization technique is one of the most powerful nonperturbative approaches to study strongly correlated many-body systems, especially in 1D/quasi-1D systems.

1.5.1.3 Bosonization

The bosonized version of the XXZ model is,

$$
H_B = \frac{v}{2} \int dx [K(\partial_x \theta)^2 + \frac{1}{K} (\partial_x \phi)^2], \tag{1.13}
$$

where θ and ϕ are bosonic scalar fields, K is the Luttinger parameter, and v is the Fermi velocity of Jordan-Wigner fermions. This Gaussian (quadratic) model (1.13) is valid for a spin chain with $-1 < \Delta \leq 1$. For the isotropic point $\Delta = 1$ and $K = 1$, the correlation functions display SU(2)-invariant behavior.

1.5.1.4 Heisenberg spin chain + DM interaction

When the DM term (1.9) is present in a Heisenberg spin chain, and the system is described by the following Hamiltonian,

$$H = \sum_x J\left[(S_x^x S_{x+1}^x + S_x^y S_{x+1}^y) + S_x^z S_{x+1}^z\right] + \boldsymbol{D}\sum_x \boldsymbol{S}_x \times \boldsymbol{S}_{x+1}. \tag{1.14}$$

where $J < 0$, $\mathbf{S}_x$ is the spin-1/2 operator at site $x = na$, with a is the lattice spacing, and spin chain runs along the $\mathbf{x}$ axis. The DM vector $\mathbf{D} = D\hat{z}$ is uniform along chain. We consider $D/J \ll 1$, which is the most natural limit relevant for real materials.[12,44,45] The DM term in Eq. (1.14) can be gauged away by a position-dependent rotation of spins about $\hat{z}$ axis, $S_x^+ \to \tilde{S}_x^+ e^{i\alpha x}$ and $S_x^z \to \tilde{S}_x^z$, where the rotation angle $\alpha = \arctan[D/J]$, which is determined by the ratio D over J; therefore the rotation angle α is small. After the rotation, we have an effective XXZ chain with Hamiltonian,

$$\tilde{H} = \sum_x \left[\frac{\tilde{J}}{2}(\tilde{S}_x^+ \tilde{S}_{x+1}^- + \text{h.c.}) + J\tilde{S}_x^z \tilde{S}_{x+1}^z\right], \tag{1.15}$$

where $\tilde{J} = \sqrt{J^2 + D^2}$ describes the transverse component of exchange interaction for the obtained XXZ chain. We see that, in addition to "twisting" spins around the $\boldsymbol{D}$ axis, the uniform DM interaction effectively introduces an Ising anisotropy.[54] The Luttinger parameter of the XXZ chain (1.15) is given by,

$$K^{-1} = 1 - \arccos[J/\sqrt{J^2 + D^2}]/\pi \simeq 1 - D/(\pi J). \tag{1.16}$$

1.5.2 Holstein-Primakoff transformation and spin-wave theory

Here, we discuss a semiclassical method to "bosonize" the spin operator, Holstein-Primakoff transformation, which has been a standard approach to study a magnetic ordered state.

1.5.2.1 Holstein-Primakoff transformation

When spin system is in a magnetic ordered state, which is associated with the fact that the expectation value $|\langle \boldsymbol{S}_i \rangle| \neq 0$, the spins can usually treated as classical, i.e., simple vectors. To study the low-temperature excitations of the classical configuration, quantum effects are added through "quantum fluctuations." A technique we use in this dissertation is Holstein-Primakoff (HP) transformation.[55] The spin operators $\boldsymbol{S}_i$ can be expressed by

bosonic creation and annihilation operators $a_i^\dagger$ and a_i, effectively truncating their infinite-dimensional Fock space to finite-dimensional subspaces.

$$\begin{aligned} S_i^+ &= \left(\sqrt{2S - n_a}\right) a_i, \\ S_i^- &= a_i^\dagger \sqrt{2S - n_a}, \\ S_i^z &= S - n_a. \end{aligned} \tag{1.17}$$

here $n_a = a^\dagger a$ is the number operator for a boson. We can check that, using the commutator $[a_i, a_i^\dagger] = 1$, the operators above indeed obey the spin commutation relation in Eq. (1.3). HP bosons in Eq. (1.17) are defined with respect to the z axis. A more general form for arbitrary classical configuration, which minimizes the system's Hamiltonian, can be found in Ref.[56]

Here we consider a bipartite model, where the sublattice A and B having spins along $\hat{z}$ and $-\hat{z}$, respectively. Starting from a Neel state $|Neel\rangle$, there is this relation,

$$S_{ai}^+ |Neel\rangle = S_{bj}^- |Neel\rangle = 0. \tag{1.18}$$

Here operators a and b are defined on two sublattices A and B, correspondingly. Spin operators on A-sublattice is mapped to a by Eq. (1.17). We notice, S^+ on B-sublattice has the same effect as S^- on A-sublattice; therefore, the HP transformation for B-sublattice is,[57]

$$\begin{aligned} S_{bj}^+ &= b_j^\dagger \sqrt{2S - n_b}, \\ S_{bj}^- &= \left(\sqrt{2S - n_b}\right) b_j, \\ S_{bj}^z &= n_b - S. \end{aligned} \tag{1.19}$$

The commutation relations between a and b are also satisfied.

This HP formalism is applied Chapter 3, where we study the instabilities of fully polarized state or the UUD phase on triangular-based lattices.

1.5.2.2 Spin-wave Hamiltonian

The square roots in Eqs. (1.17) and (1.19) are rather inconvenient and the practical usefulness of the scheme lies in the expansion of it in powers of $1/S$,

$$\sqrt{2S - n_a} = \sqrt{2S}\left(1 - \frac{n_a}{4S} - \frac{n_a^2}{32S^2} \cdots\right). \tag{1.20}$$

The above expansion of original Heisenberg Hamiltonian (1.6) leads to the spin-wave Hamiltonian,[15]

$$H = E_{\text{cl}} + \sum_{k=2}^{\infty} H^{(k)}. \tag{1.21}$$

Here E_{cl} is the classical energy of spin configuration, which scales as S^2, and the subsequent terms $H^{(k)}$ are of k-th oder in bosonic operator a and scale as $S^{2-k/2}$. Diagonalization of the quadratic term $H^{(2)}$ results in the dispersion $\omega_{\boldsymbol{k}}^m$ of spin wave excitations ($\boldsymbol{k}$ is the wave vector and m is the band index). Higher order terms produce the interaction between bosons. Interestingly, when k is odd (when the spin-orbit coupling is present) or there are terms like $H^{(4)} \propto a_1^\dagger a_2^\dagger a_3^\dagger a_4$ (for example in UUD state on triangular antiferromagnet[19]), $H^{(k)}$ describes a process that doesn't conserve the number of bosons, and the zero-point vibration should be considered.[58]

1.5.2.3 Measurement of spin waves

The spin-wave dispersion can be measured[1] by the technique called neutron scattering. The quanta of spin wave is magnon, a boson. The incident neutron scatters with magnons with energy $\hbar\omega$ and wave vector $\boldsymbol{q}$, and its wave vector change from initial $\boldsymbol{k}$ to scattered one $\boldsymbol{k}'$. The energy of the neutron also changes from $E = \hbar^2 k^2/(2m_n)$ to $E' = \hbar^2 k'^2/(2m_n)$. By conservation of energy and momentum,

$$E = E' + \hbar\omega, \qquad \boldsymbol{k} = \boldsymbol{k}' + \boldsymbol{q} + \boldsymbol{G}, \tag{1.22}$$

where $\boldsymbol{G}$ is a reciprocal lattice wave vector.[1] Therefore, ω and $\boldsymbol{q}$ can be obtained by measurements of $\boldsymbol{k}$, $\boldsymbol{k}'$, E and E'. The neutrons have energies in the meV to eV range. Magnon energies are typically in the range 10^{-3} to 10^{-2} eV, and therefore can be effectively measured using inelastic neutron scattering. **Figure 1.14** gives an example of the neutron scattering data.[59] By comparing to the theoretical dispersion relation, one can fix the spin coupling constants in the material. Also, the neutron scattering cross section is proportional to the spin-spin correlation functions.

The rest of this dissertation is organized as follows. In Chapter 2, we systematically study the phases on spin-1/2 chain system that is in the presence of uniform Dzyaloshinskii Moriya interactions and magnetic field. In Chapter 3, we identify various novel spin structures and a nematic phase on the frustrated antiferromagnets, with frustration induced by either lattice geometry or competing interactions. Chapter 4 summarizes the

[1]The addition of $\boldsymbol{G}$ is necessary because the dispersion relation of magnons is periodic in the reciprocal lattice.

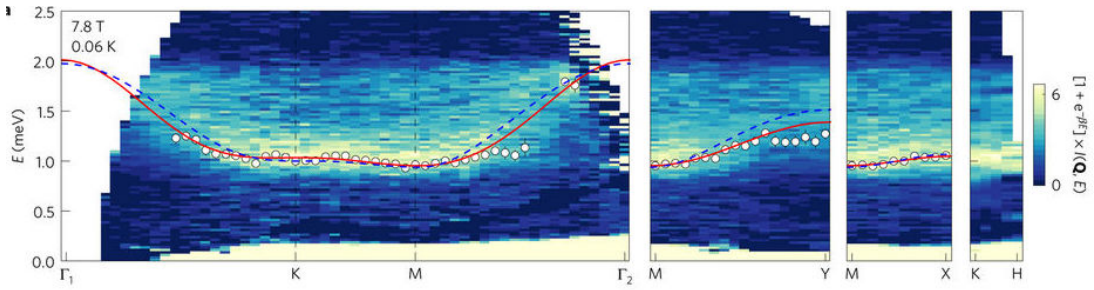

Figure 1.14. Field-polarized neutron-scattering measurements on $YbMgGaO_4$, in which Yb^{3+} ions with effective spin-1/2 occupy a triangular lattice. Energy dependence of magnetic excitations along high-symmetry directions, measured at 0.06 K in an applied field of 7.8 T. The red and blue lines show a fit to the spin-wave dispersion relation.(Adapted from Paddison et al.[59]).

main points of each project, and overviews the contributions of these projects. The renormalization group theory and chain mean field approximation are introduced in the two Appendices A and B, respectively.

CHAPTER 2

NOVEL ORDERS IN SPIN-CHAIN SYSTEMS

Quantum spin chain is an outstanding model to explore strongly correlated quantum order in low-dimensional antiferromagnets, superconductors, and ultracold atoms. It combines several interesting features: it is nontrivial, relatively simple, and describes actual physical systems. More importantly, it is the building block of many frustrated magnets. Several recent examples include triangular antiferromagnets Cs_2CuCl_4[60] and Cs_2CuBr_4,[61,62] which are actively investigated for their fractionalized spinon continuum and pronounced 1/3 magnetization plateau, correspondingly, and high-field candidate spin nematic materials such as $LiCuVO_4$[20,21] and $PbCuSO_4(OH)_2$.[63,64]

This chapter examines the question of quantum spin-1/2 chains under the uniform Dzyaloshinskii-Moriya (DM) interactions; for simplicity we call it DM spin chain. The magnetic-field-induced phase transitions are studied with special attention both at zero and finite temperature. Contrary to other parameters in the Hamiltonian (1.14), an external magnetic field is relatively easy to vary experimentally. When the Zeeman energy scale is comparable with the DM interaction, the spin chain system will leave its critical state and enter in novel magnetic ordered phases.

In this chapter, the discussion of DM spin chains goes to three directions, single mangetized DM spin chain (Sec. 2.1), weakly coupled DM spin chain (Sec. 2.2), and construction of chiral spin liquid by DM spin chains (Sec. 2.3). A variety of theoretical techniques are applied, such as bosonization, renormalization group (Appendix A), and chain mean-field approximation (Appendix B).

2.1 Ising orders in a magnetized spin chain

In this section, we further our understanding of the DM spin chain system which is described by Eq. (1.14) by adding an external magnetic field. Here we explore how the interplay between uniform DM interactions, small anisotropy, and magnetic field influences a single Heisenberg spin chain. We will show that this interplay enriches the phase diagram, including a critical Luttinger liquid (LL) and two antiferromagnetic Ising-like phases. DM interaction suppresses the LL state, because it introduces an effective anisotropy (see Eq. (1.15)) and drives quantum spin chain away from its critical point. The order parameters for two Ising orders are estimated as well. The extensive density matrix renormalization group (DMRG) study performed by Chan and Jiang[65] shows an excellent agreement with the analytical investigation used in this study. This spin chain Hamiltonian can be realized by quantum wires and cold atoms.

In this section, excerpts and figures are reprinted with permission from Y-H Chan, W. Jin, H-C Jiang, and O. A. Starykh, authors of Phys. Rev. B **96**, 214441 (2017).[65] Copyright by the American Physical Society.

2.1.1 Introduction

Physics of quantum spins is at the center of modern condensed matter research. The ever present spin-orbit interactions, long considered to be an unfortunate annoying feature of numerous real-world materials, are now recognized as the key ingredient of numerous spintronics applications[66,67] and the crucial tool for constructing topological phases.[68,69]

In magnetic insulators atomic spin-orbit coupling leads, via superexchange mechanism, to an asymmetric spin exchange $\mathbf{D}_{ij} \cdot \mathbf{S}_i \times \mathbf{S}_j$, known as Dzyaloshinskii-Moriya (DM) interaction,[70,71] between localized spins $\mathbf{S}$ at sites i and j. Classically, such an interaction induces incommensurate spiral correlations in the plane perpendicular to the DM vector $\mathbf{D}_{ij}$. Incommensurability of the spin spiral is determined by D/J, where J is the magnitude of the isotropic exchange interaction between nearest neighbor spins, and therefore is typically quite small, resulting in spiral correlations with very long wavelength. It was realized long ago that the external magnetic field, applied *perpendicular* to the DM axis, causes strong modification of the spiral state and produces chiral soliton lattice—periodic array of incommensurate with the lattice domains separated by 2π-domain walls (soli-

tons).[72] Here, this incommensurate structure undergoes a continuous incommensurate-commensurate transition into a uniform ordered state at a rather small critical magnetic field of the order of D.[72–74] This important feature makes this interesting class of magnetically ordered materials particularly attractive for multiferroics and spintronics applications.[75,76]

It is not well understood how strong quantum fluctuations modify this classical picture. To this end, and also having in mind several spin-1/2 quasi-one-dimensional quantum magnets[45,77,78] for which this consideration is highly relevant, we investigate here the joint effect of a uniform DM interaction $D\hat{z} \cdot \mathbf{S}_i \times \mathbf{S}_{i+1}$ and a transverse magnetic field h_x on the low-energy properties of the antiferromagnetic spin-1/2 Heisenberg chain with a weak XXZ anisotropy Δ. Our goal is to quantitatively check, with the help of the state of the art density-matrix renormalization group (DMRG) calculation, predictions of the recent field-theoretic studies of this interesting problem.[54,79,80] Garate and Affleck found that quantum fluctuations destroy the chiral soliton lattice and replace it with a critical Luttinger liquid (LL) phase. Additionally, the model is found to support two distinct ordered phases with staggered Ising order along directions perpendicular to the external field **h**. Stability domains of these Ising phases are found to differ significantly from the classical expectations.[54,79] In particular, when the magnitudes of DM interaction D and magnetic field h are comparable to each other, the Ising-like longitudinal spin-density wave order (of "N^z" kind, see below) is found to extend deep into classically forbidden $\Delta \leq 1$ region.

We consider antiferromagnetic Heisenberg spin-1/2 chains subject to a uniform DM interaction and an external magnetic field. The system is described by the following Hamiltonian,

$$\mathcal{H} = J \sum_x \left[(S^x_x S^x_{x+1} + S^y_x S^y_{x+1}) + \Delta S^z_x S^z_{x+1} \right] - \sum_x \boldsymbol{D} \cdot (\boldsymbol{S}_x \times \boldsymbol{S}_{x+1}) - \sum_x (h_x S^x_x + h_z S^z_x). \quad (2.1)$$

$\Delta \approx 1$ parametrizes small Ising anisotropy. The DM vector $\mathbf{D} = D\hat{z}$ is uniform along chain. $h_x(h_z)$ denotes the strength of the applied transverse (longitudinal) magnetic field. Now let us study this spin chain by bosonization theory as discussed in Sec. 1.5.1.

2.1.2 Hamiltonian in the low-energy limit

The low-energy description of spin operator is provided by the parameterization[79]

$$\boldsymbol{S}(x) \approx \boldsymbol{J}(x) + (-1)^n \boldsymbol{N}(x), \tag{2.2}$$

where $\boldsymbol{J} = \boldsymbol{J}_L + \boldsymbol{J}_R$, and $\boldsymbol{J}_L(x)$ and $\boldsymbol{J}_R(x)$ are the uniform left- and right-moving spin currents, and $\boldsymbol{N}(x)$ is the staggered magnetization (our order parameter). Here $x = na$ in terms of lattice constant a. These fields are expressed in terms of bosonic fields (ϕ, θ) (this expansion is specific to SU(2), Heisenberg, point and can be generalized easily to a more general XXZ Hamiltonian).

$$\begin{aligned} J_R^+ = \frac{1}{2\pi a} e^{-i\sqrt{2\pi}(\phi-\theta)}, \quad J_L^+ = \frac{1}{2\pi a} e^{i\sqrt{2\pi}(\phi+\theta)}, \\ J_R^z = \frac{\partial_x \phi - \partial_x \theta}{2\sqrt{2\pi}}, \quad J_L^z = \frac{\partial_x \phi + \partial_x \theta}{2\sqrt{2\pi}}, \end{aligned} \tag{2.3}$$

and

$$\boldsymbol{N} = A(-\sin[\sqrt{2\pi}\theta],\ \cos[\sqrt{2\pi}\theta],\ -\sin[\sqrt{2\pi}\phi]). \tag{2.4}$$

Here, $A \equiv \gamma/(\pi a)$, and $\gamma = \langle \cos(\sqrt{2\pi}\phi_\rho) \rangle \sim O(1)$ is determined by gapped charged modes of the chain.

The Hamiltonian in Eq. (2.1) is approximated in low energy limit as,[54,79,81]

$$H = H_0 + V + H_{\rm bs}, \tag{2.5}$$

where

$$\begin{aligned} H_0 &= \frac{2\pi v}{3} \int \mathrm{d}x (\boldsymbol{J}_R \cdot \boldsymbol{J}_R + \boldsymbol{J}_L \cdot \boldsymbol{J}_L), \\ V &= D \int \mathrm{d}x (J_R^z - J_L^z) - h_x \int \mathrm{d}x (J_R^x + J_L^x) - h_z \int \mathrm{d}x (J_R^z + J_L^z), \\ H_{\rm bs} &= -g_{\rm bs} \int \mathrm{d}x [J_R^x J_L^x + J_R^y J_L^y + (1+\lambda) J_R^z J_L^z], \end{aligned} \tag{2.6}$$

where $v \simeq J\pi a/2$ is the spin velocity and $\tilde{D} = D(1+2\gamma^2)/\pi \approx D$. V contains the last two terms of Eq. (2.62); it collects all vector-like perturbations of the bare chain Hamiltonian H_0. $H_{\rm bs}$ describes residual backscattering interaction between right- and left-moving spin modes of the chain. Its coupling is estimated as $g_{\rm bs} \approx 0.23 \times (2\pi v)$; see Ref.[54] for details. An important DM-induced anisotropy parameter λ is given,[54]

$$\lambda = c(1 - \Delta + \frac{D^2}{2J^2}). \tag{2.7}$$

The constant $c = (4v/g_{\rm bs})^2$ is about 7.66 from Bethe-ansatz solution, see (B2) in Ref.[54]

2.1.2.1 Chiral rotation

After writing the system Hamiltonian in the form of Eq. (2.6), it is convenient to exploit the extended symmetry of H_0 and treat both vector perturbations h_x and D equally. Then we perform a chiral rotation of spin currents about the $\hat{y}$ axis[54,79,81]

$$\boldsymbol{J}_{R/L} = \mathcal{R}(\theta_{R/L})\boldsymbol{M}_{R/L}, \tag{2.8}$$

with $\boldsymbol{M}_{R/L}$ spin current in the rotated frame, and $\mathcal{R}$ the rotation matrix,

$$\mathcal{R}(\theta_{R/L}) = \begin{pmatrix} \cos\theta_{R/L} & 0 & \sin\theta_{R/L} \\ 0 & 1 & 0 \\ -\sin\theta_{R/L} & 0 & \cos\theta_{R/L}. \end{pmatrix}, \tag{2.9}$$

The general form of chiral rotation angles $\theta_{R/L}$ can be found in Refs.[54,79] Here we apply it to our special $\boldsymbol{h} \perp \boldsymbol{D}$ case, which gives

$$\theta_R = \pi/2 + \theta_0,\ \theta_L = \pi/2 - \theta_0, \quad \theta_0 \equiv \arctan\left(\frac{D}{h}\right). \tag{2.10}$$

Via this chiral rotation, the vector perturbation V in Eq. (2.64) becomes

$$V = -\sqrt{D^2+h^2}\int \mathrm{d}x(M_R^z + M_L^z) = -\frac{\sqrt{D^2+h^2}}{\sqrt{2\pi}}\int \mathrm{d}x\partial_x\varphi. \tag{2.11}$$

Also the staggered magnetization transforms into,

$$\boldsymbol{N} = (\mathcal{N}^z, \cos\theta_0\mathcal{N}^y + \sin\theta_0\varepsilon, -\mathcal{N}^x), \tag{2.12}$$

Here $\boldsymbol{\mathcal{N}}$ and ε denote the *staggered magnetization* and *dimerization* in the rotated frame (while $\xi = \frac{\gamma}{\pi a_0}\cos[\sqrt{2\pi}\phi]$ is the dimerization in the original frame), and are expressed (as well as $\boldsymbol{M}_{R/L}$) in terms of Abelian bosonic fields φ and ϑ, while $\boldsymbol{N}$, the staggered magnetization in the original frame (as well as spin currents $\boldsymbol{J}_{R/L}$), is written in terms of (ϕ, θ) pair as in Eq. (2.3) and (2.4).

Relation (2.12) is obtained by observing that the chiral rotation of vector currents (2.8) corresponds to the following rotation of Dirac spinors[54,82] $\Psi_{R/L,s} = e^{-i\theta_{R/L}\sigma^y/2}\tilde{\Psi}_{R/L,s}$ in terms of which spin currents are expressed[83] as $J^a_{R/L} = \Psi^+_{R/L}\sigma^a\Psi_{R/L}/2$ and $M^a_{R/L} = \tilde{\Psi}^+_{R/L}\sigma^a\tilde{\Psi}_{R/L}/2$. The (original) staggered magnetization, $N^a = \Psi^+_R\sigma^a\Psi_L/2 + \Psi^+_L\sigma^a\Psi_R/2$,

rotates into (2.12). Similarly, staggered dimerization $\xi(x) \sim (-1)^{x/a}\mathbf{S}(x)\cdot\mathbf{S}(x+a)$ transforms as

$$\xi = \cos\theta_0\epsilon - \sin\theta_0\mathcal{N}^y. \tag{2.13}$$

Rotation (2.8) of spin currents transforms backscattering Hamiltonian in (2.64) into,

$$H_{\rm bs} = 2\pi v\int \mathrm{d}x\Big[\sum_\alpha y_\alpha M_R^\alpha M_L^\alpha + y_A(M_R^z M_L^x - M_R^x M_L^z)\Big], \tag{2.14}$$

where $\alpha = x, y, z$ and the initial values of coupling constants y_α and y_A are shown in Eq. (2.15). The initial values of coupling constants are[54]

$$\begin{aligned} y_x(0) &= -\frac{g_{bs}}{2\pi v}[(1+\frac{\lambda}{2})\cos\theta^- + \frac{\lambda}{2}],\\ y_y(0) &= -\frac{g_{bs}}{2\pi v},\\ y_z(0) &= -\frac{g_{bs}}{2\pi v}[(1+\frac{\lambda}{2})\cos\theta^- - \frac{\lambda}{2}],\\ y_A(0) &= \frac{g_{bs}}{2\pi v}(1+\frac{\lambda}{2})\sin\theta^-, \end{aligned} \tag{2.15}$$

where the angle parameters are

$$\theta^- = 2\theta_0, \quad \theta_0 = \arctan[D/h]. \tag{2.16}$$

2.1.2.2 Shift of bosonic field

We see from Eq. (2.11) that in the rotated frame the spins are subject to an effective magnetic field $h_{\rm eff} = \sqrt{D^2+h^2}$ along the z axis. The fact that the D and h terms are treated equally here represents the major technical advantage of the chiral rotation transformation (2.8). Importantly, $h_{\rm eff}$ is finite once $D \neq 0$, implying the presence of some oscillating terms in the Hamiltonian even in the absence of external magnetic field; see Eq. (2.21). Being linear in the derivative of φ_y, the term (2.11) is easily absorbed into $\mathcal{H}_0$ by a shift of field

$$\varphi \to \varphi + t_\varphi x, \quad t_\varphi \equiv \sqrt{D^2+h^2}/v = h_{\rm eff}/v. \tag{2.17}$$

As a result of the shifts, the spin currents, the staggered magnetization and the dimerization in the rotated frame are modified as

$$\begin{aligned} M_R^+ &\to M_R^+ e^{-it_\varphi x}, \quad M_L^+ \to M_L^+ e^{it_\varphi x},\\ M_R^z &\to M_R^z + \frac{t_\varphi}{4\pi}, \quad M_L^z \to M_L^z + \frac{t_\varphi}{4\pi}, \end{aligned} \tag{2.18}$$

and

$$\mathcal{N}^z \to -\frac{\gamma}{\pi a_0}\sin(\sqrt{2\pi}\varphi + t_\varphi x), \quad \varepsilon \to \frac{\gamma}{\pi a_0}\cos[\sqrt{2\pi}\varphi + t_\varphi x]. \tag{2.19}$$

The φ field shift (2.17) will also transform the expression for the chain backscattering (2.14) to Eq. (2.21), in which we neglect additional small terms coming from the shifts in $M^z_{R/L}$.

2.1.2.3 Effective Hamiltonian

After the chiral rotation in Sec. 2.1.2.1 and shift of fields in Sec. 2.1.2.3, the effective Hamiltonian now reads,

$$H = \tilde{H}_0 + \tilde{H}_{\rm bs}, \tag{2.20}$$

where $\tilde{H}_0$ has quadratic form in terms of shifted Abelian bosonic fields (φ, ϑ). The harmonic Hamiltonian is perturbed by chain backscattering $\tilde{H}_{\rm bs}$ which consists of several contributions[54,79,84]

$$\begin{aligned}
\tilde{H}_{\rm bs} &= H_A + H_B + H_C + H_\sigma, \\
H_A &= \pi v y_A \int \mathrm{d}x (M^z_R M^+_L e^{it_\varphi x} - M^+_R M^z_L e^{-it_\varphi x} + \text{h.c.}), \\
H_B &= \pi v y_B \int \mathrm{d}x (M^+_R M^-_L e^{-i2t_\varphi x} + \text{h.c.}), \\
H_C &= \pi v y_C \int \mathrm{d}x (M^+_R M^+_L + \text{h.c.}), \\
H_\sigma &= -2\pi v y_\sigma \int \mathrm{d}x M^z_R M^z_L,
\end{aligned} \tag{2.21}$$

with

$$y_C \equiv \frac{1}{2}(y_x - y_y), \;\; y_B \equiv \frac{1}{2}(y_x + y_y), \;\; y_\sigma \equiv -y_z. \tag{2.22}$$

The oscillating factor $e^{it_\varphi x}$ is introduced by the effective transverse field $h_{\rm eff} = \sqrt{h^2 + D^2}$ which accounts for the combined effect of magnetic field and DM interaction. Next we need to identify the most-relevant coupling in perturbation (2.21), which is accomplished by the renormalization group (RG) analysis [introdcution of which is discussed in Appendix A.1].

2.1.3 Two-stage RG

According to standard RG arguments as discussed in Appendix A.1, the low-energy properties of the system are determined by the couplings which renormalize to dimensionless values of order 1 first.The RG equations for coupling constants of backscattering

interaction (2.21) are obtained with the help of operator product expansion (OPE)[53,83] technique [see Appendix A.2] and read

$$\begin{aligned} \frac{dy_x}{dl} &= y_y y_z, \quad \frac{dy_y}{dl} = y_x y_z + y_A^2, \\ \frac{dy_z}{dl} &= y_x y_y, \quad \frac{dy_A}{dl} = y_y y_A. \end{aligned} \tag{2.23}$$

The presence of oscillating $e^{it_\varphi x}$ factors implies the appearance of spatial scale, $\propto 1/t_\varphi$, and, correspondingly, of the RG scale ℓ_φ

$$\ell_\varphi = \log(\frac{1}{a_0 t_\varphi}) = \ln[\frac{1}{20.4}\frac{\pi}{2}\frac{1}{\sqrt{D^2+h^2}}]. \tag{2.24}$$

where, $a_0 = 20.4a$ is the ultraviolet RG cutoff length scale (see Ref.[54] for details of how the choice of the initial value for $g_{\rm bs}$ determines a_0 also). As mentioned in Sec. A.1, see also Refs.,[50,54] the presence of oscillating terms forces us to implement a two-stage RG scheme. For $\ell < \ell_\varphi$ oscillations due to $e^{it_\varphi x}$ can be neglected and a full set of RG equations (2.92) has to be solved numerically. Once RG "time" $\ell > \ell_\varphi$, strong oscillations in H_A and H_B result in disappearance of these terms from the Hamiltonian. Correspondingly, we can set $y_A(\ell) = 0$ and $y_B(\ell) = 0$ in the RG equations. Therefore, at this second stage, RG equations for backscattering simplify to

$$\frac{dy_C}{d\ell} = y_C y_\sigma, \quad \frac{dy_\sigma}{d\ell} = y_C^2. \tag{2.25}$$

These are the well-known Kosterlitz-Thouless (KT) equations, analytic solution of which is given in Sec. 2.1.6. The initial values of backscattering couplings at second stage are,

$$\begin{aligned} y_C(\ell_\varphi) &= (y_x(\ell_\varphi) - y_y(\ell_\varphi))/2 \approx -\frac{g_{\rm bs}}{4\pi v}[(1+\frac{\lambda}{2})\cos\theta^- - 1 + \frac{\lambda}{2}], \\ y_\sigma(\ell_\varphi) &= -y_z(\ell_\varphi) \approx \frac{g_{\rm bs}}{2\pi v}[(1+\frac{\lambda}{2})\cos\theta^- - \frac{\lambda}{2}], \\ C &= y_\sigma(\ell_\varphi)^2 - y_C(\ell_\varphi)^2. \end{aligned} \tag{2.26}$$

where $\cos\theta^- = (h^2 - D^2)/(h^2 + D^2)$ and C is the constant of motion, $dC/d\ell = 0$. Provided that y's do not renormalize strongly during the first stage $\ell < \ell_\varphi$, initial values of $y_{C,\sigma}$ at ℓ_φ can be approximated by those at $\ell = 0$, as the above equation shows.

2.1.4 Ising orders

We have identified five distinct regions with different signs of $y_{C,\sigma}$ and integration constant C, which lead to different RG flows. The boundaries of these regions depend

on initial values of y's and C. When the stage 1 flow can be skipped, which happens for sufficiently large h_{eff} such that formally $\ell_\varphi < 0$, then the dependence on initial values can be directly translated into that on h/D ($\cos\theta^-$) and λ (Δ and D/J). The results are summarized in **Table 2.1** and **Figure 2.1**, which show what orders are promoted in different regions.

When the oscillation $e^{it_\varphi x}$ is significant, the backscattering (2.21) contains only two terms, H_c and H_σ. In terms of Abelian fields, interaction H_C is nonlinear one, $H_C \propto y_C \cos[2\sqrt{2\pi}\vartheta] = y_C \cos[2\beta\vartheta]$, while $H_\sigma \propto (\partial_x\varphi)^2 - (\partial_x\vartheta)^2$ and describes renormalization of β (as well as of the spinon's velocity $v \to v\sqrt{1 - y_\sigma^2/2}$, see Sec. 2.1.7, which however is neglected in the following). Then the ground state is determined by the ordering of ϑ field.

Flow to strong-coupling of KT equations (2.95) implies development of the expectation value for ϑ field. When $y_C \to +\infty$ the energy is minimized by $\sqrt{2\pi}\vartheta = (2k_1+1)\pi/2$, with k_1 an integer, and $\mathcal{N}^x \propto -\sin\sqrt{2\pi}\vartheta \neq 0$. This means that in the original frame there is an Ising order $N^z \neq 0$, and following Ref.[54] we name this state "N^z". The long-range order (staggered magnetization) in the original frame is commensurate,

$$\langle \boldsymbol{N}(x)\rangle = A\langle \sin(\sqrt{2\pi}\vartheta)\rangle \mathbf{z} \propto (-1)^{k_1+1}\mathbf{z}. \tag{2.27}$$

In the case of $y_C \to -\infty$ the energy is minimized by $\sqrt{2\pi}\vartheta = k_2\pi$, with k_2 an integer, and $\mathcal{N}^y \propto \cos\sqrt{2\pi}\vartheta \neq 0$. Therefore the Ising order is now along the $\mathbf{y}$ axis, $N^y \neq 0$, and we name it "N^y". The order parameter in the original frame reduces to

Table 2.1. Signs of y_C, y_σ, and C corresponding to the KT-flow in **Figure 2.1**. l^* is the critical RG scale at which one (or several) coupling constants reach strong coupling limit (become of order 1). This table provides a criterion for determining the ground state.

Region	1	2	3	4	5
$y_C(0)$	$+/-$	$+$	$+$	$-$	$-$
$y_\sigma(0)$	$-$	$-/+$	$+$	$+$	$-/+$
C	$+$	$-$	$+$	$+$	$-$
$y_C(l^*)$	0	$+\infty$	$+\infty$	$-\infty$	$-\infty$
$y_\sigma(l^*)$	finite	$+\infty$	$+\infty$	$+\infty$	$+\infty$
$y_B(l^*)$	finite	finite	finite	finite	finite
State	LL	"N^z"	"N^z"	"N^y"	"N^y"

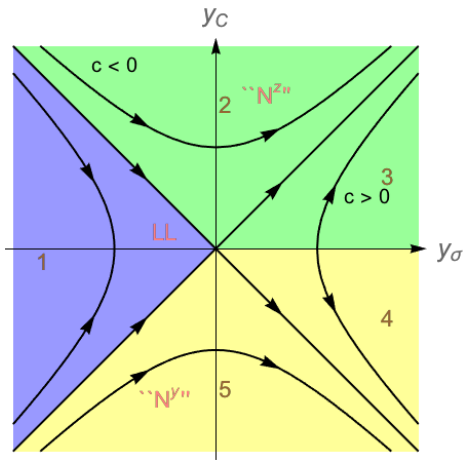

Figure 2.1. Solution of Kosterlitz-Thouless (KT) equations. Two magnetic ordered phases "N^z" (green region) ,"N^y" (yellow region) and critical Luttinger liquid phase (purple) by the criterion in **Table 2.1**.

$$\langle \boldsymbol{N}(x) \rangle = A_3 \cos\theta_0 \langle \cos(\sqrt{2\pi}\vartheta) \rangle \mathbf{y} \propto (-1)^{k_2} \mathbf{y}. \tag{2.28}$$

In addition, there is also a regime of $y_C \to 0$ for $\ell \to \infty$, which signifies finite range of stability of the critical Luttinger liquid (LL) phase.[54]

2.1.5 Phase boundaries

The $\Delta - (h/D)$ phase diagrams are obtained by solving the RG equations and are presented in **Figure 2.2** and **Figure 2.3**. **Figure 2.2** is obtained under the condition that the first-stage RG flow can be skipped, due to the fact that $l_\varphi < 0$ in (2.24), implying sufficiently large D and/or h_x. In this situation we can determine the ground state simply by studying the initial conditions of KT equations according **Table 2.1** and **Figure 2.1**.

However, if $l_\varphi > 0$, so that oscillations develop over some finite lengthscale, one needs to integrate the first-stage RG equations numerically and thus find initial conditions $y_C(l_\varphi)$, $y_\sigma(l_\varphi)$ and $C = y_\sigma^2(l_\varphi) - y_C^2(l_\varphi)$ for the second-stage of the RG flow (KT part of the flow). This is the case of $D/J = 0.01$, a phase diagram of which is presented in **Figure 2.3**.

By comparing two diagrams in **Figure 2.2** and **Figure 2.3**, we notice that large D promotes "N^z" state. Because DM interaction suppresses the quantum criticality of bare spin chain, and supports the emergence of the Ising orders. Next we study the boundaries between three different phases, for sufficiently large D and h_x.

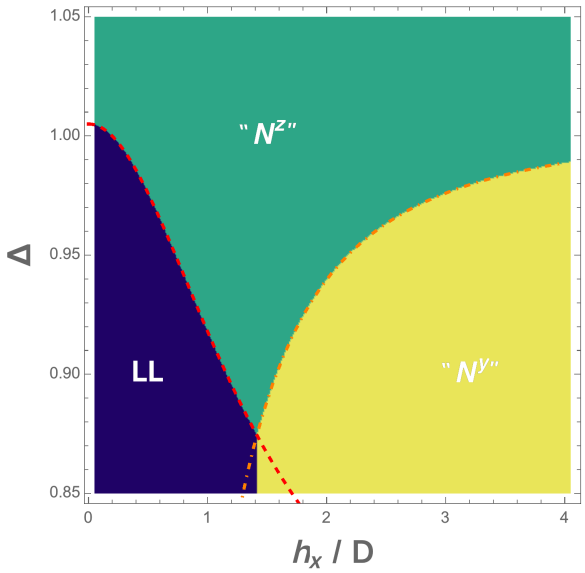

Figure 2.2. Phase diagram for the case of relatively strong DM interaction $D/J = 0.1$. Larger D promotes "N^z" state. The two phase boundaries are obtained by Eq. (2.29) (orange dot-dashed line, between "N^y" and "N^z"), and Eq. (2.30) (red dashed line, between LL and "N^z"). The phase boundary between LL and "N^y" is located at $h_x/D = \sqrt{2}$ and is independent of D.

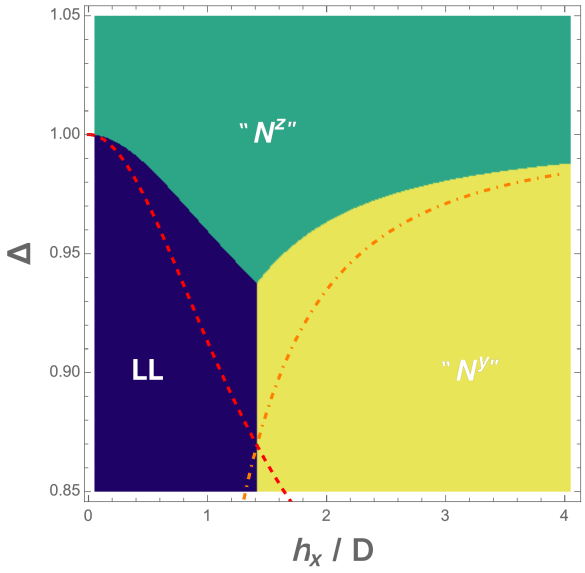

Figure 2.3. Phase diagram for the case of small DM interaction $D/J = 0.01$. The two phase boundaries by Eq. (2.29) (orange dot-dashed line, between "N^y" and "N^z"), and Eq. (2.30) (red dashed line, between LL and "N^z"). For smaller values of D, these approximate phase boundaries derived by neglecting the first stage of RG flow are far off from the actual ones.

2.1.5.1 N^y–N^z

Figure 2.1 shows that the phase transition between "N^y" and "N^z" states is related to the initial values of y_C and y_σ. The coupling $y_C(0)$ has opposite signs in the regions 3 and 4. In the phase diagram, this boundary corresponds to a critical value Δ_{c1}, at which $y_C(0) = 0$ and $C = y_\sigma^2(0) > 0$. These conditions indicate the boundary happens at $D/h = \sqrt{\lambda/2}$ and lead to expression of Δ_{c1} as

$$\Delta_{c1} = 1 + \frac{1}{2}(\frac{D}{J})^2 - \frac{2}{c}(\frac{D}{h})^2. \tag{2.29}$$

For a fixed D, a larger field h leads to a greater Δ_{c1}, which is illustrated as an orange dot-dashed line in phase diagrams of **Figure 2.2** and **Figure 2.3**. Interestingly, the limit of $D \to 0$, corresponding to $h_x/D \to \infty$ in the above figures is described by our theory as well, as we explain in Appendix 2.1.10. In that case one deals with an XXZ model in a transverse magnetic field for which the critical LL line separating the two Ising phases, "N^y" and N^z", is reduced to the horizontal asymptote $\Delta_{c1} = 1$, in agreement with the previous study in Ref.[85]

2.1.5.2 LL–N^z

The boundary between LL and "N^z" happens at $C = 0$, $y_C(0) > 0$ and $y_\sigma(0) < 0$. Therefore we have the relation that $y_\sigma(0) = -y_C(0)$. This gives the critical Δ_{c2}

$$\Delta_{c2} = 1 + \frac{1}{2}(\frac{D}{J})^2 - \frac{2}{c}\frac{1}{1+2(D/h)^2}. \tag{2.30}$$

Therefore, in contract to Eq. (2.29), larger field h results in smaller Δ_{c2}. This result is also confirmed in **Figure 2.2** and **Figure 2.3**. In **Figure 2.2**, we see that Eqs. (2.29) and (2.30) show excellent agreement of the obtained phase transition line with the numerical solution of RG equations, thanks to the fact that in this case the first stage of RG flow is not required. When $h_z = 0$ and $h_x = 0$, there are only two phases, "N^z" and LL, separated by $\Delta = 1$. When there is easy-plane anisotropy ($\Delta < 1$) the system flows to the gapless LL phase, while easy-axis anisotropy ($\Delta > 1$) make the system evolve to "N^z".

2.1.5.3 LL–N^y

Finally, the transition between LL and "N^y" is described by $C = 0$ and $y_C(0) < 0$, $y_\sigma(0) < 0$. This gives $y_C(0) = y_\sigma(0)$ which is satisfied by $\cos\theta^- = 1/3$ and $\lambda \geq 1$.

This condition implies that transition between LL and "N^y" is a vertical line located at $(h_x/D)_{c3} = \sqrt{2}$, which is again confirmed by numerical solution of RG equations in **Figure 2.2** and **Figure 2.3**. Different from the other two boundaries, the one between LL and "N^y" is independent of D as long as $D/J < 1$, and this is consistent with the classical analysis in Ref.[54] The constraint $\lambda \geq 1$ implies that this boundary exists only for $\Delta \leq \Delta_t \equiv 1 + (D/J)^2/2 - 1/c$. The crossing point of two the critical lines Δ_{c1} and Δ_{c2} also gives the condition $(h_x/D)_{c3} = \sqrt{2}$. The "triple" point where three phases intersect is at $h_x/D = \sqrt{2}$ and Δ_t, which, for $D/J = 0.1$ in **Figure 2.2**, is evaluated to be $\Delta_t \simeq 0.874$.

2.1.6 Critical RG scale ℓ^*

By solving the RG equations (2.95) we obtain the critical RG scale ℓ^* at which the order develops, $|y_C(\ell^*)| = 1$. Thus, the correlation length corresponding to two Ising-like orders can be estimated by $\varepsilon^* = \exp \ell^*$. We will show this formulation also provides a convenient way to understand some of the finite size effects unavoidable in numerical study of the problem. Here we focus on the case of relatively strong DM interaction $D/J = 0.1$, phase diagrams for which are presented in **Figure 2.2**.

As for the KT equations in Eq. (2.95), the analytical solutions are

$$y_\sigma(l) = \begin{cases} \mu \dfrac{y_\sigma(0)\cosh(\mu l) - \mu \sinh(\mu l)}{-y_\sigma(0)\sinh(\mu l) + \mu \cosh(\mu l)}, & C > 0, \\ \mu \dfrac{y_\sigma(0)\cos(\mu l) + \mu \sin(\mu l)}{-y_\sigma(0)\sin(\mu l) + \mu \cos(\mu l)}, & C < 0. \end{cases} \tag{2.31}$$

with $\mu \equiv \sqrt{|C|}$. And

$$y_C(l) = \text{sign}(y_C(0))\sqrt{y_\sigma(l)^2 - C}. \tag{2.32}$$

the sign of $y_C(l)$ depends on the sign of its initial value.

The critical ℓ^*, at which $|y_C(l = l^*)| = 1$, can be determined by Eqs. (2.31) and (2.32), and is shown is **Figure 2.4**. We find that ℓ^* grows rapidly as Δ is approaching the phase boundary between "N^y" and "N^z" states approaching $\ell \approx 50$ near the critical point $\Delta_c \simeq 0.94$, determined by Eq. (2.29). However the finite size L of the system used in the numerical methods, such as density matrix renormalization group (DMRG) or quantum Monte Carlo (QMC), corresponds to the much smaller RG scale $\ell_s = \ln[L]$, for example when $L = 1600$, $\ell_s = \ln[1600] = 7.37$. In order to detect the phase transition in **Figure 2.4**, the system size needs to be at least $L = \exp[50]$, which is astronomical for numerical

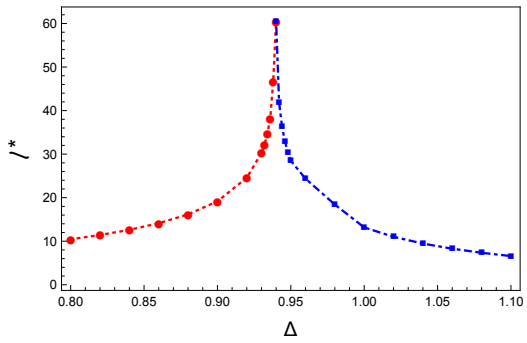

Figure 2.4. Analytical solution of the critical lengthscale l^* for which $|y_c(l^*)| = 1$ as a function of XXZ anisotropy Δ. Here, $D/J = 0.1$ and $h_x/J = 0.2$. The system is in the "N^y" phase (red) for $\Delta < \Delta_c \simeq 0.94$, while $\Delta > \Delta_c$ the system enters the "N^z" phase (blue). Near the transition point, $\ell^* \gg \ell_s$.

simulations. Therefore RG scales greater than ℓ_s are not accessible in DMRG. In other words, if we associate correlation length $\xi = ae^{\ell^*}$ with the order which develops at scale ℓ^*, and if it happens that $\ell^* > \ell_s$, than the DMRG will not be sensitive to the development of the long-range order in this case. This is the basic explanation of the unavoidable difficulty one encounters in numerical determination of the phase boundaries between various phases.

2.1.7 Order parameters of two Ising orders

In addition to calculating ℓ^* associated with the development of long-range order, we can also calculate the order parameters for "N^y" and "N^z" phases developing in the system as a function of the running RG scale ℓ. We show there that the required order parameters are given by

$$\langle N^y \rangle = A_3 \langle \mathrm{Re}[e^{i\beta\vartheta/2}] \rangle, \quad \langle N^z \rangle = A_3 \langle \mathrm{Im}[e^{i\beta\vartheta/2}] \rangle. \tag{2.33}$$

They can be calculated explicitly as a function of running RG scale ℓ as Eq. (2.52) shows; see details in Sec. 2.1.9. **Figure 2.5** illustrates our findings. Note that plotted there are $\langle N^y \rangle$ evaluated at the maximum possible $\ell = \ell_s$. There is a noticeable asymmetry between the two order parameters: the order parameter of the "N^y" phase is smaller than that of the "N^z" phase.

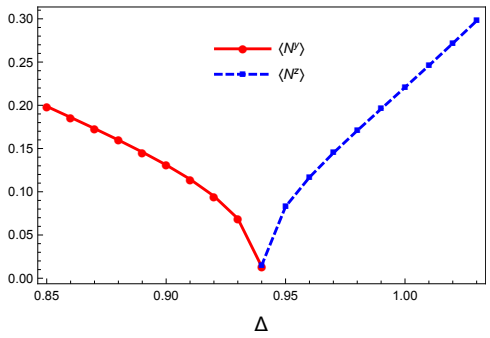

Figure 2.5. Order parameter as a function of Δ for two ordered states "N^y" and "N^z", at $D/J = 0.1$, $h_x/J = 0.2$ and RG length scale $\ell = \ell_s$. Here Δ is near the phase boundary $\Delta_c \simeq 0.94$.

2.1.8 Discussion

We have worked out full phase diagram of the model in the $\Delta - (h/D)$ plane. Our numerical findings match predictions of Ref.[54] well, and confirm the prevalence of "N^z" Néel Ising order in the regime of comparable Dzyaloshinskii-Moriya (DM) and magnetic field magnitudes.[79] In addition, we find that significant finite-size corrections observed numerically are well explained by the 'logarithmic slowness' of the KT RG flow. As a result of that, very large RG scales ℓ^*, far exceeding those set by the finite length L of the chain used in DMRG, are required for reaching the Ising-ordered phases. Extensive DMRG study shows an excellent agreement with analytical investigation based on the RG analysis of weakly perturbed Heisenberg chain.

Our numerical data also confirm the existence of the critical Luttinger liquid phase with fully broken spin-rotational invariance. This phase with dominant incommensurate spin and dimerization power-law correlations is a quantum analogue of the classical chiral soliton lattice.

Our findings open up a possibility of the experimental check of theoretical predictions in quasi-one-dimensional antiferromagnets with a uniform DM interaction.[45,78] The idea is to probe the spin correlations at a finite temperature above the critical ordering temperature of the material when interchain spin correlations, which drive the three-dimensional ordering, are not important while individual chains still possess sufficient large separations for experimental detection anisotropy of spin correlations caused by the uniform DM interaction. Under these conditions one should be able to probe the fascinating com-

petition between the uniform DM interaction and the transverse external magnetic field.

Now we provide technical details of calculations of the order parameters in Sec. 2.1.7, and examine the validity the obtained phase diagrams **Figure 2.2** and **Figure 2.3** when the system is in the absence of DM interaction. Then we discuss the specialty of the obtained Luttinger liquid phase.

2.1.9 Calculation of the order parameter

2.1.9.1 Expectation values of sine-Gordon model

Lukyanov and Zamolodchikov in Ref.,[86] Eq.(20), have worked out a general expression for the expectation value of the vertex operator $\langle e^{ia\vartheta}\rangle$ in sine-Gordon model described by

$$S_{sG} = \int d^2x \Big\{ \frac{1}{16\pi}(\partial_\nu \vartheta)^2 - 2\mu\cos(\beta'\vartheta)\Big\}. \tag{2.34}$$

Their conjecture is as follows (for $\beta'^2 < 1$, and $|\mathrm{Re}\, a| < 1/(2\beta)$, which are required for convergence) ,

$$\begin{aligned}&\langle e^{ia\vartheta}\rangle \\ &= \Big[\frac{m\Gamma(\frac{1}{2}+\frac{\xi}{2})\Gamma(1-\frac{\xi}{2})}{4\sqrt{\pi}}\Big]^{2a^2} \exp\Big\{\int_0^\infty \frac{dt}{t}\Big[\frac{\sinh^2(2a\beta' t)}{2\sinh(\beta'^2 t)\sinh(t)\cosh\big((1-\beta'^2)t\big)} - 2a^2 e^{-2t}\Big]\Big\},\end{aligned} \tag{2.35}$$

where

$$m = 2M\sin(\pi\xi/2), \quad \xi = \frac{\beta'^2}{1-\beta'^2} \tag{2.36}$$

and M is the soliton mass.

2.1.9.2 Action and the equivalence to sine-Gordon model

Here we work out the action for our KT Hamiltonian (2.21) by considering H_C and H_σ as perturbations to the harmonic Hamiltonian H_0. Provided that the field is small enough, so that scaling dimensions of various operators are given by their values at the Heisenberg point, we have

$$M_R^z = \frac{1}{2\sqrt{2\pi}}(\partial_x\varphi - \partial_x\vartheta),\ M_L^z = \frac{1}{2\sqrt{2\pi}}(\partial_x\varphi + \partial_x\vartheta). \tag{2.37}$$

and therefore

$$\begin{aligned} H_\sigma &= -\frac{vy_\sigma}{4}\int \mathrm{d}x[(\partial_x\varphi)^2 - (\partial_x\vartheta)^2], \\ H_C &= \frac{vy_C}{2\pi a^2}\int \mathrm{d}x\cos(2\sqrt{2\pi}\vartheta). \end{aligned} \tag{2.38}$$

Therefore, the action, which determines the partition function $Z = \int e^{-S}$, is

$$S = \int \mathrm{d}x\mathrm{d}\tau \Big\{ -i\partial_x\vartheta\partial_\tau\varphi + \frac{1}{2}[v_1(\partial_x\varphi)^2 + v_2(\partial_x\vartheta)^2] + \frac{vy_C}{2\pi a^2}\cos(\sqrt{8\pi}\vartheta)\Big\}. \tag{2.39}$$

where

$$v_1 = v(1 - \frac{y_\sigma}{2}), \quad v_2 = v(1 + \frac{y_\sigma}{2}). \tag{2.40}$$

We integrate out the φ field using duality $\partial_x\vartheta\partial_\tau\varphi = \partial_x\varphi\partial_\tau\vartheta$ and then completing the square in

$$S = \int \mathrm{d}x\mathrm{d}\tau \Big\{ \frac{v_1}{2}((\partial_x\varphi)^2 - \frac{2i}{v_1}\partial_x\vartheta\partial_\tau\varphi) + ...\Big\}. \tag{2.41}$$

Then the action factorizes

$$S = \int \mathrm{d}x\mathrm{d}\tau \Big\{ \frac{v_1}{2}(\partial_x\varphi - \frac{i}{v_1}\partial_\tau\vartheta)^2 + \frac{1}{2v_1}(\partial_\tau\vartheta)^2 + \frac{v_2}{2}(\partial_x\vartheta)^2 + \frac{vy_C}{2\pi a^2}\cos(\sqrt{8\pi}\vartheta)\Big\}. \tag{2.42}$$

and the first, φ-dependent piece is integrated away. The remaining ϑ part of the action is

$$S_\vartheta = \int \mathrm{d}x dy \Big\{ \frac{1}{2}\sqrt{\frac{v_2}{v_1}}((\partial_x\vartheta)^2 + (\partial_\tau\vartheta)^2) + \frac{y_C}{2\pi a^2}\frac{v}{u}\cos(\sqrt{8\pi}\vartheta)\Big\}. \tag{2.43}$$

with $y = u\tau$ and set $u = \sqrt{v_1 v_2}$. Finally we rescale ϑ,

$$\vartheta = \frac{1}{\sqrt{8\pi}}\Big(\frac{v_1}{v_2}\Big)^{\frac{1}{4}}\tilde{\vartheta}. \tag{2.44}$$

to arrive at the desired form of Eq. (2.34),

$$S_\vartheta = \int d^2x \Big\{ \frac{1}{16\pi}(\partial_\nu\tilde{\vartheta})^2 - 2\mu\cos(\tilde{\beta}\tilde{\vartheta})\Big\}. \tag{2.45}$$

where

$$\mu \equiv \frac{|y_C|}{4\pi a^2}\frac{v}{u}, \quad \tilde{\beta} \equiv \Big(\frac{v_1}{v_2}\Big)^{\frac{1}{4}}. \tag{2.46}$$

Here, for the case of $y_C > 0$, we made an additional shift $\tilde{\vartheta} \to \tilde{\vartheta} + \pi/\tilde{\beta}$ in order to change the sign of the cosine term. The case of $y_C < 0$ does not require any more shifts, $\tilde{\vartheta} = \tilde{\vartheta}$. The parameters in terms of $y_{C,\sigma}$ are

$$u = v\sqrt{1 - y_\sigma^2/4}, \quad \mu = \frac{1}{4\pi a^2}\frac{|y_C|}{\sqrt{1 - y_\sigma^2/4}}, \quad \tilde{\beta} = \Big(\frac{1 - y_\sigma/2}{1 + y_\sigma/2}\Big)^{\frac{1}{4}}, \tag{2.47}$$

The expectation value we want to compute is $\langle e^{i\sqrt{2\pi}\vartheta}\rangle = \langle e^{i\tilde{\beta}\tilde{\vartheta}/2}\rangle$, and thus a in Eq. (2.35) is just $a \equiv \tilde{\beta}/2$.

We observe that our order parameters are obtained as $N^y \sim \cos\sqrt{2\pi}\vartheta \propto \mathrm{Re}\langle e^{i\tilde{\beta}\tilde{\vartheta}/2}\rangle$, while $N^z \sim \sin\sqrt{2\pi}\vartheta \propto \mathrm{Im}\langle e^{i\tilde{\beta}\tilde{\vartheta}/2}\rangle$. The shift described just below (2.46), which is needed if $y_C > 0$, transforms $\langle e^{i\tilde{\beta}\tilde{\vartheta}/2}\rangle$ into $e^{i\pi/2}\langle e^{i\tilde{\beta}\tilde{\vartheta}/2}\rangle$ and thus precisely corresponds to the change of the order from N^y kind (realized for $y_C < 0$) to the N^z kind (realized for $y_C > 0$).

2.1.9.3 The order parameter

We want to evaluate the expectation value

$$\langle e^{i\frac{\tilde{\beta}}{2}\tilde{\vartheta}}\rangle = Ae^I, \quad A \equiv \Big[\frac{m\Gamma(\frac{1}{2}+\frac{\xi}{2})\Gamma(1-\frac{\xi}{2})}{4\sqrt{\pi}}\Big]^{\tilde{\beta}^2/2}. \tag{2.48}$$

Here I is obtained from Eq. (2.35) by setting $a = \tilde{\beta}/2$

$$I \equiv \int_0^\infty \frac{dt}{t}\Big[\frac{\sinh(\tilde{\beta}^2 t)}{2\sinh(t)\cosh\big((1-\tilde{\beta}^2)t\big)} - \frac{\tilde{\beta}^2}{2}e^{-2t}\Big]. \tag{2.49}$$

The convergence of I is easy to check: $\tilde{\beta}^2 < 1$ is required for $t \to \infty$. Using identity $\Gamma(1-x)\Gamma(x) = \pi/\sin(\pi x)$, and with m in Eq. (2.36), the expression for A becomes

$$A = \Big[\frac{\sqrt{\pi}}{2}M\frac{\Gamma(\frac{1}{2}+\frac{\xi}{2})}{\Gamma(\xi/2)}\Big]^{\tilde{\beta}^2/2}. \tag{2.50}$$

With the relation between constant μ and mass M (this is Eq.12 of Ref.[86])

$$\mu = \frac{\Gamma(\tilde{\beta}^2)}{\pi\Gamma(1-\tilde{\beta}^2)}\Big[M\frac{\sqrt{\pi}\Gamma(\frac{1}{2}+\frac{\xi}{2})}{2\Gamma(\frac{\xi}{2})}\Big]^{2-2\tilde{\beta}^2}, \tag{2.51}$$

Using all these we obtain for the order parameter

$$\langle e^{i\frac{\tilde{\beta}}{2}\tilde{\vartheta}}\rangle = \Big[\frac{\pi\mu\,\Gamma(1-\tilde{\beta}^2)}{\Gamma(\tilde{\beta}^2)}\Big]^{\tilde{\beta}^2/[4(1-\tilde{\beta}^2)]} \times \exp\Big\{\int_0^\infty \frac{dt}{t}\Big[\frac{\sinh(\tilde{\beta}^2 t)}{2\sinh(t)\cosh\big((1-\tilde{\beta}^2)t\big)} - \frac{\tilde{\beta}^2}{2}e^{-2t}\Big]\Big\}. \tag{2.52}$$

Note that Eq. (2.52) is function of $\tilde{\beta}$, which, in turn, is function of running $y_\sigma(\ell)$. It also depends on running $y_C(\ell)$, via μ dependence, see Eq. (2.47). Thus Eq. (2.52) allows us to evaluate the order parameter as a function of RG scale ℓ.

2.1.10 Sanity check at $D = 0$

If we set $D = 0$ and $h_x = h$, two rotation angles $\theta_R = \theta_L = \pi/2$, and $\theta^- = 0$. Then $y_A(0) = 0$. In this condition, our model Hamiltonian (2.62) reduces to a XXZ model in a uniform transverse field. RG equations for the backscattering interaction are,

$$\frac{dy_x}{dl} = y_y y_z, \quad \frac{dy_y}{dl} = y_x y_z, \quad \frac{dy_z}{dl} = y_x y_y, \tag{2.53}$$

and the initial values are,

$$y_x(0) = -\frac{g_{bs}}{2\pi v}[1+\lambda],\ y_y(0) = y_z(0) = -\frac{g_{bs}}{2\pi v}, \tag{2.54}$$

It is easy to find that $y_y(\ell) = y_z(\ell)$ for all ℓ so that RG equations above again acquire KT form. Now $\lambda = c(1-\Delta)$ so that we obtain

$$y_C(0) = -\frac{g_{\rm bs}}{4\pi v}\lambda,\ y_\sigma(0) = \frac{g_{bs}}{2\pi v},\ C = (\frac{g_{bs}}{2\pi v})^2(1-\frac{\lambda^2}{4}). \tag{2.55}$$

Using Eq. (2.31), we find

$$y_\sigma(\ell) = 2\mu\frac{y_C^2/(y_\sigma+\mu)^2}{e^{-2\mu\ell} - y_C^2/(y_\sigma+\mu)^2}, \tag{2.56}$$

where y's in the right-hand-side are those at $\ell = 0$ (initial values). Therefore, since $y_\sigma(0) = g_{bs}/(2\pi v) > \mu = \sqrt{y_\sigma^2 - y_C^2}$, there is a divergence, signaling strong-coupling limit, at $\ell_{\rm div} \approx \mu^{-1}\ln\left[4|\lambda|^{-1}\right]$. Observe that $\ell_{\rm div}$ is finite for any $\Delta \neq 1$, meaning that the two ordered phases are separated by the critical LL one, which is just an isotropic XXX chain in a magnetic field.

For $\Delta < 1$, we have $\lambda > 0$, $y_C(0) < 0$, and then $y_C(l) \to -\infty$, which means "N^y" state. For $\Delta > 1$, instead $\lambda < 0$, $y_C(0) > 0$, so that $y_C(l) \to +\infty$, hence one obtains "N^z" state. These two phases are separated by the critical line at $\Delta = 1$. Our phase diagrams **Figure 2.2** and **Figure 2.3** display exactly this behavior: setting $D = 0$ places one at $h_x/D \to \infty$, where the critical line separating the two Ising states approaches horizontal asymptote at $\Delta = 1$.

The above argument agrees with Ref.,[85] which studied the ground state of the following Hamiltonian,

$$\mathcal{H} = \sum_j \left[J(S_j^x S_{j+1}^x + S_j^y S_{j+1}^y + \Delta S_j^z S_{j+1}^z) - hS_j^x\right]. \tag{2.57}$$

It was found that for $h \neq 0$ spectrum is gapped for both $\Delta > 1$ and $\Delta < 1$.[85] The Ising order that develops is of "N^z" ("N^y") kind for $\Delta > 1$ ($\Delta < 1$). Our RG equations evidently capture this physics well.

2.1.11 Luttinger liquid phase

The Luttinger liquid (LL) phase of our model is characterized by $y_C = 0, y_\sigma < 0$ for $\ell \to \infty$, see **Figure 2.1**. Correspondingly, its action is given by Eq. (2.43) with $y_C = 0$.

From here it is easy to derive that the scaling dimension of the vertex operator $e^{i\sqrt{2\pi}\vartheta(x)}$ is $\Delta_\vartheta = \tilde{\beta}^2/2 \approx (1 - y_\sigma/2)/2$, while that of the dual field one $e^{i\sqrt{2\pi}\varphi(x)}$ is given by $\Delta_\varphi = 1/(2\tilde{\beta}^2) \approx (1 + y_\sigma/2)/2$. Backscattering renormalizes scaling dimensions through the RG flow of y_σ. Given that in the LL $y_\sigma < 0$, we observe that $\Delta_\varphi < \Delta_\vartheta$ which signals that the correlation functions of fields $\mathcal{N}^z$ and ξ, which are written in terms of φ bosons, decay *slower* than those of fields $\mathcal{N}^x$ and $\mathcal{N}^y$, which are expressed via ϑ bosons. Moreover, due to Eq. (2.68), correlations of $\mathcal{N}^z$ and ξ are *incommensurate*:

$$\langle \mathcal{N}^z(x)\mathcal{N}^z(0)\rangle \propto \langle \xi(x)\xi(0)\rangle \propto \frac{\cos[t_\varphi x]}{|x|^{2\Delta_\varphi}} \tag{2.58}$$

while those of $\mathcal{N}^{x,y}$ are *commensurate*

$$\langle \mathcal{N}^{x,y}(x)\mathcal{N}^{x,y}(0)\rangle \propto \frac{1}{|x|^{2\Delta_\vartheta}}. \tag{2.59}$$

Taken together with Eqs. (2.12) and (2.13), which describe the relation between spin operators in the laboratory and rotated frames, these simple relations allow us to fully describe the asymptotic spin (and dimerization) correlations in the LL phase with fully broken spin-rotational symmetry

$$\begin{aligned}
\langle S^x(x)S^x(0)\rangle &\propto \frac{\cos[(\pi - t_\varphi)x]}{|x|^{2\Delta_\varphi}},\\
\langle S^y(x)S^y(0)\rangle &\propto \sin^2\theta_0 \frac{\cos[(\pi - t_\varphi)x]}{|x|^{2\Delta_\varphi}} + \cos^2\theta_0 \frac{(-1)^x}{|x|^{2\Delta_\vartheta}},\\
\langle S^z(x)S^z(0)\rangle &\propto \frac{(-1)^x}{|x|^{2\Delta_\vartheta}},\\
\langle \epsilon(x)\epsilon(0)\rangle &\propto \cos^2\theta_0 \frac{\cos[(\pi - t_\varphi)x]}{|x|^{2\Delta_\varphi}} + \sin^2\theta_0 \frac{(-1)^x}{|x|^{2\Delta_\vartheta}}.
\end{aligned} \tag{2.60}$$

Due to $\Delta_\varphi < \Delta_\vartheta$, the LL phase is dominated by the incommensurate correlations of $S^{x,y}$ and ϵ fields. Their contribution to the equal time structure factor is easy to estimate by simple scaling analysis. For example, denoting $Q = \pi - t_\varphi$,

$$M_s^x(k) \propto \int dx \frac{e^{i(k-Q)x}}{|x|^{2\Delta_\varphi}} \sim |k - Q|^{2\Delta_\varphi - 1}, \tag{2.61}$$

where we extended limits of the integration to infinity due to convergence of the integral for $2\Delta_\varphi > 0$. The divergence at $k = Q$ is controlled by $2\Delta_\varphi - 1 = -y_\sigma/2 > 0$ and is rounded in the system of finite size L. More careful calculation of $M_s^a(k)$ and $M_d(k)$ is possible,[87–89] but is beyond the scope of the present study.

2.2 Weakly coupled spin chains with staggered between chains DM interactions

In this section, excerpts and figures are reprinted with permission from W. Jin and O. A. Starykh, authors of Phys. Rev. B **95**, 214404 (2017).[84] Copyright by the American Physical Society.

Here we study the phase diagram of weakly coupled DM spin chains. This work is strongly motivated by two new interesting materials, $K_2CuSO_4Cl_2$ and $K_2CuSO_4Br_2$,[12,45,90] which are described by Hamiltonian (2.62) representing weakly coupled spin chains (chain exchange J, interchain exchange J', and $J' \ll J$) perturbed by the uniform within the chain, but staggered between chains Dzyaloshinskii-Moriya (DM) anisotropic exchange interaction of magnitude D, as shown in **Figure 2.6**. (Similar DM geometry is also realized in a spin-ladder material $(C_7H_{10}N)_2CuBr_4$.[91]) Despite close structural similarity, the two materials are characterized by different $h-T$ phase diagrams in the situation when magnetic field $\boldsymbol{h}$ is applied along the DM axis $\boldsymbol{D}$ of the material. Our objective here is to provide theoretical explanation of those phase diagrams, and find reasons for their differences. We also extend analysis to another special field configuration, when magnetic field is perpendicular to the DM vector.

Individual spin chains with uniform[12,45,54,79] and staggered[92] DM interactions respond differently to the magnetic field. In the latter case it leads to the opening of significant spin gap[93] while in the former the (much smaller) gap opens up only in the $\boldsymbol{h} \perp \boldsymbol{D}$ geometry.[54,79] We show below that this difference persists in the presence of the weak interchain interaction and is responsible for a very different set of the ordered states for the uniform DM problem in comparison with the staggered DM one.[94]

2.2.1 Model Hamiltonian

We consider weakly coupled antiferromagnetic Heisenberg spin-1/2 chains subject to a uniform Dzyaloshinskii-Moriya (DM) interaction and an external magnetic field. The system is described by extending the single chain Hamiltonian (2.1) and setting $\Delta = 1$,

$$H = \sum_{x,y} \left[J \boldsymbol{S}_{x,y} \cdot \boldsymbol{S}_{x+1,y} + J' \boldsymbol{S}_{x,y} \cdot \boldsymbol{S}_{x,y+1} \right] + \boldsymbol{D} \cdot \sum_{x,y} (-1)^y \boldsymbol{S}_{x,y} \times \boldsymbol{S}_{x+1,y} - \boldsymbol{h} \cdot \sum_{x,y} \boldsymbol{S}_{x,y}, \qquad (2.62)$$

where $\boldsymbol{S}_{x,y}$ is the spin-1/2 operator at position x of y-th chain. J and J' denote isotropic intra- and interchain antiferromagnetic exchange couplings as shown in **Figure 2.6**, and

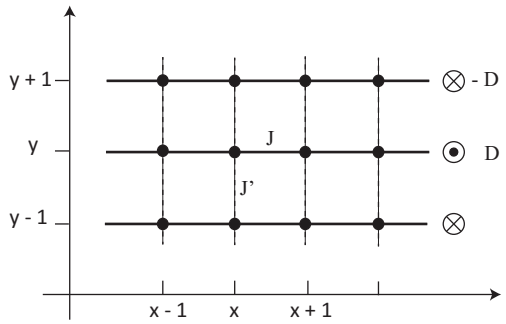

Figure 2.6. Geometry of the coupled spin chains. Intrachain bonds J (thick lines along $\hat{x}$), interchain bonds J' (dashed lines along $\hat{y}$), and $J' \ll J$. The DM vectors on neighboring chain have the opposite direction, pointing either into or out of the page.

we account for interactions between nearest neighbors only. The interchain exchange is weak, of the order of $J' \sim 10^{-2}J$. The DM vector $\boldsymbol{D} = D\hat{z}$, direction of which is staggered between adjacent chains – note the factor $(-1)^y$ in (2.62). Importantly, within a given y-th chain vector $\boldsymbol{D}$ is uniform. $\boldsymbol{h}$ is an external magnetic field.

Similarly to the low-energy Hamiltonian in Eq. (2.64), the Hamiltonian (2.62) written in terms of spin currents and staggered magnetizations is,

$$H = \sum_y [H_0 + V + H_{\rm bs} + H_{\rm inter}], \tag{2.63}$$

where

$$\begin{aligned}
H_0 &= \frac{2\pi v}{3} \int \mathrm{d}x (\boldsymbol{J}_{yR} \cdot \boldsymbol{J}_{yR} + \boldsymbol{J}_{yL} \cdot \boldsymbol{J}_{yL}), \\
V &= -h_z \int \mathrm{d}x (J^z_{yR} + J^z_{yL}) - h_x \int \mathrm{d}x (J^x_{yR} + J^x_{yL}) + (-1)^y \tilde{D} \int \mathrm{d}x (J^z_{yR} - J^z_{yL}), \\
H_{\rm bs} &= -g_{\rm bs} \int \mathrm{d}x [J^x_{yR} J^x_{yL} + J^y_{yR} J^y_{yL} + (1+\lambda) J^z_{yR} J^z_{yL}], \\
H_{\rm inter} &= J' \int \mathrm{d}x \boldsymbol{N}_y \cdot \boldsymbol{N}_{y+1},
\end{aligned} \tag{2.64}$$

The anisotropy parameter λ (2.7) is simplified when $\Delta = 1$, and

$$\lambda = c' \frac{D^2}{J^2}, \text{ where } c' = \frac{1}{2} c \simeq 3.83. \tag{2.65}$$

The interchain interaction is described by $H_{\rm inter}$, in which we kept the most relevant, in a renormalization group sense, contribution, $\boldsymbol{S}_{x,y} \cdot \boldsymbol{S}_{x,y+1} \to \boldsymbol{N}_y(x) \cdot \boldsymbol{N}_{y+1}(x)$.

2.2.2 Parallel configuration, $h \parallel D$

When the external magnetic field is parallel to DM vector $\boldsymbol{D}$ along $\hat{z}$, $h_z = h$ and $h_x = 0$. In this configuration it is convenient to use Abelian bosonization (2.3), by expressing spin currents in V of Eq. (2.64) in terms of fields (ϕ_y, θ_y),

$$\begin{aligned} H_0 &= \frac{v}{2}\int \mathrm{d}x[(\partial_x\phi_y)^2 + (\partial_x\theta_y)^2], \quad V = H_Z + H_{\mathrm{DM}}, \\ H_Z &= -\frac{h}{\sqrt{2\pi}}\int \mathrm{d}x\partial_x\phi_y, \\ H_{\mathrm{DM}} &= -(-1)^y\frac{D}{\sqrt{2\pi}}\int \mathrm{d}x\partial_x\theta_y, \end{aligned} \tag{2.66}$$

where H_Z and H_{DM} are the Zeeman and DM interactions, respectively. Evidently, these linear terms can be absorbed into H_0 by shifting fields ϕ_y and θ_y appropriately,

$$\begin{aligned} &\phi_y = \tilde{\phi}_y + \frac{t_\phi}{\sqrt{2\pi}}x, \quad t_\phi \equiv \frac{h}{v}, \\ &\theta_y = \tilde{\theta}_y + (-1)^y\frac{t_\theta}{\sqrt{2\pi}}x = \tilde{\theta}_y + \frac{t_\theta^y}{\sqrt{2\pi}}x, \qquad t_\theta^y \equiv (-1)^y t_\theta = (-1)^y\frac{D}{v}. \end{aligned} \tag{2.67}$$

Note that t_θ^y depends on the parity of the chain index y. We see that Eq. (2.17) is just the simplified version of Eq. (2.67), where $t_\theta = 0$, associated with the orthogonality between magnetic field and DM interactions. Similarly to Eq. (2.18) and (2.19), the spin currents and the staggered magnetization are modified as

$$\begin{aligned} &J_{yR}^+ \to \tilde{J}_{yR}^+ e^{-i(t_\phi - t_\theta^y)x}, \quad J_{yL}^+ \to \tilde{J}_{yL}^+ e^{i(t_\phi + t_\theta^y)x}, \\ &J_{yR}^z \to \tilde{J}_{yR}^z + \frac{(t_\phi - t_\theta^y)}{4\pi}, \quad J_{yL}^z \to \tilde{J}_{yL}^z + \frac{(t_\phi + t_\theta^y)}{4\pi}, \\ &N_y^+ \to \tilde{N}_y^+ e^{it_\theta^y x}, \quad N_y^z \to -A\sin[\sqrt{2\pi}\tilde{\phi}_y + t_\phi x]. \end{aligned} \tag{2.68}$$

It is important to observe here that the operators with tildes in (2.68) are obtained from the original ones (2.3) and (2.4) by replacing original ϕ_y and θ_y with their tilted versions $\tilde{\phi}_y$ and $\tilde{\theta}_y$. Note also that the shift introduces oscillating position-dependent factors to transverse components of $\boldsymbol{J}_y$ and $\boldsymbol{N}_y$. The Hamiltonian now reads

$$H_{\mathrm{chain}} = \tilde{H}_0 + \tilde{H}_{\mathrm{bs}} + \tilde{H}_{\mathrm{inter}}, \tag{2.69}$$

where $\tilde{H}_0$ retains its quadratic form (2.66) in terms of the tilded fields. It is perturbed by backscattering $\tilde{H}_{\mathrm{bs}}$ and interchain $\tilde{H}_{\mathrm{inter}}$ interactions, which now read

$$\tilde{H}_{\mathrm{bs}} = \int \mathrm{d}x\{\pi v y_B(\tilde{J}_{yR}^+\tilde{J}_{yL}^- e^{-i2t_\phi x} + \mathrm{h.c.}) + 2\pi v y_z \tilde{J}_{yR}^z\tilde{J}_{yR}^z\}, \tag{2.70}$$

and $\tilde{H}_{\rm inter} = H_{\rm cone} + H_{\rm sdw}$, where

$$\begin{aligned} H_{\rm cone} &= \pi v A^2 g_\theta \int \mathrm{d}x \big(e^{i[\sqrt{2\pi}(\tilde{\theta}_y - \tilde{\theta}_{y+1}) + 2t_\theta^y x]} + \text{h.c.}\big), \\ H_{\rm sdw} &= \pi v A^2 \int \mathrm{d}x \Big\{ g_\phi \big(e^{i\sqrt{2\pi}(\tilde{\phi}_y - \tilde{\phi}_{y+1})} + \text{h.c.}\big) - \tilde{g}_\phi \big(e^{i[\sqrt{2\pi}(\tilde{\phi}_y + \tilde{\phi}_{y+1}) + 2t_\phi x]} + \text{h.c.}\big) \Big\}. \end{aligned} \tag{2.71}$$

$H_{\rm cone}$ and $H_{\rm sdw}$ are the transverse and longitudinal (with respect to the z axis) components of the interchain interaction, respectively. Their effect consists of promoting a two-dimensional ordered cone and SDW state, correspondingly. Small terms resulting from the additive shifts in $J^z_{R/L}$ in (2.68) have been neglected. **Table 2.2** describes which interchain interactions produce which state.

In writing the above we introduced several running coupling constants

$$\begin{aligned} y_B &= \frac{1}{2}(y_x + y_y), \quad y_B(0) = -\frac{g_{\rm bs}}{2\pi v}, \\ g_\theta &= \frac{1}{2}(g_x + g_y), \quad g_\theta(0) = \frac{J'}{2\pi v}, \\ g_\phi &= \tilde{g}_\phi = \frac{1}{2} g_z, \quad g_z(0) = \frac{J'}{2\pi v}, \end{aligned} \tag{2.72}$$

initial values of which follow from

$$\begin{aligned} y_x(0) = y_y(0) &= -\frac{g_{\rm bs}}{2\pi v}, \quad y_z(0) = -\frac{g_{\rm bs}}{2\pi v}(1+\lambda), \\ g_x(0) = g_y(0) &= g_z(0) = \frac{J'}{2\pi v}. \end{aligned} \tag{2.73}$$

Observe that the DM interaction produces an effective anisotropy $\lambda = c'(D/J)^2 > 0$ which leads to $|y_z(0)| > |y_{x,y}(0)|$.

Table 2.2. Three relevant perturbations from interchain interaction $H_{\rm cone}$, $H_{\rm sdw}$ in Eq. (2.71) and $H_{\rm NN}$ in Eq. (2.79), their operator forms, associated coupling constants, and types of the ordered states they induce.

Interaction term	Coupling operator	Coupling constant	Induced state
$H_{\rm cone}$	$N^+_y N^-_{y+1}$	g_θ	cone
$H_{\rm sdw}$	$N^z_y N^z_{y+1}$	g_z	SDW
$H_{\rm NN}$	$N^+_y N^-_{y+2}$	G_θ	coneNN

2.2.2.1 Renormalization group analysis

The RG equations for various coupling constants are,

$$\begin{aligned} \frac{dy_B}{d\ell} &= y_B y_z, \quad \frac{dy_z}{d\ell} = y_B^2, \\ \frac{dg_\theta}{d\ell} &= g_\theta(1 - \frac{1}{2}y_z), \quad \frac{dg_z}{d\ell} = g_z(1 + \frac{1}{2}(y_z - 2y_B)). \end{aligned} \tag{2.74}$$

The first two equations in Eq. (2.74) are the well-known Kosterlitz-Thouless (KT) equations for the marginal backscattering couplings $y_{B,z}$ in (2.70). They admit the analytic solution which is illustrated in **Figure 2.7**. Initial conditions (2.72), (2.73) correspond to $y_B < 0, y_z < 0$, and $C = y_z(\ell)^2 - y_B(\ell)^2 > 0$, which places the KT flow in sector 4 in **Figure 2.7**. Physically, this corresponds to DM-induced easy-plane anisotropy ($\lambda > 0$) which, if acting alone, would drive the chain into a critical Luttinger liquid (LL) state.

This marginally irrelevant flow of $y_{B,z}$ is, however, interrupted by the exponentially fast growth of the interchain interactions $g_{\theta,\phi}$ which, according to (2.74), reach the strong-coupling limit at $\ell_{\text{inter}} \approx \ln(2\pi v/J')$. This growth describes development of the two-dimensional magnetic order in the system of weakly coupled chains. As a result, we are allowed to treat chain backscattering $y_{B,z}$, which barely changes on the scale of ℓ_{inter}, as a weak correction to the relevant interchain interaction. This is the physical content of the second line of the RG equations in (2.74).

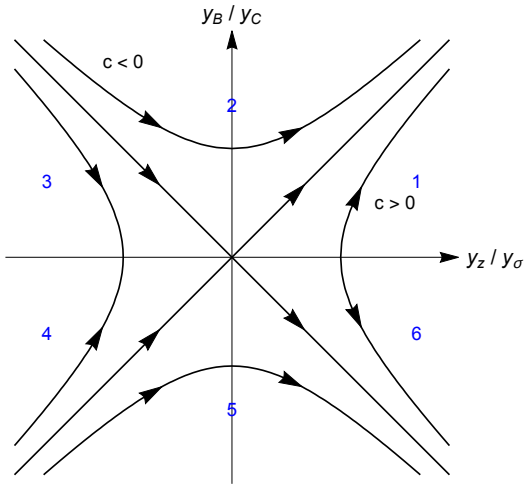

Figure 2.7. Solution of Kosterlitz-Thouless (KT) equations [first line of (2.74)]. Five sectors of the flow are divided according to the initial conditions. For example, in sector 3: $y_{z/\sigma}(0) < 0, y_{B/C}(0) > 0$, and $C > 0$.

The DM interaction and magnetic field strongly perturb RG flow (2.74) via coordinate-dependent factors $e^{i2t_\theta^y x}$ and $e^{i2t_\phi x}$, rapid oscillations of which become significant once the running RG scale ℓ becomes greater than $\ell_\theta(\ell_\phi)$, where

$$\ell_\theta = \ln(\frac{1}{a_0 t_\theta}) = \ln(\frac{v}{D a_0}),\ \ell_\phi = \ln(\frac{1}{a_0 t_\phi}) = \ln(\frac{v}{h a_0}). \tag{2.75}$$

These oscillations have the effect of nullifying, or averaging out, corresponding interaction terms in the Hamiltonian, provided that the corresponding coupling constants remain small at RG scales $\ell_{\theta,\phi}$. The affected terms are $H_{\rm cone}$ and the $\tilde{g}_\phi$ term in $H_{\rm sdw}$, respectively. Also affected is backscattering y_B term in (2.70). The short-distance cut-off a_0 that appears in (2.75) is determined by the initial value of the backscattering $g_{\rm bs}(0) = 0.23 \times (2\pi v)$; see Ref.[54] for a detailed explanation of this point.

In accordance with general discussion in Appendix. A.1, we define ℓ^* as an RG scale at which the most relevant coupling constant g reaches the value of 1, namely $|g(\ell^*)| = 1$. For interchain couplings, we find that ℓ^* is close to $\ell_{\rm inter} \approx \ln(2\pi v/J')$ introduced below Eq. (2.74), and this is noted in the captions of **Figure 2.8** and **Figure 2.9**.

Magnetic-field-induced oscillations in $H_{\rm sdw}$ are well known and describe a magnetization induced shift of longitudinal spin modes from the zero wave vector. In addition, the magnetic field works to increase the scaling dimension of the N^z field, from $1/2$ at zero magnetization $M = 0$ to 1 at full polarization $M = 1/2$, see **Table 2.3**, making the N^z field less relevant. Typically, this makes the $H_{\rm sdw}$ term less important than the $H_{\rm cone}$ one, which

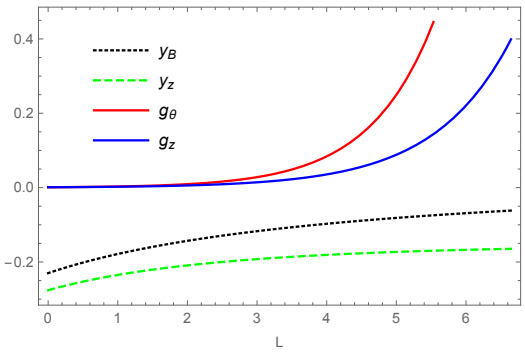

Figure 2.8. Typical RG flow of the coupling constants for weak DM interaction and $\boldsymbol{h} \parallel \boldsymbol{D}$, $h_x = 0$. $D = 1 \times 10^{-4} J$, $g_{\rm bs}/(2\pi v) = 0.23$, $J'/(2\pi v) = 0.001$, $h_z/D = 1$, and $\lambda = 0.2$. Here $\ell_{\rm inter} \simeq 6.9$, $\ell_\phi = \ell_\theta \simeq 6.6$. The dominant coupling is g_θ (red solid line), and $g_\theta(\ell^*) = 1$ at $\ell^* \simeq 6.3$.

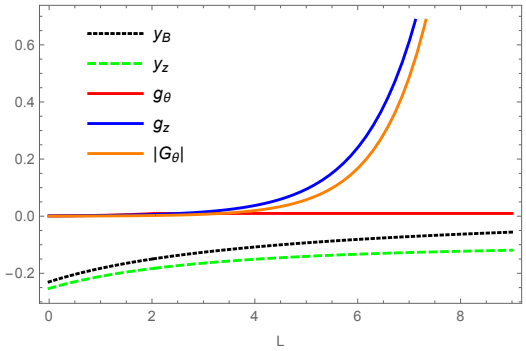

Figure 2.9. RG flow of the coupling constants for strong DM interaction and $\boldsymbol{h} \parallel \boldsymbol{D}$, $h_x = 0$. The case of low magnetic field $h_z/D = 0.005$. $D = 0.01J$, $g_{\rm bs}/(2\pi v) = 0.23$, $J'/(2\pi v) = 0.001$, and $\lambda = 0.1$. Here $\ell_{\rm inter} \simeq 6.9$, $\ell_\phi \simeq 7.4$, $\ell_\theta \simeq 2$, and g_θ remains a constant after $\ell > \ell_\theta$, due to the rapid spatial oscillation. The dominant coupling is g_z (blue solid line), and $g_z(\ell^*) = 1$ at $\ell^* \simeq 7.5$.

Table 2.3. Scaling dimensions Δ of longitudinal and transverse components for staggered magnetization $\boldsymbol{N}$ vs. magnetization M.

Operator	Δ	M=0	M=1/2
N^z	π/β^2	1/2	1
N^+	πR^2	1/2	1/4

is built out of transverse spin operators which become more relevant with the field (the corresponding scaling dimension of which becomes smaller with the field; it changes from $1/2$ at $M = 0$ to $1/4$ at $M = 1/2$).

In our problem, however, the prevalence of the cone state is much less certain due to the presence of the built-in DM-induced oscillations in $H_{\rm cone}$ (2.71), originating from the staggered geometry of the DM interaction. As a result, one needs to distinguish the cases of weak and strong DM interaction, which in the current case should be compared with the interchain exchange interaction J'.

2.2.2.2 Weak DM interaction

First, we consider the case of weak DM interaction, $D \ll J'$. This means $\ell_\theta > \ell_{\rm inter}$; the integrand of $H_{\rm cone}$ oscillates slowly so that the factor $e^{i2t_\theta^y x}$ does not affect the RG flow. As discussed in Appendix A, backscattering terms break the symmetry between g_θ and g_z,

$g_\theta(\ell) > g_z(\ell)$. As a result, interchain interaction $H_{\rm cone}$ reaches strong coupling before $H_{\rm sdw}$ and the ground state realizes the cone phase. The typical RG flow of coupling constants for this case is shown in **Figure 2.8**.

Minimization of the argument of the cosine in $H_{\rm cone}$ requires that $\sqrt{2\pi}(\tilde\theta_y - \tilde\theta_{y+1}) + 2t_\theta^y x = \pi$. This is solved by requiring $\tilde\theta_y(x) = \hat\theta - (-1)^y t_\theta x/\sqrt{2\pi} - \sqrt{\pi/2}\, y$, where $\hat\theta$ is a position-independent constant which describes orientation of the staggered magnetization $N_y^+(x) \sim (-1)^y i e^{i\sqrt{2\pi}\hat\theta}$ in the plane perpendicular to the magnetic field.

Observe that the obtained solution describes a *commensurate-cone* configuration. The original shift (2.67) is compensated by the opposite shift needed to minimize the $\tilde\theta$ configuration. As a result the obtained cone state is commensurate along the chain direction: N_y^+ is uniform along the chain direction which means the spin configuration is actually staggered, $S_y^+(x) \sim (-1)^x N_y^+$, see (2.2). Note also that N_y^+ is staggered between chains (so as to minimize the antiferromagnetic interchain exchange $J' > 0$), so that in fact $S_y^+(x)$ realizes the standard Néel configuration. Thus the ground state spin configuration of the cone phase is described by

$$\langle \mathbf{S}_y(x)\rangle = M\mathbf{z} + (-1)^{x+y}\Psi_{\rm cone}(-\sin[\sqrt{2\pi}\hat\theta]\mathbf{x} + \cos[\sqrt{2\pi}\hat\theta]\mathbf{y}). \tag{2.76}$$

Here $\Psi_{\rm cone}$ denotes the magnitude of the order parameter at the scale ℓ^*. According to (A.2) and using Eqs. (2.4) and (2.72), it can be estimated as $\Psi_{\rm cone} = \gamma/(\pi a)\sqrt{g_\theta} \propto (J'/v)^{1/2}$. The square-root dependence of the order parameter on the interchain exchange J' is a well-known feature of weakly coupled chain problems.[95] CMF theory, which we introduce in the next section, can also be used to calculate the cone order parameter. (This calculation is described in Appendix 2.2.7.) Note that its dependence on M occurs via M dependence of scaling dimensions and other parameters in the Hamiltonian which are not easy to capture with the help of the RG procedure.

2.2.2.3 Strong DM interaction

2.2.2.3.1 SDW order. Now we turn to a less trivial case of strong DM interaction, when $D \gg J'$. Here $\ell_\theta < \ell_{\rm inter}$, which simply eliminates $H_{\rm cone}$ from the competition, and from the Hamiltonian. The physical reasoning is that strong DM interaction introduces strong frustration to the transverse interchain interaction, which oscillates rapidly and

averages to zero. As a result, the only interchain interaction that survives in this situation is $H_{\rm sdw}$, Eq. (2.71), which establishes two-dimensional longitudinal SDW order.

Two types of SDW ordering are possible. The first, *commensurate* SDW order, is realized in low magnetic field $h \leq h_{\rm c-ic} \sim O(J')$ when spatial oscillations due to the $t_\phi x$ term in the N^z_y operator (2.68) are not important. This is the regime of $\ell_\phi \gg \ell_{\rm inter}$, when both the g_ϕ and $\tilde{g}_\phi$ terms in the SDW interchain interaction $H_{\rm sdw}$ in (2.71) contribute equally. In a close similarity to the commensurate-cone state discussed above, the $\tilde{\phi}$ configuration here is minimized by $\tilde{\phi}_y(x) = \hat{\phi} - t_\phi x/\sqrt{2\pi} - \sqrt{\pi/2}\ y$. Here the global constant $\hat{\varphi}$ is determined by the requirement that $\sin[\sqrt{2\pi}\hat{\phi}] = \pm 1$, corresponding to a maximum possible magnitude of $N^z_y \sim (-1)^y \sin[\sqrt{2\pi}\hat{\phi}]$. Therefore $\hat{\phi} = \hat{\phi}_k = \sqrt{\pi/2}(k+1/2)$, where $k = 0, 1$. This describes the situation of the commensurate longitudinal SDW order which is pinned to the lattice, $N^z_y \sim (-1)^y(-1)^k$. Changing $k \to k \pm 1$ corresponds to a discrete translation of the SDW order by one lattice spacing. In terms of spins this too is a Néel-like order, but it is a collinear one along the magnetic field axis,

$$\langle \boldsymbol{S}_{x,y} \rangle = (M + \Psi_{\rm sdw-c}(-1)^{x+y}(-1)^k)\mathbf{z}. \tag{2.77}$$

Increasing the field beyond $h_{\rm c-ic}$ unpins the SDW ordering from the lattice and transforms the spin configuration into collinear *incommensurate* SDW. Technical details of this are described in Appendix B and here we focus on the physics of this commensurate-incommensurate (C-IC) transition. Increasing h makes ℓ_ϕ smaller and at $\ell_\phi \approx \ell_{\rm inter}$ the oscillating $e^{i2t_\phi x}$ factor in the $\tilde{g}_\phi$ term in (2.71) becomes very strong and "washes out" that piece of the $H_{\rm sdw}$ Hamiltonian. The remaining, g_ϕ, part of $H_{\rm sdw}$ continues to be the only relevant interchain interaction and flows to the strong coupling. Therefore now $\sqrt{2\pi}(\tilde{\phi}_y - \tilde{\phi}_{y+1}) = \pi$ which is solved by $\tilde{\phi}_y = \hat{\phi} - \sqrt{\pi/2}\ y$. As a result the shift (2.67) remains intact and one finds incommensurate-SDW ordering with

$$\langle \boldsymbol{S}_y(x) \rangle \sim (M + \Psi_{\rm sdw-ic}(-1)^{x+y} \sin[\sqrt{2\pi}\hat{\phi} + hx/v])\mathbf{z}. \tag{2.78}$$

The magnitude of the SDW order parameter $\Psi_{\rm sdw-ic}$ in this equation is calculated in Appendix 2.2.7. Note that unlike the cone order, the SDW one weakens with increasing M.

The global phase $\hat{\phi} \in (0, \sqrt{2\pi})$ is not pinned to any particular value; it describes emergent translational U(1) symmetry of the "high-field" limit of the SDW Hamiltonian

[Eq. (2.71) without $\tilde{g}_\phi$ term], which does not depend on the value of $\hat{\phi}$. Spontaneous selection of some particular $\hat{\phi}$ corresponds to a spontaneous breaking of the translational symmetry. The resulting incommensurate-SDW order is characterized by the emergence of Goldstone-like longitudinal fluctuations, *phasons*. Recent discussion of some aspects of this physics can be found in Ref.[16]

2.2.2.3.2 Next-nearest chains cone order. The above SDW-only arguments, however, do not take into account the possibility of a cone-like interaction between more distant chains. Even though such interactions are absent from the lattice Hamiltonian (2.62), they can (and will) be generated by quantum fluctuations at low energies, as long as they remain consistent with symmetries of the lattice model.[96] The simplest of such interactions is given by the transverse interchain interaction between the next-neighbor (NN) chains $H_{\rm NN}$, see Sec. 2.2.6 in the Supplement for the detailed derivation,

$$H_{\rm NN} = 2\pi v G_\theta \sum_y \int {\rm d}x (\tilde{N}_y^+ \tilde{N}_{y+2}^- + {\rm h.c.}). \tag{2.79}$$

This is an indirect exchange, mediated by an intermediate chain $(y+1)$, and therefore its exchange coupling can be estimated as $2\pi v G_\theta \sim (J')^2/(2\pi v) \ll J'$. However the scaling dimension of this term (≈ 1 without the magnetic field) is the same as of the original cone interaction $H_{\rm cone}$ and thus G_θ is expected to grow exponentially fast. Importantly, $H_{\rm NN}$ is free of the DM-induced oscillations because DM vectors $\boldsymbol{D}$ on chains y and $(y+2)$ point in the same direction. That is, fields $\tilde{\theta}_y$ and $\tilde{\theta}_{y+2}$ corotate. This basic physical reason makes $H_{\rm NN}$ a legitimate candidate for fluctuation-generated interchain exchange interaction of the cone kind. The calculation in Appendix 2.2.6 gives the NN coupling constant

$$G_\theta = -\frac{\pi A_3^2}{4} f(\Delta_1) \frac{J'}{D} g_\theta,\ f(\Delta_1) = t_\theta^{2\Delta_1 - 1} \frac{\Gamma(1-\Delta_1)}{\Gamma(\Delta_1)}, \tag{2.80}$$

which depends on the magnetic field via scaling dimension Δ_1. At low fields $\Delta_1 \approx 1/2$ and $f(1/2) \approx 1$. Observe that G_θ describes ferromagnetic interaction and, contrary to the naive perturbation theory expectation, has significant magnitude: $2\pi v G_\theta \propto (J')^2/D \gg (J')^2/J$.The RG equation for G_θ coincides with that of g_θ,

$$\frac{dG_\theta}{d\ell} = G_\theta (1 - \frac{1}{2} y_z). \tag{2.81}$$

When G_θ reaches strong coupling first, the $\tilde{\theta}$ configuration is uniform, $\tilde{\theta}_y = \tilde{\theta}_{y+2} = \hat{\theta}_{\rm e/o}$, where index $\nu = {\rm e}$ for even y and $\nu = {\rm o}$ for odd y values and in general $\hat{\theta}_{\rm e} \neq \hat{\theta}_{\rm o}$. At this

level of approximation subsystems of even and odd chains decouple from each other. The obtained coneNN order is incommensurate,

$$\begin{aligned}\langle \boldsymbol{S}_{x,y}\rangle \quad &= M\mathbf{z} + (-1)^{x+y}\Psi_{\text{coneNN}}\Big(-\sin[\sqrt{2\pi}\hat{\theta}_\nu + (-1)^y t_\theta x]\boldsymbol{x} \\ &+ \cos[\sqrt{2\pi}\hat{\theta}_\nu + (-1)^y t_\theta x]\boldsymbol{y}\Big),\ \nu = \text{e, o.}\end{aligned} \tag{2.82}$$

The described situation is actually very similar to one discussed in Ref.,[97] see Sec. IV there, where spins in the neighboring layers are found to counter-rotate, due to oppositely oriented DM vectors, and are not correlated with each other.

By a simple manipulation this spin ordering can also be represented as

$$\begin{aligned}&\langle \boldsymbol{S}_{x,y}\rangle = M\mathbf{z} + (-1)^{x+y}\Psi_{\text{coneNN}}\Big(\cos[t_\theta x]\{-\sin[\sqrt{2\pi}\hat{\theta}_\nu]\mathbf{x} + \cos[\sqrt{2\pi}\hat{\theta}_\nu]\mathbf{y}\} \\ &-(-1)^y \sin[t_\theta x]\{\cos[\sqrt{2\pi}\hat{\theta}_\nu]\mathbf{x} + \sin[\sqrt{2\pi}\hat{\theta}_\nu]\mathbf{y}\}\Big).\end{aligned} \tag{2.83}$$

Expressions inside curly brackets represent orthogonal unit vectors which are obtained from the orthogonal pair $(\mathbf{x}, \mathbf{y})$ by the chain-parity dependent rotation by angle $\pm\sqrt{2\pi}\hat{\theta}_\nu$.

2.2.2.3.3 Competition between SDW and cone/coneNN orders. The quantitative description of the competition between SDW and cone orders within the RG framework represents a very difficult task. This basically has to do with the fact that RG is not well suited for describing oscillating perturbations such as (2.71) and (2.70). It is quite good at extracting the essential physics of the slow- and fast-oscillation limits, as described in Secs. 2.2.2.2 and 2.2.2.3.2 above, but is not particularly useful in describing the intermediate regime $D \sim J'$ in which the change from one behavior to the another takes place (see Ref.[93] for the example of the RG study of the much simpler problem of a single spin-1/2 chain in the magnetic field).

Applied to the cone-SDW competition, one needs to compare effects due to the DM-induced oscillations with those due to the magnetic-field-induced ones. Given that magnetic field makes cone terms more relevant and SDW ones less relevant, one can anticipate that even if the DM interaction is strong enough to destroy the cone phase in a small magnetic field, the cone can still prevail over the SDW phase at higher fields. The chain mean field approximation, described in the next section (and also in more detail in Appendix B) indeed shows that the critical D/J' ratio required for suppressing the cone phase increases with magnetization M. Nonetheless, the ratio D/J' is bounded: there exists sufficiently large D (still of the order J') above which the cone order becomes impossible for any M.

For D greater than that we need to examine competition between $H_{\rm sdw}$ and $H_{\rm NN}$. Approximating A as $1/2$ here (see Ref.;[98] transverse normalization factor A_3 is close to $1/2$ at small magnetization), we observe that $|G_\theta|$ is about $J'/(4D)$ times smaller than g_z. However, in the presence of magnetic field G_θ becomes more relevant in the RG sense (similarly to its frustrated 'parent' g_θ), and grows much faster than SDW interaction g_z, which becomes less relevant with magnetic field. Therefore there should be a range of J'/D such that $G_\theta(\ell)$ can compete with $g_z(\ell)$.

Such an example is shown in **Figure 2.9** and **Figure 2.10**, $D/J' \sim 1$ there. **Figure 2.9** shows RG flow in low magnetic field $h_z/D = 0.005$, when g_z grows faster than $|G_\theta|$, resulting in the SDW state. However, in higher magnetic field $h_z/D = 5$, which is still rather low in comparison with J, G_θ turns out to be the most relevant coupling constant. Hence the ground state changes to the coneNN one.

Details of this competition depend strongly on the magnitude of the magnetic field. At low field $h \leq h_{\rm c-ic}$ SDW is commensurate, while at higher field $h \geq h_{\rm c-ic}$ it turns incommensurate. Calculations reported in Appendix B find that $h_{\rm c-ic} \approx 1.4J'$ which is a sufficiently small value [the corresponding magnetization is very small as well, $M_{\rm c-ic} = h_{\rm c-ic}/(2\pi v) \approx 1.4J'/(\pi^2 J) \ll 1$] , especially in the most interesting to us regime of strong DM, $D \gg J'$. Given that the critical temperature of the incommensurate-SDW order is lower than that of the commensurate one (see **Figure B.2**), the SDW-coneNN competition

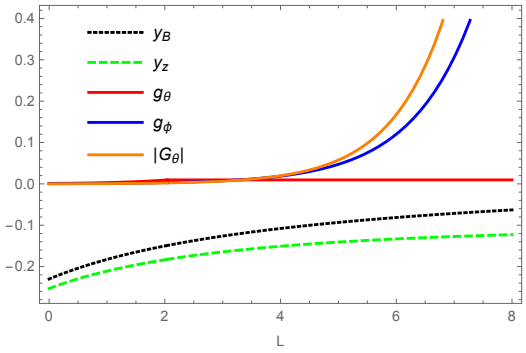

Figure 2.10. Typical flow of the coupling constants for strong DM interaction and $\boldsymbol{h} \parallel \boldsymbol{D}$, $h_x = 0$. This is the case of a relatively high magnetic field $h_z/D = 5$. $D = 0.01J$, $g_{\rm bs}/(2\pi v) = 0.23$, $J'/(2\pi v) = 0.001$, and $\lambda = 0.1$. Here $\ell_{\rm inter} \simeq 6.9$, $\ell_\varphi \simeq 0.4$, $\ell_\theta \simeq 2$. The dominant coupling is G_θ (orange solid line), and $|G_\theta(\ell^*)| = 1$ at $\ell^* \simeq 7.7$.

is most pronounced in the $h \geq h_{c-ic}$ limit, on which we mostly focus in the Sec. 2.2.3.

2.2.3 Chain mean-field calculation

A more quantitative way to characterize DM-induced competition, described in the previous section with the help of qualitative RG arguments, is provided by the chain mean-field (CMF) approximation[97] which allows one to calculate and compare critical temperatures for different magnetic instabilities. The instability with maximal T_c is assumed to describe the actual magnetic order. This calculation enables us to directly compare the resulting critical temperature of the dominant instability to the experimental lambda peak in heat capacity measurements[45] and therefore to directly compare experimental and theoretical $h - T$ phase diagrams. It provides one with a reasonable way to estimate the interchain exchange J' of the material, as we describe in Appendix B.3. It also allows for a straightforward calculation of the microscopic order parameters; see Appendix 2.2.7 .

In applying the CMF approximation to our model, there are three interchain interactions in Eqs. (2.71) and (2.79) that need to be compared,

$$\begin{aligned} H_{\text{cone}} &= c_1 \int \mathrm{d}x \cos[\beta(\tilde{\theta}_y - \tilde{\theta}_{y+1}) + 2(-1)^y t_\theta x], \\ H_{\text{sdw}-\text{ic}} &= c_2 \int \mathrm{d}x [\cos \frac{2\pi}{\beta}(\tilde{\phi}_y - \tilde{\phi}_{y+1})], \\ H_{\text{NN}} &= -c_3 \int \mathrm{d}x \cos[\beta(\tilde{\theta}_y - \tilde{\theta}_{y+2})]. \end{aligned} \tag{2.84}$$

In accordance with the discussion at the end of Sec. 2.2.2.1 we focus here on the $h \geq h_{c-ic}$ regime and neglect oscillating term $\tilde{g}_\phi$ in H_{sdw}. The amplitudes are

$$\begin{aligned} c_1 = J' A_3^2, \quad c_2 = J' A_1^2/2, \\ c_3 = \frac{\pi}{4} \frac{J'^2}{D} A_3^4 t_\theta^{2\Delta_1 - 1} \frac{\Gamma(1-\Delta_1)}{\Gamma(\Delta_1)}. \end{aligned} \tag{2.85}$$

CMF is designed for the analysis of the relevant perturbations and does not account for the marginal interactions, such as Eq. (2.70), directly. However much of their effects can still be captured by adopting a more precise expression for the staggered magnetization, which encodes magnetic field dependence of the scaling dimensions of transverse and longitudinal components via a simple generalization of (2.4),

$$\boldsymbol{N}_y(x) = (-A_3 \sin[\beta\tilde{\theta}_y], A_3 \cos[\beta\tilde{\theta}_y], -A_1 \sin[\frac{2\pi}{\beta}\tilde{\phi}_y]). \tag{2.86}$$

Here the magnetic field dependence of the scaling dimensions of transverse and longitudinal components of $\boldsymbol{N}$ is contained in the parameter $\beta = 2\pi R$, which in turn is related

to the exactly known "compactification radius" R in the sine-Gordon (SG) model. At zero magnetization $M = h = 0$, the SU(2)-invariant Heisenberg chain has $2\pi R^2 = 1$. In the magnetic field, β and R decrease toward the limit $2\pi R^2 = 1/2$ as the chain approaches full polarization. The amplitudes A_1 and A_3 have been determined numerically.[99]

Calculation of T_c is standard and well documented in Ref.;[97] additional details are provided in Appendix B.

For the weak DM interaction, we compare the ordering temperatures of H_{cone} and H_{sdw}, and the T_c for each state as a function of magnetization M is shown in **Figure 2.11**. For the chosen parameters, the critical temperature of the cone is always above that of the SDW; therefore the ground state is the cone, in agreement with the RG analysis in Sec. 2.2.2.2. As magnetization increases, the transverse correlations are enhanced, and longitudinal ones are suppressed, resulting in a greater separation between the two critical temperatures. At larger magnetization, T_{cone} also decreases, basically due to the Zeeman effect; spins align more along the direction of the magnetic field, thereby reducing the magnitude of the transverse spin component.

Increasing the DM interaction frustrates H_{cone} until, at some critical D/J' value, its mean-field solution disappears completely, signifying the impossibility of the standard cone state. This feature is described in greater detail in Appendices B and B.2. **Figure 2.12**

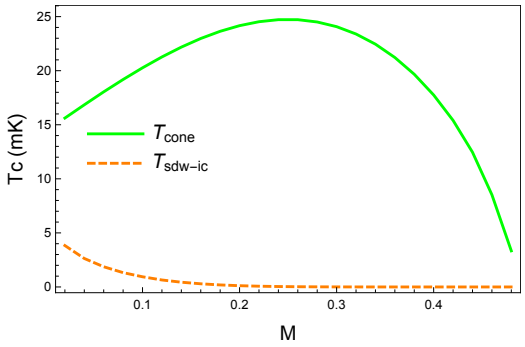

Figure 2.11. Ordering temperatures of the cone (T_{cone}; green solid line) and incommensurate-SDW ($T_{\text{sdw}-\text{ic}}$; orange dashed line) states, vs. magnetization M, for the case of weak DM interaction. $J = 1$ K, $J' = 0.01$ K, and $D = 0.01$ K. Commensurate-SDW state ($T_{\text{sdw}-\text{c}}$) is characterized by $T_{\text{sdw}-\text{ic}} < T_{\text{sdw}-\text{c}} < T_{\text{cone}}$ but is present only as the very narrow magnetization interval $0 < M < M_{\text{c}-\text{ic}} < 0.01$ and is not shown here. The larger ordering temperature is dominant; thus the ground state is a cone in the whole field/magnetization range.

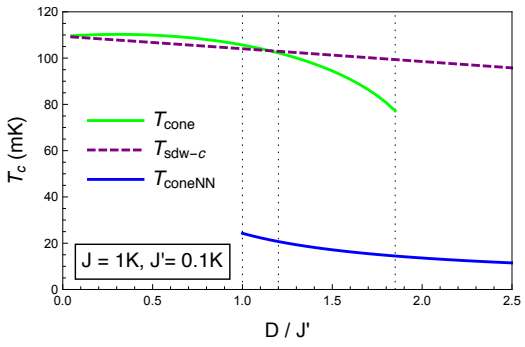

Figure 2.12. Ordering temperatures of the cone (green solid line), commensurate-SDW (purple dashed line), and coneNN (blue solid line) states as a function of D/J' ratio, and in the limit of zero magnetic field, $M = 0$. Here, $J = 1$ K, $J' = 0.1$ K. Note that the solution for coneNN state has physical meaning in the limit $D/J' \gg 1$. $T_{\mathrm{sdw-c}}$ overcomes T_{cone} at $D/J' \simeq 1.2$ and the solution for T_{cone} disappears at $D/J' \simeq 1.9$. See Sec. 2.2.3 and Appendix B.

illustrates it.

With the cone state out of the picture, we now need to consider the transverse NN-chain coupling H_{NN} and its competition with the SDW state as magnetization increases from 0 to the saturation at $M = 0.5$. The result is shown in **Figure 2.13**. In a small magnetic field [when $M \approx h/(2\pi v)$)], T_{sdw} is above T_{coneNN}. As magnetization increases, the scaling dimensions are modified, and the two curves intersect, which indicates a phase transition from the SDW to the coneNN phase. This result is fully consistent with our qualitative RG analysis in Sec. 2.2.2.3.

2.2.4 Orthogonal configuration, $h \perp D$

2.2.4.1 Effective Hamiltonian

When $\boldsymbol{h} \perp \boldsymbol{D}$, the system Hamiltonian is described by Eq. (2.64) with $h_x = h$ and $h_z = 0$. In this configuration, the same procedure of chiral rotation (Sec. 2.1.2.1) and shift of fields (Sec. 2.1.2.3), introduced for individual chain, are applied to the coupled chains system. The derivations have been omitted here; see Ref.[100] for more details.

In this case, the effective Hamiltonian has the same form as that in Eq. (2.69). The expression for back-scatteirng Hamiltonian is,

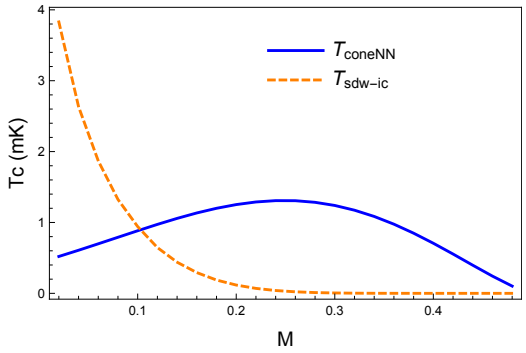

Figure 2.13. Ordering temperatures of the incommensurate-SDW (orange dashed line) and coneNN (blue solid line) states, as a function of magnetization M, in the case of strong DM interaction. $J = 1$ K, $J' = 0.01$ K, and $D = 0.1$ K. Two lines intersect at small magnetization $M \simeq 0.1$, above which the critical temperature of the coneNN state overcomes that of the SDW one.

$$
\begin{aligned}
&H_{\text{bs}} \to H_A + H_B + H_C + H_\sigma, \\
&H_A = \pi v y_A \int \mathrm{d}x (M^z_{y,R} M^+_{y,L} e^{i t_\varphi x} - M^+_{y,R} M^z_{y,L} e^{-i t_\varphi x} + \text{h.c.}), \\
&H_B = \pi v y_B \int \mathrm{d}x (M^+_{y,R} M^-_{y,L} e^{-i 2 t_\varphi x} + \text{h.c.}), \\
&H_C = \pi v y_C \int \mathrm{d}x (M^+_{y,R} M^+_{y,L} + \text{h.c.}), \\
&H_\sigma = -2\pi v y_\sigma \int \mathrm{d}x M^z_{y,R} M^z_{y,L},
\end{aligned}
\tag{2.87}
$$

where

$$
y_C \equiv \frac{1}{2}(y_x - y_y),\ y_B \equiv \frac{1}{2}(y_x + y_y),\ y_\sigma \equiv -y_z. \tag{2.88}
$$

Here $\boldsymbol{M}_{R/L}$ is the spin current in the rotated frame, and $t_\varphi = h_{\text{eff}}/v$ with $h_{\text{eff}} \equiv \sqrt{D^2 + h^2}$. The interchain interaction in terms of rotated operators reads,

$$
H_{\text{inter}} = 2\pi v \sum_y \int \mathrm{d}x \Big[\sum_a g_a \mathcal{N}^a_y \mathcal{N}^a_{y+1} + g_E \varepsilon_y \varepsilon_{y+1} \Big]. \tag{2.89}
$$

The interchain couplings are

$$
\begin{aligned}
g_x(0) &= \frac{J'}{2\pi v}, \quad g_y(0) = \frac{J'}{2\pi v} \cos^2 \theta^y_0, \\
g_z(0) &= \frac{J'}{2\pi v}, \quad g_E(0) = -\frac{J'}{2\pi v} \sin^2 \theta^y_0,
\end{aligned}
\tag{2.90}
$$

Two terms in (2.89), namely g_z and g_E, are expressed in terms of the φ field and therefore contain parts oscillating with position x. In order to keep the presentation simple, we

refrain here from writing this dependence out explicitly. Beyond the oscillating RG scale $\ell_\varphi = -\ln[a_0 t_\varphi]$, introduced in Sec. 2.2.4.2 below, these two terms combine into

$$\begin{aligned} H_{\text{inter},'} &= 2\pi v A^2 \sum_y \int \mathrm{d}x \; g_{\varphi_1} \cos[\sqrt{2\pi}(\varphi_y - \varphi_{y+1})], \\ g_{\varphi_1} &\equiv \frac{1}{2}(g_E + g_z), \quad g_{\varphi_1}(0) = \frac{J'}{4\pi v}\cos^2\theta_0^y. \end{aligned} \tag{2.91}$$

Interchain interactions (2.89) (terms with $g_{x/y}$) and (2.91) are the most relevant perturbations. Three parts of the interchain Hamiltonian (namely the g_x, g_y, and g_{φ_1} terms) and the ordered states they induce are summarized in **Table 2.4**.

As discussed previously, Eq. (2.11), as well as its consequence, Eq. (2.91), implies an effective magnetic field along z in the rotated frame. Recalling the effect of the magnetic field on the scaling dimensions of various operators, which was discussed in Secs. 2.2.2 and 2.2.3, we must conclude that this magnetic field will suppress the longitudinal ordering and enhance transverse ones. Therefore we expect the $g_{x,y}$ terms in (2.89) to be more relevant than g_{φ_1} one.

2.2.4.2 Two-stage RG

As discussed in Sec. 2.2.4.2, the presence of oscillating terms forces us to implement a two-stage RG scheme. RG flow of the backscattering Hamiltonian (2.88) is given by

$$\begin{aligned} \frac{dy_x}{dl} &= y_y y_z, \quad \frac{dy_y}{dl} = y_x y_z + y_A^2, \\ \frac{dy_z}{dl} &= y_x y_y, \quad \frac{dy_A}{dl} = y_y y_A. \end{aligned} \tag{2.92}$$

The interchain interaction (2.89) changes as

Table 2.4. When $\boldsymbol{h} \perp \boldsymbol{D}$, three relevant interchain interactions are $H_x \propto \mathcal{N}_y^x \mathcal{N}_{y+1}^x$, $H_y \propto \mathcal{N}_y^y \mathcal{N}_{y+1}^y$, and $H_{\text{inter},'}$ in Hamiltonians (2.89) and (2.91). The table shows their operator forms in the rotated frame, associated coupling constants and the ordered states they induce.

Interaction term	Coupling operator	Coupling constant	Induced state
H_x	$\mathcal{N}_y^x \mathcal{N}_{y+1}^x$	g_x	SDW(z)
H_y	$\mathcal{N}_y^y \mathcal{N}_{y+1}^y$	g_y	SDW (y)
$H_{\text{inter},'}$	$\cos[\sqrt{2\pi}(\varphi_y - \varphi_{y+1})]$	g_{φ_1}	Distorted-cone

$$\begin{aligned}
\frac{dg_x}{dl} &= g_x[1+\frac{1}{2}(y_x-y_y-y_z)],\\
\frac{dg_y}{dl} &= g_y[1+\frac{1}{2}(y_y-y_z-y_x)],\\
\frac{dg_z}{dl} &= g_z[1+\frac{1}{2}(y_z-y_x-y_y)],\\
\frac{dg_E}{dl} &= g_E[1+\frac{1}{2}(y_x+y_y+y_z)].
\end{aligned} \tag{2.93}$$

Similarly to discussion around Eq. (2.75) for the $\boldsymbol{h} \parallel \boldsymbol{D}$ case, here too magnetic-field-induced oscillations $e^{it_\varphi x}$ become prominent beyond the RG scale

$$l_\varphi = -\ln(a_0 t_\varphi). \tag{2.94}$$

We find that for sufficiently strong DM interaction, approximately $D/J' > 0.01$, the oscillating scale is shorter than the interchain one, $l_\varphi < l_{\text{inter}}$. This means that the RG flow consists of two stages, $0 < l < l_\varphi$ and $l_\varphi < l < l_{\text{inter}}$. During the first stage, $0 < l < l_\varphi$, the full set of RG equations (2.92) and (2.93) needs to be analyzed. At this stage all of the couplings remain small. During the second stage, for $l > l_\varphi$, strong oscillations in H_A, H_B, see (2.88), and in the "oscillating part" of (2.89) lead to the disappearance of these terms. Setting $y_A(l) = 0$ and $y_B(l) = 0$ reduces backscattering RG to the Kosterlitz-Thouless (KT) equations

$$\frac{dy_C}{dl} = y_C y_\sigma, \quad \frac{dy_\sigma}{dl} = y_C^2, \tag{2.95}$$

the analytic solution of which is illustrated in **Figure 2.7**. At the same time, interchain RG reduces to

$$\begin{aligned}
\frac{dg_x}{dl} &= g_x(1+y_C+\frac{1}{2}y_\sigma),\\
\frac{dg_y}{dl} &= g_y(1-y_C+\frac{1}{2}y_\sigma),\\
\frac{dg_{\varphi_1}}{dl} &= g_{\varphi_1}(1-\frac{1}{2}y_\sigma).
\end{aligned} \tag{2.96}$$

The initial conditions for y_C, y_σ and $g_{\varphi 1}$ at the start of the second RG stage are

$$\begin{aligned}
y_C(l_\varphi) = \frac{1}{2}[y_x(l_\varphi) - y_y(l_\varphi)], \quad y_\sigma(l_\varphi) = -y_z(l_\varphi),\\
g_{\varphi_1}(l_\varphi) = \frac{1}{2}[g_E(l_\varphi) + g_z(l_\varphi)].
\end{aligned} \tag{2.97}$$

2.2.4.3 Distinguishing the most relevant interaction

The above Eq. (2.96) shows that the flow of interchain interactions is controlled by the signs of marginal couplings y_C and y_σ, and their relative magnitude, which are determined

by the initial condition in Eq. (2.15) as well as by their subsequent first stage flow. Given that DM-induced anisotropy λ is very small, the effect of the first stage RG flow reduces to the overall renormalization of the value of $g_{\rm bs}$. This really is a direct consequence of the assumed near-SU(2) symmetry of the backscattering Hamiltonian (2.88), which, in the absence of the field $h_{\rm eff}$ (which is the essence of the first stage RG where oscillating factors do not play any role, therefore $e^{it_\varphi x} \to 1$) is just a rotated version of the marginally-irrelevant interaction of spin currents $g_{\rm bs} \boldsymbol{J}_R \cdot \boldsymbol{J}_L$. Therefore the main effect of the first stage consists of the renormalization $g_{\rm bs}(0) \to \mathcal{G}_{\rm bs} \equiv g_{\rm bs}(0)/(1 - g_{\rm bs}(0) l_\varphi/(2\pi v))$; see Ref.[81] for the discussion of a similar situation.

Thus, initial values of backscattering couplings for the second stage of the RG are

$$\begin{aligned} y_C(l_\varphi) &= -\frac{\mathcal{G}_{\rm bs}}{4\pi v}\big[(1+\frac{\lambda}{2})\cos[2\theta_0^y] - 1 + \frac{\lambda}{2}\big], \\ y_\sigma(l_\varphi) &= \frac{\mathcal{G}_{\rm bs}}{2\pi v}\big[(1+\frac{\lambda}{2})\cos[2\theta_0^y] - \frac{\lambda}{2}\big], \\ C &= y_\sigma(l)^2 - y_C(l)^2 = y_\sigma(l_\varphi)^2 - y_C(l_\varphi)^2, \end{aligned} \tag{2.98}$$

Finite $h_{\rm eff} = \sqrt{D^2+h^2}$ breaks spin-rotational symmetry and forces couplings $y_{C,\sigma}$ off the marginal diagonal directions in **Figure 2.7**. Note that situations with significant $\lambda \sim O(1)$ require separate analysis with explicit numerical solution of the first-stage equations (2.92).

Noting that $\cos[2\theta_0^y] = (h^2 - D^2)/(h^2 + D^2)$, we have identified 5 distinct regions with different signs of $y_{C,\sigma}$ and integration constant C, which lead to different RG flows. The boundaries of these regions depend on h/D and λ. Expression for C is approximated to $O(\lambda)$ accuracy because $\lambda \sim (D/J)^2 \ll 1$. The results are summarized in **Table 2.5** which shows which interchain orders are promoted in different regions. Several examples of $y_C(0)$, $y_\sigma(0)$, and C vs h/D, for three different values of λ, are shown as **Figure 2.14**, **Figure 2.15**, and **Figure 2.16**.

Practically, $\lambda \sim 10^{-4}$ is very small, as in **Figure 2.14**. In low magnetic field one observes regions II, III, and IV, all of which result in the two-dimensional commensurate-SDW order along the DM vector ($\hat{z}$). At large h/D values (> 50, see the inset in the same figure), the region V appears, leading to a commensurate SDW order along the $\hat{y}$ axis, orthogonal to the DM vector. This indicates a spin-flop phase transition where spins change their direction suddenly. The actual value of the corresponding critical magnetic field $h_{\rm flop}$ does not have to be very high, and is experimentally accessible for most material. For instance,

Table 2.5. Signs of y_C, y_σ, and C in different field regions for intermediate value of λ of order 0.1. This table summarizes conditions of the fastest growing coupling constant in RG system (2.96).

Region	I	II	III	IV	V
$y_C(0)$	+	+	+	+	−
$y_\sigma(0)$	−	−	+	+	+
C	+	−	−	+	+
Fastest growing	g_{φ_1}	g_x			g_y

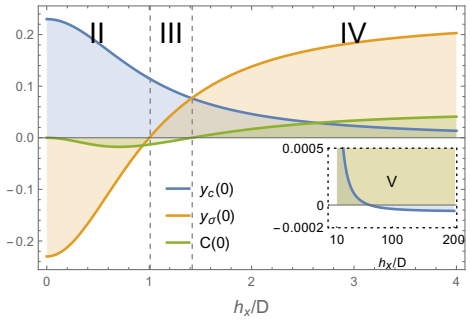

Figure 2.14. $y_C(0)/\eta$, $y_\sigma(0)/\eta$, and C/η in Eq. (2.98) as a function of the ratio h_x/D. Here we denote $\eta = \mathcal{G}_{\text{bs}}/(2\pi v)$. $\lambda = 1 \times 10^{-4}$, and $D/J = \sqrt{\lambda/c'} \sim 0.005$. Here only regions II, III, and IV in **Table 2.5** are present in the low magnetic field. The inset shows region V appearing when the ratio h_x/D increases to about 50, which indicates a phase transition from SDW(z) to SDW(y).

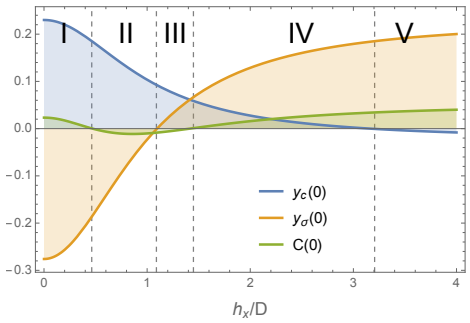

Figure 2.15. Plot of $y_C(0)/\eta$, $y_\sigma(0)/\eta$ and C/η in Eq. (2.98) versus the ratio h_x/D. Here $\eta = \mathcal{G}_{\text{bs}}/(2\pi v)$, $\lambda = 0.2$, and $D/J = \sqrt{\lambda/c'} \sim 0.23$. Here all five distinct regions from **Table 2.5** are present.

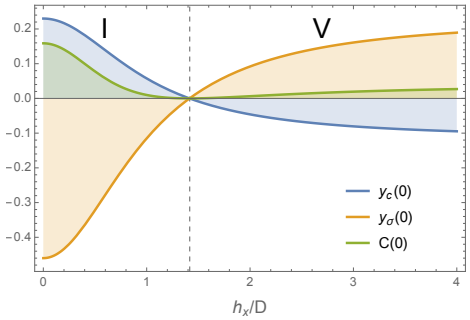

Figure 2.16. $y_C(0)/\eta$, $y_\sigma(0)/\eta$ and C/η in Eq. (2.98) versus the ratio h_x/D, and $\eta = \mathcal{G}_{\rm bs}/(2\pi v)$. $\lambda = 1$, and $D/J = \sqrt{\lambda/c'} \sim 0.5$. Here regions I and V from **Table 2.5** are present.

for $D = 0.01J$ we get $h_{\rm flop} \sim 50D = 0.5J$.

In **Figure 2.15**, all 5 different regions are present, and we expect two phase transitions to be present. As the magnetic field increases from zero the system transits from the distorted cone to the SDW(z), and then to the SDW(y). However, the small initial value of $g_{\varphi_1} \propto \cos^2[\theta_0^y] \sim h^2/D^2$ at low field prevents it from reaching the strong-coupling limit. Instead, coupling g_x gets there first. As a result, the distorted-cone phase is not realized at low magnetic field. This feature of the RG flow is evident in the phase diagrams in **Figure 2.17** and **Figure 2.18**, in which the distorted-cone state is present only in the strong-DM limit of $D \sim O(1)$. We therefore conclude that the distorted-cone phase is unlikely to be realized in real materials with small D/J ratio.

2.2.4.4 Phase diagram

2.2.4.4.1 Types of two-dimensional order. In the $\boldsymbol{h} \perp \boldsymbol{D}$ configuration, three competing interchain interactions g_{x,y,φ_1} lead to three kinds of two-dimensional magnetic orders. When g_x (or g_y) is the most relevant coupling, one needs to minimize $\mathcal{N}_y^x \mathcal{N}_{y+1}^x$ (or $\mathcal{N}_y^y \mathcal{N}_{y+1}^y$), correspondingly. It is clear that in both cases the appropriate component of $\boldsymbol{\mathcal{N}}$ should be staggered as $(-1)^y$ between chains. In terms of ϑ_y, this order is described by a simple $\vartheta_y = \sqrt{\pi/2}(y+1/2)$ (correspondingly, $\vartheta_y = \sqrt{\pi/2}y$) in the case of g_x (correspondingly, g_y) relevance. The resulting spin ordering is of the commensurate-SDW kind, which, according to (2.136), can be more informatively described as SDW(z) [correspondingly, SDW(y)] order when the coupling g_x (correspondingly, g_y) is the most relevant one:

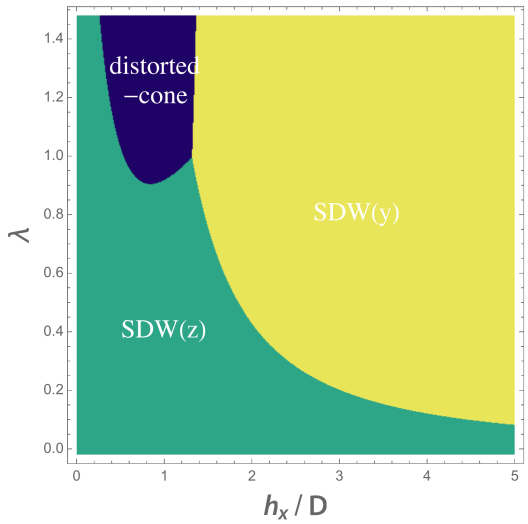

Figure 2.17. Phase diagram for the case of $\boldsymbol{h} \perp \boldsymbol{D}$, $h_z = 0$. Here $g_{\rm bs} = 0.23 \times 2\pi v$, $J' = 10^{-3} \times 2\pi v$, and $D = 0.01J$. We vary λ and h_x, and treat λ as independent from the D parameter. At large λ there is a phase transition from the distorted-cone to SDW(y) state. At small λ the SDW(z) and SDW(y) phases are separated by the transition line which approaches $\lambda = 0$ as $h_x/D \to \infty$.

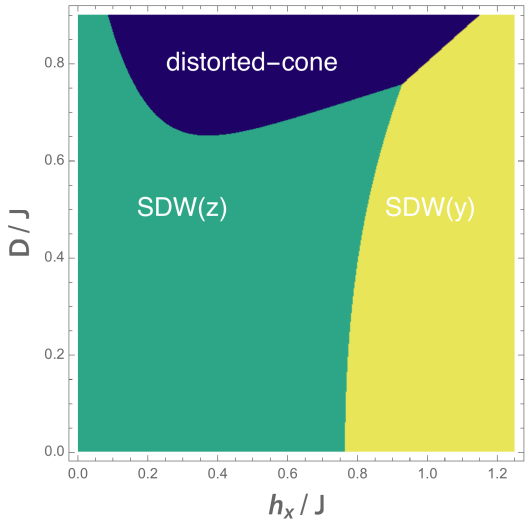

Figure 2.18. $h - D$ phase diagram for the case of $\boldsymbol{h} \perp \boldsymbol{D}$, $h_z = 0$. Here $\lambda \approx 3.8(D/J)^2$, see Eq. (2.7), and $g_{\rm bs} = 0.23 \times 2\pi v$ and $J' = 10^{-3} \times 2\pi v$. For small D/J, the critical field separating SDW(z) to SDW(y) phases is given by $h_x \simeq 0.23\pi$. The line separating the distorted-cone and SDW(y) phases is described by $h_x/D \simeq 1.5$.

$$\begin{aligned}\langle \boldsymbol{S}_{x,y}\rangle &\sim M\mathbf{x}+(-1)^{x+y}\Psi_{\mathrm{sdw(z)}}\mathbf{z},\\ \langle \boldsymbol{S}_{x,y}\rangle &\sim M\mathbf{x}+(-1)^{x+y}\frac{h}{\sqrt{h^2+D^2}}\Psi_{\mathrm{sdw(y)}}\mathbf{y}.\end{aligned} \tag{2.99}$$

Note that uniform magnetization is along the direction of the external magnetic field h_x, see (2.64), while the antiferromagnetically ordered component is orthogonal to it. As noted at the end of Sec. 2.2.4.1, in the rotated frame the effective field h_{eff} makes $g_{x,y}$ interchain interactions more relevant by reducing their scaling dimensions. Therefore, we expect that the critical temperatures of SDW(z) and SDW(y) orders will vary with magnetization M similarly to those of the cone and coneNN phases, see for example $T_{\mathrm{coneNN}}(M)$ in **Figure 2.13**, which is indeed in semiquantitative agreement with the experiment.[90] Correspondingly, the magnetization dependence of the orders parameters $\Psi_{\mathrm{sdw(z,y)}}$ in (2.99), for a fixed J'/J, should look similar to that of cone and coneNN orders in Sec. 2.2.7.

When the most relevant coupling is g_{φ_1}, minimization of (2.91) leads to $\varphi_y=\sqrt{\pi/2}y+\hat{\varphi}$ so that the spin order is given by the incommensurate distorted-cone (see **Figure 2.19**) in the $\mathbf{x}-\mathbf{y}$ plane

$$\begin{aligned}\langle \boldsymbol{S}_{x,y}\rangle \quad &\sim M\mathbf{x}+(-1)^{x+y}\Psi_{\mathrm{dist-cone}}\Big(\sin[\sqrt{2\pi}\hat{\varphi}+t_{\varphi}x]\mathbf{x}\\ &-\frac{(-1)^y D}{\sqrt{h^2+D^2}}\cos[\sqrt{2\pi}\hat{\varphi}+t_{\varphi}x]\mathbf{y}\Big).\end{aligned} \tag{2.100}$$

The $N^{x/y}$ components of the staggered magnetization form an ellipse. We used the staggered nature of DM interactions in deriving this expression. Notice that the spin pattern (2.100) represents a rotated, by the chain-dependent angle, and then elliptically distorted version of the coneNN state (2.83).

2.2.4.4.2 Phase diagrams. The ground state of the two-dimensional system is determined by the fastest growing coupling constant of (2.96). For λ not vanishingly small (practically, for $\lambda>0.01$) we numerically solve both the first step, Eqs. (2.92), (2.93), and the second step, Eqs. (2.95) and (2.96), RG equations. The $\lambda-h/D$ phase diagram is shown in **Figure 2.17**. For small λ, which for a moment is treated as an independent parameter, there is a phase transition from SDW(z) to SDW(y) at large ratio of h_x/D, and the line separating the two states tends to be horizontal as $h_x/D\to\infty$. The distorted-cone state appears only at unrealistically large λ. It transforms to SDW(y) at $h_x/D\simeq 1.5$, for any $\lambda>1$. This can be understood from Eq. (2.98) and **Table 2.5**: in order to change the sign of $y_C(0)$ and $y_\sigma(0)$ at

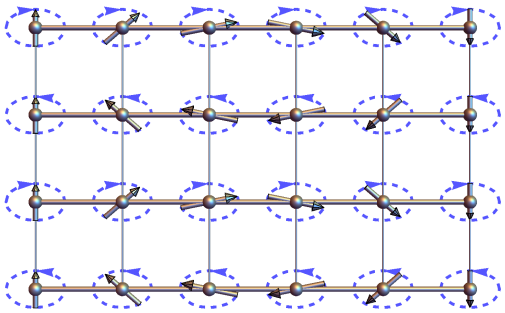

Figure 2.19. Staggered magnetization in the distorted-cone phase, Eq. (2.100), in the transverse to ***D*** plane. This distortion is caused by the magnetic field; the stronger the field the bigger the distortion. The opposite sense of spin precession in the neighboring chains is due to the staggered DM interaction.

the same time, one needs $1+\lambda > 2/\lambda$, which implies $\lambda > 1$. The distorted-cone–SDW(y) transition is of the incommensurate-commensurate kind in agreement with the classical analysis prediction in Ref.[54]

It is easy to see that stronger DM interaction leads to a more stable SDW(z). Indeed, stronger DM interaction shortens the RG scale l_φ thereby extending the seond-stage RG flow which favors the g_x process.

Using the relation $\lambda = c'D^2/J^2$, with $c' = (2\sqrt{2}v/g_{\rm bs})^2$, we are now in position to calculate the physical $h-D$ phase diagram; the result is presented in **Figure 2.18**. The boundary between SDW(y) and distorted cone is linear with $h_x/D \simeq 1.5$, which corresponds to the vertical boundary in **Figure 2.17**. The line separating SDW(z) and SDW(y) phases is determined by the condition $g_y(l) = g_x(l)$, which leads to

$$[\cos\theta_0^y]^2 \exp[-\int_0^l dl' 2y_C(l')] = 1. \tag{2.101}$$

If D is small, $\cos\theta_0^y \sim 1$, which implies $y_C(l) < 0$. Using (2.98), Eq. (2.101) reduces to $h^2/D^2 = 2/\lambda$. Hence the critical magnetic field $h_c/J = (2\pi v/g_{\rm bs})\pi \sim 0.23\pi$ is independent of the value of D. Being quite large, this value should be considered an order-of-magnitude estimate. (Here we have used $g_{\rm bs} \simeq 0.23\times(2\pi v)$ from Ref.[101]) Typical flows of coupling constants for each of the phases can be found in Figures 16-18 in Ref.[100]

2.2.5 Discussion

Many of the recent revolutionary developments in condensed matter physics, ranging from ferroelectrics[75] to spintronics[67] to topological quantum phases,[102–104] are associated with strong spin-orbit interactions. Even when not particularly strong, spin-orbit coupling is seen to control important aspects of low-energy physics of systems such as $\alpha-$ and $\kappa-$phase BEDT-TTF and BEDT-TSF organic salts, which are made of light C, S, and H atoms.[105]

Our study adds a physically motivated model to this fast growing list: a quasi-2d (or 3d) system of weakly coupled antiferromagnetic Heisenberg spin-1/2 chains subject to the uniform but *staggered between chains* Dzyaloshinskii-Moriya interaction.

2.2.5.1 Experimental implications

The obtained $T-$ vs $-M(h)$ phase diagrams in **Figure 2.11** and **Figure 2.13** have a striking resemblance to the experimentally determined, via specific heat measurements,[45] phase diagrams of chain materials $K_2CuSO_4Cl_2$ and $K_2CuSO_4Br_2$, respectively. The first of these is interpreted as a weak-DM material with $(D/J')_{\rm Cl} = 1.3$, see Appendix B.3, in which the only magnetic order is of the standard cone type.

The Br-based material is more interesting and exhibits a low-field phase transition between two different orders of experimentally-yet-unknown nature. Interaction parameters for this material have been estimated experimentally[45] to be $J = 20.5$ K, and $D = 0.28$ K. Fitting zero-field T_c of this material to that of the commensurate SDW order gives us $J' = 0.09$ K; see Appendix B.3 for more details. Therefore $(D/J')_{\rm Br} \approx 3.1$, which places $K_2CuSO_4Br_2$ in the intermediate-DM range. **Figure 2.20** shows that $D/J' = 3.1$ is strong enough to suppress cone ordering at small magnetic fields, but nonetheless is not sufficiently strong to prevent the cone phase from emerging at slightly greater magnetic field. Analysis in Appendix B.3 shows that for this particular value of D/J' one encounters three quantum phase transitions in the narrow interval of magnetization $0 \leq M \leq 0.025$: commensurate-incommensurate SDW, incommensurate SDW to coneNN, and finally coneNN to the commensurate-cone phase. The cone gets stabilized above $M = 0.025$. This rapid progression of phase transitions is not seen in the experiment.[45] There, rather, a single transition at $B_{\rm Br} = 0.1$T is observed, although it must be said that the commensurate-

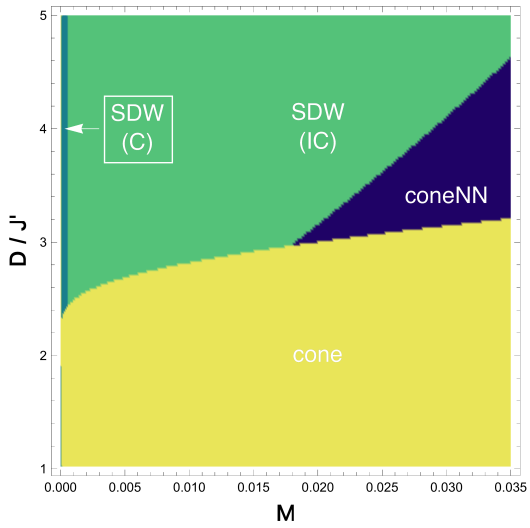

Figure 2.20. Small-magnetization $M - D$ phase diagram for the case of $\boldsymbol{h} \parallel \boldsymbol{D}$, obtained by the CMF calculation. Here $J = 20.5$ K, $J' = 0.0045J = 0.09$ K. The cone phase is bounded by $D/J' \approx 4.2$ from above for all $M \in (0, 0.5)$.

incommensurate SDW may be just too difficult to identify. Converting the observed field magnitude to energy units, via $h_{\rm Br} = g\mu_B B_{\rm Br}/k_B = 0.134$ K, we estimate the corresponding magnetization value as $M_{\rm Br} = h_{\rm Br}/(2\pi v) = h_{\rm Br}/(\pi^2 J_{\rm Br}) \approx 0.0007$. This is much smaller than the critical cone magnetization $M = 0.025$ estimated above.

However the present discussion, much of which is summarized graphically in **Figure 2.20**, shows that the region of $D/J' \approx 3$ is particularly tricky. Small, order of $5\% - 10\%$, changes in J' and D can significantly affect the ratio D/J' and lead to dramatically different predictions for the phase composition at small magnetization. Specifically, increasing D/J' to $\simeq 4$ eliminates the cone phase from the competition completely as now one observes only C-IC SDW and SDW-to-coneNN transitions, in a much closer qualitative agreement with the experiment. Given significant uncertainties in parameter values of $K_2CuSO_4Br_2$, a more quantitative description of the full experimental situation is not possible at the moment.

We hope that our detailed investigation will prompt further experimental studies of these interesting compounds, in particular in the less studied so far $\boldsymbol{h} \perp \boldsymbol{D}$ configuration, and will shed more light on the intricate interplay between the magnetic field, DM and interchain interactions present in this interesting class of quasi-one-dimensional materials.

It is interesting to note that the unique geometry of DM interactions makes $K_2CuSO_4Br_2$ somewhat similar to the honeycomb iridate material Li_2IrO_3, the incommensurate magnetic order of which is characterized by unusual counter-rotating spirals on neighboring sublattices.[106,107]

2.2.5.2 Summary and future directions

We have systematically investigated the complicated interplay of DM interaction and external magnetic field, applied either along or perpendicular to the DM vector $\boldsymbol{D} = D\hat{z}$. Combining techniques of bosonization, renormalization group, and chain mean-field theory, we are able to identify the phase diagram of the system. In all considered cases the ground state is determined by the interchain interaction, which is however strongly affected by the chain backscattering, which in turn is very sensitive to the mutual orientation of $\boldsymbol{D}$ and $\boldsymbol{h}$.

In $\boldsymbol{h} \parallel \boldsymbol{D}$ configuration the phase diagram is strongly dependent on the ratio D/J'. For the weak DM interaction, $D < 1.9J'$, there is only a single cone phase, with spins spiraling in the plane perpendicular to $\boldsymbol{D}$. The strong DM interaction is found to promote the collinear SDW state. The basic reason for this is strong frustration of the interchain cone channel, caused by the opposite sense of rotation of spins in neighboring chains (which, in turn, is caused by the opposite directions of the DM vectors in the neighboring chains). As a result, the transverse cone ordering is strongly frustrated and the less-relevant SDW state gets stabilized. However, the SDW is the ground state only in a very low magnetic field. Increasing the magnetic field up to critical value $h_c \sim J'$, we find a (most likely, discontinuous) phase transition from the incommensurate-SDW state to the coneNN state which is driven by the fluctuation-generated cone-type interaction between the next-neighbor (NN) chains. These RG-based arguments are fully supported by the chain mean-field calculations.

For $\boldsymbol{h} \perp \boldsymbol{D}$, we find two distinct SDW states in the plane normal to the magnetic field in the experimentally relevant limit of not too strong DM interaction, $D \ll J$. Since none of these states is a lower-symmetry version of the other, the phase transition between the different SDWs is of spin-flop kind, and is expected to be of the first order. The transition field $h_c \sim 0.23\pi J$ is (almost) independent of D. In the limit of $D \sim J$ (impractical for

the experiment), there is also a "distorted-cone" state in which spins rotate in the plane normal to vector $\boldsymbol{D}$; see **Figure 2.18**. We have carried out two-stage RG calculations and determined the $\lambda - h/D$ and $h - D$ phase diagrams for this geometry numerically.

All of the obtained results are based on perturbative calculations, framed in either RG or CMF language. The complete consistency between these two techniques observed in our work provides strong support in favor of its validity. Nonetheless, an independent check of the presented arguments is highly desired. We hope our work will stimulate numerical studies of this interesting problem along the lines of quantum Monte Carlo studies in Refs.[108,109]

In concluding, we would like to mention the potential relevance of our model to the currently popular coupled-wire approach to construct (mostly chiral) spin liquids.[37,110,111] The essence of this approach consists in devising interchain interactions in such a way as to suppress all interchain couplings between the relevant, in the RG sense, degrees of freedom (such as staggered magnetization and dimerization). The remaining marginal interactions of current-current kind then conspire to produce a gapped chiral phase with gapless chiral excitations on the edges. Staggered DM interactions of the kind considered here are, as we have shown, actually quite effective in removing $N_y^+ N_{y+1}^-$ terms. At the same time, the remaining interchain SDW term grows progressively less relevant as the magnetic field is increased towards the saturation value. Provided that one finds a way to suppress fluctuation-generated relevant coneNN like couplings between more distant chains, described in Sec. 2.2.2.3.2, one can hope to be able to destabilize weak SDW long-ranged magnetic order with the help of additional weak interactions (of yet unknown kind) and drive the system into a two-dimensional spin-liquid phase. In Sec. 2.3, we propose a way to construct the chiral spin liquid on coupled spin chains by taking advantage of the staggered geometries of DM interactions.

We would like to thank M. Hälg, K. Povarov, A. I. Smirnov and A. Zheludev for detailed discussions of the experiments, and L. Balents for insightful theoretical remarks. This work is supported by the National Science Foundation Grant No. NSF DMR-1507054.

2.2.6 Generation of next-neighbor chain coupling

Starting from interaction H_{cone} in Eq. (2.71) we obtain the partition function Z_θ as

$$Z_\theta = \int D\theta e^{-S_0} e^{\sum_y \int \mathrm{d}x\mathrm{d}\tau H_{\text{cone}}}. \tag{2.102}$$

where, S_0 and Z_0 are the action and partition function of independent spin chains. We expand Z_θ in power of H_{cone} to the second order,

$$Z_\theta = \int D\theta e^{-S_0}\Big\{1 + \sum_y \int \mathrm{d}x\mathrm{d}\tau H_{\text{cone}} + S^{(2)}\Big\}. \tag{2.103}$$

The first-order term contributes nothing to the next-neighbor (NN) chain coupling. We are interested in the second-order term which reads

$$S^{(2)} = \frac{1}{2}\iint \mathrm{d}x_1\mathrm{d}x_2\mathrm{d}\tau_1\mathrm{d}\tau_2(\sum_y H_{\text{cone}})^2. \tag{2.104}$$

Introduce short-hand notation $A_\mu(y) = e^{i\mu[\sqrt{2\pi}(\tilde{\theta}_y - \tilde{\theta}_{y+1}) + 2t_\theta^y x]}$ in terms of which the inter-chain Hamiltonian reads

$$H_{\text{cone}} = \pi v A^2 g_\theta \sum_{\mu=\pm 1} \int \mathrm{d}x A_\mu(y), \tag{2.105}$$

The terms which produce interaction between next-nearest chains can then be written as

$$S^{(2)} = \frac{1}{2}(\pi v A^2 g_\theta)^2 \sum_y \sum_{\mu=\pm 1} \sum_{\nu=\pm 1} \int \mathrm{d}x_1\mathrm{d}\tau_1 \int \mathrm{d}x_2\mathrm{d}\tau_2 A_\mu(y) A_\nu(y+1). \tag{2.106}$$

Rewrite the expression in the integral

$$\begin{aligned}
&\sum_{\mu=\pm 1}\sum_{\nu=\pm 1} A_\mu(y)A_\nu(y+1) \\
&= \sum_{\mu=\pm 1}\sum_{\nu=\pm 1} e^{i\mu\sqrt{2\pi}\tilde{\theta}_y(x_1)} e^{-i\nu\sqrt{2\pi}\tilde{\theta}_{y+2}(x_2)} e^{-i[\mu\tilde{\theta}_{y+1}(x_1) - \nu\tilde{\theta}_{y+1}(x_2)]} e^{i2[\mu t_\theta^y x_1 + \nu t_\theta^{y+1} x_2]}, \\
&= \sum_{\mu=\nu} e^{i\mu\sqrt{2\pi}[\tilde{\theta}_y(x_1) - \tilde{\theta}_{y+2}(x_2)]} e^{-i\mu[\tilde{\theta}_{y+1}(x_1) - \tilde{\theta}_{y+1}(x_2)]} e^{i2\mu[t_\theta^y x_1 + t_\theta^{y+1} x_2]} \\
&\quad + \sum_{\mu=-\nu} e^{i\mu\sqrt{2\pi}[\tilde{\theta}_y(x_1) + \tilde{\theta}_{y+2}(x_2)]} e^{-i\mu[\tilde{\theta}_{y+1}(x_1) + \tilde{\theta}_{y+1}(x_2)]} e^{i2\mu[t_\theta^y x_1 - t_\theta^{y+1} x_2]}.
\end{aligned} \tag{2.107}$$

Now we integrate out field $\tilde{\theta}_{y+1}$ from the intermediate $(y+1)$ chain in $S^{(2)}$; only $\mu = \nu$ produces the finite contribution,

$$\begin{aligned}
S^{(2)} = \frac{1}{2}(\pi v A^2 g_\theta)^2 \sum_y \int \mathrm{d}x_1\mathrm{d}\tau_1 \int \mathrm{d}x_2\mathrm{d}\tau_2 \sum_{\mu=\pm 1} & e^{i\mu\sqrt{2\pi}[\tilde{\theta}_y(r_1) - \tilde{\theta}_{y+2}(r_2)]} e^{i2\mu t_\theta^y [x_1 - x_2]} \\
& \big\langle e^{-i\mu\sqrt{2\pi}[\tilde{\theta}_{y+1}(r_1) - \tilde{\theta}_{y+1}(r_2)]} \big\rangle.
\end{aligned} \tag{2.108}$$

Here the $(y+1)$ chain correlation function

$$\langle e^{-i\mu\sqrt{2\pi}[\tilde{\theta}_{y+1}(r_1)-\tilde{\theta}_{y+1}(r_2)]}\rangle = \frac{1}{|r_1-r_2|^{1/K}}, \tag{2.109}$$

where $K = 2\pi/\beta^2$, $K = 1$ in the absence of magnetic field, and $r_{1/2} = (x_{1/2}, v\tau_{1/2})$, are the coordinates in space-time. Switch to the center-of-mass and relative coordinates, $R = (r_1+r_2)/2,\ r = r_1 - r_2, y = v\tau$; then $\tilde{\theta}_y(r_1) = \tilde{\theta}_y(R+r/2) \simeq \tilde{\theta}_y(R)$, and

$$S^{(2)} = \sum_y \frac{(\pi v A^2 g_\theta)^2}{2v^2} \sum_{\mu=\pm 1} \int \mathrm{d}^2 R e^{i\mu\sqrt{2\pi}[\tilde{\theta}_y(R)-\tilde{\theta}_{y+2}(R)]} \int \mathrm{d}x\mathrm{d}y e^{i2\mu t_\theta^y x} \frac{1}{(x^2+y^2)^{\Delta_1}}, \tag{2.110}$$

Here $\Delta_1 = 1/(2K)$ is the scaling dimension of $N^\pm$, which depends on magnetic field as shown in **Table 2.3**. The integral over relative (x, y) coordinates is easy to evaluate:

$$\begin{aligned} S^{(2)} &= \frac{(\pi v A^2 g_\theta)^2}{v} \pi t_\theta^{2\Delta_1-2} \frac{\Gamma(1-\Delta_1)}{\Gamma(\Delta_1)} \sum_y \int \mathrm{d}x\mathrm{d}\tau \cos[\sqrt{2\pi}(\tilde{\theta}_y(r) - \tilde{\theta}_{y+2}(r))] \\ &= -\int \mathrm{d}\tau \sum_y H_{NN}, \end{aligned} \tag{2.111}$$

Re-exponentiating this term we obtain the desired effective action describing the interaction between next-nearest chains. Using $N_y^+ N_{y+2}^- = A^2 \cos[\sqrt{2\pi}(\tilde{\theta}_y - \tilde{\theta}_{y+2})]$, we can read off the coupling for Eq. (2.79),

$$\begin{aligned} 2\pi v G_\theta &= -\frac{\pi A^2}{4} f(\Delta_1) \frac{(J')^2}{D}, \\ f(\Delta_1) &= t_\theta^{2\Delta_1-1} \frac{\Gamma(1-\Delta_1)}{\Gamma(\Delta_1)}. \end{aligned} \tag{2.112}$$

Here, $f(\Delta_1)$, as a function of Δ_1, starts from 1 as the field increases from zero, when the scaling dimension Δ_1 is $1/2$. The plot of G_θ vs M is shown in **Figure 2.21**.

2.2.7 Order parameter at $T = 0$ by CMF

Here we propose to study the magnetic orders in more detail by calculating the associate order parameters, even though experimental attempts to measure them, via neutron scattering and muon-spin spectroscopy, remain inconclusive for now.[90] Our calculation of the order parameters is based on the CMF approximation in Appendix B, where the effective Hamiltonian reduces to a sine-Gordon model[50,53] as in Eq. (B.3); its action reads

$$S_{\mathrm{sG}} = \int dxdy \Big(\frac{1}{2}(\partial_x\theta)^2 + \frac{1}{2}(\partial_y\theta)^2 - 2\mu\cos[\beta\theta] \Big). \tag{2.113}$$

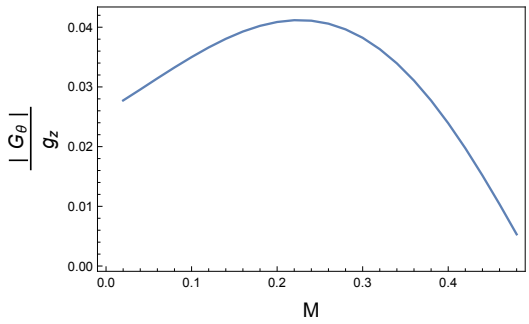

Figure 2.21. Coupling constant of the transverse interaction between next-nearest chains, G_θ, shown as the ratio of $|G_\theta(0)|/g_z(0)$ versus magnetization M. Here DM interaction is strong: $J' = 0.001J$, $D/J = 0.01$.

Here, $\mu = c\langle\cos\beta\theta\rangle/v$, and $\tau = y/v$. According to Refs.,[86,97] the expression for $\Psi \equiv \langle\cos\beta\theta\rangle$ as a function of magnetization M reads

$$\Psi(M) = \left[(\frac{c}{v})^{\beta'^2}\sigma'(M)^{1-\beta'^2}\right]^{1/(1-2\beta'^2)}, \tag{2.114}$$

where $\beta' = \beta/\sqrt{8\pi}$, and

$$\sigma'(M) = \frac{\tan[\pi\xi/2]}{2\pi(1-\beta'^2)}\left[\frac{\Gamma(\frac{\xi}{2})}{\Gamma(\frac{1+\xi}{2})}\right]^2\left[\frac{\pi\Gamma(1-\beta'^2)}{\Gamma(\beta'^2)}\right]^{1/(1-\beta'^2)},$$
$$\xi = \frac{\beta'^2}{1-\beta'^2} = \frac{\beta^2}{8\pi-\beta^2}. \tag{2.115}$$

Equation (2.114) is a general form of order parameter for sine-Gordon model. The three interactions in consideration are Eq. (B.10), (B.17) and (B.22), with $\beta = 2\pi R$, and their corresponding parameters β' are

$$\beta'_{1,3} = \Delta_1/2, \quad \beta'_2 = \Delta_2/2, \tag{2.116}$$

where $\beta'_{1,2,3}$ are associated with $\Psi_{1,2,3}$, and $\Psi_1 = \langle\cos(\beta\breve{\theta}_y)\rangle$ (defined below Eq. (B.10)), $\Psi_2 = \langle\cos\frac{2\pi}{\beta}\breve{\phi}_y\rangle$ (defined below Eq. (B.17)) and $\Psi_3 = \langle\cos\beta\tilde{\theta}_y\rangle$.

Now we can compute the order parameters for the two materials $K_2CuSO_4Cl_2$ and $K_2CuSO_4Br_2$, the exchange constants of which are estimated in Appendix B.3. For the compound $K_2CuSO_4Cl_2$ the only phase to be considered is the cone. Its order parameter Ψ_{cone}

$$\Psi_{\text{cone}} = A_3\left[(\frac{c_1}{v})^{\Delta_1}\sigma'(M)^{2-\Delta_1}\right]^{1/(2-2\Delta_1)} \tag{2.117}$$

is shown in **Figure 2.22**. For $K_2CuSO_4Br_2$ two order parameters need to be considered,

$$\Psi_{\text{sdw}} = A_1\left[(\frac{c_2}{v})^{\Delta_2}\sigma'(M)^{2-\Delta_2}\right]^{1/(2-2\Delta_2)},$$
$$\Psi_{\text{coneNN}} = A_3\left[(\frac{c_3}{v})^{\Delta_1}\sigma'(M)^{2-\Delta_1}\right]^{1/(2-2\Delta_1)} \tag{2.118}$$

and they are shown in **Figure 2.23**. Observe that the scaling of Ψ with J'/v follows the RG prediction (A.2).

Comparing **Figure 2.22** and **Figure 2.23**, we notice that the order parameters have smaller magnitude in the Br compound, due to its stronger DM interaction, which frustrates the system more. Also, cone-type orders are enhanced by magnetic field, while the SDW order is suppressed by it.

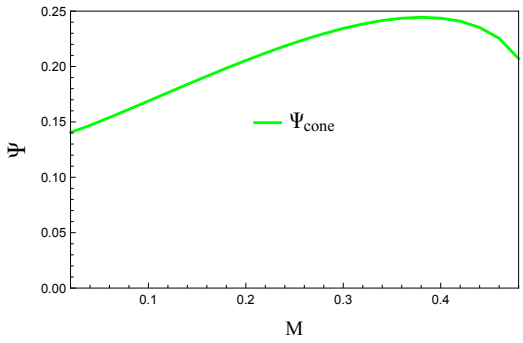

Figure 2.22. Order parameter of cone (Ψ_{cone}; green solid line) in $K_2CuSO_4Cl_2$, where $J'/J = 0.027$ and $D/J' = 1.3$. Note that Ψ_{cone} is enhanced by field.

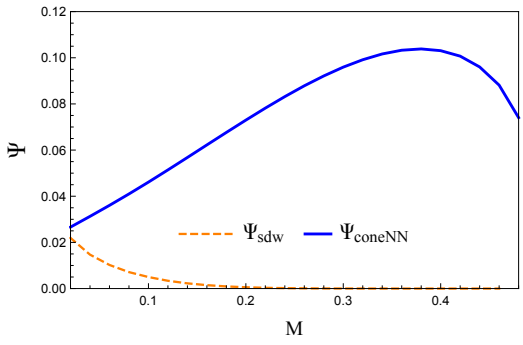

Figure 2.23. Order parameters of SDW (Ψ_{sdw}; orange dashed line) and coneNN (Ψ_{coneNN}; blue solid line) in $K_2CuSO_4Br_2$, where $J'/J = 0.004$ and $D/J' = 3.1$. Note that the magnetic field enhances the coneNN order but suppresses the SDW one.

2.3 Construction of chiral spin liquid from coupled spin chains

Inspired by the fact that the staggered-between-chain geometry of DM interactions suppress the relevant, in RG sense, transverse interchain couplings [see details in Sec. 2.2], we find that after removing the relevant part of couplings by staggered DM interactions, the remaining marginal interactions between left- and right-moving fermion currents from neighboring chains produce a energy gap. Then the left- and right-moving modes in the spatially separated edge chains are unpaired. This picture implies the emergence of a chiral edge state. This sate corresponds to a topologically nontrivial state known as Kalmeyer-Laughlin[29] chiral spin liquid (CSL).

Here we propose to construct chiral spin liquids from a weakly-coupled spin chain system. The system is subject to magnetic field and Dzyaloshinskii-Moriya (DM) interaction, which is uniform along each chain, but its characteristic vector, the DM vector, rotates from chain to chain. By adjusting the magnitude and direction of DM vectors and g (gyromagnetic) tensors properly, it is possible to remove the relevant interchain couplings, and the remaining marginal interactions develop to an Abelian chiral spin liquid. This work is inspired by Ref.,[36] in which CSL is constructed from coupled wires.

2.3.1 Introduction

Seeking for spin liquid state is one of the most important lines of research in the field of frustrated magnetism. Recent study focuses on coupled zigzag ladders[112,113] and Kagome lattice[114] induced by DM interaction. It was first proposed by Kane[37,115] that it is promising to realize the chiral spin liquid (CSL) from arrays of quantum wires. Inspired by the work done by Meng et al.,[36] in which they constructed CSL from coupled wires, by adjusting the shifts of Fermi momentum which is dependent on the spin projection of particles (right- and left-moving fermions). In real materials, we can realize the adjusting shifts of Fermi momentum by applying external magnetic field and with proper spin-orbit coupling (or equivalently DM interaction in our model).

In this section, we present that if we adjust the magnitude and direction of DM vectors and g (gyromagnetic) tensors properly, it is promising to realize CSL state from a set of weakly coupled DM spin chains. The spin chain system is depicted in **Figure 2.24**, and described by Hamiltonian (2.119).

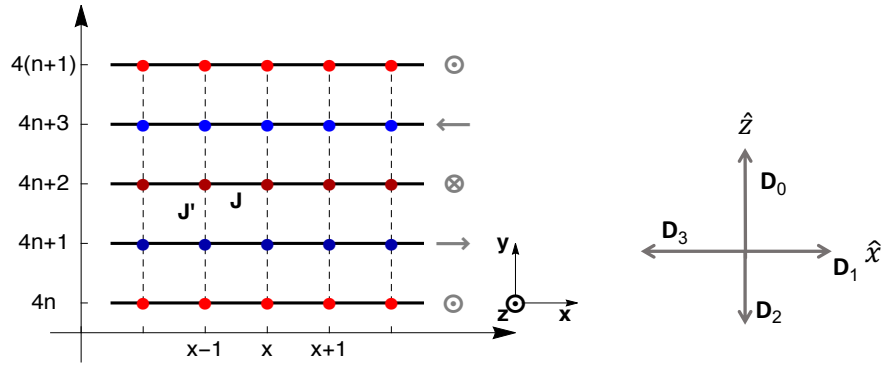

Figure 2.24. The spin chain system to construct a chiral spin liquid. *Left*: a system of coupled spin chains, solid bond is intrachain exchange J, and dashed bond is interchain exchange J', where $J' \ll J$. Four consecutive chains form a unit cell, and the chain index $y = 4n + a$, with n being an integer and $a = 0, 1, 2, 3$. DM interactions are orthogonal between neighboring chains. The DM vector, which is depicted by gray vectors, clockwise rotates around y-axis by $\pi/2$ from y-th chain to $(y+1)$-th chains. *Right*: the DM vectors $\boldsymbol{D}_a$ on each chain.

2.3.2 Model Hamiltonian

We study a system of weakly coupled Heisenberg spin-1/2 chains, which is subject to Dzyaloshinskii-Moriya (DM) interactions and external magnetic field. Four consecutive chains form a unit cell, as shown in **Figure 2.24**. The system's Hamiltonian contains four parts, $H = \sum_{y=4n+a} H_0^a + H_{\rm DM}^a + H_{\rm Z}^a + H_{\rm inter}$, with

$$\begin{aligned} H_0^a &= J_a \sum_x \boldsymbol{S}_{x,y} \cdot \boldsymbol{S}_{x+1,y}, \\ H_{\rm DM}^a &= \sum_x \boldsymbol{D}_a \cdot \boldsymbol{S}_{x,y} \times \boldsymbol{S}_{x+1,y}, \\ H_{\rm Z}^a &= -\mu_B \sum_x g_a h \cdot \boldsymbol{S}_{x,y}^z = -\sum_x h_a \cdot \boldsymbol{S}_{x,y}^z, \\ H_{\rm inter} &= J' \sum_x \boldsymbol{S}_{x,y} \cdot \boldsymbol{S}_{x,y+1}. \end{aligned} \tag{2.119}$$

$\boldsymbol{S}_{x,y}$ is spin-1/2 operator on the lattice site (x, y); $y = 4n + a$, and $a = 0, 1, 2, 3$, n is an integer. J and J' denoting the intra- and interchain antiferromagnetic exchange, respectively. The coupling between neighbor chains is weak so that $J' \ll J$. The H_0 and $H_{\rm inter}$ terms describe intra- and interchain exchange interactions, respectively. The $H_{\rm DM}$ accounts for the DM interactions, which are uniform within chain, but the DM vectors $\boldsymbol{D}_a$ rotate between neighboring chains. The $\boldsymbol{D}_a$ on four consecutive chains in a unit are,

$$\boldsymbol{D}_0 = D_0\hat{z},\ \boldsymbol{D}_1 = D_1\hat{x},\ \boldsymbol{D}_2 = -D_2\hat{z},\ \boldsymbol{D}_3 = -D_3\hat{x}. \tag{2.120}$$

The DM vector clockwise rotates around y-axis by $\pi/2$ from y-th chain to $(y+1)$-th chains. The magnitude of DM interactions on $a = 0$ and $a = 2$ chains are the same. B is the magnetic field along $\hat{z}$, and the g_a are (gyromagnetic) g-factors corresponding to Zeeman splitting, sign of which is shown in **Table 2.6**. Here the strength of magnetic field is also chain-dependent $h_a = \text{Sign}(g_a)\mu_B g_a h$.

Note that the DM vector is anti-parallel between next-neighbor chains, and this arrangement is motivated by our previous work,[84] where we showed that staggered between chain DM interaction will suppress the relevant interchain coupling in the plane transverse to the DM vector. Therefore, in this model, staggered between next-neighbor DM interaction is expected to exclude the relevant perturbations, in energy scale J'^2/J, between ext-neighbor chains.

We notice the B on $a = 3$ chain has to be negative, which is very rare for crystal materials. *Ab initio* calculations have shown that negative g-factor is possible for lanthanide and transition metal complexes.[116] Also, sometimes one can ask about what other systems can produce the same physics. In the context of cold atoms in optical lattice, the staggered particle current in the tight-binding regime may result in an artificially staggered magnetic field.[117] We hope our coupled chain model (2.119) will stimulate the research along the lines of realization of the chiral spin liquid.

2.3.2.1 Effective Hamiltonian

As mentioned before, to construct the chiral spin liquid state, we need to make the relevant part of the interchain coupling H_{inter} irrelevant, and keep the marginal part. Therefore, how the DM interactions and Zeeman term influence the H_{inter} in Eq. (2.119) is the key of our investigation.

Now let us consider three neighboring chains $y = 4n-1$, $y = 4n$, and $y+1 = 4n+1$ with DM vectors, $\boldsymbol{D}_{y-1} = -D_3\hat{\boldsymbol{x}}$, $\boldsymbol{D}_y = D_0\hat{\boldsymbol{z}}$, and $\boldsymbol{D}_{y+1} = D_1\hat{\boldsymbol{x}}$, respectively. To eliminate

Table 2.6. g factor in a unit of four consecutive chains.

a	0	1	2	3
Sign of g_a	$+$	$+$	$+$	$-$

the nondiagonal components, which come from the DM interaction $H_{\rm DM}$, in the Hamiltonian (2.119), we perform a rotation of spin operators,

$$S_{x,y-1} = \mathcal{R}_3(\gamma_x)\cdot\tilde{S}_{x,y-1};\;\; S_{x,y} = \mathcal{R}_0(\theta_x)\cdot\tilde{S}_{x,y};\;\; S_{x,y+1} = \mathcal{R}_1(\beta_x)\cdot\tilde{S}_{x,y+1}. \tag{2.121}$$

with the rotation matrices

$$\begin{aligned}
\mathcal{R}_3(\gamma_x) &= \begin{pmatrix} 1 & 0 & 0 \\ 0 & \cos\gamma_x & -\sin\gamma_x \\ 0 & \sin\gamma_x & \cos\gamma_x \end{pmatrix}; \\
\mathcal{R}_0(\theta_x) &= \begin{pmatrix} \cos\theta_x & -\sin\theta_x & 0 \\ \sin\theta_x & \cos\theta_x & 0 \\ 0 & 0 & 1 \end{pmatrix}; \\
\mathcal{R}_1(\beta_x) &= \begin{pmatrix} 1 & 0 & 0 \\ 0 & \cos\beta_x & -\sin\beta_x \\ 0 & \sin\beta_x & \cos\beta_x \end{pmatrix}.
\end{aligned} \tag{2.122}$$

The position-dependent rotation angles $\gamma_x = \alpha_3 x$, $\theta_x = \alpha_0 x$, and $\beta_x = \alpha_1 x$, where $\alpha_0 = \arctan[D_0/J]$, $\alpha_1 = \arctan[D_1/J_1]$, and $\alpha_3 = \arctan[-D_3/J_3]$. $\tilde{S}_{x,y}$ is the rotated spin operator on y-th chain. These rotations gauge away the $H_{\rm DM}$, and result in one XXZ chain and two XZZ chains with

$$\begin{aligned}
\tilde{H}_{0,y-1} &= \sum_x \left[J_3 \tilde{S}^x_{x,y+1}\tilde{S}^x_{x+1,y+1} + \tilde{J}_3(\tilde{S}^y_{x,y}\tilde{S}^y_{x+1,y+1} + \tilde{S}^z_{x,y+1}\tilde{S}^z_{x+1,y+1}) \right], \\
\tilde{H}_{0,y} &= \sum_x \left[\tilde{J}_0 \left(\tilde{S}^x_{x,y}\tilde{S}^x_{x+1,y} + \tilde{S}^y_{x,y}\tilde{S}^y_{x+1,y} \right) + J_0 \tilde{S}^z_{x,y}\tilde{S}^z_{x+1,y} \right], \\
\tilde{H}_{0,y+1} &= \sum_x \left[J_1 \tilde{S}^x_{x,y+1}\tilde{S}^x_{x+1,y+1} + \tilde{J}_1(\tilde{S}^y_{x,y}\tilde{S}^y_{x+1,y+1} + \tilde{S}^z_{x,y+1}\tilde{S}^z_{x+1,y+1}) \right],
\end{aligned} \tag{2.123}$$

Here the effective exchange constants $\tilde{J}_3 = \sqrt{J_3^2 + D_3^2}$, $\tilde{J}_0 = \sqrt{J_0^2 + D_0^2}$, and $\tilde{J}_1 = \sqrt{J_1^2 + D_1^2}$. Again the DM interactions drive the spin chain away from the Heisenberg point, $\tilde{H}_0 = H_0 + H_{\rm DM}$. For the Zeeman terms in Eq. (2.119),

$$\begin{aligned}
H_{\rm Z}^{a=0,2} &= -\sum_x h_a \tilde{S}^z_{x,y}, \\
H_{\rm Z}^{a=1,3} &= -\sum_x \left(h_a \sin[\alpha_a x]\tilde{S}^y_{x,y} + h_a \cos[\alpha_a x]\tilde{S}^z_{x,y} \right),
\end{aligned} \tag{2.124}$$

again $\alpha_1 = \arctan[D_1/J_1]$ and $\alpha_3 = -\arctan[D_3/J_3]$.

For a chain labeled as y, the rotations (2.121) modify the interaction H_{inter} with two neighbors $y-1$ and $y+1$ chains,

$$\begin{aligned}
H^{a=0}_{\text{inter}} =&\frac{1}{2}J'\sum_x \boldsymbol{S}_{x,y-1}\cdot(\boldsymbol{S}_{x,y-1}+\boldsymbol{S}_{x,y+1})\\
=&\frac{1}{2}J'\sum_x\Big\{\cos\theta_x\tilde{S}^x_{x,y}(\tilde{S}^x_{x,y+1}+\tilde{S}^x_{x,y-1})+\cos\theta_x\tilde{S}^y_{x,y}(\cos\beta_x\tilde{S}^y_{x,y+1}+\cos\gamma_x\tilde{S}^y_{x,y-1})\\
&+\tilde{S}^z_{x,y}(\cos\beta_x\tilde{S}^z_{x,y+1}+\cos\gamma_x\tilde{S}^z_{x,y-1})+\sin\theta_x\tilde{S}^x_{x,y}(\cos\beta_x\tilde{S}^y_{x,y+1}+\cos\gamma_x\tilde{S}^y_{x,y-1})\\
&-\sin\theta_x\tilde{S}^x_{x,y}(\sin\beta_x\tilde{S}^z_{x,y+1}+\sin\gamma_x\tilde{S}^z_{x,y-1})-\sin\theta_x\tilde{S}^y_{x,y}(\tilde{S}^x_{x,y+1}+\tilde{S}^x_{x,y-1})\\
&-\cos\theta_x\tilde{S}^y_{x,y}(\cos\beta_x\tilde{S}^z_{x,y+1}+\cos\gamma_x\tilde{S}^z_{x,y-1})+\sin\beta_x\tilde{S}^z_{x,y}(\tilde{S}^y_{x,y+1}+\tilde{S}^y_{x,y-1})\Big\}.
\end{aligned} \tag{2.125}$$

We notice all the terms above accompanied with oscillations. We hope these DM-induced oscillating terms remove the relevant part of interchain coupling H_{inter}. To see this point, we need to consider the model in the continuum limit.

2.3.3 Low-energy Hamiltonian

In the continuum limit, the expression for Hamiltonian (2.119) is

$$H=\sum_{y=4n+a}\left(H_{0,y}+V^{(a)}+H^s_{\text{inter}}+H^u_{\text{inter}}+H^{(a)}_{\text{bs}}\right), \tag{2.126}$$

with

$$H_{0,y}=\frac{2\pi v}{3}\int dx(\boldsymbol{J}_{Ry}\cdot\boldsymbol{J}_{Ry}+\boldsymbol{J}_{Ly}\cdot\boldsymbol{J}_{Ly}), \tag{2.127}$$

and

$$V^{(a)}=H^a_{\text{DM}}+H^a_{\text{Z}}, \tag{2.128}$$

which contains the DM interaction H_{DM} and Zeeman term H_{Z}. The expression for $V^{(a)}$ in a unit cell is,

$$\begin{aligned}
V^{(0)}&=-h_0\int dx(J^z_{Ry}+J^z_{Ly})+D_0\int dx(J^z_{Ry}-J^z_{Ly}),\\
V^{(1)}&=-h_1\int dx(J^z_{Ry}+J^z_{Ly})+D_1\int dx(J^x_{Ry}-J^x_{Ly}),\\
V^{(2)}&=-h_2\int dx(J^z_{Ry}+J^z_{Ly})-D_2\int dx(J^z_{Ry}-J^z_{Ly}),\\
V^{(3)}&=+h_3\int dx(J^z_{Ry}+J^z_{Ly})-D_3\int dx(J^x_{Ry}-J^x_{Ly}).
\end{aligned} \tag{2.129}$$

The backscattering (spin flip) term $H^{(a)}_{\text{bs}}$ in a unit cell is,

$$\begin{aligned}
H^{(1,3)}_{\text{bs}}&=-g_{\text{bs}}\int dx\left[(1+\lambda_a)J^x_{Ry}J^x_{Ly}+J^y_{Ry}J^y_{Ly}+J^z_{Ry}J^z_{Ly}\right],\\
H^{(0,2)}_{\text{bs}}&=-g_{\text{bs}}\int dx\left[J^x_{Ry}J^x_{Ly}+J^y_{Ry}J^y_{Ly}+(1+\lambda_a)J^z_{Ry}J^z_{Ly}\right],
\end{aligned} \tag{2.130}$$

with, $\lambda_a \simeq c'(D_a/J)^2$. The interchain interaction H_{inter} splits in two parts,

$$\begin{aligned} H^s_{\text{inter}} &= \frac{1}{2}J' \int dx \boldsymbol{N}_y \cdot (\boldsymbol{N}_{y+\frac{1}{2}} + \boldsymbol{N}_{y-\frac{1}{2}}), \\ H^u_{\text{inter}} &= \frac{1}{2}J' \int dx \Big[\boldsymbol{J}_{R,y} \cdot (\boldsymbol{J}_{R,y+\frac{1}{2}} + \boldsymbol{J}_{R,y-\frac{1}{2}}) + \boldsymbol{J}_{R,y} \cdot (\boldsymbol{J}_{L,y+\frac{1}{2}} + \boldsymbol{J}_{L,y+\frac{1}{2}}) + R \leftrightarrow L \Big]. \end{aligned} \tag{2.131}$$

H^s_{inter} is the interchain coupling between the staggered magnetization $\boldsymbol{N}_y$, which has scaling dimension 1; H^u_{inter} is coupling between the spin currents $\boldsymbol{J}_y$ which is marginal, namely having scaling dimension 2. The coupling between $\boldsymbol{N}$ and $\boldsymbol{J}$ has been neglected. In order to realize the chiral spin liquid state, which keeps uncoupled right (left) current on the top (bottom) chain and makes the bulk chains gapped, we need to make the relevant coupling H^s_{inter} irrelevant by introducing oscillation terms. Indeed, we have observed these oscillations in the lattice model in Eq. (2.125). Now let us see how oscillations are introduced in the continuum model. The first step is to simplify Eq. (2.129) using the tricks of chiral rotation and shift of fields. We have been familiar with these tricks in Secs. 2.1 and 2.2.

2.3.4 Effective magnetic field and DM interaction

We notice the orientation between magnetic field and DM interaction is different in four subchains, either perpendicular or parallel to each other. We consider these two cases separately. First, for $a = 1, 3$ subchains, where the magnetic field is perpendicular to DM interaction, we perform the chiral rotation,

$$\boldsymbol{J}_{R/L,y} = \mathcal{R}(\theta^{(a)}_{R/L})\tilde{\boldsymbol{J}}_{R/L,y}, \tag{2.132}$$

where $\tilde{\boldsymbol{J}}_{R/L}$ is spin current in the rotated frame, and $\mathcal{R}$ is the rotation matrix,

$$\mathcal{R}(\theta^{(a)}_{R/L}) = \begin{pmatrix} \cos\theta^{(a)}_{R/L} & 0 & \sin\theta^{(a)}_{R/L} \\ 0 & 1 & 0 \\ -\sin\theta^{(a)}_{R/L} & 0 & \cos\theta^{(a)}_{R/L} \end{pmatrix}. \tag{2.133}$$

To eliminate x component in $V^{(1)}$ and $V^{(3)}$, the rotation angles are,

$$\begin{aligned} &\theta^{(1)}_R = -\theta_1,\ \theta^{(1)}_L = \theta_1,\ \theta_1 \equiv \arctan[\frac{D_1}{h_1}]. \\ &\theta^{(3)}_R = -\theta_3,\ \theta^{(3)}_L = \theta_3,\ \theta_3 \equiv \arctan[\frac{-D_3}{h_3}]. \end{aligned} \tag{2.134}$$

If the rotation angles are the same on two chains with $a = 1\,\text{or}\,3$, then $\theta_1 = -\theta_3$, which leads to $h_1/D_1 = h_3/D_3 = \beta$, $\theta_R^{(1)} = -\theta_R^{(3)} = -\theta_0$, $\theta_L^{(1)} = -\theta_L^{(3)} = \theta_0$, and $\theta_0 \equiv \arctan[1/\beta]$. With these rotation (2.132), the expressions for $V^{(1)}$ and $V^{(3)}$ reduce to,

$$\begin{aligned} V^{(1)} &= -\sqrt{h_1^2 + D_1^2}\int dx(J^z_{R,1} + J^z_{L,1}) = -\frac{h^{(1)}_{\text{eff}}}{\sqrt{2\pi}}\int dx\partial_x\phi_y, \\ V^{(3)} &= \sqrt{h_3^2 + D_3^2}\int (J^z_{R,3} + J^z_{L,3}) = -\frac{h^{(3)}_{\text{eff}}}{\sqrt{2\pi}}\int dx\partial_x\phi_y. \end{aligned} \tag{2.135}$$

We see $a = 1(3)$ chain experiences an effective field along $\hat{z}$ ($-\hat{z}$); and h_{eff} are defined in **Table 2.7**. Also, this rotation (2.132) transforms the staggered magnetization,

$$\boldsymbol{N}_y(x) = (\mathcal{N}^x_y,\, \cos\theta_0\mathcal{N}^y_y - \sin\theta_a\varepsilon_y,\, \mathcal{N}^z_y); \quad a = 1, 3, \tag{2.136}$$

Here $\boldsymbol{\mathcal{N}}_y$ and ε_y are the staggered magnetization and dimerization operator in the rotated frame.

On the other hand, for $a = 0, 2$ chains, where the magnetic field is parallel to the DM interaction, the $V^{(0,2)}$ term can be expressed by Abelian bosonization,

$$\begin{aligned} V^{(0)} &= -\frac{h_0}{\sqrt{2\pi}}\int \mathrm{d}x\partial_x\phi_y - \frac{D_0}{\sqrt{2\pi}}\int \mathrm{d}x\partial_x\theta_y, \\ V^{(2)} &= -\frac{h_2}{\sqrt{2\pi}}\int \mathrm{d}x\partial_x\phi_y + \frac{D_2}{\sqrt{2\pi}}\int \mathrm{d}x\partial_x\theta_y. \end{aligned} \tag{2.137}$$

We see $V^{(0,2)}$ are in terms of both bosonic fields θ_y and ϕ_y, while expressions (2.135) are only dependent on ϕ_y.

2.3.4.1 Shift of Abelian fields

Collecting Eqs. (2.137) and (2.135), we have an effective system with magnetic field and DM interactions both along the z-axis on every chain. Evidently, these linear terms can be

Table 2.7. The effective magnetic field $h^{(a)}_{\text{eff}}$ and DM interactions $D^{(a)}_{\text{eff}}$ along $\hat{z}$ in a unit of four spin chains.

a	0	1	2	3
$h^{(a)}_{\text{eff}}$	h_0	$\sqrt{h_1^2 + D_1^2}$	h_2	$-\sqrt{h_3^2 + D_3^2}$
$D^{(a)}_{\text{eff}}$	D_0	0	$-D_2$	0

absorbed into $H_{0,y}$ by shifting the bosonic fields ϕ_y and θ_y appropriately,

$$\begin{aligned}\phi_y &= \tilde{\phi}_y + \frac{t_\phi^{(a)}}{\sqrt{2\pi}}x, \;\; t_\phi^{(a)} \equiv \frac{h_{\text{eff}}^{(a)}}{v_a}, \\ \theta_y &= \tilde{\theta}_y + \frac{t_\theta^{(a)}}{\sqrt{2\pi}}x, \;\; t_\theta^{(a)} \equiv \frac{D_{\text{eff}}^{(a)}}{v_a},\end{aligned} \tag{2.138}$$

with, $h_{\text{eff}}^{(a)}$ and $D_{\text{eff}}^{(a)}$ being the effective the field and DM interactions along $\hat{z}$ on four consecutive chains, and they are summarized in **Table 2.7**. Here v_a is the spin velocity on each chain. As a result of the shifts, the spin currents $\boldsymbol{J}_y$ and staggered magnetization $\boldsymbol{N}_y$ are modified as

$$\begin{aligned}&J_{R,y}^+ \to \tilde{J}_{R,y}^+ e^{-i(t_\phi^{(a)} - t_\theta^{(a)})x}, \quad J_{L,y}^+ \to \tilde{J}_{L,y}^+ e^{i(t_\phi^{(a)} + t_\theta^{(a)})x}, \\ &J_{R,y}^z \to \tilde{J}_{R,y}^z + \frac{(t_\phi^{(a)} - t_\theta^{(a)})}{4\pi}, \quad J_{L,y}^z \to \tilde{J}_{L,y}^z + \frac{(t_\phi^{(a)} + t_\theta^{(a)})}{4\pi}, \\ &N_y^+ \to \tilde{N}_y^+ e^{i t_\theta^{(a)} x}, \quad N_y^z \to -A\sin[\sqrt{2\pi}\tilde{\phi}_y + t_\phi^{(a)} x].\end{aligned} \tag{2.139}$$

Now we are ready to see how oscillation terms are introduced in the relevant interchain coupling term H_{inter}^s in Eq. (2.131).

2.3.5 Interchain interaction H_{inter}

2.3.5.1 Relevant interaction H_{inter}^s

The interchain coupling between staggered magnetizations H_{inter}^s is,

$$\begin{aligned}H_{\text{inter}}^s = J' \int dx \Big[&\frac{1}{4}(1-\cos\theta_0)(N_y^+ N_{y+1}^+ + h.c.) \\ &+ \frac{1}{4}(1+\cos\theta_0)(N_y^+ N_{y+1}^- + h.c.) + N_y^z N_{y+1}^z\Big],\end{aligned} \tag{2.140}$$

with $\theta_0 = \arctan[D_1/h_1] = \arctan[D_3/h_3]$. Here we have omitted the coupling $\varepsilon_y N_{y\pm1}^y$ (because it doesn't renormalize under RG process). To simplify the expression, we replace $\mathcal{N}_y$ by N_y in $a = 1, 3$ chains. As a result of Eq. (2.139), the above expression is,

$$\begin{aligned}H_{\text{inter}}^s = J' \int dx \Big\{&\frac{1}{4}(1-\cos\theta_0)(N_y^+ N_{y+1}^+ e^{i(t_{\theta_y} + t_{\theta_{y+1}})x} + h.c.) \\ &+ \frac{1}{4}(1+\cos\theta_0)(N_y^+ N_{y+1}^- e^{i(t_{\theta_y} - t_{\theta_{y+1}})x} + h.c.) \\ &+ \frac{1}{4}\Big[(e^{i\sqrt{2\pi}(\phi_y - \phi_{y+1})} e^{i(t_{\phi_y} - t_{\phi_{y+1}})x} + h.c.) - (e^{i\sqrt{2\pi}(\phi_y + \phi_{y+1})} e^{i(t_{\phi_y} + t_{\phi_{y+1}})x} + h.c.)\Big]\Big\},\end{aligned} \tag{2.141}$$

Now the oscillation terms have been introduced to the relevant part of interchain coupling, which depend on the parameters $(t_{\theta_y} \pm t_{\theta_{y+1}})$ and $(t_{\phi_y} \pm t_{\phi_{y+1}})$, the explicit forms of which

can be obtained according to **Table 2.7** and Eq. (2.138). These parameters are summarized in **Table 2.8**. The magnitude of $(t_{\theta_y} \pm t_{\theta_{y+1}})$ depends on D_0 and D_2 only. From the analysis in the previous section, we know if $D_0 > J'$ and $D_2 > J'$, then the oscillation is strong enough to remove its associated terms, which is the transverse component of H^s_{inter}. We still need to analyze the oscillation terms in the longitudinal component, and $(t_{\phi_y} \pm t_{\phi_{y+1}})$ can be simplified in the next section.

2.3.5.2 Marginal interaction H^u_{inter}

For the marginal coupling H^u_{inter} in Eq. (2.131), we neglect the $\boldsymbol{J}_{R,y}\boldsymbol{J}_{R,y+1} + (R \to L)$ coupling because it does not renormalize to lowest-order. The remaining H^u_{inter} has two parts,

$$\begin{aligned} H^u_{\text{inter}} &= H_{RL} + H_{LR}, \\ H_{RL} &= J' \int dx \boldsymbol{J}_{Ry} \cdot \boldsymbol{J}_{Ly+1}, \quad H_{LR} = J' \int dx \boldsymbol{J}_{Ly} \cdot \boldsymbol{J}_{Ry+1}. \end{aligned} \tag{2.142}$$

The shift in Eq. (2.139) brings oscillation to Eq. (2.142). To construct a chiral spin liquid, which is depicted in **Figure 2.25**, we need to make the oscillation terms associating with $J_{R,y} \cdot J_{L,y+1}$ vanish, and this chirality is automatically selected by the geometry of DM interactions on four subchains, by adjusting the values of $t_{\phi,y}$ and $t_{\theta,y}$. Namely for the term

$$J^+_{R,y}J^-_{L,y+1} \to J^+_{R,y}J^-_{L,y+1}e^{-i(t_{\phi y} - t_{\theta y} + t_{\phi y+1} + t_{\theta y+1})x}, \tag{2.143}$$

to make the oscillation term vanish, the following condition should be satisfied,

$$t_{\phi y} - t_{\theta y} + t_{\phi y+1} + t_{\theta y+1} = 0. \tag{2.144}$$

Table 2.8. Oscillation factors in the relevant interchain coupling H^s_{inter} (2.141). Here $y = 4n + a$, and the relation (2.145) have been applied. Every oscillation factor mainly depends on $t^{(0)}_\theta$.

a	$t_{\theta_y} + t_{\theta_{y+1}}$	$t_{\theta_y} - t_{\theta_{y+1}}$	$t_{\phi_y} + t_{\phi_y}$	$t_{\phi_y} - t_{\phi_{y+1}}$
0	$t^{(0)}_\theta$	$t^{(0)}_\theta$	$t^{(0)}_\theta$	$2t^{(0)}_\phi - t^{(0)}_\theta$
1	$-t^{(0)}_\theta$	$t^{(0)}_\theta$	$t^{(0)}_\theta$	$-2t^{(0)}_\phi + t^{(0)}_\theta$
2	$-t^{(0)}_\theta$	$-t^{(0)}_\theta$	$-t^{(0)}_\theta$	$2t^{(0)}_\phi + t^{(0)}_\theta$
3	$t^{(0)}_\theta$	$-t^{(0)}_\theta$	$-t^{(0)}_\theta$	$-2t^{(0)}_\phi - t^{(0)}_\theta$

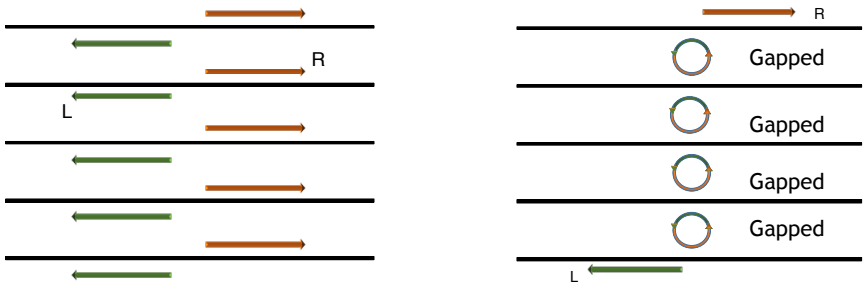

Figure 2.25. Construction of chiral spin liquid. *Left*: the two modes of the spin current on each chain, with green (orange) arrows denoting left (right) moving modes. *Right*: $J_{R,y}$ couples with $J_{L,y+1}$ forming a gapped state in the bulk, while the decoupled spin currents are retained only on the top and bottom chains.

By solving Eq. (2.144) in a unit cell, we have the following relations,

$$\begin{aligned} t_\phi^{(1)} &= t_\theta^{(0)} - t_\phi^{(0)}, \\ t_\phi^{(2)} &= t_\phi^{(0)}, \quad t_\theta^{(2)} = -t_\theta^{(0)}, \\ t_\phi^{(3)} &= -t_\theta^{(0)} - t_\phi^{(0)}. \end{aligned} \tag{2.145}$$

Substitute the expression of $t_{\theta/\phi}^{(a)}$ in **Table 2.7** and Eq. (2.138), we obtain

$$\frac{D_2}{v_2} = \frac{D_0}{v_0}, \quad \frac{h_2}{v_2} = \frac{h_0}{v_0}, \tag{2.146}$$

and

$$\frac{D_1}{v_1} = \frac{1-\beta}{\sqrt{1+\beta^2}}\frac{D_0}{v_0}, \quad \frac{D_3}{v_3} = \frac{1+\beta}{\sqrt{1+\beta^2}}\frac{D_0}{v_0}; \quad \frac{h_a}{D_a} \equiv \beta. \tag{2.147}$$

Eq. (2.147) is obtained under the assumption that h_a/D_a is the same on every chain and $\beta < 1$ is also required ($h_a/D_a = \beta$). The relation (2.147) is illustrated in **Figure 2.26**.

Return back to the oscillation terms, determined by parameters $(t_{\theta_y} \pm t_{\theta_{y+1}})$ and $(t_{\phi_y} \pm t_{\phi_{y+1}})$, in H^s_{inter} (2.141). By using relation (2.145), these parameters are summarized in **Table 2.8**. We notice that if $h_0 \ll D_0$ holds, then these oscillations are strong enough to remove the relevant interchain interaction H^s_{inter} under the condition that $D_0 > J'$ (when we implement the RG analysis, all the terms in H^s_{inter} average to zero).

Now implement condition (2.144) to H^u_{inter} in Eq. (2.149), the expression for the H_{RL} term is,

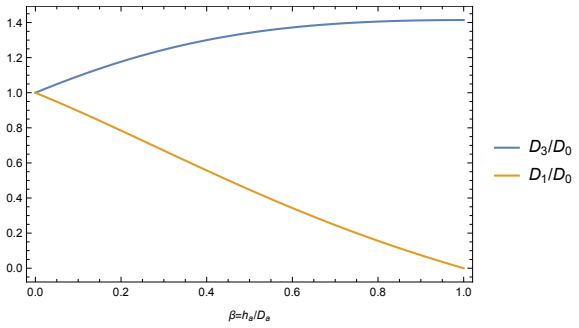

Figure 2.26. The ratios D_1/D_0 and D_3/D_0 as functions of $\beta \equiv h_a/D_a$, under the assumption that β is the same on every chain.

$$\begin{aligned} H_{RL} = J' \int dx \Big[& \frac{1}{4}(\cos\theta_0 - 1)(J^+_{R,y} J^+_{L,y+1} e^{i2(t_{\theta_{y+1}} + t_{\phi_{y+1}})x} + h.c.) \\ & + \frac{1}{4}(\cos\theta_0 + 1)(J^+_{R,y} J^-_{L,y+1} + h.c.) \\ & + \cos\theta_0 J^z_{R,y} J^z_{L,y+1} - \frac{1}{2}\sin\theta_0 (J^z_{R,y} J^+_{L,y+1} e^{i(t_{\theta_{y+1}} + t_{\phi_{y+1}})x} + h.c.) \\ & + \frac{1}{2}\sin\theta_0 (J^+_{R,y} J^z_{L,y+1} e^{i(t_{\theta_y} - t_{\phi_y})x} + h.c.) \Big]. \end{aligned} \tag{2.148}$$

We notice the $J^+_{R,y} J^-_{L,y+1}$ is free from oscillation, while all the terms in H_{LR} are accompanied by oscillation factors,

$$\begin{aligned} H_{LR} = J' \int dx \Big[& \frac{1}{4}(\cos\theta_0 - 1)(J^+_{L,y} J^+_{R,y+1} e^{i2(t_{\theta_y} - t_{\phi_{y+1}})x} + h.c.) \\ & + \frac{1}{4}(\cos\theta_0 + 1)(J^+_{L,y} J^-_{R,y+1} e^{i2(t_{\theta_y} - t_{\theta_{y+1}})x} + h.c.) \\ & + \cos\theta_0 J^z_{L,y} J^z_{R,y+1} + \frac{1}{2}\sin\theta_0 (J^z_{L,y} J^+_{R,y+1} e^{i(t_{\theta_{y+1}} - t_{\phi_{y+1}})x} + h.c.) \\ & - \frac{1}{2}\sin\theta_0 (J^+_{L,y} J^z_{R,y+1} e^{i(t_{\theta_y} + t_{\phi_y})x} + h.c.) \Big]. \end{aligned} \tag{2.149}$$

The oscillation factors in Eq. (2.149) are summarized in **Table 2.9**. The $J^+_{L,y} J^+_{R,y+1}$ term is accompanied by an small oscillation factor which depends on the magnetic field only ($t^0_\phi \propto h_0$). However, in the next section we will see this term $J^+_{L,y} J^+_{R,y+1}$ doesn't develop to strong coupling.

Removing rapid oscillation terms in Eq. (2.149), H^u_{inter} reduces to,

$$\begin{aligned} H^u_{\text{inter}} = J' \int dx \Big[& \frac{1}{4}(\cos\theta_0 + 1)(J^+_{R,y} J^-_{L,y+1} + h.c.) + \cos\theta_0 J^z_{R,y} J^z_{L,y+1} \\ & + \frac{1}{4}(\cos\theta_0 - 1)(J^+_{L,y} J^+_{R,y+1} e^{i2(t_{\theta_y} - t_{\phi_{y+1}})x} + h.c.) + \cos\theta_0 J^z_{L,y} J^z_{R,y+1} \Big]. \end{aligned} \tag{2.150}$$

Table 2.9. Oscillation factors in H^u_{inter} (2.149). Here $y = 4n + a$, and the relation (2.145) have been applied. Every oscillation factor mainly depends on $t^{(0)}_\theta$, besides $2(t_{\theta_y} - t_{\phi_{y+1}})$ which depends on $2t^{(0)}_\phi$ only.

a	$2(t_{\theta_{y+1}} + t_{\phi_{y+1}})$	$t_{\theta_{y+1}} + t_{\phi_{y+1}}$	$t_{\theta_y} - t_{\phi_y}$	$2(t_{\theta_y} - t_{\phi_{y+1}})$	$2(t_{\theta_y} - t_{\theta_{y+1}})$	$t_{\theta_{y+1}} - t_{\phi_{y+1}}$	$t_{\theta_y} + t_{\phi_y}$
0	$2(t^{(0)}_\theta - t^{(0)}_\phi)$	$t^{(0)}_\theta - t^{(0)}_\phi$	$t^{(0)}_\theta - t^{(0)}_\phi$	$2t^{(0)}_\phi$	$2t^{(0)}_\theta$	$-t^{(0)}_\theta + t^{(0)}_\phi$	$t^{(0)}_\theta + t^{(0)}_\phi$
1	$2(-t^{(0)}_\theta + t^{(0)}_\phi)$	$-t^{(0)}_\theta + t^{(0)}_\phi$	$-t^{(0)}_\theta + t^{(0)}_\phi$	$-2t^{(0)}_\phi$	$2t^{(0)}_\theta$	$-t^{(0)}_\theta - t^{(0)}_\phi$	$t^{(0)}_\theta - t^{(0)}_\phi$
2	$2(-t^{(0)}_\theta - t^{(0)}_\phi)$	$-t^{(0)}_\theta - t^{(0)}_\phi$	$-t^{(0)}_\theta - t^{(0)}_\phi$	$2t^{(0)}_\phi$	$-2t^{(0)}_\theta$	$t^{(0)}_\theta + t^{(0)}_\phi$	$-t^{(0)}_\theta + t^{(0)}_\phi$
3	$2(t^{(0)}_\theta + t^{(0)}_\phi)$	$t^{(0)}_\theta + t^{(0)}_\phi$	$t^{(0)}_\theta + t^{(0)}_\phi$	$-2t^{(0)}_\phi$	$-2t^{(0)}_\theta$	$-t^{(0)}_\theta - t^{(0)}_\phi$	$-t^{(0)}_\theta - t^{(0)}_\phi$

2.3.5.3 Chiral spin liquid

Writing spin currents J_R and J_L in terms of bosonic fields (ϕ, θ),

$$J^+_{R,y} = \frac{1}{2\pi a} e^{-i\sqrt{2\pi}(\phi_y - \theta_y)}; \quad J^+_{L,y} = \frac{1}{2\pi a} e^{i\sqrt{2\pi}(\phi_y + \theta_y)}. \tag{2.151}$$

Then the dominant coupling in Eq. (2.149) reduces to,

$$\begin{aligned} J^+_{R,y} J^-_{L,y+1} + h.c. &= \frac{1}{(2\pi a)^2} (e^{-i\sqrt{2\pi}(\phi_y - \theta_y + \phi_{y+1} + \theta_{y+1})} + h.c.) \\ &= \frac{2}{(2\pi a)^2} \cos[\sqrt{2\pi}(\phi_y - \theta_y + \phi_{y+1} + \theta_{y+1})]. \end{aligned} \tag{2.152}$$

with its coupling constant $g = \frac{1}{4}(\cos\theta_0 + 1) > 0$, then this term tends to pin the spins to satisfies

$$\sqrt{2\pi}(\phi_y - \theta_y + \phi_{y+1} + \theta_{y+1}) = 2\pi n + \pi, \quad n \in N. \tag{2.153}$$

Plug this condition into the expression of $J^+_{L,y} J^+_{R,y+1}$ term,

$$\begin{aligned} J^+_{L,y} J^+_{R,y+1} + h.c. &= \frac{2}{(2\pi a)^2} \cos[\sqrt{2\pi}(\phi_y - \theta_y - \phi_{y+1} + \theta_{y+1})] \\ &= -\frac{2}{(2\pi a)^2} \cos[2\sqrt{2\pi}(\phi_y + \theta_{y+1})]. \end{aligned} \tag{2.154}$$

This term is not stable.

2.3.6 In the absence of magnetic field $h = 0$

When the system is in the absence of magnetic field, $h = 0$, then $\theta = \pi/2$ and $\beta = 0$. The oscillation operators in **Table 2.8** and **Table 2.9** are only related to D_0. When J_a is the

same on every chain, from Eq. (2.146) and (2.147), the magnitude of DM interaction D_a is the same on every chain. H^u_{inter} reduces to,

$$H^u_{\text{inter}} = J' \int dx \Big[\frac{1}{4}(J^+_{R,y} J^-_{L,y+1} + h.c.) - \frac{1}{4}(J^+_{L,y} J^+_{R,y+1} + h.c.) \Big]. \tag{2.155}$$

2.3.7 Discussion

In this section, we present a feasible way to construct a chiral spin liquid from weakly coupled spin chains in the presence of Dzyaloshinskii-Moriya (DM) interactions and magnetic field. The spin chain system is illustrated in **Figure 2.24**, and modeled by Hamiltonian (2.119). The orientation of magnetic field and DM vector is either parallel or perpendicular to each other. This arrangement ensures us to remove the relevant interchain interaction between nearest-neighbor chains. At the same time, the staggered-between-next-neighbor-chain DM interactions prevent the relevant couplings between next-neighbor chains.[84] As a result, the nearest-neighbor chains influence each other by the coupling between left- or right-moving spin currents, as depicted in **Figure 2.25**. Only two branches of spin current with opposite chirality are left unpaired on the top and bottom chains, and hence a Kalmeyer-Laughlin chiral spin liquid is established. This work is strongly inspired by Ref.[36] We hope this coupled spin chain model (2.119) will stimulate the research along this line to realize the chiral spin liquid, both in the field of crystal solids and cold atoms.

CHAPTER 3

NOVEL ORDERS IN TRIANGULAR ANTIFERROMAGNETS

In this chapter, we study antiferromagnets sit in a frustrated geometry, the triangular-based lattices as shown in **Figure 1.2**. In this geometry, magnetic orders are suppressed to temperatures below what is expected from near neighbor magnetic interactions, and the magnetic field also induces many unconventional spin structures.

These spin systems are studied by the use of semiclassical approach, the *spin wave* theory, which has been found to be remarkably successful in dealing with ordered phases of both the Heisenberg ferromagnets and antiferromagnets. The excitation of spin degree of freedom above a magnetic ordered state can be described by quasi-boson, namely magnon. Other techniques, such as Green's function, are also used. In Sec. 3.1, we study the phases of triangular lattice antiferromagnet near saturation, that is the one-magnon instability of the fully polarized state, while in Sec. 3.2, we consider the two-magnon instability of UUD state (1/3 magnetization plateau) on an effective zigzag ladder.

3.1 Phases of triangular lattice antiferromagnet near saturation

Here we consider 2D Heisenberg antiferromagnets on a triangular lattice with spatially anisotropic interactions in a high magnetic field close to saturation. We show that this system possesses rich phase diagram in field/anisotropy plane due to competition between classical and quantum orders: an incommensurate noncoplanar spiral state, which is favored classically, and a commensurate coplanar state, which is stabilized by quantum fluctuations. We show that the transformation between these two states is highly non-trivial and involves two intermediate phases – the phase with coplanar incommensurate

spin order and the one with noncoplanar double-**Q** spiral order. The transition between the two coplanar states is of commensurate-incommensurate type, not accompanied by softening of spin-wave excitations. We show that a different sequence of transitions holds in triangular antiferromagnets with exchange anisotropy, such as $Ba_3CoSb_2O_9$.

3.1.1 Introduction

The field of frustrated quantum magnetism witnessed a remarkable revival of interest in the last few years due to rapid progress in synthesis of new materials and in understanding previously unknown states of matter. The two main lines of research in the field are searches for spin-liquid phases and for new ordered phases with highly nontrivial spin structures.[4] For the latter, the most promising system is a 2D Heisenberg antiferromagnet on a triangular lattice in a finite magnetic field, as this system is known to possess an "accidental" classical degeneracy: every classical spin configuration with a triad of neighboring spins satisfying $\mathbf{S}_{\mathbf{r}} + \mathbf{S}_{\mathbf{r}+\delta_1} + \mathbf{S}_{\mathbf{r}+\delta_2} = \mathbf{h}/(3J)$, where J is the exchange interaction, belongs to the ground state manifold.

An infinite degeneracy holds only for an ideal Heisenberg system with isotropic nearest-neighbor interaction. Real systems have either spatial anisotropy of exchange interactions, as in Cs_2CuCl_4[119,120] and Cs_2CuBr_4[62,121,122] for which the interaction J on horizontal bonds is larger than J' on diagonal bonds (see insert in **Figure 3.1**), or exchange anisotropy in spin space, as in $Ba_3CoSb_2O_9$, for which $J_z < J_\perp = J$ (an easy plane anisotropy).[123–125] An anisotropy of either type breaks accidental degeneracy already at a classical level and for fields $\mathbf{h} = h\hat{z}$ slightly below the saturation field $h_{\rm sat}$ selects a noncoplanar cone state with

$$\langle \mathbf{S}_{\mathbf{r}} \rangle = (S-\rho)\hat{z} + \sqrt{2S\rho}(\cos[\mathbf{Q}\cdot\mathbf{r}+\varphi]\hat{x} + \sin[\mathbf{Q}\cdot\mathbf{r}+\varphi]\hat{y}), \tag{3.1}$$

where $\rho \sim S(h_{\rm sat}-h)/h_{\rm sat}$ is the density of magnons (the *condensate fraction*) which determines the magnetization $M = S-\rho$, $\varphi \in (0, 2\pi)$ is a phase of a condensate, and $\mathbf{Q} = (Q, 0)$ is the ordering wave vector. It is incommensurate with $Q = Q_i = 2\cos^{-1}(-J'/2J)$ in the spatially anisotropic case $J' \neq J$ and commensurate with $Q = Q_0 = 4\pi/3$ for the easy-plane anisotropy (in the last case, the values of $\mathbf{Q}_0 \cdot \mathbf{r} = 2\pi\nu/3 \pmod{2\pi}$, with $\nu = \pm 1, 0$).

Quantum fluctuations are also known to lift accidental degeneracy, and do so already in the *isotropic* system. However, they select a different ordered state, which is the copla-

nar, commensurate state with two parallel spins in every triad, often called the V state (**Figure 3.1**).[126–128]

This order is described by

$$\langle \mathbf{S}_\mathbf{r} \rangle = (S - 2\rho \cos^2[\mathbf{Q}\cdot\mathbf{r} + \theta])\hat{z} + \sqrt{4S\rho}\cos[\mathbf{Q}\cdot\mathbf{r} + \theta] \times (\cos\varphi\hat{x} + \sin\varphi\hat{y}), \qquad (3.2)$$

where $\mathbf{Q} = \mathbf{Q}_0$, $\rho = \rho_{\mathbf{Q}_0} + \rho_{-\mathbf{Q}_0}$ is the sum of two equal contributions from condensates with wave vectors $\pm\mathbf{Q}_0 = (\pm Q_0, 0)$, φ is a common phase of the two condensates, and θ is their *relative* phase. The values of θ in the commensurate V phase are constrained to $\theta = \pi\ell/3$, where $\ell = 0, 1, 2$, describe three distinct degenerate spin configurations (three choices to select two parallel spins in any triad, see **Figure 3.1**).

The issue we consider in this paper is how the system evolves at $h \leq h_{\rm sat}$ from the coplanar V state, selected by quantum fluctuations, to the noncoplanar cone state, selected by classical fluctuations, as the anisotropy increases. We show that this evolution is highly nontrivial and involves commensurate-incommensurate transition (CIT) and, in the case of $J - J'$ model, an intermediate double cone phase.

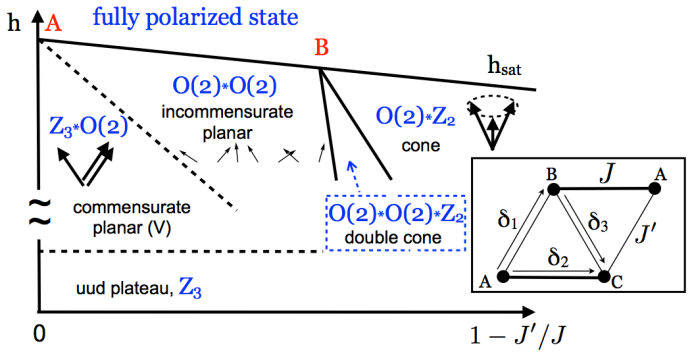

Figure 3.1. Phase diagram of the spatially anisotropic triangular lattice antiferromagnet with large S near saturation field, as a function of spatial anisotropy of the interactions. The phases at small and large anisotropy are commensurate coplanar V-phase, which breaks $Z_3 \times O(2)$ symmetry, and incommensurate noncoplanar chiral cone phase, which breaks $Z_2 \times O(2)$ symmetry. In between, there are two incommensurate phases: a coplanar phase, which breaks $O(2) \times O(2)$ symmetry, and a noncoplanar double cone phase, which breaks $Z_2 \times O(2) \times O(2)$ symmetry. The CI transition from the V phase to the incommensurate planar phase is shown by a dashed line. The insert shows the geometry of the lattice exchange constant is J on horizontal bonds (bold) and J' on diagonal bonds (thin).

3.1.2 The phase diagrams

To begin, it is instructive to compare order parameter manifolds in the two phases. The order parameter manifold in the V phase is $O(2) \times Z_3$ and that in the cone phase is $O(2) \times Z_2$. In both phases, a continuous $O(2)$ reflects a choice of the phase φ. Z_3 in the V phase corresponds to choosing one of three values of θ in (3.2)), and Z_2 in the cone phase is a chiral symmetry between left- and right-handed spiral orders (chiralities), i.e., orders with $+Q$ and $-Q$ in (3.1)). The symmetry breaking patterns in the two phases are not compatible. Hence one should expect either first-order transition(s) or an intermediate phase(s). We show that in $J - J'$ model the evolution occurs via two intermediate phases, see **Figure 3.1**. As $\delta J = J - J'$ increases, the V phase first undergoes a CIT at $\delta J_{c1} \sim (J/\sqrt{S})(h_{\rm sat} - h)/h_{\rm sat}$ (line AC in **Figure 3.1**). The new phase remains coplanar, as in (3.2)), but the phase θ becomes incommensurate and coordinate-dependent. and order parameter manifold extends to $O(2) \times O(2)$ (spontaneous selection of φ and the origin of coordinates). The incommensurate coplanar state exists up to a second critical $\delta J_{c2} \sim J/\sqrt{S}$, where the system breaks the Z_2 symmetry between the two condensates (line BC in **Figure 3.1**). At larger δJ the two condensates still develop, one of them shifts to a new wave vector $\bar{\mathbf{Q}}$ and its magnitude gets smaller. The resulting state is a noncoplanar double cone state with order parameter manifold $O(2) \times O(2) \times Z_2$. Finally, at the third critical anisotropy $\delta J_{c3} = \delta J_{c2}[1 + O((h_{\rm sat} - h)/h_{\rm sat})]$ the magnitude of the condensate at $\bar{\mathbf{Q}}$ vanishes and the double cone transforms into a single cone (line BD in **Figure 3.1**).

In systems easy-plane anisotropy $\Delta = (J - J_z)/J > 0$, the the ordering wave vector remains commensurate, $Q = Q_0 = \pm 4\pi/3$, for all $\Delta > 0$, and the evolution from quantum-preferred V state to classically-preferred cone state proceeds differently, via two first-order phase transitions (see **Figure 3.2**). The V state with $\theta = \ell\pi/3$ survives up to some critical $\Delta_{c1} \sim 1/S$, where another commensurate coplanar order develops, for which $\theta = (2\ell + 1)\pi/6$. The corresponding spin pattern resembles Greek letter Ψ and we label this state a Ψ phase. The Ψ phase survives up to $\Delta_{c2} \geq \Delta_{c1}$, beyond which the spin configuration turns into the commensurate cone state.

We now discuss the model and the calculations which lead to phase diagrams in **Figure 3.1** and **Figure 3.2**.

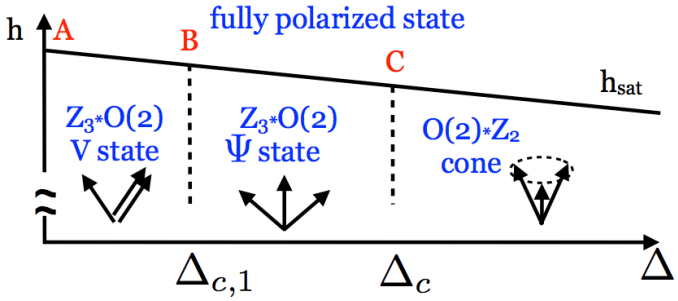

Figure 3.2. The phase diagram of the XXZ model in a magnetic field near a saturation value, $\Delta = (J - J_z)/J$. The cone and V states are the same as in **Figure 3.1**, but the transformation from one phase to the other with increasing spin exchange anisotropy proceeds differently from the case of spatial exchange anisotropy and involves one intermediate coplanar commensurate phase with Ψ-like spin pattern.

3.1.3 The model

The isotropic Heisenberg antiferromagnet on a triangular lattice is described by the Hamiltonian

$$\mathcal{H}_0 = \frac{1}{2} J \sum_{\mathbf{r},\delta} \mathbf{S}_{\mathbf{r}} \cdot \mathbf{S}_{\mathbf{r}+\delta} - \sum_{\mathbf{r}} h S^z_{\mathbf{r}}, \tag{3.3}$$

where δ are nearest-neighbor vectors of the triangular lattice. The two perturbations we consider are

$$\delta\mathcal{H}_{\text{anis}} = (J' - J) \sum_{\mathbf{r}} \mathbf{S}_{\mathbf{r}} \cdot (\mathbf{S}_{\mathbf{r}+\delta_1} + \mathbf{S}_{\mathbf{r}+\delta_3}), \tag{3.4}$$

$$\delta\mathcal{H}_{\text{xxz}} = \frac{1}{2}(J_z - J) \sum_{\mathbf{r},\pm\delta_{1,2,3}} S^z_{\mathbf{r}} S^z_{\mathbf{r}+\delta}. \tag{3.5}$$

where $\langle \mathbf{r}, \mathbf{r} + \delta_{1,3} \rangle$ are diagonal bonds.

We consider a quasiclassical limit $S \gg 1$, when quantum fluctuations are small in $1/S$ and quantum and classical tendencies compete at small anisotropy $\delta J/J \sim 1/\sqrt{S}$ and/or $\Delta/J \sim 1/S$. In this limit, the calculations in the vicinity of the saturation field can be done using a well-established dilute Bose gas expansion and are controlled by simultaneous smallness of $1/S$ and of $(h_{\text{sat}} - h)/h_{\text{sat}}$.[127,129–131] We argue that our results are applicable for all values of S, down to $S = 1/2$, because (i) quantum selection of the V state holds even for $S = 1/2$,[130] and (ii) numerical analysis of $S = 1/2$ systems[130,132] identified the same phases near saturation field as found here.

We set quantization axis along the field direction and express spin operators $\mathbf{S_r}$ in terms of Holstein-Primakoff bosons a, a^+ as $S^-_{\mathbf{r}} = [2S - a^+_{\mathbf{r}} a_{\mathbf{r}}]^{1/2} a^+_{\mathbf{r}}$, $S^z_{\mathbf{r}} = S - a^+_{\mathbf{r}} a_{\mathbf{r}}$. Substituting this transformation into $\mathcal{H}_{\text{anis}/xxz}$ and expanding the square root one obtains the spin-wave Hamiltonian $\mathcal{H} = \mathcal{E}_{\text{cl}} + \sum_{j=2}^{\infty} \mathcal{H}^{(j)}$, where $\mathcal{E}_{\text{cl}}$ stands for the classical ground state energy, and $\mathcal{H}^{(j)}$ are of j-th order in operators a, a^+. For our purposes, terms up to $j = 6$ have to be retained in the expansion (see the Supplement for technical details). The quadratic part of the spin-wave Hamiltonian reads

$$\mathcal{H}^{(2)} = \sum_{\mathbf{k}} (\omega_{\mathbf{k}} - \mu) a^+_{\mathbf{k}} a_{\mathbf{k}}, \tag{3.6}$$

where $\omega_k = S(J_{\mathbf{k}} - J_{\mathbf{Q}})$ is the spin-wave dispersion, measured relative to its minimum at the saturation field h_{sat}, and $\mu = (h_{\text{sat}} - h)/h_{\text{sat}}$ plays the role of chemical potential. For $J - J'$ model, $J_{\mathbf{k}} = \sum_{\pm\delta_j} J_{\delta_j}(e^{i\mathbf{k}\cdot\delta_j} - 1)$, where $J_{\delta_{1,3}} = J'$ and $J_{\delta_2} = J$. Here $\mathbf{Q} = \mathbf{Q}_{\text{i}} = (Q_{\text{i}}, 0)$ with $Q_{\text{i}} = 2\cos^{-1}(-J'/2J)$. For XXZ model, $J_{\mathbf{k}} = \sum_{\pm\delta_j}(Je^{i\mathbf{k}\cdot\delta_j} - J_z)$ and $\mathbf{Q} = \mathbf{Q}_0 = (4\pi/3, 0)$. In both cases, lowering of a magnetic field below h_{sat} makes $(\omega_{\mathbf{k}} - \mu)$ negative at $\mathbf{k} \approx \pm\mathbf{Q}$, where $\mathbf{Q}$ is either $\mathbf{Q}_{\text{i}}$ or $\mathbf{Q}_0$, and drives the Bose-Einstein condensation (BEC) of magnons. To account for BEC, we introduce two condensates, $\langle a_{\mathbf{Q}} \rangle = \sqrt{N}\psi_1$ and $\langle a_{-\mathbf{Q}} \rangle = \sqrt{N}\psi_2$, where $\psi_{1,2}$ are complex order parameters. In real space,

$$\langle a_{\mathbf{r}} \rangle = \frac{1}{\sqrt{N}} \sum_{\mathbf{k}} e^{i\mathbf{k}\cdot\mathbf{r}} \langle a_{\pm\mathbf{k}} \rangle = \psi_1 e^{i\mathbf{Q}\cdot\mathbf{r}} + \psi_2 e^{-i\mathbf{Q}\cdot\mathbf{r}}. \tag{3.7}$$

The ground state energy, per site, of the *uniform* condensed ground state is expanded in powers of $\psi_{1,2}$ as

$$\begin{aligned} E_0/N = &-\mu(|\psi_1|^2 + |\psi_2|^2) + \frac{1}{2}\Gamma_1(|\psi_1|^4 + |\psi_2|^4) \\ &+\Gamma_2|\psi_1|^2|\psi_2|^2 + \Gamma_3((\bar{\psi}_1\psi_2)^3 + \text{h.c.})... \end{aligned} \tag{3.8}$$

where $\bar{\psi}_j$ denotes complex conjugated of ψ_j, dots stand for higher order terms, and we omitted a constant term. We verified [in the Supplement] that higher orders in ψ_j do not modify our analysis.

Whether the state at $\mu = 0+$ is coplanar or chiral is decided by the sign of $\Gamma_1 - \Gamma_2$.[127] For $\Gamma_1 < \Gamma_2$, it is energetically favorable to break Z_2 symmetry between condensates and choose $\psi_1 \neq 0, \psi_2 = 0$ or vice versa. Parameterizing the condensate as $\psi_1 = \sqrt{\rho}e^{i\varphi}$, where $\rho = \mu/\Gamma_1$, and using Eq.(3.34), we obtain the cone configuration, Eq.(3.1). The order parameter manifold of this state is $O(2) \times Z_2$, where $O(2)$ is associated with the phase φ.

When $\Gamma_1 > \Gamma_2$, it is energetically favorable to preserve Z_2 symmetry and develop both condensates with equal magnitude $\rho = \mu/(\Gamma_1 + \Gamma_2)$, i.e., set $\psi_1 = \sqrt{\rho}e^{i\theta_1}$, $\psi_2 = \sqrt{\rho}e^{i\theta_2}$. This corresponds to coplanar state with the common phase $\varphi = (\theta_1 + \theta_2)/2$ and the relative phase $\theta = (\theta_1 - \theta_2)/2$. The order parameter in this state is given by Eq. (3.2) with $\mathbf{Q}$ equal to either $\mathbf{Q}_{\rm i}$ ($J - J'$ model) or $\mathbf{Q}_0$ (XXZ model). For $\mathbf{Q} = \mathbf{Q}_{\rm i}$, the state is incommensurate coplanar configuration in **Figure 3.1**. The order parameter manifold of this state is $O(2) \times O(2)$, where one $O(2)$ is associated with φ and the other with θ. For $\mathbf{Q} = \mathbf{Q}_0$, the coplanar order is commensurate. In this case, the symmetry is further reduced by Γ_3 term, which is allowed because $e^{i3\mathbf{Q}_0\cdot\mathbf{r}} = 1$ for all sites $\mathbf{r}$ of the lattice. This term locks the relative phase of the condensates θ to three values, reducing the broken symmetry to $O(2) \times Z_3$. For $\Gamma_3 < 0$, $\theta = \pi\ell/3$, where $\ell = 0, 1, 2$. For $\Gamma_3 > 0$, $\theta = (2\ell + 1)\pi/6$. These are V and Ψ states in **Figure 3.1** and **Figure 3.2**.

Accidental degeneracy of the isotropic model (3.3) in the classical limit shows up via $\Gamma_1^{(0)} = \Gamma_2^{(0)} = 9J$ and $\Gamma_3^{(0)} = 0$, where the superscript '0' indicates that these expressions are of zeroth order in $1/S$. We now analyze the situation in the presence of anisotropy and quantum fluctuations. We first consider $J - J'$ model with $J \neq J'$, and then XXZ model with $J_z \neq J$.

3.1.4 Phases of the $J - J'$ model

We computed $\Gamma_{1,2}^{(0)}$ for classical spins, but in the presence of the the spatial anisotropy and found that it tilts the balance in favor of the cone phase: $\Delta\Gamma^{(0)} = \Gamma_2^{(0)} - \Gamma_1^{(0)} = J(1 - J'/J)^2(2 + J'/J)^2 > 0$. Quantum $1/S$ corrections, on the other hand, favor the coplanar state: $\Delta\Gamma^{(1)} < 0$. We obtained [see Sec.3.1.10.2.1]

$$\Delta\Gamma^{(1)} = \frac{1}{16S}\sum_{\mathbf{k}\in \mathrm{BZ}}\Big(\frac{(J_0 + 5J_{\mathbf{k}})^2}{J_0 - J_{\mathbf{k}}} - \frac{(J_0 - 4J_{\mathbf{Q}+\mathbf{k}})^2}{J_{\mathbf{Q}+\mathbf{k}} - J_{\mathbf{Q}}}\Big) + \frac{3J}{8S} \approx -\frac{1.6J}{S}. \tag{3.9}$$

Combining classical and quantum contributions, we find that

$$\Delta\Gamma = \Delta\Gamma^{(0)} + \Delta\Gamma^{(1)} = \frac{9(\delta J)^2}{J} - \frac{1.6J}{S}, \tag{3.10}$$

where, we recall, $\delta J \equiv J - J'$. We see that $\Delta\Gamma < 0$ for $\delta J < \delta J_c = 0.42J/\sqrt{S}$, and $\Delta\Gamma > 0$ for larger δJ. The condition $\Delta\Gamma = 0$ selects the point B in **Figure 3.1**. [1]

[1] For the special case of $S = 1/2$, this transition is absent as $\Delta\Gamma < 0$ for all $J' < J$; see[130]

3.1.5 Split transitions near δJ_c

At $\mu = 0+$, the transition between incommensurate planar and cone phases is first order with no hysteresis. We now analyze how this transition occurs at a finite positive $\mu \neq 0$. We depart from the cone state to the right of point B in **Figure 3.1** and move to smaller δJ. Suppose that the condensate in the cone state has momentum $+\mathbf{Q}_i$. Then Goldstone spin-wave mode is at $\mathbf{k} = \mathbf{Q}_i$, while excitations near $\mathbf{k} = -\mathbf{Q}_i$ have a finite gap. We computed the excitation spectrum $\omega_{\mathbf{k}}^{(1)}$ with quantum $1/S$ corrections and found [see Sec. 3.1.11.1 in the Supplement] that near $\mathbf{k} \approx -\mathbf{Q}_i$

$$\omega_{\mathbf{k}}^{(1)} \approx \frac{3J}{4}\left[(k_x + \bar{Q}_i)^2 + k_y^2 + \epsilon_{\min}\right], \tag{3.11}$$

$$\epsilon_{\min} = \frac{12\mu}{h_{\text{sat}} J^2}\left[(\delta J)^2 - (\delta J_c)^2\left(1 + \frac{\mu}{h_{\text{sat}}}\right)\right], \tag{3.12}$$

where $\bar{Q}_i = Q_i + (4\pi/3 - Q_i)(3\mu/h_{\text{sat}}) \approx Q_i + 1.45\mu/(h_{sat}\sqrt{S})$. The cone state becomes unstable at $\epsilon_{\min} = 0$, i.e., at $\delta J_{c3} \approx \delta J_c(1 + \mu/(2h_{\text{sat}}))$, and gives rise to magnon condensation with momentum $(-\bar{Q}_i, 0)$, which is *different* from $-\mathbf{Q}_i$. The condensation of magnons with $(-\bar{Q}_i, 0)$ then gives rise to a secondary cone order, with momentum not related by symmetry to that of the primary cone order. The resulting spin configuration is a double cone with $O(2) \times O(2) \times Z_2$ order parameter manifold. The primary condensate sets the transverse component of $\langle \mathbf{S}_{\mathbf{r}}^{\perp} \rangle = \langle S_{\mathbf{r}}^x + iS_{\mathbf{r}}^y \rangle$ to be $\exp[i\mathbf{Q}_i \cdot \mathbf{r} + i\theta_1]$ and the second condensate adds $\exp[-i\bar{\mathbf{Q}}_i \cdot \mathbf{r} + i\theta_2]$.

At smaller $\delta J \leq \delta J_{c3}$ the position of the minimum in $\omega_k^{(1)}$ in (3.11) evolves and drifts towards $-\mathbf{Q}_i$. Once it reaches $-\mathbf{Q}_i$, at $\delta J = \delta J_{c2}$, the two cone configurations interfere constructively and give rise to an incommensurate coplanar state. Critical δJ_{c2} can be estimated by requiring that $\omega_k^{(1)} = 0$ at $\mathbf{k} = -\mathbf{Q}_i$. This yields $\delta J_{c2} = \delta J_{c3}(1 - O(\mu/h_{\text{sat}})) < \delta J_{c3}$. We see therefore that the transformation from a cone to an incommensurate coplanar state at at a finite μ (i.e, at $h \leq h_{\text{sat}}$) occurs via two transitions at δJ_{c2} and δJ_{c3} and involves an intermediate double cone phase (**Figure 3.1**).

3.1.6 Instability of the V phase

We now return to Eq. (3.8) and consider the transition between the V phase and the incommensurate coplanar phase. At $\mu = 0+$, this transition holds at infinitesimally small δJ (point A in **Figure 3.1**). We show that at a finite μ, the V phase survives up to a finite

$\delta J_{c1} \sim (J/\sqrt{S})(\mu/h_{\rm sat})$. The argument is that in the V phase $\mathbf{Q} = \mathbf{Q}_0$ is commensurate and Γ_3 term in Eq. (3.8) is allowed. We recall that at $\delta J = 0$ and for classical spins $\Gamma_3 = 0$. We computed the classical contribution to Γ_3 at $\delta J > 0$ and the contribution due to quantum fluctuations at $\delta J = 0$. We found [see Supplement] that the classical contribution vanishes, but the quantum contribution is finite to order $1/S^2$ and makes Γ_3 negative:

$$\Gamma_3 = \frac{3}{32S^2}\sum_{\mathbf{k}\in \rm BZ}\Big(\frac{(5J_{\mathbf{k}}+J_0)(5J_{\mathbf{Q}+\mathbf{k}}+J_0)J_{\mathbf{Q}-\mathbf{k}}}{(J_0-J_{\mathbf{k}})(J_0-J_{\mathbf{Q}+\mathbf{k}})} - \\ -\frac{(5J_{\mathbf{k}}+J_0)(J_{\mathbf{k}}+J_0)}{2(J_0-J_{\mathbf{k}})}\Big) + \frac{3J_0}{64S^2} \approx -\frac{0.69J}{S^2} \tag{3.13}$$

Because $\Gamma_3 < 0$, the V phase has extra negative energy compared to incommensurate phases, and one needs a finite δJ to overcome this energy difference.

We now argue that the transition at δJ_{c1} belongs to the special class of CIT. To see this, we allow for spatially non-uniform configurations of the condensate $\psi_{1,2}(\mathbf{r})$. This adds spatial gradient terms to (3.4): the isotropic term $\mathcal{H}_0$ produces conventional quadratic in gradient contribution $\propto \rho(\partial_x\theta)^2$, while $\delta\mathcal{H}_{\rm anis}$ adds a *linear* gradient term $\propto \rho S\delta J\partial_x(\theta_1-\theta_2)$. Combining these two classical contributions with the quantum Γ_3 term in (3.8), we obtain the energy density for the relative phase $\theta = (\theta_1-\theta_2)/2$:

$$\mathcal{E} = \frac{3JS^2\mu}{4h_{\rm sat}}(\partial_x\theta)^2 + \frac{\sqrt{3}\delta JS^2\mu}{h_{\rm sat}}\partial_x\theta + S\frac{(\Gamma_3 S^2)}{4}\frac{\mu^3}{h_{\rm sat}^3}\cos[6\theta] \tag{3.14}$$

Eq. (3.14) is of standard sine-Gordon form, which allows us to borrow the results from:[130] the equilibrium value of θ shifts from the commensurate $\theta = \pi\ell/3$ in the V phase to an incommensurate value when the coefficient of the linear gradient term in (3.14) exceeds the geometric mean of the coefficients of two other terms in (3.14). Using Eq. (3.14)) we find that CIT occurs at $\delta J_{c1} = 1.17(J/\sqrt{S})(\mu/h_{\rm sat}) = 0.13\mu/S^{3/2}$ (line AC in **Figure 3.1**). At $\delta J > \delta J_{c1}$, θ acquires linear dependence on x: $\theta = \tilde{Q}x + \tilde{\theta}$. In this situation, the spin configuration becomes incommensurate but remains coplanar (**Figure 3.1**).

The critical δJ_{c1} for the CIT has to be compared with $\delta J_{\rm sw}$ at which spin-wave excitations in the V phase soften. We computed spin-wave velocity with quantum $1/S$ corrections and found that it does go down with increasing δJ but vanishes only at $\delta J_{\rm sw} \sim (J/\sqrt{S})(\mu/h_{\rm sat})^{1/2} \gg \delta J_{c1}$. This implies that the spin-wave velocity remains finite across the CIT.

3.1.7 Phases of $\mathcal{H}_{xxz}$

For the XXZ model with exchange anisotropy, J and J' remain equal, but $J_z < J_\perp = J$ on all bonds. We verified (in Sec. 3.1.8.3) that $\mathbf{Q}$ remains commensurate for all $J_z/J \leq 1$, i.e., $\mathbf{Q} = \mathbf{Q}_0 = (4\pi/3, 0)$. In this situation, we found $\Gamma_2^{(0)} - \Gamma_1^{(0)} = -J_{\mathbf{Q}}(1 - J_z/J) = 3J\Delta$. Quantum corrections to Γ_1 and Γ_2 are determined within the same isotropic model (3.3) and are given by (3.10). Using this, we immediately find that the ground state of the quantum XXZ model is coplanar for $\Delta \leq \Delta_{c2} = 0.53/S$ and is a cone for $\Delta > \Delta_{c2}$. The transition between coplanar and cone states near Δ_{c2} remains first-order for a finite $\mu > 0$, i.e., no intermediate double spiral state appears. This is the consequence of the fact that $\mathbf{Q} = \mathbf{Q}_0$ remains commensurate. Still, the transformation from the V phase to the cone phase does involve a new intermediate state, which comes about due to the change of sign of Γ_3. Exchange anisotropy Δ gives rise to a positive Γ_3 to order $1/S$: $\Gamma_3^{(1)} = J(1 + 2J_z/J)(1 - J_z/J)/(2S) \approx 3J\Delta/(2S)$ (see Supplement for details). At the same time the quantum corrections give rise to *negative* Γ_3 to order $1/S^2$ already at $\Delta = 0$, see (3.57). Combining the two, we find that

$$\Gamma_3 = \Gamma_3^{(1)} + \Gamma_3^{(2)} = \frac{3J\Delta}{2S} - \frac{0.69J}{S^2}. \tag{3.15}$$

changes sign at $\Delta_{c1} = 0.45/S < \Delta_{c2} = 0.53/S$. At smaller $\Delta < \Delta_{c1}$, $\Gamma_3 < 0$, and the spin configuration is the V state (the energy is minimized by setting $\cos 6\theta = 1$, see (3.8)). However, in the interval $\Delta_{c1} < \Delta < \Delta_{c2}$, $\Gamma_3 > 0$ becomes positive. The energy is now minimized by $\cos 6\theta = -1$, which corresponds to the Ψ state in **Figure 3.2**. The transition is highly unconventional symmetry-wise because the order parameter manifold is $O(2) \times Z_3$ in both phases, but extends to a larger $O(2) \times O(2)$ symmetry at the transition point.

We present the phase diagram of XXZ model in **Figure 3.2**. A very similar phase diagram has been recently obtained in the numerical cluster mean-field analysis of the $S = 1/2$ XXZ model.[132]

To summarize, in this paper we considered anisotropic 2D Heisenberg antiferromagnets on a triangular lattice in a high magnetic field close to the saturation. We analyzed the cases of spatially anisotropic interactions, as in Cs_2CuCl_4 and Cs_2CuBr_4 and of exchange anisotropy, as in $Ba_3CoSb_2O_9$. We showed that the phase diagram in field/anisotropy plane is quite rich due to competition between classical and quantum orders, which favor

noncoplanar and coplanar states, respectively. This competition leads to multiple transitions and highly nontrivial intermediate phases, including a novel double cone state. We demonstrated that one of the transition in each of the two cases studied is of CIT type and is not accompanied by softening of spin-wave excitations.

The analysis of this paper can be easily extended to quasi-2D layered systems, with interlayer antiferromagnetic interaction $0 < J'' \ll J$. This additional exchange interaction leads to the staggering of coplanar spin configurations, of either V or Ψ kind, between the adjacent layers, as can easily be seen by treating $\varphi \to \varphi_z$ in Eq.(3.2) as layer-dependent variable with discrete index z. One then immediately finds that $J'' \sum_{\mathbf{r},z} \vec{S}_{\mathbf{r},z} \cdot \vec{S}_{\mathbf{r},z+1}$ is minimized by $\varphi_z = \varphi + \pi z$, in agreement with earlier spin-wave[133] and Monte Carlo[125] studies.

We acknowledge useful conversations with L. Balents and C. Batista. This work is supported by DOE grant DE-FG02-ER46900 (AC) and NSF grant DMR-12-06774 (OAS and WJ).

Here we present technical details of calculations reported in the manuscript. All calculations were carried out in one-sublattice and in three-sublattice basis, and led to identical results. For definiteness, we present the details of calculations in the one-sublattice basis.

3.1.8 The Hamiltonian and the expansion in bosons

We consider Heisenberg Hamiltonian of 2D triangular lattice (Eq. (3) of the main text), and expand it to sixth order in Holstein Primakoff bosons around the ferromagnetic state, which holds at $h > h_{sat}$. We then move to fields below the saturation value by introducing magnon condensates and using the technique of dilute Bose-gas expansion.

The Hamiltonian in terms of Holstein Primakoff bosons has the form

$$\begin{aligned}
\mathcal{H} &= \mathcal{H}^{(2)} + \mathcal{H}^{(4)} + \mathcal{H}^{(6)}, \\
\mathcal{H}^{(2)} &= \sum_{\mathbf{k}} (\omega_{\mathbf{k}} - \mu) a^{\dagger}_{\mathbf{k}} a_{\mathbf{k}}, \qquad (3.16) \\
\mathcal{H}^{(4)} &= \frac{1}{2N} \sum_{\mathbf{k},\mathbf{k}',\mathbf{q}} V_{\mathbf{q}}(\mathbf{k},\mathbf{k}') a^{\dagger}_{\mathbf{k}+\mathbf{q}} a^{\dagger}_{\mathbf{k}'-\mathbf{q}} a_{\mathbf{k}'} a_{\mathbf{k}}, \qquad (3.17) \\
\mathcal{H}^{(6)} &= \frac{1}{16\mathrm{SN}^2} \sum_{\mathbf{k},\mathbf{k}',\mathbf{k}'',\mathbf{q},\mathbf{p}} U_{\mathbf{q},\mathbf{p}}(\mathbf{k},\mathbf{k}',\mathbf{k}'') a^{\dagger}_{\mathbf{k}+\mathbf{q}+\mathbf{p}} a^{\dagger}_{\mathbf{k}'-\mathbf{q}} a^{\dagger}_{\mathbf{k}''-\mathbf{p}} a_{\mathbf{k}''} a_{\mathbf{k}'} a_{\mathbf{k}}. \qquad (3.18)
\end{aligned}$$

Here, $a, a^{\dagger}$ are boson operators, ω_k is the magnon dispersion, $\mu = h_{\mathrm{sat}} - h$ is the chemical potential, and $V_{\mathbf{q}}(\mathbf{k},\mathbf{k}'), U_{\mathbf{q},\mathbf{p}}(\mathbf{k},\mathbf{k}',\mathbf{k}'')$ are 2- and 3-body interaction potentials which we

list below separately for isotropic and anisotropic models. Both $\omega_{\mathbf{k}}$ and h_{sat} are of order S, and we consider μ also of order S.

3.1.8.1 Isotropic Heisenberg model

In the isotropic case

$$\begin{aligned}
\omega_{\mathbf{k}} &= S(J_{\mathbf{k}} - J_{\mathbf{Q}}), && (3.19)\\
V_{\mathbf{q}}(\mathbf{k},\mathbf{k}') &= \frac{1}{2}[J_{\mathbf{k}-\mathbf{k}'+\mathbf{q}} + J_{\mathbf{q}} - \frac{1}{2}(J_{\mathbf{k}+\mathbf{q}} + J_{\mathbf{k}'-\mathbf{q}} + J_{\mathbf{k}} + J_{\mathbf{k}'})], && (3.20)\\
U_{\mathbf{q},\mathbf{p}}(\mathbf{k},\mathbf{k}',\mathbf{k}'') &= \frac{1}{9}\Big(J_{\mathbf{k}+\mathbf{q}} + J_{\mathbf{k}''+\mathbf{q}} + J_{\mathbf{k}+\mathbf{k}''-\mathbf{k}'+\mathbf{q}} + J_{\mathbf{k}+\mathbf{p}} + J_{\mathbf{k}'+\mathbf{p}} + J_{\mathbf{k}+\mathbf{k}'-\mathbf{k}''+\mathbf{p}} \\
&\quad + J_{\mathbf{k}'+\mathbf{k}''-\mathbf{k}-\mathbf{q}-\mathbf{p}} + J_{\mathbf{k}''-\mathbf{q}-\mathbf{p}} + J_{\mathbf{k}''-\mathbf{q}-\mathbf{p}}\Big) \\
&\quad - \frac{1}{6}\Big(J_{\mathbf{k}+\mathbf{q}+\mathbf{p}} + J_{\mathbf{k}'-\mathbf{q}} + J_{\mathbf{k}''-\mathbf{p}} + J_{\mathbf{k}} + J_{\mathbf{k}'} + J_{\mathbf{k}''}\Big). && (3.21)
\end{aligned}$$

where $J_{\mathbf{k}} = 2J(\cos[k_x] + 2\cos[\frac{k_x}{2}]\cos[\frac{\sqrt{3}k_y}{2}])$, with its minimum $J_{\mathbf{Q}}$ at $\mathbf{Q} = (Q_0, 0)$, and $Q_0 = 4\pi/3$.

3.1.8.2 Anisotropic J-J' model

In this model, $\omega_{\mathbf{k}}$, $V_{\mathbf{q}}(\mathbf{k},\mathbf{k}')$, and $U_{\mathbf{q},\mathbf{p}}(\mathbf{k},\mathbf{k}',\mathbf{k}'')$ are all in the same form as $J_{\mathbf{k}}$ above, except replacing all $J_{\mathbf{k}}$ with $\tilde{J}_{\mathbf{k}}$, where $\tilde{J}_{\mathbf{k}} = 2(J\cos[k_x] + 2J'\cos[\frac{k_x}{2}]\cos[\frac{\sqrt{3}k_y}{2}])$. $\tilde{J}_{\mathbf{k}}$ has minimum $\tilde{J}_{\mathbf{Q}}$ at $\mathbf{Q} = (Q_{\mathrm{i}}, 0)$, and $Q_{\mathrm{i}} = 2\cos^{-1}[-J'/2J]$.

3.1.8.3 XXZ model

In this model, $\omega_{\mathbf{k}}$ is same as Eq.(3.19), and $U_{\mathbf{q},\mathbf{p}}(\mathbf{k},\mathbf{k}',\mathbf{k}'')$ is same as Eq.(3.21). The difference comes from $V_{\mathbf{q}}(\mathbf{k},\mathbf{k}')$, which now contains the exchange anisotropy in the z direction:

$$V_{\mathbf{q}}(\mathbf{k},\mathbf{k}') = \frac{1}{2}\Big[J^z_{\mathbf{k}-\mathbf{k}'+\mathbf{q}} + J^z_{\mathbf{q}} - \frac{1}{2}(J_{\mathbf{k}+\mathbf{q}} + J_{\mathbf{k}'-\mathbf{q}} + J_{\mathbf{k}} + J_{\mathbf{k}'})\Big], \tag{3.22}$$

where $J^z_{\mathbf{k}} = 2J^z(\cos[k_x] + 2\cos[\frac{k_x}{2}]\cos[\frac{\sqrt{3}k_y}{2}])$. The minimum of $J^z_{\mathbf{k}}$ is at $\mathbf{k} = (Q_0, 0)$.

3.1.9 Calculation of $\Gamma_1, \Gamma_2, \Gamma_3$

We follow[128] and split magnon operators into condensate and noncondensate fractions as

$$a_{\mathbf{k}} = \sqrt{N}\psi_1\delta_{\mathbf{k},\mathbf{Q}} + \sqrt{N}\psi_2\delta_{\mathbf{k},-\mathbf{Q}} + \tilde{a}_{\mathbf{k}}, \tag{3.23}$$

where $\psi_{1,2}$ describe condensates at momenta $\mathbf{k} = \mathbf{Q}$ and $\mathbf{k} = -\mathbf{Q}$, and $\tilde{a}_{\mathbf{k}}$ describes noncondensate magnons. The ground state energy density reads

$$E_0/N = -\mu(|\psi_1|^2 + |\psi_2|^2) + \frac{1}{2}\Gamma_1(|\psi_1|^4 + |\psi_2|^4) + \Gamma_2|\psi_1|^2|\psi_2|^2 + \Gamma_3((\bar{\psi}_1\psi_2)^3 + \mathbf{h.c.}) \quad (3.24)$$

The classical expressions for Γ_1 and Γ_2 (the ones at order $1/S^0$) are obtained by neglecting all noncondensate modes and are shown schematically in **Figure 3.3**. These contributions are related to potential $V_{\mathbf{q}}(\mathbf{k}, \mathbf{k}')$ via

$$\Gamma_1^{(0)} = V_{\mathbf{0}}(\mathbf{Q}, \mathbf{Q}), \quad (3.25)$$

$$\Gamma_2^{(0)} = V_{\mathbf{0}}(\mathbf{Q}, -\mathbf{Q}) + \mathbf{V_{2Q}}(-\mathbf{Q}, \mathbf{Q}). \quad (3.26)$$

The classical expression for Γ_3 (at order $1/S$) is shown schematically in **Figure 3.3** and it is related to potential $V_{\mathbf{q}}(\mathbf{k}, \mathbf{k}')$ and $U_{\mathbf{q},\mathbf{p}}(\mathbf{k}, \mathbf{k}', \mathbf{k}'')$ via

$$\Gamma_3^{(1)} = \frac{U_{2\mathbf{Q},2\mathbf{Q}}(\mathbf{Q}, \mathbf{Q}, \mathbf{Q})}{16S} - \frac{[\mathrm{V}_{2\mathbf{Q}}(\mathbf{Q}, \mathbf{Q})]^{\mathbf{2}}}{\omega_{3\mathbf{Q}}}. \quad (3.27)$$

Here the first term comes directly from the Hamiltonian (3.18), and the second one originates from the condensate $\psi_0 \equiv \langle \tilde{a}_0 \rangle \neq 0$, which is induced at the momentum $\mathbf{k} = 3\mathbf{Q} = 0$ in the case of *commensurate* ordering at wave vector $\mathbf{Q} = (4\pi/3_0, 0)$. This novel condensate adds the term $|\psi_0|^2\omega_{\mathbf{0}} + V_{2\mathbf{Q}}(\mathbf{Q}, \mathbf{Q})(\psi_0(\bar{\psi}_1\psi_2^2 + \psi_1^2\bar{\psi}_2) + \mathbf{h.c})$ to the ground state energy. Minimizing this extra energy contribution, we find the expression for ψ_0

$$\psi_0 = -\frac{V_{2\mathbf{Q}}(\mathbf{Q}, \mathbf{Q})}{\omega_0}(\bar{\psi}_1\psi_2^2 + \psi_1^2\bar{\psi}_2) = \frac{1}{4\mathrm{S}}(\bar{\psi}_1\psi_2^2 + \psi_1^2\bar{\psi}_2). \quad (3.28)$$

It is important to keep in mind that this result is derived for $\mathbf{Q} = (4\pi/3_0, 0)$, when $e^{i3\mathbf{Q}\cdot\mathbf{r}} = 1$ for all sites of the triangular lattice $\mathbf{r}$.

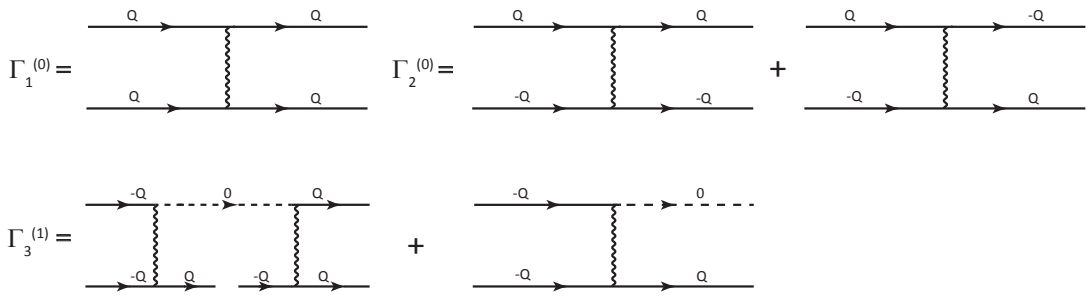

Figure 3.3. Diagrams for Γ_1 ,Γ_2, and Γ_3 in the classical limit.

The expressions for $\Gamma_1^{(0)}, \Gamma_2^{(0)}$, and $\Gamma_3^{(1)}$ are different in the isotropic case and in the two anisotropic cases.

For the isotropic model,

$$\Gamma_1^{(0)} = J_{\mathbf{0}} - J_{\mathbf{Q}}, \Gamma_2^{(0)} = J_{\mathbf{0}} + J_{2\mathbf{Q}} - J_{\mathbf{Q}},$$
$$\Gamma_3^{(1)} = 0. \tag{3.29}$$

For $J - J'$ model,

$$\Gamma_2^{(0)} - \Gamma_1^{(0)} = \tilde{J}_{2\mathbf{Q}} - \tilde{J}_{\mathbf{Q}} = J(2 + \frac{J'}{J})^2(1 - \frac{J'}{J})^2 \approx \frac{9(\delta J)^2}{J},$$
$$\Gamma_3^{(1)} = 0. \tag{3.30}$$

For XXZ model,

$$\Gamma_2^{(0)} - \Gamma_1^{(0)} = J_{2\mathbf{Q}}^z - J_{\mathbf{Q}} = 3J\Delta,$$
$$\Gamma_3^{(1)} = \frac{J_{\mathbf{0}} - J_{\mathbf{Q}}}{16S} - \frac{(4J_{\mathbf{Q}}^z - 3J_{\mathbf{Q}} - J_{\mathbf{0}})^2}{16S(J_{\mathbf{0}} - J_{\mathbf{Q}})} = \frac{J}{2S}(1 + \frac{J_z}{J})(1 - \frac{J_z}{J}) \approx \frac{3J\Delta}{2S}. \tag{3.31}$$

3.1.10 Quantum corrections to $\Gamma_1, \Gamma_2, \Gamma_3$

In this section, we compute quantum corrections to $\Gamma_1, \Gamma_2, \Gamma_3$. Because these corrections already contain extra factor of $1/S$, they can be calculated by neglecting anisotropy. Quantum corrections to $\Gamma_{1,2}$ are of order $1/S$, and quantum corrections to Γ_3 are of order $(1/S)^2$. In both cases, the quantum term has the extra factor $1/S$ compared to classical results. Each quantum correction is a sum of the two terms – one comes from normal ordering of Holstein-Primakoff bosons, and the other from second- and third-order terms in the perturbation expansion in $1/S$.

3.1.10.1 Corrections from normal ordering

The Holstein-Primakoff transformation

$$S^z(r) = S - a_{\mathbf{r}}^+ a_{\mathbf{r}}, S^+ = \sqrt{2S - a_{\mathbf{r}}^+ a_{\mathbf{r}}} a_{\mathbf{r}}, S^- = \sqrt{2S} a_{\mathbf{r}}^+ \sqrt{2S - a_{\mathbf{r}}^+ a_{\mathbf{r}}} \tag{3.32}$$

contains the square-root $\sqrt{2S - a_{\mathbf{r}}^+ a_{\mathbf{r}}}$, which needs to be expanded in the *normal-ordered* form to perform dilute gas analysis (all $a_{\mathbf{r}}^+$ have to stand to the left of $a_{\mathbf{r}}$). Because $a_{\mathbf{r}}^+ a_{\mathbf{r}} =$

$a_{\mathbf{r}}a_{\mathbf{r}}^{+}-1$, i.e., $(a_{\mathbf{r}}^{+}a_{\mathbf{r}})^2 = a_{\mathbf{r}}^{+}a_{\mathbf{r}}^{+}a_{\mathbf{r}}a_{\mathbf{r}} + a_{\mathbf{r}}^{+}a_{\mathbf{r}}$, etc, the prefactors in this *normal-ordering* are not simply powers of $1/S$ but rather contain series of $1/S$ terms. To order $1/S^3$ we have

$$S_{\mathbf{r}}^{-} = \sqrt{2S}a_{\mathbf{r}}^{+}\Big\{1 - \frac{1}{4S}(1+\frac{1}{8S}+\frac{1}{32S^2})a_{\mathbf{r}}^{+}a_{\mathbf{r}} - \frac{1}{32S^2}(1+\frac{3}{4S})a_{\mathbf{r}}^{+}a_{\mathbf{r}}^{+}a_{\mathbf{r}}a_{\mathbf{r}} - \frac{a_{\mathbf{r}}^{+}a_{\mathbf{r}}^{+}a_{\mathbf{r}}^{+}a_{\mathbf{r}}a_{\mathbf{r}}a_{\mathbf{r}}}{128S^3} + O(1/S^4)\Big\}$$

The $1/S$ corrections to the prefactors modify Eqs.(3.17) and (3.18) to

$$\begin{aligned}
\delta\mathcal{H}^{(4)} &= -\frac{J}{32S}\sum_{r,\delta}(a_r^{\dagger}a_r^{\dagger}a_r a_{r+\delta} + \mathbf{h.c}),\\
\delta\mathcal{H}^{(6)} &= \frac{J}{128S^2}\sum_{r,\delta}(a_r^{\dagger}a_{r+\delta}^{\dagger}a_{r+\delta}^{\dagger}a_r a_r a_{r+\delta} + \boldsymbol{h}.c) - \frac{3J}{128S^2}\sum_{r,\delta}(a_r^{\dagger}a_r^{\dagger}a_{r+\delta}^{\dagger}a_r a_r a_r + \mathbf{h.c}).
\end{aligned} \tag{3.33}$$

Substituting the form of the condensate in real space

$$\langle a_{\mathbf{r}}\rangle = \frac{1}{\sqrt{N}}\sum_{\mathbf{k}} e^{i\mathbf{k}\cdot\mathbf{r}}\langle a_{\pm\mathbf{Q}}\rangle = \psi_1 e^{i\mathbf{Q}\cdot\mathbf{r}} + \psi_2 e^{-i\mathbf{Q}\cdot\mathbf{r}}. \tag{3.34}$$

we obtain $1/S$ corrections to classical expressions for $\Gamma_{1,2,3}$:

$$\begin{aligned}
\Delta\Gamma_a^{(1)} &= \Gamma_{2a}^{(1)} - \Gamma_{1a}^{(1)} = (-\frac{J_{\mathbf{Q}}}{4S}) - (-\frac{J_{\mathbf{Q}}}{8S}) = \frac{3J}{8S},\\
\Gamma_{3a}^{(2)} &= \frac{5J_{\mathbf{0}}}{128S^2} + \frac{J_{\mathbf{0}}}{128S^2} = \frac{9J}{32S^2}.
\end{aligned} \tag{3.35}$$

3.1.10.2 Corrections from quantum fluctuations

To find quantum corrections to parameters $\Gamma_{1,2,3}$, we evaluate corrections to the ground state energy density δE from non condensed modes $\tilde{a}_{\mathbf{k}}$ in (3.23) in perturbation theory up to third order and obtain the correction to the ground state energy density ΔE to sixth order in the condensates ψ_1 and ψ_2. The prefactors for the ψ^4 and ψ^6 term in ΔE yield quantum corrections to interaction parameters $\Gamma_{1,2,3}$.

Quite generally, under perturbation H_i, the partition function is

$$Z = \int\prod_{\mathbf{k}} da_{\mathbf{k}}^{\dagger}da_{\mathbf{k}} e^{\int_0^{\beta}d\tau(L_0-H_i)} = Z_0\frac{\int\prod_{\mathbf{k}} da_{\mathbf{k}}^{\dagger}da_{\mathbf{k}} e^{\int_0^{\beta}d\tau(L_0-H_i)}}{\int\prod_{\mathbf{k}} da_{\mathbf{k}}^{\dagger}da_{\mathbf{k}} e^{\int_0^{\beta}L_0}} \equiv Z_0\langle e^{-\int_0^{\beta}H_i}\rangle_0. \tag{3.36}$$

Here $L_0 = \sum_k(a_k^{\dagger}\frac{\partial}{\partial\tau}a_k) - \mathcal{H}^{(2)}$ represents Lagrangian of noninteracting magnons described by the quadratic Hamiltonian (3.6), and $\beta = 1/T$. The internal energy density is

$$E = -\frac{\partial\ln Z}{\partial\beta} \approx -\frac{\partial\ln Z_0}{\partial\beta} - \frac{\partial(\beta\ln\langle e^{-H_i}\rangle)}{\partial\beta} = E_0 + \Delta E \tag{3.37}$$

The correction term ΔE is represented by the standard cumulant expansion, which involves only connected averages of the perturbation H_i

$$\Delta E = \langle H_i\rangle_0 - \frac{1}{2!}\langle\int_{\tau}H_i^2\rangle_0 + \frac{1}{3!}\langle\int_{\tau}\int_{\tau'}H_i^3\rangle_0 + \ldots. \tag{3.38}$$

In the the zero-temperature limit, in which all our calculations are done, $E = E_0 + \Delta E$ determines the ground state energy. Integration over relative times $\tau, \tau' \ldots$ ensures conservation of frequencies in the internal vertices of the diagrams. The role of the perturbation H_i is played by interacting Hamiltonians (3.17), (3.18) expressed in terms of condensates $\psi_{1,2}$ and noncondensed magnons $\tilde{a}_{\mathbf{k}}$ after the substitution (3.23). We recall that the averaging is over the free-boson Hamiltonian for isotropic system at $h = h_{sat}$.

3.1.10.2.1 Quantum corrections to $\Gamma_{1,2}$. Quantum corrections to $\Gamma_{1,2}$ al of order $1/S$, and to get them we only need the fourth-order term in bosons (3.17):

$$\begin{aligned}\mathcal{H}_{\mathrm{i},\mathbf{k}} = \sum_{\mathbf{k}} \Big[\Big(\frac{1}{2} V_{\mathbf{k}}(\mathbf{Q},\mathbf{Q}) \psi_1^2 a^\dagger_{\mathbf{Q}+\mathbf{k}} a^\dagger_{\mathbf{Q}-\mathbf{k}} + V_{\mathbf{k}}(\mathbf{Q},-\mathbf{Q}) \psi_1 \psi_2 a^\dagger_{\mathbf{Q}+\mathbf{k}} a^\dagger_{-\mathbf{Q}-\mathbf{k}} + \\ \frac{1}{2} V_{\mathbf{k}}(-\mathbf{Q},-\mathbf{Q}) \psi_2^2 a^\dagger_{-\mathbf{Q}+\mathbf{k}} a^\dagger_{-\mathbf{Q}-\mathbf{k}} \Big) + \mathbf{h.c.} \Big],\end{aligned} \tag{3.39}$$

where $V_{\mathbf{q}}(k,k')$ is defined in Eq.(3.20). The first-order correction to the energy density obviously vanishes, and the second-order perturbative correction yields

$$\begin{aligned}\Delta E &= -\frac{1}{2} \sum_{\mathbf{k},\mathbf{q}} \langle \mathcal{H}_{\mathrm{i},\mathbf{k}} \cdot \mathcal{H}_{\mathrm{i},\mathbf{q}} \rangle_0 \\ &= -\sum_{\mathbf{k},\mathbf{q}} \Big[\frac{1}{4} |\psi_1|^4 V_{\mathbf{k}}(\mathbf{Q},\mathbf{Q}) V_{\mathbf{q}}(\mathbf{Q},\mathbf{Q}) \langle a^\dagger_{\mathbf{Q}+\mathbf{k}} a^\dagger_{\mathbf{Q}-\mathbf{k}} a_{\mathbf{Q}+\mathbf{q}} a_{\mathbf{Q}-\mathbf{q}} \rangle_0 \\ &\quad + \frac{1}{4} |\psi_2|^4 V_{\mathbf{k}}(-\mathbf{Q},-\mathbf{Q}) V_{\mathbf{q}}(-\mathbf{Q},-\mathbf{Q}) \langle a^\dagger_{-\mathbf{Q}+\mathbf{k}} a^\dagger_{-\mathbf{Q}-\mathbf{k}} a_{-\mathbf{Q}+\mathbf{q}} a_{-\mathbf{Q}-\mathbf{q}} \rangle_0 \\ &\quad + \frac{1}{2} |\psi_1|^2 |\psi_2|^2 V_{\mathbf{k}}(\mathbf{Q},-\mathbf{Q}) V_{\mathbf{q}}(\mathbf{Q},-\mathbf{Q}) \langle a^\dagger_{\mathbf{Q}+\mathbf{k}} a^\dagger_{-\mathbf{Q}-\mathbf{k}} a_{\mathbf{Q}+\mathbf{q}} a_{-\mathbf{Q}-\mathbf{q}} \rangle_0 \Big].\end{aligned} \tag{3.40}$$

By Wick's theorem,

$$\langle a^\dagger_{k_1} a^\dagger_{k_2} a_{k_3} a_{k_4} \rangle_0 = \langle a^\dagger_{k_1} a_{k_3} \rangle_0 \langle a^\dagger_{k_2} a_{k_4} \rangle_0 + \langle a^\dagger_{k_1} a_{k_4} \rangle_0 \langle a^\dagger_{k_2} a_{k_3} \rangle_0. \tag{3.41}$$

where the pair average is[134]

$$\langle a^\dagger_{k_1} a_{k_2} \rangle_0 = -\delta_{k_1,k_2} G_0(k_1), \tag{3.42}$$

and $G_0(k) \equiv G_0(k,\epsilon)$ is the free boson Green's function

$$G_0(k) = (i\omega_k - \epsilon)^{-1}, \tag{3.43}$$

Utilizing the properties of (3.41) and (3.42), we obtain the terms in the form

$$\sum_{\mathbf{k},\mathbf{q}} V_{\mathbf{k}}(\mathbf{Q},\mathbf{Q}) V_{\mathbf{q}}(\mathbf{Q},\mathbf{Q}) \langle a^\dagger_{\mathbf{Q}+\mathbf{k}} a^\dagger_{\mathbf{Q}-\mathbf{k}} a_{\mathbf{Q}+\mathbf{q}} a_{\mathbf{Q}-\mathbf{q}} \rangle_0 = \sum_{\mathbf{k},!} \frac{2V_{\mathbf{k}}^2(\mathbf{Q},\mathbf{Q})}{(i\omega - \epsilon_{\mathbf{Q}+\mathbf{k}})(i\omega - \epsilon_{\mathbf{Q}-\mathbf{k}})} \tag{3.44}$$

Using

$$\text{with } \sum_{!} \frac{1}{(i\omega-\epsilon_1)(i\omega-\epsilon_2)} = \int \frac{d\omega}{2\pi} \frac{1}{(i\omega-\epsilon_1)(i\omega-\epsilon_2)} = \frac{1}{\epsilon_1+\epsilon_2} \tag{3.45}$$

and collecting prefactors we obtain the corrections to $\Gamma_{1,2}$ in the form

$$\begin{aligned}
\Gamma_{1b}^{(1)} &= -\sum_{\mathbf{k}} \frac{V_{\mathbf{k}}^2(\mathbf{Q},\mathbf{Q})}{\omega_{\mathbf{Q}+\mathbf{k}}+\omega_{\mathbf{Q}-\mathbf{k}}} = -\frac{1}{16S}\sum_{\mathbf{k}} \frac{(J_0+5J_{\mathbf{k}})^2}{J_0-J_{\mathbf{k}}}, \\
\Gamma_{2b}^{(1)} &= -\sum_{\mathbf{k}} \frac{V_{\mathbf{k}}^2(\mathbf{Q},-\mathbf{Q})}{\omega_{\mathbf{Q}+\mathbf{k}}} = -\frac{1}{16S}\sum_{\mathbf{k}} \frac{(J_0-4J_{\mathbf{Q}+\mathbf{k}})^2}{J_{\mathbf{Q}+\mathbf{k}}-J_{\mathbf{k}}}.
\end{aligned} \tag{3.46}$$

These corrections can be equally obtained diagrammatically, by evaluating second-order corrections to ϕ^4 vertices, as in **Figure 3.4**.

Each of the two integrals above is logarithmically divergent, but these divergences cancel out in their difference, resulting in a finite result

$$\Delta\Gamma_b^{(1)} = \Gamma_{2b}^{(1)} - \Gamma_{1b}^{(1)} = -\frac{1.97J}{S}. \tag{3.47}$$

3.1.10.2.2 Quantum corrections to Γ_3. Correction to Γ_3 is in order of $(1/S)^2$, and to get such a term in the ground state energy density we need to include both four-boson and six-boson terms in the Hamiltonian, Eqs. (3.17) and (3.18). We have

$$\begin{aligned}
\mathcal{H}_{\rm i}^{(4)} &= \frac{1}{8}\sum_{\mathbf{k}}(5J_{\mathbf{k}}-2J_{\mathbf{Q}})\Big[(\bar{\psi_1^2}a_{\mathbf{Q}+\mathbf{k}}a_{\mathbf{Q}-\mathbf{k}}+\bar{\psi_2^2}a_{-\mathbf{Q}+\mathbf{k}}a_{-\mathbf{Q}-\mathbf{k}})+\mathbf{h.c.}\Big] \\
&\quad -\frac{1}{4}\sum_{\mathbf{k}}(J_{\mathbf{k}}-J_{\mathbf{Q}})\Big[(\psi_0\psi_2 a^\dagger_{\mathbf{Q}+\mathbf{k}}a^\dagger_{\mathbf{Q}-\mathbf{k}}+\psi_0\psi_1 a^\dagger_{-\mathbf{Q}+\mathbf{k}}a^\dagger_{-\mathbf{Q}-\mathbf{k}})+\mathbf{h.c.}\Big], \qquad (3.48) \\
\mathcal{H}_{\rm i}^{(6)} &= \frac{1}{16S}\sum_{\mathbf{k}}(\frac{5}{2}J_{\mathbf{k}}-4J_{\mathbf{Q}})\Big[(\bar{\psi_1}\psi_2^3 a^\dagger_{\mathbf{Q}+\mathbf{k}}a^\dagger_{\mathbf{Q}-\mathbf{k}}+\psi_1^3\bar{\psi_2}a^\dagger_{-\mathbf{Q}+\mathbf{k}}a^\dagger_{-\mathbf{Q}-\mathbf{k}})+\mathbf{h.c.}\Big]. \qquad (3.49)
\end{aligned}$$

We use the expression of ψ_0 in Eq.(3.28), to rewrite $\mathcal{H}_{\rm i}^{(4)}$ as,

$$\begin{aligned}
\mathcal{H}_{\rm i}^{(4)} &= \frac{1}{8}\sum_{\mathbf{k}}(5J_{\mathbf{k}}-2J_{\mathbf{Q}})\Big[(\bar{\psi_1^2}a_{\mathbf{Q}+\mathbf{k}}a_{\mathbf{Q}-\mathbf{k}}+\bar{\psi_2^2}a_{-\mathbf{Q}+\mathbf{k}}a_{-\mathbf{Q}-\mathbf{k}})+\mathbf{h.c.}\Big] \\
&\quad -\frac{1}{16S}\sum_{\mathbf{k}}(J_{\mathbf{k}}-J_{\mathbf{Q}})\Big[(\bar{\psi_1}\psi_2^3 a^\dagger_{\mathbf{Q}+\mathbf{k}}a^\dagger_{\mathbf{Q}-\mathbf{k}}+\psi_1^3\bar{\psi_2}a^\dagger_{-\mathbf{Q}+\mathbf{k}}a^\dagger_{-\mathbf{Q}-\mathbf{k}})+\mathbf{h.c.}\Big]. \qquad (3.50)
\end{aligned}$$

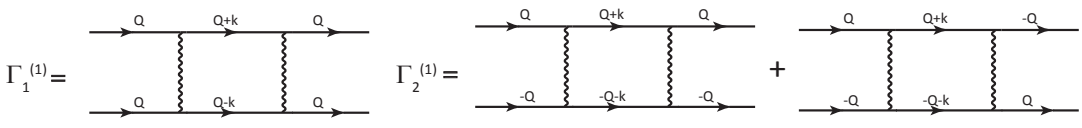

Figure 3.4. Diagrams for perturbative corrections to Γ_1 and Γ_2 .

The total perturbation Hamiltonian is now

$$\begin{aligned}\mathcal{H}_{\mathrm{i},\mathbf{k}} &= \mathcal{H}_{\mathrm{i}}^{(4)} + \mathcal{H}_{\mathrm{i}}^{(6)} \\ &= \frac{1}{8}\sum_{\mathbf{k}}(5J_{\mathbf{k}} - 2J_{\mathbf{Q}})\Big[(\bar{\psi}_1^2 a_{\mathbf{Q}+\mathbf{k}} a_{\mathbf{Q}-\mathbf{k}} + \bar{\psi}_2^2 a_{-\mathbf{Q}+\mathbf{k}} a_{-\mathbf{Q}-\mathbf{k}}) + \mathbf{h.c.}\Big] \\ &\quad -\frac{3}{32S}\sum_{\mathbf{k}}(J_{\mathbf{k}} - 2J_{\mathbf{Q}})\Big[(\bar{\psi}_1\psi_2^3 a^\dagger_{\mathbf{Q}+\mathbf{k}} a^\dagger_{\mathbf{Q}-\mathbf{k}} + \psi_1^3\bar{\psi}_2 a^\dagger_{-\mathbf{Q}+\mathbf{k}} a^\dagger_{-\mathbf{Q}-\mathbf{k}}) + \mathbf{h.c.}\Big], \quad (3.51)\end{aligned}$$

Because of two terms in (3.51), there are two contributions to ΔE to order ψ^6/S^2. One comes from taking the product of ψ^2 and ψ^4 terms in the second-order perturbation theory. This yields

$$\begin{aligned}\Delta E_a &= -\frac{1}{2}\sum_{\mathbf{k},\mathbf{q}}\langle \mathcal{H}_{\mathrm{i},\mathbf{k}} \cdot \mathcal{H}_{\mathrm{i},\mathbf{q}}\rangle_0 = -\frac{3}{128S}\sum_{\mathbf{k},\mathbf{q}}(5J_{\mathbf{k}} - 2J_{\mathbf{Q}})(J_{\mathbf{q}} - 2J_{\mathbf{Q}}) \times \\ &\times \quad \Big[\psi_1^3\bar{\psi}_2^3\langle a^\dagger_{\mathbf{Q}+\mathbf{k}} a^\dagger_{\mathbf{Q}-\mathbf{k}} a_{\mathbf{Q}+\mathbf{q}} a_{\mathbf{Q}-\mathbf{q}}\rangle_0 + \bar{\psi}_1^3\psi_2^3\langle a^\dagger_{-\mathbf{Q}+\mathbf{k}} a^\dagger_{-\mathbf{Q}-\mathbf{k}} a_{-\mathbf{Q}+\mathbf{q}} a_{-\mathbf{Q}-\mathbf{q}}\rangle_0\Big] \quad (3.52)\end{aligned}$$

and

$$\Delta\Gamma^{(2)}_{3,a} = -\frac{3}{64S^2}\sum_{\mathbf{k}}\frac{(5J_{\mathbf{k}} - 2J_{\mathbf{Q}})(J_{\mathbf{k}} - 2J_{\mathbf{Q}})}{J_{\mathbf{0}} - J_{\mathbf{k}}}. \quad (3.53)$$

Diagrammatically, this correction to Γ_3 is given by the first two diagrams in **Figure 3.5**.

Another contribution to ΔE of order ψ^6/S^3 comes from taking ψ^2 term in (3.51) to third order in perturbation theory. The corresponding term in the perturbative Hamiltonian (3.51) comes from fourth-order term in Holstein-Primakoff bosons and we write it separately:

$$\begin{aligned}\mathcal{H}_{\mathrm{i}}^{(4)} &= \sum_{\mathbf{k}}\Big[\frac{1}{8}(5J_{\mathbf{k}} - 2J_{\mathbf{Q}})(\psi_1^2 a^\dagger_{\mathbf{Q}+\mathbf{k}} a^\dagger_{\mathbf{Q}-\mathbf{k}} + \bar{\psi}_2^2 a_{-\mathbf{Q}+\mathbf{k}} a_{-\mathbf{Q}-\mathbf{k}}) + \mathbf{h.c.}\Big] \\ &\quad + \sum_{\mathbf{k}}\frac{3}{2}J_{\mathbf{Q}-\mathbf{k}}(\psi_1\bar{\psi}_2 a^\dagger_{\mathbf{k}} a_{\mathbf{Q}+\mathbf{k}} + \mathbf{h.c.}). \quad (3.54)\end{aligned}$$

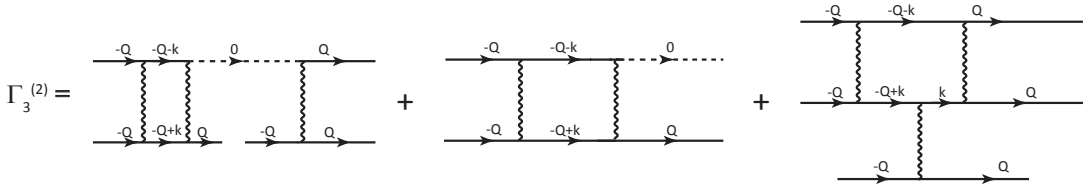

Figure 3.5. Diagrams for $1/S$ corrections to Γ_3. The first two diagrams are second-order perturbation corrections from the product of ψ^2 and ψ^4 terms in Eq. (3.51). The last diagram is third-order perturbative correction from (3.52).

The third-order perturbative correction to the ground state density is

$$\Delta E_b = \frac{1}{3!}\sum_{\mathbf{k},\mathbf{q},\mathbf{l}} \langle \mathcal{H}_{\mathrm{i},\mathbf{k}} \cdot \mathcal{H}_{\mathrm{i},\mathbf{q}} \cdot \mathcal{H}_{\mathrm{i},\mathbf{l}} \rangle_0$$
$$= \frac{3}{128}\sum_{\mathbf{k},\mathbf{q},\mathbf{l}} \frac{3}{2} J_{\mathbf{Q}-\mathbf{k}}(5J_{\mathbf{q}} - 2J_{\mathbf{Q}})(5J_{\mathbf{l}} - 2J_{\mathbf{Q}})(\psi_1^3\bar{\psi}_2^3 + \mathbf{h.c.})\langle a_{\mathbf{k}}^\dagger a_{\mathbf{Q}+\mathbf{q}}^\dagger a_{\mathbf{Q}-\mathbf{q}}^\dagger a_{\mathbf{Q}+\mathbf{k}} a_{-\mathbf{Q}+\mathbf{l}} a_{-\mathbf{Q}-\mathbf{l}}\rangle_0. \tag{3.55}$$

This leads to second $1/S^2$ contribution to Γ_3 in the form

$$\Gamma_{3b}^{(2)} = \frac{3}{32S^2}\sum_{\mathbf{k}} \frac{J_{\mathbf{Q}-\mathbf{k}}(5J_{\mathbf{k}} + J_0)(5J_{\mathbf{Q}+\mathbf{k}} + J_0)}{(J_0 - J_{\mathbf{k}})(J_0 - J_{\mathbf{Q}+\mathbf{k}})}. \tag{3.56}$$

In diagrammatic approach, this correction comes from the third diagram in **Figure 3.5**.

The total $\Gamma_3^{(2)}$ is the sum of terms in Eqs.(3.53) and Eq.(3.56)

$$\Gamma_3^{(2)} = \frac{3}{32S^2}\sum_{\mathbf{k}} \Big(\frac{J_{\mathbf{Q}-\mathbf{k}}(5J_{\mathbf{k}} + J_0)(5J_{\mathbf{Q}+\mathbf{k}} + J_0)}{(J_0 - J_{\mathbf{k}})(J_0 - J_{\mathbf{Q}+\mathbf{k}})} - \frac{(5J_{\mathbf{k}} + J_0)(J_{\mathbf{k}} + J_0)}{2(J_0 - J_{\mathbf{k}})} \Big) = -\frac{0.97J}{S^2} \tag{3.57}$$

Here again we observe the cancellation of logarithmic singularities, present in the individual integrals.

3.1.11 Intermediate double cone state for $J - J'$ model

In this section, we analyze the phase transition from the cone to the coplanar state, when magnetic field h is below h_{sat}, i.e., $\mu = h_{\mathrm{sat}} - h$ is positive. We recall that at $\mu = 0+$, the cone state is stable at $\delta J = J - J' > \delta J_c = 0.42J/\sqrt{S}$. Accordingly, we treat $\delta J \approx \delta J_c$ as a small parameter.

Our goal will be to obtain the spin-wave spectrum in the cone state to leading order in δJ and with quantum corrections. The magnon modes in the cone state are

$$a_{\mathbf{k}} = \sqrt{N}\psi_1 \delta_{\mathbf{k},\mathbf{Q}} + \tilde{a}_{\mathbf{k}}. \tag{3.58}$$

where, we recall, $\tilde{a}_{\mathbf{k}}$ describe noncondensed bosons and $\psi_1 \propto \sqrt{S}$ describes the condensate fraction.

We first consider classical spin-wave excitations at the leading order in $1/S$, but a non-zero δJ, and then add quantum $1/S$ corrections to the excitation spectrum. As before, the latter already contain $1/S$ and can be computed in the isotropic limit.

3.1.11.1 Classical spin-wave excitations

Spatially anisotropic Hamiltonian to second order in $\tilde{a}_{\mathbf{k}}$ reads

$$\begin{aligned}
\mathcal{H}_{\text{anis}} &= H_1 + H_2 \\
H_1 &= \mathcal{H}^{(2)}_{\text{anis}} = \sum_{\mathbf{k}} \Big[S(\tilde{J}_{\mathbf{k}} - \tilde{J}_{\mathbf{Q}}) - \mu \Big] \tilde{a}^{\dagger}_{\mathbf{k}} \tilde{a}_{\mathbf{k}}, \qquad (3.59) \\
H_2 &= \frac{1}{8} \sum_{\mathbf{q}} \Big[(5\tilde{J}_{\mathbf{q}} - 2\tilde{J}_{\mathbf{Q}}) \psi_1^2 \tilde{a}^{\dagger}_{\mathbf{Q}+\mathbf{q}} \tilde{a}_{\mathbf{Q}-\mathbf{q}} + \mathbf{h.c.} \Big] \\
&\quad + \sum_{\mathbf{k}} (\tilde{J}_{\mathbf{0}} - \tilde{J}_{\mathbf{Q}} + \tilde{J}_{\mathbf{Q}-\mathbf{k}} - \tilde{J}_{\mathbf{k}}) |\psi_1|^2 \tilde{a}^{\dagger}_{\mathbf{k}} \tilde{a}_{\mathbf{k}}, \qquad (3.60)
\end{aligned}$$

where, we recall, $\tilde{J}_{\mathbf{k}}$, where $\tilde{J}_{\mathbf{k}} = 2(J\cos[k_x] + 2J'\cos[\frac{k_x}{2}]\cos[\frac{\sqrt{3}k_y}{2}])$. $\tilde{J}_{\mathbf{k}}$ has minimum $\tilde{J}_{\mathbf{Q}}$ at $\mathbf{Q} = (Q_{\text{i}}, 0)$, and $Q_{\text{i}} = 2\cos^{-1}[-J'/2J]$. At small $\delta J \sim \delta J_c$, $\mathbf{Q}$ by $\mathbf{Q} \approx (4\pi/3 - \Delta Q, 0)$, where $\Delta Q = 4\pi/3 - Q_{\text{i}} = 2\delta J/\sqrt{3}$.

Our goal is to obtain the renormalization of the excitation spectrum ω_k to second order in the condensate, i.e., to order ψ^2. The first term in H_2 is irrelevant for this purpose as it describes excitations with momentum transfer $2\mathbf{Q}$,which can only contribute to ω_k at second order in perturbation theory, but such term will be of order ψ^4. The remaining term in H_2 is quadratic in noncondensed bosons and directly contribute to spin-wave spectrum to second order in ψ.

We will be interested in magnon excitations for $\mathbf{k}$ near $-\mathbf{Q} = -(Q_{\text{i}}, 0)$. Accordingly, we set $\mathbf{k} = -\mathbf{Q} + \mathbf{p}$ and treat $\mathbf{p}$ as small momentum. Restricting with small $\mathbf{p}$ and using the approximate form of $\mathbf{Q}$, we rewrite Eqs.(3.59) and (3.60) as

$$\begin{aligned}
H_1 &= \sum_{\mathbf{p}} \Big[\frac{3}{4} SJ \Big((p_x^2 + p_y^2) + \frac{1}{\sqrt{3}} p_x^2 \Delta Q - \sqrt{3} p_y^2 \Delta Q \Big) - \mu \Big] \tilde{a}^{\dagger}_{-\mathbf{Q}+\mathbf{p}} \tilde{a}_{-\mathbf{Q}+\mathbf{p}}, \qquad (3.61) \\
H_2 &= J \sum_{\mathbf{p}} \Big[\frac{h_{\text{sat}}}{SJ} + \frac{9}{2} p_x \Delta Q + \frac{27}{4} (\Delta Q)^2 \Big] |\psi_1|^2 \tilde{a}^{\dagger}_{-\mathbf{Q}+\mathbf{p}} \tilde{a}_{-\mathbf{Q}+\mathbf{p}}, \qquad (3.62)
\end{aligned}$$

where $h_{\text{sat}} = S(\tilde{J}_{\mathbf{0}} - \tilde{J}_{\mathbf{Q}}) = S\Gamma_1^{(0)}$. Combining the two expressions, we obtain

$$\begin{aligned}
\mathcal{H}_K &= \sum_{\mathbf{p}} S\omega^{(1)}_{\mathbf{k}} \tilde{a}^{\dagger}_{\mathbf{k}} \tilde{a}_{\mathbf{k}}, \\
\omega^{(1)}_{\mathbf{k}} &= \frac{3}{4} J \Big[(1 + \frac{\Delta Q}{\sqrt{3}})(k_x + \bar{Q}_{\text{i}})^2 + k_y^2 + \varepsilon_{\min} \Big], \qquad (3.63) \\
\varepsilon_{\min} &= 9 \frac{|\psi_1|^2}{S} (1 - \frac{|\psi_1|^2}{S}) (\Delta Q)^2 + \frac{4}{3} \frac{1}{SJ} (\frac{|\psi_1|^2}{S} h_{\text{sat}} - \mu), \qquad (3.64)
\end{aligned}$$

where $\bar{Q}_{\rm i} = 4\pi/3 - \Delta Q + 3|\psi_1|^2 \Delta Q/S$. In the cone state $|\psi_1|^2/S = \mu/S\Gamma_1^{(0)} = \mu/h_{\rm sat}$, and $\bar{Q}_{\rm i} = Q_{\rm i} + (4\pi/3 - Q_{\rm i})(3\mu/h_{\rm sat})$. This is the expression that we presented in the main text. Also, Eq.(3.80) becomes

$$\varepsilon_{\rm min} = \frac{12\mu}{h_{\rm sat} J^2} \frac{h}{h_{\rm sat}} (\delta J)^2. \tag{3.65}$$

3.1.11.2 Quantum corrections

Observed that $(\delta J)^2 \sim 1/S$ in (3.81), we need to collect all $1/S$ contributions to $\varepsilon_{\rm min}$.

First of all, in quantum condition, $\Gamma_1 = \Gamma_1^{(0)} + \Gamma_1^{(1)}$, where the second term (with superscript (1)) contains all $1/S$ contributions to Γ_1. Now $|\psi_1|^2/S = \mu/S\Gamma_1$,and Eq.(3.80) becomes,

$$\varepsilon_{\rm min} = \frac{12\mu}{h_{\rm sat} J^2} \frac{h}{h_{\rm sat}} (\delta J)^2 - \frac{4}{3} \frac{\mu}{SJ} \frac{\Gamma_1^{(1)}}{\Gamma_1^{(0)}} + O(1/S^2). \tag{3.66}$$

This gives correction to $\varepsilon_{\rm min}$ in (3.81),

$$\Delta\varepsilon_{\rm min,1} = -\frac{4}{3} \frac{\mu}{h_{\rm sat} J} \Gamma_1^{(1)}. \tag{3.67}$$

Secondly, cone state magnon modes in real space is,

$$a_{\mathbf{r}} = \psi_1 e^{i\mathbf{Q}\cdot\mathbf{r}} + \tilde{a}_{\mathbf{r}}, \tag{3.68}$$

where $\tilde{a}_{\mathbf{r}}$ is noncondensate magnon. Substituting this to Eq.(3.33),

$$\delta\mathcal{H}^{(4)} = -\frac{|\psi_1|^2}{8S} \sum_{\mathbf{k}} (\tilde{J}_{\mathbf{k}} + \tilde{J}_{\mathbf{Q}}) \tilde{a}^\dagger_{\mathbf{k}} \tilde{a}_{\mathbf{k}} \approx -\frac{|\psi_1|^2}{4S} \sum_{\mathbf{p}} \tilde{J}_{\mathbf{Q}} \tilde{a}^\dagger_{-\mathbf{Q}+\mathbf{p}} \tilde{a}_{-\mathbf{Q}+\mathbf{p}}, \tag{3.69}$$

which is a correction to (3.79). This gives the correction to $\varepsilon_{\rm min}$,

$$\Delta\varepsilon_{\rm min,2} = \frac{4}{3} \frac{\mu}{h_{\rm sat} J} \Gamma_{2a}^{(1)}. \tag{3.70}$$

Finally, the expansion of the isotropic Hamiltonian in powers of $\tilde{a}_{\mathbf{k}}$ contain the term with three noncondensate operators and one power of ψ:

$$H_3 = \frac{1}{\sqrt{N}} \sum_{\mathbf{k},\mathbf{q}} V_{\mathbf{q}}(\mathbf{k}, \mathbf{Q}) \left(\psi_1 \tilde{a}^\dagger_{\mathbf{Q}-\mathbf{q}} \tilde{a}^\dagger_{\mathbf{k}+\mathbf{q}} \tilde{a}_{\mathbf{k}} + \mathbf{h.c.} \right). \tag{3.71}$$

This term contributes $1/S$ correction to $\varepsilon_{\rm min}$ in the second-order perturbation theory.

$$\begin{aligned} \Delta\varepsilon_{\rm min,3} &= -\frac{4}{3} \frac{1}{JS} \sum_{\mathbf{q},\mathbf{q}'} V_{\mathbf{q}}(-\mathbf{Q}, \mathbf{Q}) V_{\mathbf{q}'}(-\mathbf{Q}, \mathbf{Q}) |\psi_1|^2 \langle \tilde{a}^\dagger_{\mathbf{Q}-\mathbf{q}} \tilde{a}^\dagger_{-\mathbf{Q}+\mathbf{q}} \tilde{a}_{\mathbf{Q}-\mathbf{q}'} \tilde{a}_{-\mathbf{Q}+\mathbf{q}'} \rangle_0, \\ &= \frac{4}{3} \frac{|\psi_1|^2}{SJ} \Gamma_{2b}^{(1)} \approx \frac{4}{3} \frac{\mu}{h_{\rm sat} J} \Gamma_{2b}^{(1)}. \end{aligned} \tag{3.72}$$

Adding up Eq.(3.82), Eq. (3.84), and Eq.(3.85), we obtain the total correction to $\varepsilon_{\min}$:

$$\Delta\varepsilon_{min} = \frac{4}{3}\frac{\mu}{h_{\rm sat}J}(\Gamma_2^{(1)} - \Gamma_1^{(1)}), \tag{3.73}$$

where $\Gamma_2^{(1)} - \Gamma_1^{(1)} = -1.6J/S$. Combining this with Eq.(3.81), we find that the minimum energy of magnons near $-\mathbf{Q}$ is

$$\varepsilon_{\min} = \frac{12\mu}{h_{\rm sat}J^2}\Big[\frac{h}{h_{\rm sat}}(\delta J)^2 - (\delta J_c)^2\Big] \approx \frac{12\mu}{h_{\rm sat}J^2}\Big[(\delta J)^2 - (\delta J_c)^2(1+\frac{\mu}{h_{\rm sat}})\Big]. \tag{3.74}$$

At $\mu = +0$, magnon energy vanishes at $\delta J = \delta J_c$, as expected, and the instability holds at $\mathbf{k} = -\mathbf{Q}$. However, at a finite μ, the instability occurs at $\delta J = \delta J_c h_{\rm sat}/h > \delta J_c$, and below the instability magnon dispersion becomes unstable at $\mathbf{k} = (-\bar{Q}, 0) \neq -\mathbf{Q}$. This gives rise to the development of the second condensate with momentum different from $-\mathbf{Q}$. The resulting state is the double cone phase described in the main text.

$$H_1 = \sum_{\mathbf{p}}\Big[S(J_{\mathbf{Q}-\mathbf{p}} - J_{\mathbf{Q}}) - \mu\Big]\tilde{a}^\dagger_{-\mathbf{Q}+\mathbf{p}}\tilde{a}_{-\mathbf{Q}+\mathbf{p}}, \tag{3.75}$$

$$H_2 = \sum_{\mathbf{p}}\Big(\frac{h_{sat}}{S} + J_{2\mathbf{Q}-\mathbf{p}} - J_{\mathbf{Q}-\mathbf{p}}\Big)|\psi_1|^2\tilde{a}^\dagger_{-\mathbf{Q}+\mathbf{p}}\tilde{a}_{-\mathbf{Q}+\mathbf{p}}, \tag{3.76}$$

where $h_{\rm sat} = S(J_{\mathbf{0}} - J_{\mathbf{Q}}) = S\Gamma_1^{(0)}$.

$$H_1 = \sum_{\mathbf{p}}\Big[\frac{3}{4}SJ\Big((p_x^2+p_y^2) + \frac{1}{\sqrt{3}}p_x^2\Delta Q - \sqrt{3}p_y^2\Delta Q\Big) - \mu\Big]\tilde{a}^\dagger_{-\mathbf{Q}+\mathbf{p}}\tilde{a}_{-\mathbf{Q}+\mathbf{p}}, \tag{3.77}$$

$$H_2 = J\sum_{\mathbf{p}}\Big[\frac{h_{sat}}{SJ} + \frac{9}{2}p_x\Delta Q + \frac{27}{4}p_x^2(\Delta Q)^2\Big]|\psi_1|^2\tilde{a}^\dagger_{-\mathbf{Q}+\mathbf{p}}\tilde{a}_{-\mathbf{Q}+\mathbf{p}}. \tag{3.78}$$

These two together describe magnons' motion near $\mathbf{k} = -\mathbf{Q} + \mathbf{p}$,

$$\mathcal{H}_K = \sum_{\mathbf{p}} S\omega^{(1)}_{\mathbf{k}}\tilde{a}^\dagger_{\mathbf{k}}\tilde{a}_{\mathbf{k}},$$

$$\omega^{(1)}_{\mathbf{k}} = \frac{3}{4}J\Big[(1+\frac{\Delta Q}{\sqrt{3}})(k_x+\tilde{Q}_i)^2 + k_y^2 + \varepsilon_{\min}\Big], \tag{3.79}$$

$$\varepsilon_{\min} = 9\frac{|\psi_1|^2}{S}(1-\frac{|\psi_1|^2}{S})(\Delta Q)^2 + \frac{4}{3}\frac{1}{SJ}(\frac{|\psi_1|^2}{S}h_{\rm sat} - \mu), \tag{3.80}$$

where $\tilde{Q}_i = 4\pi/3 + 3|\psi_1|^2\Delta Q/S$. For cone state, $|\psi_1|^2/S = \mu/S\Gamma_1 \approx \mu/h_{sat}$, so that Eq.(3.80) is,

$$\varepsilon_{\min} = \frac{12\mu}{h_{\rm sat}J^2}\frac{h}{h_{\rm sat}}(\delta J)^2. \tag{3.81}$$

Now let us calculate the correction to $\varepsilon_{\min}$ in Eq.(3.81), which is done for the isotropic model. Firstly, quantum correction to Γ_1 gives the correction of $\varepsilon_{\min}$,

$$\Delta\varepsilon_{\min,1} = -\frac{4}{3}\frac{\mu}{h_{\rm sat}J}\Gamma_1^{(1)}. \tag{3.82}$$

Secondly, (3.33) gives correction to (3.79),

$$\Delta\mathcal{H}_K = -\frac{1}{4}\frac{|\psi_1|^2}{S}\sum_{\mathbf{p}} J_{\mathbf{Q}}\tilde{a}^\dagger_{-\mathbf{Q}+\mathbf{p}}\tilde{a}_{-\mathbf{Q}+\mathbf{p}}. \tag{3.83}$$

This gives the correction to $\varepsilon_{\min}$,

$$\Delta\varepsilon_{\min,2} = \frac{4}{3}\frac{\mu}{h_{\rm sat}J}\Gamma_{2a}^{(1)}. \tag{3.84}$$

Finally, quantum correction of $\varepsilon_{\min}$ from perturbation (3.71), with $\mathbf{k}$ near$-\mathbf{Q}$,

$$\begin{aligned}\Delta\varepsilon_{\min,3} &= -\frac{4}{3}\frac{1}{JS}\sum_{\mathbf{q},\mathbf{q}'} V_{\mathbf{q}}(-\mathbf{Q},\mathbf{Q})V_{\mathbf{q}'}(-\mathbf{Q},\mathbf{Q})|\psi_1|^2\langle\tilde{a}^\dagger_{\mathbf{Q}-\mathbf{q}}\tilde{a}^\dagger_{-\mathbf{Q}+\mathbf{q}}\tilde{a}_{\mathbf{Q}-\mathbf{q}'}\tilde{a}_{-\mathbf{Q}+\mathbf{q}'}\rangle_0, \\ &= \frac{4}{3}\frac{1}{JS}\frac{|\psi_1|^2}{S}\tilde{\Gamma}_{2b}^{(1)} \approx \frac{4}{3}\frac{\mu}{h_{\rm sat}J}\Gamma_{2b}^{(1)}.\end{aligned} \tag{3.85}$$

Add up Eq.(3.82), Eq. (3.84) and Eq.(3.85), and the total correction of $\varepsilon_{\min}$ is,

$$\Delta\varepsilon_{min} = \frac{4}{3}\frac{\mu}{h_{\rm sat}J}(\Gamma_2^{(1)} - \Gamma_1^{(1)}), \tag{3.86}$$

where $\Gamma_2^{(1)} - \Gamma_1^{(1)} = -1.6J/S$.

From Eq.(3.81) and (3.86), minimum energy of magnons near $-\mathbf{Q}$ is,

$$\varepsilon_{\min} = \frac{12\mu}{h_{\rm sat}J^2}\Big[\frac{h}{h_{\rm sat}}(\delta J)^2 - (\delta J_c)^2\Big]. \tag{3.87}$$

For $\delta J = \delta J_c h_{\rm sat}/h$, the magnon dispersion touches zero at $\pm\tilde{\mathbf{Q}} = (-\tilde{Q}_{\rm i}, 0)$, which results in additional condensate at momentum different from $\pm\mathbf{Q}$. This is the double cone phase described in the main text.

3.2 Spin-current order in antiferromagnetic zigzag ladder

In the previous sections, we study the properties of magnetic ordered states which spontaneously break both spin-rotation and time-reversal symmetries. Such examples are Ising-like orders (Sec. 2.1), various two-dimensional orders (Sec. 2.2), and novel spin structures on triangular lattice (Sec. 3.1). Besides these long range ordered states, many exotic states of matter exist because of the quantum property of frustrated systems. One

example is the *spin nematic* phase, which has no magnetic order, but nevertheless breaks spin-rotation symmetry. In this section, we focus on a new exotic state called bond-nematic state, a highly correlated quantum spin state resembling nematic liquid crystals.[135–137] characterized by a pseudovector $\boldsymbol{S}_i \times \boldsymbol{S}_j$, and also known as *spin current*.[19] The spin current state has been proposed as the instability of $1/3$ magnetization plateau of Heisenberg two-dimensional (2D) antiferromagnets on a triangular lattice, either an edge-sharing[19] or corner-sharing[138] one.

Here we study the stability of the collinear up-up-down (UUD) phase in the $1/3$ magnetization plateau on a frustrated spin chain, with competing nearest and next-nearest neighbor coupling J_1 and J_2. Via the large-S expansion, we find that near the end of plateau, quantum fluctuations induce a two-magnon instability. This instability corresponds to the spin current (bond nematic) state, which was proposed in [Phys. Rev. Lett.**110**, 217210] of a two-dimensional spatially anisotropic triangular lattice antiferromagnet.

3.2.1 Introduction

Frustrated quantum systems have been a subject of active research. Besides the geometrical frustration as mentioned in Sec. 3.1, the frustrations always come from the competing interactions. Spin systems with competing interactions have played a crucial role in exploring exotic quantum states such as various types of spin liquids, valence bond solids, or spin nematics.[139]

The antiferromagnetic Heisenberg spin chain with competing nearest and next-nearest neighbor exchange interactions J_1 and J_2, depicted in the left-hand side of **Figure 3.6**, has attracted many investigations in recent years. As shown in **Figure 3.6**, this exchange frustration can be converted to a geometrical frustration on an effective zigzag ladder. Quite recently, the density matrix renormalization group (DMRG) studies[7,14] have shown the existence of $1/3$ magnetization plateau in frustrated chain with $S = 1/2$, when the ratio J_2/J_1 near the Majumdar-Ghosh[140,141] point with $J_2/J_1 = 0.5$. In the absence of the magnetic field, the system is in a dimerized sate with two neighbor spins forming a singlet. Extensive numerical calculations[142] have observed the $1/3$ magnetization plateaux for spin $S > 1/2$ zigzag ladder. The plateau is accompanied by a broken translation symmetry with three sublattices. Within the plateau, an *up-up-down* (UUD) structure is formed with

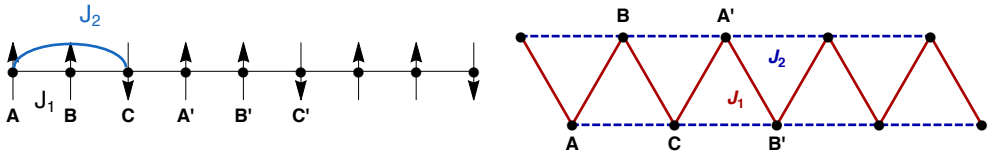

Figure 3.6. Equivalence between $J_1 - J_2$ spin chain and zigzag ladder. *Left*: $J_1 - J_2$ frustrated antiferromagnetic spin chain with nearest exchange $J_1 > 0$ and next-nearest exchange $J_2 > 0$. *Right*: An effective zigzag ladder. Within an elementary triangle, three spins A (up), B (up), and C (down) form the UUD phase.

all spins parallel or antiparallel to the external field, as shown in left side of **Figure 3.6**.

It is the purpose of this work to study the stability of the UUD phase of a frustrated quantum spin chain. We demonstrate that the instability of UUD phase results from the repulsive interactions between composite bosons, formed by two bounded magnons, and actually leads to a spin-current state. The spin current is a part of the plateau, with $\langle S^z \rangle = 1/3$ (the magnetic field is along the z-axis), but without magnetic order in the transverse direction. Our results are open to numerical calculations, such as density matrix renormalization group (DMRG) and quantum Monte Carlo (QMC). As for real materials that can realize the spin current state, examples are the CaV_2O_4[143–146] and $NaV(WO_4)_2$ compounds. These two materials can be modeled as a spin-1 chain with competing antiferromagnetic interactions. The bond nematic has been investigated below the fully polarized state on square lattice.[136,147,148]

3.2.2 The model

The Heisenberg $J_1 - J_2$ antiferromagnetic spin-S chain is illustrated in **Figure 3.6**, and described by a Hamiltonian,

$$H = \sum_i (J_1 \boldsymbol{S}_i \cdot \boldsymbol{S}_{i+1} + J_2 \boldsymbol{S}_i \cdot \boldsymbol{S}_{i+2} - h S_i^z). \tag{3.88}$$

Here, $\boldsymbol{S}_i$ is spin-S operator on site i, the nearest neighbor and next-nearest neighbor exchange couplings are both antiferromagnetic, namely $J_1 > 0$ and $J_2 > 0$. The magnetic field h is applied along z-axis.

As mentioned before, this chain is equivalent to the zigzag ladder in the right hand side of **Figure 3.6**. Our purpose is to study the instability of UUD phase, where there are three sublattices A, B, and C, occupied by spin up, up, and down, respectively. With this spin

configuration, it is easy to see the magnetization is at $1/3$ of its saturation value. Linear spin wave theory shows that UUD state is eigenstate only when $J_2/J_1 = 1/2$, namely the Majumdar-Ghosh (MG) point,[140,141] and $h = 3/2J_1S = h_0$, and there is no plateau in the magnetization curve; see details in Sec. 3.2.5 in the Supplement.

Different from the XXZ model on the antiferromagnetic triangular lattice,[132] the magnetization plateau is classically unfavorable for the $J_1 - J_2$ spin chain. However, quantum fluctuations stabilize this UUD state, which extends along the two axes of the phase diagram in **Figure 3.7**. UUD state preserves inside a finite field interval as h increasing, and the magnetization keeps at $1/3$ of its saturation, resulting the magnetization plateau. This plateau originates purely from a quantum effect, and thus we call it a quantum plateau. Technically, we take account for the quantum effect by expanding the square-root in the Holstein-Primakoff representation; see details in Sec. 1.5.2.1. The four-magnon interactions at the MG point give $1/S$ corrections to the dispersions obtained from linear spin wave analysis.

In this work, we look for spin current state for large spin-S near the MG point and assume $w \equiv (J_2/J_1 - 1/2)$ and $1/S$ are small. Here w measures the deviation from the MG point.

3.2.3 The quantum $1/3$ magnetization plateau

For simplicity, we define a dimensionless parameter $\hat{h} = h/[(J_1 + J_2)S]$. We will use $\hat{h}$ to study the field region which supports the UUD phase. The results are presented in

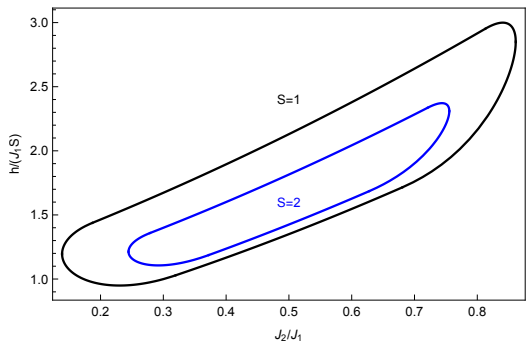

Figure 3.7. Phase boundaries of the UUD phase for $S = 1$ and $S = 2$, respectively. With larger spin S, the plateau shrinks.

Figure 3.7 for $S = 1, 2$. The energy scale of h will be recovered when it's necessary.

At GM point $J_2/J_1 = 1/2$, or $w = 0$, the plateau preserves at $h^0_{c1} < h < h^0_{c2}$, with

$$\hat{h}^0_{c1} = 1 - \frac{0.099}{S}, \quad \hat{h}^0_{c2} = 1 + \frac{0.423}{S}. \tag{3.89}$$

Detailed calculations are in Sec. 3.2.7. The width of the plateau is $\Delta\hat{h} = 0.522/S$. Within this field range, the two low-energy spin wave modes are gapped. The gap closes at $\hat{h}^0_{c1}$ ($\hat{h}^0_{c2}$), which corresponds to a Bose condensation of the corresponding magnon. Long wavelength limit is taken near $k = 0$.

Near the GM point, $w \neq 0$ and $w \ll 1$, we account for the quantum corrections from magnon interactions at $J_2/J_1 = 1/2$. The effective Hamiltonian of the UUD phase describing two low-energy excitations is,

$$H_{\text{uud}} = \frac{3}{2} J_1 S \sum_k (\omega_1 d^\dagger_{1,k} d_{1,k} + \omega_2 d^\dagger_{2,k} d_{2,k}), \tag{3.90}$$

with

$$\omega_{1,2} = \pm(h - 1 - \frac{I_2}{S} - \frac{2}{3}w - k^2) + Z_k, \quad Z_k \equiv 2\sqrt{(k_0^2 - k^2)^2 + (4-d)k_0^2 k^2}. \tag{3.91}$$

Here w and d measure the deviation from the MG point, and they are defined as $w \equiv J_2/J_1 - 1/2$ and $d \equiv 16w^2/(\Delta\hat{h}/4) \simeq 7.66S(1 - 2J_2/J_1)^2$. Inside the plateau, the range of d is $0 < d < 4$. There is a critical momentum $k_0^2 \equiv \Delta\hat{h}/4 \simeq 0.13/S$. The critical field is obtained by the conditions,

$$\hat{h}_{c_1} = \hat{h}^0_{c_1} + \frac{2}{3}w + \min[k_1^2 + \frac{1}{2}\Delta\hat{h} - Z_k], \quad \hat{h}_{c_2} = \hat{h}^0_{c_2} + \frac{2}{3}w + \min[k_2^2 - \frac{1}{2}\Delta\hat{h} + Z_k]. \tag{3.92}$$

Here $\hat{h}^0_{c1}$ and $\hat{h}^0_{c2}$ are defined in Eq. (3.89). We find the critical field depends on the ratio of J_2/J_1 through w and d,

$$\hat{h}_{c_1} = \begin{cases} \hat{h}^0_{c_1} + \frac{2}{3}w, \ 0 < d \leq 1 \\ \hat{h}_{\text{end}} + \frac{1}{8}\Delta\hat{h}\left[d - 4 - f(d)\right], \ 1 < d \leq 4 \end{cases}, \tag{3.93}$$

and

$$\hat{h}_{c_2} = \begin{cases} \hat{h}^0_{c_2} + \frac{2}{3}w, \ 0 < d \leq 3 \\ \hat{h}_{\text{end}} + \frac{1}{8}\Delta\hat{h}\left[d - 4 + f(d)\right], \ 3 < d \leq 4. \end{cases} \tag{3.94}$$

where $f(d) \equiv 3\sqrt{d(4-d)/3}$ and $\hat{h}_{\text{end}} \equiv \hat{h}^0_{c_1} + 3\sqrt{\Delta\hat{h}}/4 + 4\Delta\hat{h}/3$. $\hat{h}_{c1}$ and $\hat{h}_{c_2}$ correspond to the lower and upper boundary, respectively. Eqs. (3.93) and (3.94) are plotted in **Figure 3.8**,

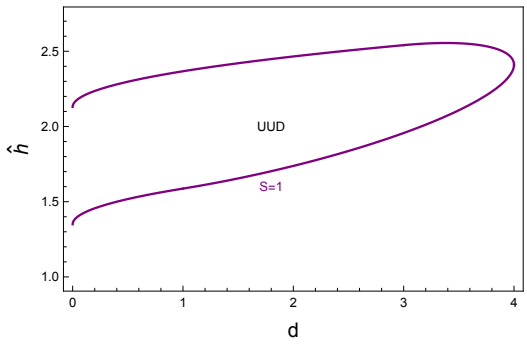

Figure 3.8. Boundaries of the $1/3$ magnetization plateau as functions of d. Here spin $S = 1$.

which resembles the case of anisotropic triangular antiferromagnet.[149] The plateau width $\hat{h}_{c_2} - \hat{h}_{c_1} = \Delta\hat{h}$ is unchanged compared with the $J_2/J_1 = 1/2$ $(d = 0)$ case. As for $1 < d < 3$, the upper field boundary keeps the same form of d, while the lower one shifts up. As a result, the $\Delta\hat{h}$ is narrowed. For $3 < d < 4$, $\hat{h}_{c_1}$ still shifts up and $\hat{h}_{c_2}$ starts to shift down, so $\Delta\hat{h}$ is further narrowed. Finally, the plateau closes at the end point $d = 4$.

The boundaries of the UUD phase in the $h - J_2$ plane are illustrated in **Figure 3.7**, which is based on **Figure 3.8** and obtained by recovering the $\hat{h}$ to magnetic field h. From previous discussions, we notice two properties of these phase boundaries. Firstly, the plateau is unfavorable in the classical limit, and thus we expect the region that allows UUD phase should shrink with S increasing. Secondly, since the plateau is induced by the frustration effect, it should vanish as $J_2 \to 0$, as well as for $J_2 \gg J_1$. **Figure 3.7** confirms these two properties very well. The shape of the boundaries resembles those in Ref.[150] The low-energy excitations ω_1 and ω_2 at two boundaries induce the one-magnon condensation, which leads to an incommensurate spiral order as shown in Ref.[150]

3.2.4 The magnon pairing

At the end of the plateau, $d = 4$, the two low-energy spin-wave modes approaches to 0 at the same time, with $k = \pm k_0$. Around $\pm k_0$, these two branches of the excitations interact with each other, and form a two-magnon bound state. To study the interaction between magnons, we need to convert the fourth-order Hamiltonian H^4, originally in terms of a, b and c, to expression in terms of low-energy modes d_1 and d_2. The transformation process is presented in Sec. 3.2.9.1. Here we claim that near $\pm k_0$, this transformation is,

$$
\begin{aligned}
a_k &= \frac{g(k)}{\sqrt{2}}\left(e^{is_k}d_{1,k} - e^{-is_k}d^\dagger_{2,-k}\right), \\
b_k &= \frac{-g(k)}{\sqrt{2}}\left(e^{-is_k}d_{1,k} + e^{is_k}d^\dagger_{2,-k}\right), \\
c_k &= g(k)(d_{2,k} - e^{i2s_k}d^\dagger_{1,-k}),
\end{aligned}
\tag{3.95}
$$

where $g(k) = \sqrt{2}k_0[(k^2 - k_0^2)^2 + (4-d)k_0^4]^{-\frac{1}{4}}$, and $s_k = \pi \mathrm{Sgn}(-kw)/4$.

The interactions between magnons have two species. One corresponds to that within the same mode d_1 or d_2, for example the process of two d_1 magnons scattering. This leads to a one magnon condensation of d_1 mode. The same holds for d_2 mode near upper boundary h_{c2}. The other kind of magnon interaction is the interaction between different modes d_1 and d_2.

What is more interesting happens at the end of plateau $d \simeq 4$. The interaction between different modes d_1 and d_2 is divergent when they are in the vicinity of $\pm k_0$. This interaction is

$$
H^{(4)}_{d_1 d_2} = \frac{3}{N}\sum_{p,q}\Gamma(p,q)[\Psi^\dagger_R(q)\Psi_L(p) - \Psi_R(q)\Psi_L(p) + h.c.], \tag{3.96}
$$

where $\Psi_R(p) = d_{1,k_0+p}d_{2,-k_0-p}$ and $\Psi_L(p) = d_{1,-k_0+p}d_{2,k_0-p}$. The scattering amplitude $\Gamma(p,q)$ (the vertex) is

$$
\Gamma(p,q) = -(J_1+J_2)g^2(\pm k_0 + p)g^2(\pm k_0 + q) \xrightarrow[d=4]{} -(J_1+J_2)\frac{k_0^2}{|p||q|}. \tag{3.97}
$$

This interaction includes both the normal $2 \to 2$, which is attractive and "anomalous" $4 \to 0$ or $0 \to 4$ process, which is repulsive. $\Gamma(p,q)$ is divergent for magnons moving around $\pm k_0$. This signals a divergent interaction near $d = 4$, which induces a phase transition to the spin-current state. The critical d_c corresponding to this transition can be determined by the following self-consistent condition,

$$
\frac{1}{4S}\frac{3}{N}\sum_p \frac{k_0}{[p^2 + (1-d_c/4)k_0^2]^{3/2}} = 1. \tag{3.98}
$$

Integrating p leads to the expression of critical d_c as,

$$
4 - d_c = \frac{3}{\pi}\frac{1}{Sk_0} = \frac{3}{\pi}\sqrt{\frac{4}{0.522}}\frac{1}{\sqrt{S}} \simeq \frac{2.64}{\sqrt{S}}. \tag{3.99}
$$

We find that the width of the spin-current phase is scaled as $1/\sqrt{S}$, which is much stronger than $1/S^2$ dependence found previously in the 2D cases.[19,138]

In summary, by a semiclassical large-S approach, we studied the phase diagram of an antiferromagnetic $J_1 - J_2$ spin chain, also known as zigzag ladder. The interactions between nearest and next-nearest neighbors compete with each other, and produce magnetic frustrations. We argue that the quantum fluctuations and magnetic frustration establish a classically unfavorable $1/3$ magnetization plateau, which survives through a large range away from the Majumdar-Ghosh point. Within the plateau, the UUD phase is stable until it is replaced by a two-magnon instability, resulting in a bond-nematic state—spin current state.[19] We hope our results will stimulate further numerical and experimental work on this subject.

Here we present some technical calculations. Firstly, by linear spin wave analysis, we showed the $1/3$ magnetization plateau is absent in the classical limit. Then we take account for the quantum effect by expanding the square-root in the Holstein-Primakoff (HP) representation, and demonstrate that there is a quantum $1/3$ magnetization plateau on $J_1 - J_2$ spin chain. Within this plateau, we found a two-magnon instability, which leads to spin-current state of the UUD phase. Here we assume $(J_2/J_1 - 1/2)$ and $1/S$ are small.

3.2.5 Classical counterpart

To begin with the Hamiltonian in Eq. (3.88), three magnon modes a, b, and c on sublattices A and B, and site C, with the Holstein-Primakoff transformation (see Sec.1.5.2.1),

$$\begin{aligned} S_A^+ &= \sqrt{2S}a_r, \quad S_A^z = S - a_r^\dagger a_r, \\ S_B^+ &= \sqrt{2S}b_r, \quad S_B^z = S - b_r^\dagger b_r, \\ S_C^+ &= \sqrt{2S}c_r^\dagger, \quad S_C^z = c_r^\dagger c_r - S. \end{aligned} \tag{3.100}$$

We keep only the leading term in an expansion of the Hamiltonian in powers of S. Perform Fourier transformation of magnons, for example $a_r = \frac{1}{\sqrt{N/3}} \sum_{k_1} e^{ikr} a_k$. N is the total number of lattice sites. The Hamiltonian (3.88) reduces to,

$$\begin{aligned} H^{(2)} = J_1(1+j)S \sum_k \hat{h} \Big\{ & \left(a_k^\dagger a_k + b_k^\dagger b_k \right) + (2 - \hat{h}) c_k^\dagger c_k + \\ & + \left(f_k (a_k^\dagger b_k + b_k^\dagger c_{-k}^\dagger) + f_{-k} a_k^\dagger c_{-k}^\dagger + h.c. \right) \Big\}, \end{aligned} \tag{3.101}$$

with

$$f_k = e^{ik} + j e^{-i2k}, \quad f_{-k} = f_k^*. \quad \hat{h} = \frac{h}{J_1 S}, \quad j \equiv J_2/J_1. \tag{3.102}$$

All the above parameters are dimensionless, f_k is the geometry factor. To diagonalize $H^{(2)}$ and solve for eigenvalues, details of which are in Sec. 3.2.5.1, we find this UUD configuration only exists when $j = 1/2$ and $\hat{h} = 1$ (equivalently $J_2/J_1 = 1/2$ and $h = 3/2J_1S$). This UUD phase will be extended around $j = 1/2$, and one-third plateau will appear when we consider the quantum fluctuations, that is the interactions between magnons, as shown in Sec. 3.2.6.

3.2.5.1 Diagonalize $H^{(2)}$

Here we present technical details to diagonalize and prove the UUD phase is an eigenstate of Eq. (3.101).

First we replace $c_k^\dagger c_k \to 1 - c_{-k}c_{-k}^\dagger$, then the Hamiltonian (3.101) in matrix form is $H^{(2)}/(SJ_1) + 2(1+j) - h = X^+ H X$, with

$$X = \begin{pmatrix} a_k \\ b_k \\ c_{-k}^\dagger \end{pmatrix}, \quad H = \begin{pmatrix} h & f_{-k} & f_k \\ f_{-k} & \hat{h} & f_k \\ f_k & f_{-k} & 2-\hat{h} \end{pmatrix} \tag{3.103}$$

The linear transformation matrix S diagonalizes the H in Eq. (3.103), and $X = SX'$. Then $HS = (S^+)^{-1}\Omega_H$, where Ω_H is the diagonal eigenvalue matrix. A metric g is the commutator for boson operators X, so that $g = [X, X^+] \equiv X(X^*)^T - (X^* X^T)^T = \mathrm{diag}(1, 1, -1)$. Substitute $X = SX'$ into the commutator, we find $g = SX'(X'^*)^T(S^*)^T - S(X'^* X'^T)^T(S^*)^T$. We are seeking the new operators X' also having the same commutator g, then

$$S^{-1} = gS^+g^{-1} \text{ or } (S^+)^{-1} = g^{-1}Sg. \tag{3.104}$$

Therefore the condition $HS = (S^+)^{-1}\Omega_H$ reduces to,

$$HS = g^{-1}Sg\Omega_H \to S^{-1}gHS = g\Omega_H. \tag{3.105}$$

This is the eigenvalue equation, $\det[gH - x] = 0$, which determines S and Ω_H, and $\Omega_H = diag(x_1, x_2, -x_3)$. The eigenvalues of gH should satisfy the cubic equation,

$$x^3 + a_2x^2 + a_1x + a_0 = 0, \tag{3.106}$$

with,

$$a_2 = 2 - 3\hat{h}, \quad a_1 = |f_k|^2 + 3\hat{h}^2 - 4\hat{h}, \quad a_0 = f_k^3 + f_{-k}^3 - (2+\hat{h})|f_k|^2 - \hat{h}^3 + 2\hat{h}^2. \tag{3.107}$$

The discriminant D of cubic polynomial is $D = (p/3)^3 + (q/2)^2$, with

$$p = (3a_1 - a_2^2)/3 = |f_k|^2 - \frac{4}{3}, \;\; q = (9a_1a_2 - 27a_0 - 2a_2^3)/27 = \frac{8|f_k|^2}{3} - f_k^3 - f_{-k}^3 - \frac{16}{27}, \tag{3.108}$$

The cubic equation (3.106) has three real solutions when $D \leq 0$ (this condition is required because UUD state should not have complex modes). Three solutions are,

$$\begin{aligned} x_1 &= 2\sqrt{-\frac{p}{3}}\cos[\frac{\theta}{3}] - \frac{1}{3}a_2, \\ x_2 &= 2\sqrt{-\frac{p}{3}}\cos[\frac{\theta+4\pi}{3}] - \frac{1}{3}a_2, \\ x_3 &= 2\sqrt{-\frac{p}{3}}\cos[\frac{\theta+2\pi}{3}] - \frac{1}{3}a_2, \end{aligned} \tag{3.109}$$

where,

$$\theta \equiv \arccos[\frac{q/2}{\sqrt{-(p/3)^3}}]. \tag{3.110}$$

They satisfy the relation, $x_1 + x_2 + x_3 = -a_2 = 3\hat{h} - 2$.

We find that the condition of $D \leq 0$ is satisfied in momentum space only when $j = 1/2$. Therefore, we set $j = 1/2$ now. The minimum of dispersions are at $k = 0$, and the low-energy limit of Eq. (3.109) is,

$$x_1(k) = 2k^2 + h, \qquad x_1(k) = k^2 + h - 1, \qquad x_1(k) = -3k^2 + h - 1. \tag{3.111}$$

These solutions are shown in **Figure 3.9**. Then the dispersions corresponding to $(X')^\dagger = (A_k, B_k, C_{-k}^\dagger)$ are,

$$\omega_A(k) = \frac{3}{2}J_1S(k^2 + \hat{h} - 1), \quad \omega_B(k) = \frac{3}{2}J_1S(3k^2 - \hat{h} + 1), \quad \omega_C(k) = \frac{3}{2}J_1S(2k^2 + \hat{h}). \tag{3.112}$$

So far, the linear spin wave analysis shows that the UUD sate is stable only when $\hat{h} = 1$ and $j = 1/2$.

3.2.6 Magnon interactions

Here we account for effects from magnon interactions using Oguchi's approach.[151] We expand the square root in HP representation, and keep terms to fourth order in cre-

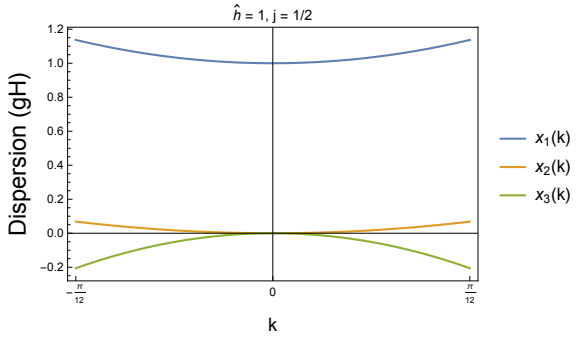

Figure 3.9. Eigenvalues of Ω_H, approximate solutions of $x_1(k)$, $x_2(k)$ and $x_3(k)$ near $k = 0$.

ation/annihilation operators (in order of S^0), $H^{(4)} = H_z^{(4)} + H_\perp^{(4)}$. It contains longitudinal (z) and transverse $(\perp)$ contributions, with

$$H_z^{(4)} = \frac{3}{N}(1+j)J_1 \sum_{k_1,k_2,k_3} \Big(b_{k_1}^\dagger b_{k_2} (f_{k_2-k_1} a_{k_3}^\dagger a_{k_1-k_2+k_3} - f_{k_1-k_2} c_{k_3}^\dagger c_{k_1-k_2+k_3}) - f_{k_2-k_1} a_{k_1}^\dagger a_{k_2} c_{k_3}^\dagger c_{k_1-k_2+k_3} \Big). \tag{3.113}$$

and

$$H_\perp^{(4)} = -\frac{3}{N}(1+j)J_1 \frac{1}{4} \sum_{k_1,k_2,k_3} \Big[f_{k_1} (c_{k_1}^\dagger a_{k_2}^\dagger a_{k_3}^\dagger a_{k_1+k_2+k_3} + a_{k_1}^\dagger b_{k_2}^\dagger b_{k_3} b_{k_1+k_2-k_3} + b_{k_1}^\dagger c_{k_2}^\dagger c_{k_3}^\dagger c_{k_1+k_2+k_3}) + f_{-k_1} (a_{k_1}^\dagger c_{k_2}^\dagger c_{k_3}^\dagger c_{k_1+k_2+k_3} + b_{k_1}^\dagger a_{k_2}^\dagger a_{k_3} a_{k_1+k_2-k_3} + c_{k_1}^\dagger b_{k_2}^\dagger b_{k_3}^\dagger b_{k_1+k_2+k_3}) + h.c. \Big]. \tag{3.114}$$

The interactions between magnons in $H^{(4)}$ give $1/S$ corrections to the magnon spectrum in $H^{(2)}$, and the effective quadratic Hamiltonian $H^{(2)}$ of the UUD phase is,

$$H_{\text{uud}} = J_1 S \sum_k (1+j) \Big\{ (\hat{h} + \Sigma_1)(a_k^\dagger a_k + b_k^\dagger b_k) + (2 - \hat{h} + \Sigma_2) c_k^\dagger c_k + [\tilde{f}_{1k} a_k^\dagger b_k + \tilde{f}_{2k} (b_k^\dagger c_{-k}^\dagger + c_k^\dagger a_{-k}^\dagger) + h.c.] \Big\}, \tag{3.115}$$

with

$$\Sigma_1 = -\frac{I_1 + I_2 + I_3}{S} = \frac{0.053}{S}, \quad \Sigma_2 = -\frac{2I_1 + 2I_3}{S} = \frac{0.43}{S},$$
$$\tilde{f}_{1k} = f_k + \Sigma_1', \quad \tilde{f}_{2k} = f_k + \Sigma_2', \quad \Sigma_1' = -\frac{I_1 - I_2}{S} = -\frac{0.046}{S}, \quad \Sigma_2' = -\frac{1.5I_1 + I_3}{S} = \frac{0.111}{S}. \tag{3.116}$$

We see all the Σs and $\Sigma' s$ are in order of $1/S$, and they originate from $H^{(4)}$ terms. In the limit of $S \to \infty$, H_{uud} is equivalent to $H^{(2)}$ in Eq. (3.101). The numerical values of Is are summarized in **Table 3.1**.

Table 3.1. Numerical values of Is.

I_1	I_2	I_3
0.208	0.162	-0.423

3.2.7 Quantum plateau at $J_2/J_1 = 1/2$

In Sec. 3.2.5, results from linear spin wave demonstrate that the UUD phase is the ground state when $\hat{h} = 1$ and $J_2/J_1 = 1/2$. Here we show how quantum magnetization plateau is formed at $J_2/J_1 = 1/2$ and how the UUD phase is extended along the h-axis.

We study the low-energy excitations near $k = 0$, and $f_k \simeq 1 - k^2$. Let us introduce two new operators d_k and p_k,

$$d_k = \frac{1}{\sqrt{2}}(a_k + b_k), \quad p_k = \frac{1}{\sqrt{2}}(a_k - b_k). \tag{3.117}$$

Plug into Hamiltonian (3.115) and set $j = 1/2$, we have

$$H_{\text{uud}} = \frac{3}{2}J_1 S \sum_k \left(\omega_p(k) p_k^\dagger p_k + \epsilon_d d_k^\dagger d_k + \epsilon_c c_{-k}^\dagger c_{-k} + \chi(d_k^\dagger c_{-k}^\dagger + d_k c_{-k})\right), \tag{3.118}$$

where,

$$\omega_p = \hat{h} + \Sigma_1 - \tilde{f}_{1k}, \quad \epsilon_p = \hat{h} + \Sigma_1 + \tilde{f}_{1k}, \quad \epsilon_c = 2 - \hat{h} + \Sigma_2, \quad \chi = \sqrt{2}\tilde{f}_{2k}. \tag{3.119}$$

The p mode is decoupled. Next we decouple d and c by a rotation,

$$\begin{aligned} d_k &= \cosh\theta u_k + \sinh\theta v_{-k}^\dagger, \\ c_{-k}^\dagger &= \sinh\theta u_k + \cosh\theta v_{-k}^\dagger, \end{aligned} \tag{3.120}$$

and the rotation angle is,

$$\tanh[2\theta] = -\left(\frac{\chi + \chi^*}{\epsilon_d + \epsilon_c}\right) \simeq -\frac{2}{3}\sqrt{2}. \tag{3.121}$$

Now UUD Hamiltonian reads,

$$H'_{\text{uud}} = \frac{3}{2}J_1 S \sum_k [\omega_p p_k^\dagger p_k + \omega_u u_k^\dagger u_k + \omega_v v_k^\dagger v_k], \tag{3.122}$$

with dispersions near $k = 0$

$$\omega_p(k) = \hat{h} - \hat{h}_{c1}^0 + k^2, \quad \omega_v(k) \simeq \hat{h}_{c2}^0 - \hat{h} + 3k^2, \quad \omega_u(k) \simeq \hat{h} + 2k^2. \tag{3.123}$$

In the above expression,

$$\hat{h}^0_{c1} = 1 + \frac{2I_2 + I_3}{S} = 1 - \frac{0.099}{S}, \quad \hat{h}^0_{c2} = 1 - \frac{I_3}{S} = 1 + \frac{0.423}{S}. \tag{3.124}$$

This result leads to Eq. (3.89) in the main text. There are two low-energy modes, p (linear combination of a and b) and v (linear combination of a, b and c), and they are illustrated in **Figure 3.10**. These two modes open a window for the UUD phase around $\hat{h} = 1$, $\hat{h}^0_{c1} \leq \hat{h} \leq \hat{h}^0_{c2}$. The UUD phase is stable in the interval,

$$\Delta\hat{h} = -\frac{2I_2 + 2I_3}{S} = 0.522/S. \tag{3.125}$$

The high energy u mode describes total spin procession, while the other two modes describe the fluctuations of spins. From **Figure 3.10**, we see p and v are gapped. The gap closes at $\hat{h}^0_{c1}$ ($\hat{h}^0_{c2}$), which corresponds to a Bose condensation of p (v) magnon.

Hereto, we have investigated the local stability (at $J_2/J_1 = 1/2$) of the UUD phase. The UUD phase forms a plateau in the magnetization process, within field width $\Delta h = 0.783 J_1$. Now let us study how quantum fluctuations induce a UUD phase for $j \neq 1/2$.

3.2.8 Quantum plateau around $J_2/J_1 = 1/2$

Here we consider when J_2/J_1 is near $1/2$, denoting $j = 1/2 + w$, and w can be both negative and positive. Then the Hamiltonian in second order of low-energy bosons p and v is,

$$H''_{\text{uud}} = H'_{\text{uud}} + H^{(2)}_w, \tag{3.126}$$

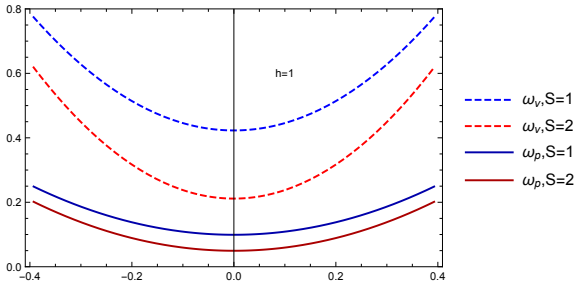

Figure 3.10. Two low-energy modes v (red line) and p (blue line) in Eq. (3.119). Here $\hat{h} = 1$ and $S = 1, 2$. The dispersions are gapped corresponding to the spin gap in the magnetization plateau.

where, H'_{uud} is defined in Eq. (3.122). The corrections to long-wave length dispersions, $\omega_{u,p,v} \to \omega_{u,p,v} + \delta\omega_{u,p,v}$, are given by $H_w^{(2)}$,

$$H_w^{(2)} = \frac{3}{2}J_1 S \sum_k \left\{ \delta\omega_u u_k^\dagger u_k + \delta\omega_p p_k^\dagger p_k + \delta\omega_v v_k^\dagger v_k - i\Lambda_2(k)(p_k^\dagger v_{-k}^\dagger - v_{-k}p_k) \right\}, \tag{3.127}$$

with,

$$\delta\omega_u \simeq \frac{8}{3}wk^2,\ \delta\omega_p \simeq \frac{2}{3}w(2k^2-1),\ \delta\omega_v \simeq \frac{2}{3}w(6k^2+1),\ \Lambda_2(k) \simeq 4wk. \tag{3.128}$$

Then combine Eqs. (3.127) and (3.127), we have

$$H''_{\text{uud}} = \frac{3}{2}J_1 S \sum_k \left\{ \omega_u u_k^\dagger u_k + \omega_p p_k^\dagger p_k + \omega_v v_{-k}^\dagger v_{-k} - i\Lambda_2(k)(p_k^\dagger v_{-k}^\dagger - v_{-k}p_k) \right\}. \tag{3.129}$$

with new dispersion relations,

$$\begin{aligned} \omega_p &= h - 1 - \frac{2I_2 + I_3}{S} - \frac{2}{3}w + (1 + \frac{4}{3}w)k^2, \\ \omega_v &= 1 - \frac{I_3}{S} - h + \frac{2}{3}w + (3 + 4w)k^2, \\ \omega_u &= h + 2k^2 + \frac{8}{3}wk^2. \end{aligned} \tag{3.130}$$

Now we need to decouple v and p in Eq. (3.129) by a rotation,

$$\begin{aligned} p_k &= \cosh\phi_k d_{1,k} + i\sinh\phi_k d_{2,-k}^\dagger, \\ v_{-k}^\dagger &= \cosh\phi_k d_{2,-k}^\dagger - i\sinh\phi_k d_{1,k}, \end{aligned} \tag{3.131}$$

with the rotation angle defined by

$$\tanh[2\phi_k] = -\frac{2\Lambda_2}{\omega_p + \omega_v} = -\frac{8kw}{\Delta\hat{h} + 4k^2}, \tag{3.132}$$

and the sign of ϕ_k depends on $\Lambda_2(w)$. $\Delta\hat{h}$ is defined in Eq. (3.125). The quadratic Hamiltonian in terms of $d_{1,k}$ and $d_{2,k}$ up to a constant,

$$\tilde{H}_{uud} = \frac{3}{2}J_1 S \sum_k \left(\omega_1 d_{1,k}^\dagger d_{1,k} + \omega_2 d_{2,k}^\dagger d_{1,k} \right), \tag{3.133}$$

where at small k,

$$\begin{aligned} &\omega_{1,2} = \pm(h - 1 - \frac{I_2}{S} - \frac{2}{3}w - k^2) + Z_k, \quad Z_k \equiv 2\sqrt{(k_0^2 - k^2)^2 + (4-d)k_0^2k^2}, \\ &d \equiv 16w^2/\Delta\hat{h}, \quad k_0^2 \equiv \Delta\hat{h}/4. \end{aligned} \tag{3.134}$$

Here d is the degree of deviation from the $J_2/J_1 = 1/2$ point. We will show that the width of the plateau is determined by d, and the one-third plateau persists up to $d_c = 4$. Obviously, Z_k should take real value, and this is satisfied when $0 < d < 4$, and $(1 + 4w/3) > 0$.

3.2.8.1 k_1 and k_2

The minima of ω_1 and ω_2 happen at $(\pm k_1, 0)$ and $(\pm k_2, 0)$, respectively, with

$$\begin{aligned} k_1^2(d) &= \frac{\Delta\hat{h}}{4} f_+(d) = k_0^2 f_+(d),\ 1 \le d \le 4, \\ k_2^2(d) &= \frac{\Delta\hat{h}}{4} f_-(d) = k_0^2 f_-(d),\ 3 \le d \le 4. \end{aligned} \tag{3.135}$$

k_1 and k_2 move away from $k = 0$ for $d > 1$ and $d > 3$, respectively. The complete expressions for k_1^2 and k_2^2 in a different region of d are shown in **Table 3.2**. Here $f_\pm(d)$ are functions of d,

$$f_+(d) = \frac{1}{2}d - 1 + \sqrt{\frac{d - d^2/4}{3}}, \quad f_-(d) = \frac{1}{2}d - 1 - \sqrt{\frac{d - d^2/4}{3}}, \tag{3.136}$$

and they are illustrated in **Figure 3.11**. Once k_1 and k_2 are obtained, the plateau boundaries can be determined.

3.2.8.2 $\hat{h}_{c1}$ and $\hat{h}_{c2}$

The $1/3$ magnetization plateau preserves for $\hat{h}_{c_1} < \hat{h} < \hat{h}_{c_2}$, with

$$\hat{h}_{c_1} = \hat{h}^0_{c_1} + \frac{2}{3}w + \min[k_1^2 + \frac{\Delta\hat{h}}{2} - Z_k], \quad \hat{h}_{c_2} = \hat{h}^0_{c_2} + \frac{2}{3}w + \min[k_2^2 - \frac{\Delta\hat{h}}{2} + Z_k]. \tag{3.137}$$

Since k_1 and k_2 change with d, shown in **Table 3.2**, $\hat{h}_{c_1}$ and $\hat{h}_{c_2}$ also depend on the value of d. This dependence is summarized in **Table 3.3** and illustrated in **Figure 3.8**. For $d \le 1$, both modes are minimized at $k = 0$, which leads to the fact that the plateau width $\hat{h}_{c_2} - \hat{h}_{c_1}$ is unchanged compared with the $J_2/J_1 = 1/2$ $(d = 0)$ point; the d value only shifts the plateau's location by $2w/3$ and softens the dispersion at $k = 0$. Here $\hat{h}_{c_1} = \hat{h}^0_{c_1} + \frac{2}{3}w$ and $\hat{h}_{c_2} = \hat{h}^0_{c_2} + \frac{2}{3}w$. As for $1 < d < 3$, the minimum of ω_1 shifts to $\pm k_1$, with $k_1 = \frac{1}{2}\sqrt{\Delta h f_+(d)}$. The upper field boundary keeps the same form of d, while the lower one shifts up,

$$\hat{h}_{c_1} = \hat{h}_{\text{end}} + \frac{1}{8}\Delta\hat{h}\left((d-4) - 6\sqrt{d(4-d)/12}\right). \tag{3.138}$$

Table 3.2. Expression for k_1^2 and k_2^2, at which momentum ω_1 and ω_2 take minima, for different regions of d. Here $k_0^2 \equiv \Delta\hat{h}/4$.

	$0 \le d \le 1$	$1 < d \le 3$	$3 < d < 4$	$d = 4$
k_1^2	0	$\frac{1}{4}\Delta\hat{h} f_+(d)$	$\frac{1}{4}\Delta\hat{h} f_+(d)$	k_0^2
k_2^2	0	0	$\frac{1}{4}\Delta\hat{h} f_-(d)$	k_0^2

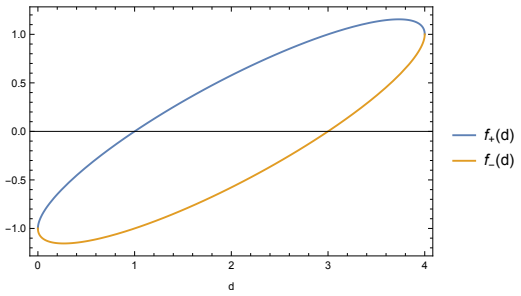

Figure 3.11. Plots of $f_+(d)$ and $f_-(d)$ as functions of d. We notice $f_+(d=4) = f_-(d=4) = 1$.

Table 3.3. Critical fields of lower (h_{c_1}) and higher (h_{c_2}) boundaries of phase diagram **Figure 3.7**, with $h_{\text{end}} = 1 + \frac{0.37}{S} + \text{Sgn}(w)\frac{1}{3}\sqrt{\Delta h}$ and $\mathbb{S} = \sqrt{d(4-d)/12}$.

	$d=0$	$0<d\leq 1$	$1<d\leq 3$	$3<d<4$	$d=4$
h_{c_1}	$h^0_{c_1}$	$h^0_{c_1}+\frac{2}{3}w$	$h_{\text{end}}+\frac{1}{8}\Delta h[d-4-6\mathbb{S}]$	$h_{\text{end}}+\frac{1}{8}\Delta h[d-4-6\mathbb{S}]$	h_{end}
h_{c_2}	$h^0_{c_2}$	$h^0_{c_2}+\frac{2}{3}w$	$h^0_{c_2}+\frac{2}{3}w$	$h_{\text{end}}+\frac{1}{8}\Delta h[d-4+6\mathbb{S}]$	h_{end}

As a result, the $\Delta\hat{h}$ is narrowed. For $3 < d < 4$,the minimum of ω_2 shifts to $\pm k_2$, with $k_2 = \frac{1}{2}\sqrt{\Delta\hat{h} f_-(d)}$. The upper field boundary as function of d is,

$$\hat{h}_{c_2} = \hat{h}_{\text{end}} + \frac{1}{8}\Delta\hat{h}\left(d-4+6\sqrt{d(4-d)/12}\right). \tag{3.139}$$

$\hat{h}_{c_1}$ keeps shift up and $\hat{h}_{c_2}$ starts to shift down, so $\Delta\hat{h}$ is further narrowed. Finally, at end point $d=4$, $k_1^2 = k_2^2 = \Delta\hat{h}/4$. $\hat{h}_{c_1} = \hat{h}^0_{c_1} + \frac{2}{3}w + \frac{3}{4}\Delta\hat{h} = \hat{h}_{\text{end}}$, $\hat{h}_{c_2} = \hat{h}^0_{c_2} + \frac{2}{3}w - \frac{1}{4}\Delta\hat{h} = \hat{h}_{\text{end}}$. Therefore, $\hat{h}_{c_2} - \hat{h}_{c_1} = 0$, and the plateau closes.

The above discussion of the plateau boundary gives the UUD phase diagram is shown in **Figure 3.7**, where the two axes are more physically meaningful.

3.2.9 Instability near $d = 4$

We see that the dispersions of $d_{1,2}$ modes are unstable beyond end point $d = 4$, namely the plateau is destroyed. We are seeking the spin current (nematic) states near the end point. So, from now on, we focus on the end point with $d = 4$ and momentum $k = \pm k_0$.

The limit of w corresponding to $d = 4$, at which the magnetization plateau closes, is $|w_c| = |j - \frac{1}{2}| = \sqrt{\Delta\hat{h}}/2 = \sqrt{0.261/(2S)}$. This relation gives the limit of J_2 to make the

$M = 1/3$ plateau stable; its numeric values for different spins are shown in **Figure 3.12**.

When $d = 4$, the dispersions (3.134) are simplified by,

$$\omega_{1,2} = \pm(\hat{h} - \hat{h}_{\text{end}} + k_0^2 - k^2) + 2|k^2 - k_0^2|. \tag{3.140}$$

If field $\hat{h} = \hat{h}_{\text{end}}$, Eq. (3.140) are further simplified as,

$$\omega_1 = 2|k^2 - k_0^2| - (k^2 - k_0^2), \quad \omega_2 = 2|k^2 - k_0^2| + (k^2 - k_0^2). \tag{3.141}$$

These dispersions are schematically shown in **Figure 3.13**.

3.2.9.1 Divergent ϕ

Now let us focus on the rotation angle ϕ, which is k-dependent and defined in (3.132). At $d = 4$ or $|w| = \sqrt{\Delta\hat{h}}/2$, the Eq. (3.132) as a function of k is,

$$\tanh[2\phi_k]|_{d=4} = \text{Sign}(-kw) \times \frac{4(k/\sqrt{\Delta h})}{1 + 4(k/\sqrt{\Delta h})^2}. \tag{3.142}$$

For the purpose of this study, we are interested in k near $\pm k_0$. When $k = \pm k_0$, $\tanh[2\phi_{\pm k_0}] = \pm 1$. This implies $\phi_{\pm k_0}$ diverges near $\pm k_0$,

S	$\frac{1}{2}$	1	$\frac{3}{2}$	2
|w|	0.510882	0.361248	0.294958	0.255441
J_2max	1.01088	0.861248	0.794958	0.755441
J_2min	−0.0108816	0.138752	0.205042	0.244559

Figure 3.12. Limit of the ratio J_2/J_1, within which the magnetization plateau exists, determined from end point $d = 4$.

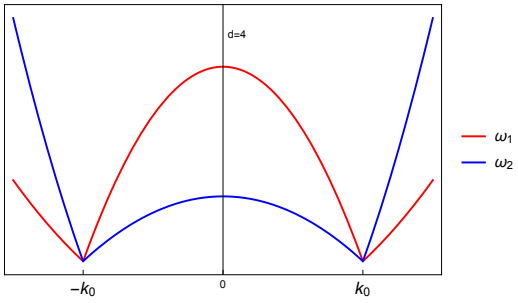

Figure 3.13. The dispersions of two low-energy modes at end point $d = 4$.

$$\begin{aligned}
&\cosh[2\phi_k]|_{d=4+\delta} = \frac{k_0^2+k^2}{\sqrt{(k^2-k_0^2)^2+(4-d)k^2k_0^2}} \simeq \frac{2k_0^2}{\sqrt{(k^2-k_0^2)^2+(4-d)k_0^4}},\\
&\sinh[2\phi_k] \simeq \begin{cases} \cosh[2\phi_k] = \frac{1}{2}e^{2\phi_k}, \text{ for } \phi_k > 0, \\ -\cosh[2\phi_k] = -\frac{1}{2}e^{-2\phi_k}, \text{ for } \phi_k < 0. \end{cases}
\end{aligned} \tag{3.143}$$

Denote $g^2(k) \equiv \cosh[2\phi_k]$, then $g(k)$ is,

$$g(k) = \frac{\sqrt{2}k_0}{[(k^2-k_0^2)^2+(4-d)k_0^4]^{\frac{1}{4}}}. \tag{3.144}$$

In the vicinity of $k = \pm k_0$,

$$g(k)|_{k\sim\pm k_0} \simeq \frac{\sqrt{k_0}}{[(k\pm k_0)^2+(1-d/4)k_0^2]^{\frac{1}{4}}}, \quad \text{and} \quad g^2(k)|_{k=\pm k_0+p,d=4} \simeq \frac{k_0}{|p|}. \tag{3.145}$$

Now express original magnons a, b, c in terms of decoupled low-energy modes d_1 and d_2, (combining Eq. (3.117), (3.120), and (3.131))

$$\begin{aligned}
a_k &= \frac{1}{\sqrt{2}}\left\{(\cosh\phi_k + i\sinh\phi_k)d_{1,k} - (\cosh\phi_k - i\sinh\phi_k)d^\dagger_{2,-k}\right\},\\
b_k &= \frac{-1}{\sqrt{2}}\left\{(\cosh\phi_k - i\sinh\phi_k)d_{1,k} + (\cosh\phi_k + i\sinh\phi_k)d^\dagger_{2,-k}\right\},\\
c_{-k} &= \sqrt{2}(\cosh\phi_k d_{2,-k} - i\sinh\phi_k d^\dagger_{1,k}).
\end{aligned} \tag{3.146}$$

Here $\cosh\phi_k + i\sinh\phi_k$ can be expressed by $g(k)$,

$$\cosh\phi_k + i\sinh\phi_k = g(k)e^{is_k}, \quad s_k = \frac{\pi}{4}\mathrm{Sgn}(-kw). \tag{3.147}$$

Then near $d = 4$ and $k = \pm k_0$, the transformation (3.146) can be simplified as Eq. (3.95) in the main text.

3.2.9.2 Pairing interaction between d_1 and d_2

Plug into the fourth-order Hamiltonian Eq. (3.113) and (3.114), namely, $H^{(4)} = H_z^{(4)} + H_\perp^{(4)}$, we obtain the interaction between low-energy magnons, with momentum k near $\pm k_0$. Here, we only consider the $w < 0$ case, so that s_k only depends on the sign of k. And we consider the reduced problem of the magnon pair with **zero** total momentum.

Magnon pairs with total momentum zero, with $\Psi_k = d_{1,k}d_{2,-k}$, $\Phi_1(k) = d_{1,k}d_{1,-k}$, and $\Phi_2(k) = d_{2,k}d_{2,-k}$. And near $k = \pm k_0$, $f_{k_2-k_1} \sim 1$. From the expression for $g(k)$ in Eq.(3.144), we see $g(k)$ is an even function of k. And s_k is an odd function of k. After the pairing, the 4 boson Hamiltonian has two contributions, coupling between the same mode, and one from different modes.

(a) The $d_1 - d_1$ interaction,

$$H^{(4)}_{d_1-d_1} = \frac{3}{N}(J_1+J_2)\sum_{k,p} g(k)^2 g(p)^2 \Phi_1^\dagger(k)\Phi_1(p) \begin{cases} 0, \text{for } k,\ p \text{ same sign}, \\ \frac{1}{2}, \text{for } k,\ p \text{ different sign}. \end{cases} \tag{3.148}$$

We see near $d = 4$, and $k = \pm k_0$, the d_1 mode does not form bound states. Therefore,

$$H^{(4)}_{d_1-d_1} = \frac{3}{N}(J_1+J_2)\sum_{k,p} g(k)^2 g(p)^2 \Phi_{1,R}^\dagger(k)\Phi_{1,L}(p), \tag{3.149}$$

the interaction between d_1 modes is repulsive.

(b) The $d_1 - d_2$ interaction,

$$H^{(4)}_{d_1-d_2} = \frac{3}{N}(J_1+J_2)\frac{1}{4}\sum_{k,p} g(k)^2 g(p)^2 [1 - \mathrm{Sgn}(k)\mathrm{Sgn}(p)][\Psi(k) - \Psi^\dagger(k)][\Psi(p) - \Psi^\dagger(p)]. \tag{3.150}$$

If k and p have different signs, the interaction between $d_1 - d_2$ is negative (attractive), namely k near k_0 and p near $-k_0$, or vice versa. The two-magnon condensates and forms a bond state. Then,

$$H^{(4)}_{d_1-d_2} = \frac{3}{N}(J_1+J_2)\sum_{k\in R, p\in L} g(k)^2 g(p)^2 [\Psi_R(k)\Psi_L(p) - \Psi_R^\dagger(k)\Psi_L(p) + h.c.]. \tag{3.151}$$

The prefactor $\frac{1}{4} \times 2 \times 2 = 1$; the first 2 comes from the different signs of k and p, and 2 from the way to choose R. Here, R and L just stand for k near k_0 or $-k_0$, respectively. This interaction includes both the normal $2 \to 2$, which is attractive and "anomalous" $4 \to 0$ or $0 \to 4$ process, which is repulsive. To summarize above, the normal $2 \to 2$ processes between different channels are attractive and dominant. The attraction diverges when the bosons are near k_0 (to exploit the scattering potential as much as possible). Therefore, we consider things only near k_0 below. (Strongly gapped modes do not contribute to magnon condensation for weak interactions, so near the critical fields we need only consider interactions between near-gapless modes.[138]) At $k = \pm k_0 + p$, and $p \ll k_0$,

$$\gamma^2(p) \equiv g^2(\pm k_0 + p) \simeq \frac{k_0}{\sqrt{p^2 + (1-d/4)k_0^2}} \xrightarrow[d=4]{} \frac{k_0}{|p|}. \tag{3.152}$$

To have the same notation with,[19] we denote $\Psi_R(p) = d_{1,k_0+p}d_{2,-k_0-p}$, and $\Psi_L(p) = d_{1,-k_0+p}d_{2,k_0-p}$. Then Eq. (3.151) is,

$$H^{(4)}_{d_1d_2} = \frac{3}{N}\sum_{p,q}\Gamma(p,q)[\Psi_R^\dagger(q)\Psi_L(p) - \Psi_R(q)\Psi_L(p) + h.c.], \tag{3.153}$$

with

$$\Gamma(p,q) = -(J_1+J_2)\gamma^2(p)\gamma^2(q) \xrightarrow[d=4]{} -(J_1+J_2)\frac{k_0^2}{|p||q|}. \tag{3.154}$$

This is the scattering interaction between d_1 and d_2 modes from two sides of the minimum momentum point.

3.2.9.3 Two-magnon condensation

If a stable bound state of magnons (a magnon pair) exists, the single-magnon BEC is not necessarily the leading instability from the UUD state. In fact, if the gap of the magnon pair is smaller than double that of the single-magnon, magnon-pair condensation occurs and the spin-nematic order $\langle S^{\pm}\rangle = 0$, $\langle S_1^+ S_1^+\rangle \neq 0$ takes place.

Follow the pairing approximation in superconductivity[152] (to have linearized equation of motion), with the reduced UUD Hamiltonian,

$$H^{(2)}_{\text{uud}} = \frac{3}{2}J_1 S\sum_k(\omega_1 d^\dagger_{1,k}d_{1,k} + \omega_2 d^\dagger_{2,k}d_{2,k}). \tag{3.155}$$

$\Psi_R(p)$ satisfy,

$$\begin{aligned}
[H^{(2)}_{\text{uud}}, \Psi_R(p)] &= -\Omega_R(p)\Psi_R(p), \quad [H^{(2)}_{\text{uud}}, \Psi^\dagger_R(p)] = \Omega_R(p)\Psi^\dagger_R(p),\\
[H^{(2)}_{\text{uud}}, \Psi_L(p)] &= -\Omega_L(p)\Psi_L(p), \quad [H^{(2)}_{\text{uud}}, \Psi^\dagger_L(p)] = \Omega_L(p)\Psi^\dagger_L(p),
\end{aligned} \tag{3.156}$$

with excitation energy

$$\Omega_R(p) \equiv \frac{3}{2}J_1 S[\omega_1(k_0+p)+\omega_2(-k_0-p)], \quad \Omega_L(p) \equiv \frac{3}{2}J_1 S[\omega_1(-k_0+p)+\omega_2(k_0-p)], \tag{3.157}$$

and $\Psi_R(p)^\dagger$ create a magnon pair near k_0, $\Psi_L(p)^\dagger$ create a magnon pair near $-k_0$, and they are eigenoperators of reduced Hamiltonian. Now we are interested at the commutators,

$$\begin{aligned}
&[\Psi_R(p), \Psi^\dagger_R(q)] = \delta_{p,q}(1 + d^\dagger_{1,k_0+p}d_{1,k_0+p} + d^\dagger_{2,-k_0-p}d_{2,-k_0-p}),\ [\Psi_R(p), \Psi^\dagger_L(q)] = 0 (p,q \ll k_0),\\
&[\Psi_L(p), \Psi^\dagger_L(q)] = \delta_{p,q}(1 + d^\dagger_{1,-k_0+p}d_{1,-k_0+p} + d^\dagger_{2,k_0-p}d_{2,k_0-p}),\ [\Psi_{R/L}(p), \Psi_{R/L}(q)] = 0.
\end{aligned} \tag{3.158}$$

Now we see, $\Psi_R(p)$ and $\Psi_L(p)$ are boson-like objects. Notice: for the commutator between R and L composite bosons is,

$$[\Psi_R(k), \Psi^\dagger_L(p)] = \delta(k_0+k, -k_0+p)(d_{1,k_0+k}d^\dagger_{1,k_0+k} + d^\dagger_{2,-k_0-k}d_{2,-k_0-k}). \tag{3.159}$$

The delta function above implies for non-zero when $p-k = 2k_0$, which is not possible for considering the strong interaction only (with $p,k \ll k_0$). At the UUD plateau, there is a

gap for excitation of d_1 and d_2. Therefore, average $\langle d^\dagger_{1/2,k} d_{1/2,k}\rangle_0 = 0$ over the ground state. Then the commutators above are,

$$\begin{aligned}
&[\Psi_R(p), \Psi_R^\dagger(q)] = \delta_{p,q}, \quad [\Psi_R(p), \Psi_L^\dagger(q)] = 0(p, q \ll k_0), \\
&[\Psi_L(p), \Psi_L^\dagger(q)] = \delta_{p,q}, \quad [\Psi_{R/L}(p), \Psi_{R/L}(q)] = 0.
\end{aligned} \tag{3.160}$$

Thus there are canonical bosonic commutation relations for boson-pair operator $\Psi_{R/L}$.

3.2.9.4 Self-consistent condition

The total Hamiltonian for UUD state is,

$$\begin{aligned}
&H_{\text{uud}} = H^{(2)}_{\text{uud}} + H^{(4)}_{\text{uud}} \\
&H^{(4)}_{\text{uud}} = \frac{3}{N}\sum_{p,q}\Gamma(p,q)[\Psi_R^\dagger(q)\Psi_L(p) - \Psi_R(q)\Psi_L(p) + \Psi_L^\dagger(p)\Psi_R(q) - \Psi_L^\dagger(p)\Psi_R^\dagger(q)],
\end{aligned} \tag{3.161}$$

Then the commutator,

$$[\Psi^\dagger_{R/L}(k), H^{(4)}_{\text{uud}}] = [\Psi_{R/L}(k), H^{(4)}_{\text{uud}}] = \frac{3}{N}\sum_p \Gamma(p,k)(\Psi_{L/R}(p) - \Psi^\dagger_{L/R}(p)). \tag{3.162}$$

Therefore, the equation of motion for pair operator $\Psi_{R/L}$ is,

$$\begin{aligned}
i\frac{\partial \Psi_R(k)}{\partial t} &= \Omega_R(k)\Psi_R(k) + \frac{3}{N}\sum_p \Gamma(p,k)(\Psi_L(p) - \Psi_L^\dagger(p)), \\
i\frac{\partial \Psi_R^\dagger(k)}{\partial t} &= -\Omega_R(k)\Psi_R^\dagger(k) + \frac{3}{N}\sum_p \Gamma(p,k)(\Psi_L(p) - \Psi_L^\dagger(p)), \\
i\frac{\partial \Psi_L(k)}{\partial t} &= \Omega_L(k)\Psi_L(k) + \frac{3}{N}\sum_p \Gamma(p,k)(\Psi_R(p) - \Psi_R^\dagger(p)), \\
i\frac{\partial \Psi_L^\dagger(k)}{\partial t} &= -\Omega_L(k)\Psi_L^\dagger(k) + \frac{3}{N}\sum_p \Gamma(p,k)(\Psi_R(p) - \Psi_R^\dagger(p)),
\end{aligned} \tag{3.163}$$

and we notice the equations above are linear in $\Psi_{R/L}$. Fourier transform $\Psi_{R/L}(k,t)$,

$$\Psi_{R/L}(k,t) = \int_{-\infty}^{\infty} \Psi_{R/L}(k,\omega)e^{-i\omega t}d\omega, \tag{3.164}$$

and plug into the above equations, we get,

$$\begin{aligned}
\omega\Psi_R(k,\omega) &= \Omega_R(k)\Psi_R(k,\omega) + \frac{3}{N}\sum_p \Gamma(p,k)(\Psi_L(p,\omega) - \Psi_L^\dagger(p,\omega)), \\
\omega\Psi_R^\dagger(k,\omega) &= -\Omega_R(k)\Psi_R^\dagger(k,\omega) + \frac{3}{N}\sum_p \Gamma(p,k)(\Psi_L(p,\omega) - \Psi_L^\dagger(p,\omega)),
\end{aligned} \tag{3.165}$$

For the pair state to be condensate, the pair operator would be static, and $\omega = 0$, then

$$\langle \Psi_R^\dagger(k) - \Psi_R(k)\rangle = \frac{3}{N}\frac{2(J_1+J_2)\gamma^2(k)}{\Omega_R(k)}\sum_p \gamma^2(p)\langle \Psi_L^\dagger(p) - \Psi_L(p)\rangle, \tag{3.166}$$

where we have used $\Gamma(k,p) = -(J_1+J_2)\gamma^2(k)\gamma^2(p)$. Also, we would have

$$\langle \Psi_L^\dagger(k) - \Psi_L(k)\rangle = \frac{3}{N}\frac{2(J_1+J_2)\gamma^2(k)}{\Omega_L(k)}\sum_p \gamma^2(p)\langle \Psi_R^\dagger(p) - \Psi_R(p)\rangle. \tag{3.167}$$

Here because $k, p \ll k_0$, then $\Omega_R(k) \simeq \Omega_L(k) \equiv \Omega_k$, then the self-consistent condition gives,

$$2(J_1+J_2)\frac{3}{N}\sum_p \frac{\gamma^4(p)}{\Omega_p} = 1, \xrightarrow[d=4]{} \left(\frac{1}{4}\right)\frac{1}{S}\frac{3}{N}\sum_p \frac{k_0}{|p|^3} = 1. \tag{3.168}$$

There is a factor of $1/4$ difference from the result in the 2D case,[19] and the difference comes from the dispersion relations. We see the above equation is divergent at $d = 4$. Therefore the self-consistent equation must have a solution before $d = 4$ at d_c . That corresponds to a magnon pair condensation, and it is before the single magnon condensation which happens at $d = 4$.

Now we need to find that d_c, which is near $d = 4$, from Eq. (3.152) and (3.91),

$$\gamma^2(p) \simeq \frac{k_0}{\sqrt{p^2 + (1-d/4)k_0^2}}, \quad \Omega_p \simeq (J_1+J_2)8k_0\sqrt{p^2+(1-d/4)k_0^2}. \tag{3.169}$$

Then the $|p|$ in Eq. (3.168) is replaced by $\sqrt{p^2+(1-d/4)k_0^2}$, and the self-consistent equation which gives d_c is,

$$\frac{1}{4S}\frac{3}{N}\sum_p \frac{k_0}{[p^2+(1-d_C/4)k_0^2]^{3/2}} = 1. \to \frac{3}{2\pi}\int_{\pi/3}^{\pi/3}\frac{dp}{[p^2+(1-d_C/4)k_0^2]^{3/2}} = 4S/k_0. \tag{3.170}$$

The above integral is convergent, and make a approximation

$$\frac{3}{2\pi}\int_{\pi/3}^{\pi/3}\frac{dp}{[p^2+(1-d_c/4)k_0^2]^{3/2}} \simeq \frac{3}{\pi}\int_0^\infty \frac{dp}{[p^2+(1-d_c/4)k_0^2]^{3/2}}. \tag{3.171}$$

This is a standard integral,[153]

$$\int_0^\infty \frac{dx}{(x^2+a^2)^{3/2}} = \frac{1}{a^2}. \tag{3.172}$$

Therefore, the critical d_c when the magnon pair condensate is,

$$\frac{1}{(1-d_c/4)k_0^2} = \frac{\pi}{3}\frac{4S}{k_0}, \quad \to 4 - d_c = \frac{3}{\pi}\frac{1}{Sk_0} = \frac{3}{\pi}\sqrt{\frac{4}{0.522}}\frac{1}{\sqrt{S}} \simeq \frac{2.64}{\sqrt{S}}. \tag{3.173}$$

Therefore, the instability happens at $4 - d_c = c_1/\sqrt{S}$, the corresponding numeric value of d_c to different spin S shown in **Figure 3.14**.

S	$\frac{1}{2}$	1	$\frac{3}{2}$	2	$\frac{5}{2}$	3	$\frac{7}{2}$	4	$\frac{9}{2}$
$4-d_c$	3.74	2.64	2.16	1.87	1.67	1.53	1.41	1.32	1.25
d_c	0.26	1.36	1.84	2.13	2.33	2.47	2.59	2.68	2.75

Figure 3.14. Corresponding critical d_c, at which two-magnon condensation happens, to different spin S.

CHAPTER 4

CONCLUSION

This chapter is divided into three sections. Sec. 4.1 is a summary of this dissertation. Sec. 4.2 presents a discussion of the contributions and limitations of the current work. Sec. 4.3 discusses the future work.

4.1 Summary

For this dissertation, I successfully implement quantum field theory and spin-wave theory to predict and characterize novel magnetic states of matter in the context of low-dimensional frustrated magnets, namely, the antiferromagnetic Heisenberg spin chains and triangular antiferromagnets. The states are "novel" in a way that the interplay between quantum fluctuations and interactions generates behaviors not expected classically. In the current work, we have identified a wide variety of novel ordered phases with nontrivial spin structures, and construct microscopic models for quantum spin liquid.

In Chapter 2, we investigated the behavior of quantum spin chains in the presence of a uniform Dzyaloshinskii-Moriya (DM) interaction[42,43] using the bosonization[50,52,53] approach. Quantum spin chain is an outstanding model exploring strongly correlated quantum orders in low dimensional antiferromagnets and cold atoms. It is the building block of many 2D/3D spin systems. DM interaction originates from spin-orbit coupling, and is widely present in real materials. This line of study of the DM spin chain system provides a better understanding of novel phases in real spin chain materials and cold atoms under spin-orbit couplings.

In Sec. 2.1, we investigated how the interplay between uniform DM interactions, small anisotropy, and a magnetic field influences a single Heisenberg spin chain. We showed that this interplay enriches the phase diagram, including a critical Luttinger liquid and two antiferromagnetic spin-density-wave (Ising-like) phases. The critical Luttinger liquid is characterized by incommensurate spin and dimerization power-law correlations, and is

a quantum analogue of the classical chiral soliton lattice.[72] The order parameters for two Ising-like orders are estimated as well. In addition, we found that significant finite-size corrections observed numerically[65] are well explained by the 'logarithmic slowness' of the Kosterlitz-Thouless (KT) renormalization group (RG) flow.

The work presented in Sec. 2.2 is closely related to experiments on two new materials[12,45,90] ($K_2CuSO_4(Cl/Br)_2$), both of which are modeled as weakly coupled spin chains. Despite the structural similarity, they are characterized by different phase diagrams. This phenomenon results from the special geometry of DM interactions—staggered between chains, but uniform within a given chain. Such a geometry leads to a peculiar type of frustration: strong DM interaction (in comparison with interchain exchange) forces the spins on neighboring chains to rotate in opposite directions, effectively canceling the transverse interchain coupling. This has the effect of strongly reducing the ordering temperature. I explore the response of this interesting system to an external magnetic field under two experimentally relevant geometries, with the field parallel and perpendicular to the DM vector, respectively. The phase diagrams obtained for a field parallel to DM interaction configuration have a striking resemblance with the experimental determined ones,[12,45] when Cl- and Br-based materials are interpreted as that with weak and strong DM interaction, respectively. The phase diagrams for a field perpendicular to DM interaction resemble that of the single spin chain in Sec. 2.1 (compare **Figure 2.18** with **Figure 2.3**). This resemblance in turn confirms that the interchain interactions are wiped out by the DM-induced frustration.

In Sec. 2.3, we presented a feasible way to construct a chiral spin liquid from a weakly coupled spin chain system. Inspired by the fact that the staggered-between-chain geometry of DM interactions suppresses the relevant, in an RG sense, transverse interchain couplings, we found that after removing the relevant part of couplings by staggered DM interactions, the remaining marginal interactions between left- and right-moving fermion currents from neighboring chains produce a energy gap. Then the left- and right-moving modes in the spatially separated edge chains are unpaired. This picture implies the emergence of chiral edge states. This model realizes a topologically nontrivial state known as Kalmeyer-Laughlin[29] chiral spin liquid.

In Chapter 3, we studied antiferromagnets where the geometry of lattice is based on

triangles. Such magnets continue to be of substantial interest. For these magnets, magnetic ordering is often suppressed to temperatures below what is expected from near neighbor interactions. The ordered state that finally occurs is a consequence of a subtle balance among different factors. Here in this dissertation, we considered factors such as spatial anisotropy, exchange anisotropy and interactions between second nearest neighbors. These factors were analyzed on a case-by-case basis.

In Sec. 3.1, we considered anisotropic 2D Heisenberg antiferromagnets on a triangular lattice in a high magnetic field close to the saturation. The anisotropy can be spatial, whereby exchange interactions on three bonds of the elementary triangle take two different values, or in spin space with XXZ-type exchange anisotropy. For both cases, classical degeneracies and quantum fluctuations are favored to select magnetic orders with different order parameter manifolds. The competition between classical and quantum orders leads to multiple transitions and highly nontrivial intermediate phases, including a novel state that arises from magnons condensate at two nondegenerate energy minima. The analysis of this section can be easily extended to quasi-2D layered systems, with small interlayer antiferromagnetic interaction. This additional exchange interaction leads to the staggering of coplanar spin configurations between the adjacent layers, in agreement with earlier studies.[125,133]

In Sec. 3.2, we identified a bond nematic state in a frustrated Heisenberg spin chain with both nearest-neighbor and next-neighbor antiferromagnetic exchanges, namely a zigzag chain. A one-third magnetization plateau exists for a zigzag chain near the Majumdar-Ghosh[140,141] point. Within the plateau, spin structure is known as the up-up-down in an elementary triangle. We showed the plateau ends via formation of bound magnon pairs, which undergo a Bose Einstein Condensation prior to the onset of a conventional one-magnon instability. The resulting state possesses, instead of standard dipolar order, a hidden quadrupolar-nematic order. The corresponding order parameter is defined on the bond between two neighboring sites by a rank-2 tensor mode of local spin degrees of freedom. We found that the width of this bond nematic phase is scaled as $1/\sqrt{S}$, which is much stronger than $1/S^2$ dependence found previously in 2D triangular[19] and Kagome[138] lattice.

4.2 Contributions and limitations

The two main lines of research in the field of frustrated quantum magnets are searches for spin-liquid phases and for new ordered phases with highly nontrivial spin structures.[4] This dissertation provides efforts in both research directions.

Usually, magnetic frustrations are introduced through lattice geometry (see **Figure 1.2**) or competing exchange interactions (see **Figure 1.3** and **Figure 3.6**). One of the most important contributions of our work is that we found a new mechanism to produce the magnetic frustration. This is achieved by including the uniform-within-chain, but staggered-between-chain Dzyaloshinskii-Moriya (DM) interactions, as stated in Sec. 2.2, to a weakly coupled Heisenberg spin chain system. Furthermore, by taking advantage of the frustrations generated by the geometry of DM interactions, we devise a new feasible microscopic model to construct the chiral spin liquid in magnetic insulators, spin counterparts of fractional quantum Hall effect. Our model supports a potential candidate for the currently popular coupled-wire approach to (mostly chiral) spin liquids.[37,110,111] This line of study deepens our understanding of new physics associated with strong spin-orbit interactions.

In addition, my study offers a suggestive candidate to search for experimental realization of bond nematic on the antiferromagnetic zigzag chain. Unlike ferromagnetic chain candidate[154,155] $LiCuVO_4$, which may host a similar bond-nematic state within a narrow magnetic field range around 40 T and just below saturation, in our antiferromagnetic chain model, this novel order appears at a magnetic field at one third of its saturation, which is much lower than 40 T. This model serves as a more experimentally accessible alternative to study and observe the long sought spin nematic order.

All of the obtained results are based on perturbative calculations, framed in either RG, chain mean field (CMF), or semiclassical language. The complete consistency between these two techniques observed in our work on DM spin chain provides strong support in favor of its validity. Higher order magnon interactions up to the sixth order have been considered in the study of phases of triangular antiferromagnets. Nonetheless, some independent numerical checks of the present arguments are highly desired. The predicted bond nematic state is unexplored at the experimental level, and the realizations of materials are still lacking.

4.3 Implications and future work

In condensed matter physics, one of the ultimate goals is to determine and understand all phases or states of matter. Frustrated magnetism has presented an excellent proving ground to discover new states and new properties of matter. In this dissertation, we have proposed several novel states on experimentally relevant frustrated lattices. We hope these results will stimulate both further experimental and numerical studies. The ever rapid progress in synthesis of new materials and in development of computation and measurement facilities also motivates our analytical understanding of new states of matter.

The study of a single DM spin chain opens up a possibility of the experimental check of theoretical predictions in quasi-one-dimensional antiferromagnets with a uniform DM interaction.[45,78] The idea is to probe the spin correlations at a finite temperature above the critical ordering temperature of the material when interchain spin correlations, which drive the three-dimensional ordering, are not important while individual chains still possess sufficient large separations for experimental detection anisotropy of spin correlations caused by the uniform DM interaction. Under these conditions one should be able to probe the fascinating competition between the uniform DM interaction and the transverse external magnetic field.

We hope that our detailed investigation on system of weakly coupled DM spin chains will prompt further experimental studies of the interesting experimentally relevant compounds, $K_2CuSO_4Cl_2$ and $K_2CuSO_4Br_2$, in particular in the less studied so far $\boldsymbol{h} \perp \boldsymbol{D}$ configuration. In Ref.,[90] the magnetic field is applied in the diagonal direction in the plane perpendicular to DM vector. It should be possible to apply the magnetic field perpendicular to the DM vector, and obtain magnetic phase diagram through thermal dynamic measurements. Alternatively, one can develop an analytical study of the phase diagram for a field orientation in Ref.[90] These works will shed more light on the intricate interplay between the magnetic field, DM and interchain interactions present in this interesting class of quasi-one-dimensional materials. We also hope our work will stimulate numerical studies of this interesting problem along the lines of quantum Monte Carlo studies in Refs.[108,109]

A possible future direction along the construction of chiral spin liquid is to develop a gauge field understanding of the existing model. At the same time, there are difficulties

in finding materials that realize this model approximately. Sometimes one can ask about what other systems can produce the same physics. In the example of chiral spin liquid model, staggered-between-chains g tensors are also required, which is rare for crystal materials. However, in the context of cold atoms in optical lattice, the staggered particle current in the tight-binding regime may result in an artificially staggered magnetic field.[117]

The statement of the presence of bond nematic on zigzag chain is also open to numerical calculations, such as density matrix renormalization group (DMRG)[7,14] and quantum Monte Carlo (QMC).[142] Even though, identification of the bond nematic, at the end of magnetization plateau, in a narrow range of parameter would be challenging. As for real materials it is promising to realize the nematic spin state are[143–146] the CaV_2O_4 and $NaV(WO_4)_2$ compounds. We hope material scientists can invent new families of compounds that can be modeled as zigzag chains to probe nematic behavior.

APPENDIX A

RENORMALIZATION GROUP AND OPERATOR PRODUCT EXPANSION

A.1 Perturbative renormalization group

For real magnetic systems, it is natural that they are in the presence of many kinds of perturbations. It is very important to know which interactions are important and which are not. Obviously, we can neglect interactions whose effect on the correlation functions is small. However, usually the correlation functions are affected differently on a different scale. It can happen that a certain perturbation causes only tiny changes at short distances, but changes the large distance behavior profoundly. That is when we come to the renormalization group (RG) technique, by comparing the growth of the coupling constant associated with the perturbing operator.

RG proceeds by integrating short-distance modes (small distance x or large momentum k_x) and by progressively reducing the large-momentum cutoff from its bare value $\Lambda \sim 1/a$, which is of the order of the inverse lattice spacing a [which we take to be $O(1)$], to $\Lambda_\ell = \Lambda e^{-\ell}$, where $\ell \in (0, \infty)$ is the logarithmic RG scale. Correspondingly, the minimal real-space scale increases as ae^{ℓ}. Various interaction couplings γ_i, which enter the Hamiltonian as $\mathcal{H} = \mathcal{H}_0 + \sum_i \int dx \gamma_i \mathcal{O}^i(x)\mathcal{O}^i(x)$, see (2.64), where $\mathcal{O}^i_y$ represent the y-th chain operator J^a_y in (2.3) or N^a_y in (2.4), get renormalized (flow) during this procedure. This renormalization is described by the perturbative RG flow equation of the dimensionless coupling[97] $\tilde{\gamma}_i = \gamma_i/(v\Lambda_\ell^2)$:

$$\frac{d\tilde{\gamma}_i}{d\ell} = (2 - 2\Delta_i)\tilde{\gamma}_i \tag{A.1}$$

Here Δ_i is the scaling dimension of the operator $\mathcal{O}^i_y$, which in the case of relevant operator (2.4) (the staggered magnetization), can be represented as $\Delta_i = 1/2 + O(y)$, where y stands

for the dimensionless marginal coupling. For the marginal operator, say $\mathcal{O}_y^k$, the scaling dimension is close to 1, $\Delta_k = 1 + O(y)$, and as a result the flow of the marginal operator obeys $dy/d\ell \sim y^2$. [See (2.74) below for the specific example of both of these features.] Dimensionless coupling constants of the relevant operators increase with ℓ. RG flow needs to be stopped at the RG scale ℓ^* at which the first coupling, say $\tilde{\gamma}_j$, reaches the value $C \sim O(1)$ of order 1. According to (A.1) ℓ^* can be estimated as $\ell^* = \ln[C/\tilde{\gamma}_j(\ell = 0)]/(2 - 2\Delta_j)$. The length scale $\xi = ae^{\ell^*}$ defines the correlation length above which the system needs to be treated as two- or three-dimensional. The type of the developed two-dimensional order is determined by the most relevant operator $\mathcal{O}_y^j$, the coupling constant of which has reached $C \sim O(1)$ first. Its expectation value can be estimated as $\langle \mathcal{O}^j \rangle \sim \xi^{-\Delta_j}$ and therefore, using $\tilde{\gamma}_j(\ell = 0) = \gamma_j/(v\Lambda_{\ell=0}^2)$ and $\Lambda_{\ell=0} \sim O(1)$, we obtain

$$\langle \mathcal{O}^j \rangle \sim \xi^{-\Delta_j} = \left(\frac{\gamma_j}{Cv}\right)^{\Delta_j/(2-2\Delta_j)}. \tag{A.2}$$

This discussion makes it clear that the perturbative RG procedure is inherently uncertain since both Eq. (A.1) and the "strong-coupling value" estimate C are based on the perturbation expansion in terms of the coupling constants γ_i. Moreover, in the case of the competition between the two orders, associated with operators $\mathcal{O}^j$ and $\mathcal{O}^i$ correspondingly, the transition from one order to another can only be *estimated* from the condition $\ell_j^* = \ell_i^*$.

This approximate treatment becomes more complicated when some of the interactions acquire a coordinate-dependent oscillating factor, symbolically $\int dx \gamma_i \mathcal{O}_y^i(x) \mathcal{O}_{y+1}^i(x) e^{ifx}$. Such a dependence is caused by external magnetic field and/or DM interactions; see for example equations (2.68) and (2.71) below. Perturbative RG calculation is still possible, see for example Sec.4.2.3 of Giamarchi[52] for its detailed description, but becomes technically challenging. At the same time the key effect of the oscillating term e^{ifx} can be understood with the help of much simpler qualitative consideration outlined, for example, in Ref.[93] and in Sec.18.IV of Gogolin *et al.*[50] Oscillation becomes noticeable on the spatial scale $x \sim 1/f$ which has to be compared with the running RG scale ae^{ℓ}. As a result, RG flow can be separated into two stages. During the first stage $0 \leq \ell \leq \ell_{\rm osc} = \ln(1/f)$ oscillating factor e^{ifx} can be approximated by 1, i.e., it does not influence the RG flow. At this stage all RG equations can be well approximated by their zero-f form. During the second stage $\ell_{\rm osc} \leq \ell \leq \ell^*$ and the product fx is not small anymore. The factor e^{ifx} produces a sign-

changing integrand. Provided that the coupling constant of that term remains small (which is the essence of the condition $\ell \leq \ell^*$), the integration over x removes such an oscillating interaction term from the Hamiltonian altogether.

This is the strategy we assume in this paper. It is clearly far from being exact but it is an exceedingly good approximation in the two important limits: the small-f limit when $\ell_{\rm osc} \gg \ell^*$ and the external field/DM interaction is not important at all, and in the large-f limit when $\ell_{\rm osc} \ll \ell^*$ and the oscillations are so fast that corresponding interactions average to zero. In between these two clear limits the proposed two-stage scheme[50,54] provides for a physically sensible interpolation.

A.2 Operator product expansion

We have a set of operators $O_i(x)$ in the perturbation Eq. (2.70) and (2.71) , with $O_i(x) = J^a_{R/L}(x)$ or $N^a(x)$, where $a = x, y, z$. The product of any two operators can be replaced by a series of terms involving operators of the same set,

$$\lim_{x\to 0} O_i(x)O_j(0) = \sum_k C^k_{ij} \frac{1}{|x|^{\Delta_i+\Delta_j-\Delta_k}} O_k(0). \tag{A.3}$$

This identity is known as the *operator product expansion* (OPE).[53] It tells us how different operators *fuse* with one another. In our case, the fusion rules of spin currents $\boldsymbol{J}_{R/L}$, staggered magnetization $\boldsymbol{N}$ and dimerization ξ are,[83]

$$\begin{aligned}
J^a_R(x,\tau)J^b_R(0) &= \frac{\delta^{ab}}{8\pi^2(v\tau - ix)^2} + \frac{i\epsilon^{abc}J^c_R(0)}{2\pi(v\tau - ix)},\\
J^a_L(x,\tau)J^b_L(0) &= \frac{\delta^{ab}}{8\pi^2(v\tau + ix)^2} + \frac{i\epsilon^{abc}J^c_L(0)}{2\pi(v\tau + ix)}.\\
J^a_R(x,\tau)N^b(0) &= \frac{i\epsilon^{abc}N^c(0) - i\delta^{ab}\xi(0)}{4\pi(v\tau - ix)},\\
J^a_L(x,\tau)N^b(0) &= \frac{i\epsilon^{abc}N^c(0) + i\delta^{ab}\xi(0)}{4\pi(v\tau + ix)}.\\
J^a_R(x,\tau)\xi(0) &= \frac{iN^a(0)}{4\pi(v\tau - ix)},\\
J^a_L(x,\tau)\xi(0) &= \frac{-iN^a(0)}{4\pi(v\tau + ix)}.
\end{aligned} \tag{A.4}$$

It can be shown that the coefficients C^k_{ij}, which are known as *structure constants* of the OPE, fix the quadratic terms in the RG (*renormalization group*) flow of coupling constants, specifically,

$$\frac{dg_k}{dl} = (2-\Delta_k)g_k - \sum_{i,j} C_{ij}^k g_i g_j. \tag{A.5}$$

Δ_k is the scaling dimension of the coupling term, which we approximate by its zero field value, namely Δ_k is 2 and 1 for $\boldsymbol{J}_{yR}\cdot\boldsymbol{J}_{yL}$ and $\boldsymbol{N}_y\cdot\boldsymbol{N}_{y+1}$ coupling terms.

Here, we provide an example of applying OPE and RG to $g_x N_y^x N_{y+1}^x$ term in our inter-chain Hamiltonian (2.71). In perturbative RG, there is a term,

$$\begin{aligned}
&\frac{1}{2}(2\pi v\int \mathrm{d}x\mathrm{d}\tau N_y^x(x,\tau)N_{y+1}^x(x,\tau))(2\pi v\int \mathrm{d}x'\mathrm{d}\tau' y_x M_{R,y}^x(x',\tau')M_{L,y}^x(x',\tau'))\\
=&\frac{1}{2}(2\pi v)^2\frac{1}{(4\pi)^2}\int \mathrm{d}x\mathrm{d}\tau\int \mathrm{d}X\mathrm{d}T\; g_x y_x \frac{N_y^x(X,T)N_{y+1}^x(X,T)}{(v\tau-ix)(v\tau+ix)}\\
=&2\pi v\;\delta g_x\int \mathrm{d}X\mathrm{d}T\; N_y^x(X,T)N_{y+1}^x(X,T).
\end{aligned} \tag{A.6}$$

Here,we have applied the OPE in the first step. In the second line (X, vT) are the center of mass coordinates, while $x\to x-x'$ and $\tau\to\tau-\tau'$ are the relative ones. The correction δg_x is given by the integral over RG shell from a to $a'=e^\delta l$,

$$\delta g_x = 2\times 2\times\frac{1}{8}g_x y_x\int_a^{a'}\mathrm{d}r\frac{1}{r} = \frac{1}{2}g_x y_x\ln(\frac{a'}{a}). \tag{A.7}$$

The first 2 comes from two neighboring chain, the second 2 is due to the fact that there are two equivalent terms as in Eq. (A.6) when one does perturbative expansion. This is equivalent to

$$\frac{dg_x}{dl} = g_x + \frac{1}{2}g_x y_x + \dots. \tag{A.8}$$

The other two terms which complete the RG equation (A.8) are similar as Eq. (A.6), and they are proportional to,

$$\int \mathrm{d}x\mathrm{d}\tau N_y^x N_{y+1}^x(x,\tau)\int \mathrm{d}x'\mathrm{d}\tau' y_y M_{R,y}^y M_{L,y}^y(x',\tau'), \tag{A.9}$$

and

$$\int \mathrm{d}x\mathrm{d}\tau N_y^x N_{y+1}^x(x,\tau)\int \mathrm{d}x'\mathrm{d}\tau' y_z M_{R,y}^z M_{L,y}^z(x',\tau'). \tag{A.10}$$

In the end the complete RG equation for g_x is,

$$\frac{dg_x}{dl} = g_x + \frac{1}{2}g_x y_x - \frac{1}{2}g_x y_y - \frac{1}{2}g_x y_z. \tag{A.11}$$

The minus sign of the last two terms is from the Levi-Civita epsilon in the fusion rules (A.4).

Then the RG equations of all the perturbation terms in Hamiltonian (2.69) are,

$$\begin{gathered}\frac{dy_x}{dl} = y_y y_z,\ \ \frac{dy_y}{dl} = y_z y_x,\ \ \frac{dy_z}{dl} = y_x y_y,\\ \frac{dg_x}{dl} = g_x[1+\frac{1}{2}(y_x - y_y - y_z)],\\ \frac{dg_y}{dl} = g_y[1+\frac{1}{2}(y_y - y_z - y_x)],\\ \frac{dg_z}{dl} = g_z[1+\frac{1}{2}(y_z - y_x - y_y)].\end{gathered} \tag{A.12}$$

With $y_x(0) = y_y(0)$ (see (2.73)), we have $y_x(l) = y_y(l)$ and $g_x(l) = g_y(l)$. Therefore, Eq. (A.12) reduces to,

$$\begin{gathered}\frac{dy_B}{d\ell} = y_B y_z,\ \frac{dy_z}{d\ell} = y_B^2,\\ \frac{dg_\theta}{d\ell} = g_\theta(1-\frac{1}{2}y_z),\ \frac{dg_z}{d\ell} = g_z[1+\frac{1}{2}(y_z - 2y_B)].\end{gathered} \tag{A.13}$$

Here g_θ and y_B are defined in Eq. (2.72). Marginal couplings $y_{z,B}$ grow much slower than $g_{\theta,z}$, so that we can approximate (A.13) by replacing $y_{z,B}$ with their initial values,

$$\frac{dg_\theta}{d\ell} = g_\theta[1+\frac{g_{\rm bs}}{4\pi v}(1+\lambda)],\ \frac{dg_z}{d\ell} = g_z[1+\frac{g_{\rm bs}}{4\pi v}(1-\lambda)]. \tag{A.14}$$

With $g_{\rm bs}, \lambda > 0$, we see g_θ grows faster than g_z.

APPENDIX B

CHAIN MEAN-FIELD APPROXIMATION

The perturbative RG procedure outlined in Appendix A is great for understanding the relative relevance of competing interchain interactions and for approximate understanding of the role of various perturbations. Its inherent ambiguity makes one look for a more quantitative description which matches RG at the scaling level but also allows us to account for the numerical factors associated with various interaction terms at the better than logarithmic accuracy level. Such description is provided by the chain mean-field (CMF) theory proposed in Ref.[95] and numerically tested for the system of weakly coupled chains in Refs.[108,109] In CMF, interchain interactions are approximated by a self-consistent Weiss field introduction of which reduces the coupled-chains problem to an effective single-chain one of the classical sine-Gordon kind, which is understood extremely well.[86,95] This approximation allows one to calculate the critical temperature T_i of the order associated with operator $\mathcal{O}^i$. The order with the highest T_i is assumed to be dominant. As mentioned in Appendix A.1, at the scaling level CMF theory matches the RG procedure and the highest T_i corresponds to the order with the shortest ℓ_i^*. The benefit of the CMF approach consists of the ability to account for the field-dependent scaling dimensions of various chain operators in a more systematic and uniform way as we detail below.

B.1 Chain mean-field (CMF) approximation

The chain mean-field (CMF) approximation consists of replacing the interchain interaction[97] by the self-consistent single-chain model

$$-\cos(\sqrt{2\pi}\theta_y)\cos(\sqrt{2\pi}\theta_{y+1}) \to -\Psi\cos(\sqrt{2\pi}\theta_y), \tag{B.1}$$

where Ψ stands for the expectation value of the staggered magnetization

$$\Psi \equiv \langle \cos(\sqrt{2\pi}\theta_y) \rangle. \tag{B.2}$$

Therefore the Hamiltonian of the system reduces to the sum of independent sine-Gordon models

$$\mathcal{H} = \sum_y \int \mathrm{d}x \frac{v}{2}[(\partial_x \phi)^2 + (\partial_x \theta)^2] - 2c\Psi \cos(\sqrt{2\pi}\theta_y), \tag{B.3}$$

where the factor of 2 arises from coupling to the two neighboring chains. To determine the critical temperature, we expand the partition function corresponding to the Hamiltonian (B.3) to the first order in Ψ and arrive at the self-consistent condition for $\Psi \neq 0$, which is[52]

$$\begin{aligned} \frac{1}{2c} &= \chi(q = 0, \omega_n = 0; T_c) \\ &= \int \mathrm{d}x \int_0^{1/T_c} \mathrm{d}\tau e^{i(qx+\omega\tau)} \langle O(x,\tau) O(0,0) \rangle_0, \end{aligned} \tag{B.4}$$

where $\chi(q, \omega_n; T)$ is momentum and frequency dependent susceptibility at finite temperature T. Depending on the type of order we consider, the operator O stands for

$$O = \cos(\sqrt{4\pi\Delta_1}\,\theta) \quad \text{or} \quad O = \cos(\sqrt{4\pi\Delta_2}\,\phi). \tag{B.5}$$

The scaling dimensions are listed in **Table 2.3**, $\Delta_1 = \pi R^2$ and $\Delta_2 = \pi/\beta^2$. Now we examine the ordering temperatures of each interaction in Eq. (2.71) and (2.79) individually. Here we follow the standard calculation in Ref.[97] which gives the following expressions for static susceptibilities (these are Eqs. (D.55) and (D.57) of Ref.[97]): for SDW order

$$\chi(q = 0, \omega_n = 0; T) = \frac{\pi}{2v}\Big[(2\pi T/v)^{2\Delta-2} \frac{\Gamma(1-\Delta)\Gamma(\Delta/2)^2}{\Gamma(\Delta)\Gamma(1-\Delta/2)^2} - \frac{\Gamma(\Delta - 1/2)}{\sqrt{\pi}(1-\Delta)\Gamma(\Delta)}\Big], \tag{B.6}$$

and for cone order

$$\begin{aligned} \chi(q = q_0, \omega_n = 0; T) &= \frac{\pi}{2v}(2\pi T/v)^{2\Delta-2} \frac{\Gamma(1-\Delta)}{\Gamma(\Delta)} \Big| \frac{\Gamma(\Delta/2 + ivq_0/4\pi T)}{\Gamma(1-\Delta/2 + ivq_0/4\pi T)} \Big|^2 \\ &= \frac{1}{4\pi v}(2\pi T/v)^{2\Delta-2} \frac{\Gamma(1-\Delta)}{\Gamma(\Delta)} |\Gamma(1-\Delta/2 + ivq_0/4\pi T)|^4 \times [\cosh(vq_0/2T) - \cos(\pi\Delta)]. \end{aligned} \tag{B.7}$$

Here, Δ is either Δ_1 or Δ_2. The second term in the brackets of Eq. (B.6) removes the non-physical divergence in the limit $\Delta \to 1$ near the saturation field. A similar compensating term is not needed in Eq. (B.7) because there $\Delta \approx 1/2$.

B.1.1 Cone order

Consider first the cone order in finite temperature, and its Hamiltonian is given by the first line in Eq. (2.84),

$$\mathcal{H}_{\text{cone}} = c_1 \sum_y \int \mathrm{d}x \cos[\beta(\tilde{\theta}_y - \tilde{\theta}_{y+1}) + 2(-1)^y t_\theta x], \tag{B.8}$$

with $c_1 = J' A_3^2$. We apply a position-dependent shift to the $\tilde{\theta}$ field to remove the oscillation and change the overall sign,

$$\tilde{\theta}_y = \breve{\theta}_y + (-1)^y \frac{\pi}{2\beta} - (-1)^y \frac{t_\theta}{\beta} x, \tag{B.9}$$

Next we apply the CMF approximation

$$\begin{aligned} \mathcal{H}_{\text{cone}} &= \sum_y \int \mathrm{d}x \frac{v}{2} [(\partial_x \tilde{\phi})^2 + (\partial_x \breve{\theta} - (-1)^y t_\theta/\beta)^2] \\ &\quad -2c_1 \Psi_1 \int \mathrm{d}x \cos(\beta \breve{\theta}_y), \end{aligned} \tag{B.10}$$

where $\Psi_1 = \langle \cos(\beta \breve{\theta}_y) \rangle$. Susceptibilities of the original field $\tilde{\theta}$ and shifted field $\breve{\theta}$ are related by[97]

$$\chi_{\breve{\theta}-\breve{\theta}}(q = 0, \omega = 0; T) = \chi_{\tilde{\theta}-\tilde{\theta}}(q_0 = \frac{D}{v}, \omega = 0; T), \tag{B.11}$$

Using (B.7) and (B.4) the ordering temperature for this cone state T_{cone} is obtained as

$$\begin{aligned} 1 = \eta_1 \left(\frac{2\pi T_{\text{cone}}}{v} \right)^{2\Delta_1 - 2} \frac{\Gamma(1-\Delta_1)}{\Gamma(\Delta_1)} |\Gamma(\Delta_1/2 + iy)|^4 \\ \times [\cosh(2\pi y) - \cos(\pi \Delta_1)], \end{aligned} \tag{B.12}$$

with $\eta_1 = c_1/(2\pi v) = J' A_3^2/(2\pi v)$, and

$$y = \frac{q_0 v}{4\pi T} = \frac{D}{4\pi T}, \qquad \Delta_1 = \pi R^2.$$

Plots of T_{cone} for system with weak DM interaction and in the presence of magnetic field are shown as the green curves in **Figure 2.11** and **Figure 2.12**.

Figure 2.12 shows that increasing D suppresses the cone state. When D/J' is bigger than a critical value, the solution of T_{cone} starts to disappear. We can estimate the critical D/J' ratio by rearranging (B.12) as

$$\frac{D}{J'} = 2 \left(\frac{v}{J'} \right)^{\frac{1-2\Delta_1}{2-2\Delta_1}} y \left(\frac{A_3^2}{2\pi} \frac{\Gamma(1-\Delta_1)}{\Gamma(\Delta_1)} |\Gamma(\Delta_1/2 + iy)|^4 [\cosh(2\pi y) - \cos(\pi \Delta_1)] \right)^{\frac{1}{2-2\Delta_1}}. \tag{B.13}$$

The scaling of D/J' with the v/J' ratio obtained here matches that in (B.27), which is obtained via a different, commensurate-incommensurate based reasoning in Appendix B.2.

The right side of Eq. (B.13) for relatively low field is shown in **Figure B.1**, where we set $v = \pi J/2$, and $A_3 \simeq 1/2$, so that Δ_1 is the only parameter dependent on field. The magnetization dependence of $\Delta_1 = \pi R^2$ appears via M dependence of the compactification radius R[97]

$$2\pi R^2 = 1 - \frac{1}{2\ln(M_0/M)}, \tag{B.14}$$

where $M_0 = \sqrt{8/(\pi e)}$ and the limit of small magnetization M is assumed. Therefore, **Figure B.1** shows that the critical D increases with field: critical $D/J' \approx 1.9$ at $\Delta_1 = 0.5$, which corresponds to $M = 0$, but increases to ≈ 2.75 at $\Delta_1 = 0.45$, which corresponds to $M \approx 0.0065$, according to (B.14). Note that this corresponds to a rather small magnetic field $h = 2\pi v M \approx \pi^2 MJ = 0.064J$ on the scale of the chain exchange J. Therefore material with $D = 2.75J'$ will be in the longitudinal SDW phase at zero magnetic field but transitions, in a discontinuous fashion, to the commensurate-cone phase in a small, but finite, magnetic field. This behavior seems to correspond to the case of $K_2CuSO_4Br_2$, as we describe in Appendix B.3.

Importantly, the right-hand side of (B.13) is bounded by the absolute maximum which is a weak function of the J'/J ratio. For $J'/J = 0.004$, chosen in **Figure B.1**, that maximum value is approximately 6.5. Therefore for the material with $D/J' \geq 6.5$ the cone phase is not realized at all; the remaining competition is between the SDW phase, which prevails at small magnetization, and the coneNN phase which emerges at higher M, as is discussed in Sec. 2.2.2.3.

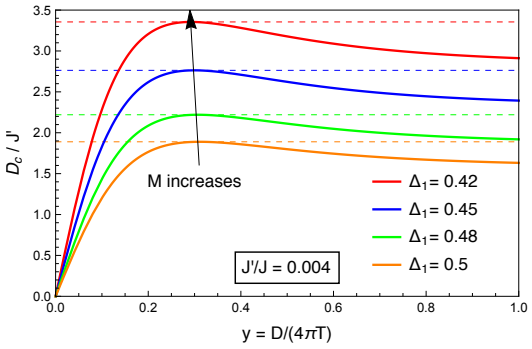

Figure B.1. Plot of right side of Eq. (B.13), showing maximum increases when Δ_1 decreases, implying the critical D_c increases with field. Here, we consider the low-field condition only, where field dependence of v and A_3 has been neglected. Horizontal dotted lines indicate critical D/J' required to destroy the cone state.

B.1.2 SDW order

As discussed in Sec. 2.2.2.3, the SDW order is commensurate for $h < h_{c-ic}$ and becomes incommensurate in higher fields. In the commensurate case we have

$$\mathcal{H}_{sdw} = 2c_2 \sum_y \int dx \sin(\frac{2\pi}{\beta}\tilde{\phi}_y + t_\phi x) \sin(\frac{2\pi}{\beta}\tilde{\phi}_{y+1} + t_\phi x), \tag{B.15}$$

with $c_2 = J' A_1^2/2$. Shifting $\tilde{\phi}$ by

$$\tilde{\phi}_y \to \breve{\phi}_y - \beta t_\phi x/2\pi - \sqrt{\pi/2}\, y \tag{B.16}$$

and applying the CMF approximation, (B.15) is transformed into

$$\mathcal{H}_{sdw} = -4c_2\Psi_2 \sum_y \int dx [\cos\frac{2\pi}{\beta}\breve{\phi}_y], \tag{B.17}$$

where $\Psi_2 = \langle \cos\frac{2\pi}{\beta}\breve{\phi}_y \rangle$. In complete similarity with (B.12), the shift produces wave vector $q_0 = t_\phi$ which strongly affects the critical temperature of the commensurate-SDW state,

$$\begin{aligned} 1 =& \eta_2 (\frac{2\pi T_{sdw-c}}{v})^{2\Delta_2 - 2} \frac{\Gamma(1-\Delta_2)}{\Gamma(\Delta_2)} |\Gamma(\frac{\Delta_2}{2} + iy)|^4 \\ & \times \big[\cosh(2\pi y) - \cos(\pi\Delta_2)\big]. \end{aligned} \tag{B.18}$$

Here $y = t_\phi v/(4\pi T_{sdw-c}) = h/(4\pi T_{sdw-c})$, $\eta_2 = c_2/(\pi v) = J' A_1^2/(2\pi v)$. Similarly to the case of the cone ordering, the solution of (B.18) exists as long as $h < h_{c-ic}$. If one estimates the right-hand side of (B.18) by its $h = 0$ value when $\Delta_2 = 1/2$, then one obtains that $h_{c-ic} = 1.9J'$. This is because Eqs. (B.12) and (B.18) are identical in the limit of small magnetic field when $\Delta_1 = \Delta_2 = 1/2$. Solving (B.18) numerically, which accounts for the magnetic field dependence of the scaling dimension (Δ_2 increases with the field, which means that SDW order weakens), results in a smaller critical field $h_{c-ic} \approx 1.4J'$ as **Figure B.2** shows.

For $h > h_{c-ic}$ we consider incommensurate SDW, the Hamiltonian of which differs from (B.15) by the absence of the oscillatory term. This, of course, is equivalent to neglecting $\tilde{g}_\phi$ in $\mathcal{H}_{sdw}$ in (2.71). Therefore now

$$\mathcal{H}_{sdw} = c_2 \sum_y \int dx \cos\big[\frac{2\pi}{\beta}(\tilde{\phi}_y - \tilde{\phi}_{y+1})\big], \tag{B.19}$$

Here we shift $\tilde{\phi} \to \tilde{\phi}_y + \beta y/2$ which changes the sign of $\mathcal{H}_{sdw}$. The CMF approximation then leads to

$$1 = 2c_2\chi(q = 0, \omega = 0; T_{sdw-ic}), \tag{B.20}$$

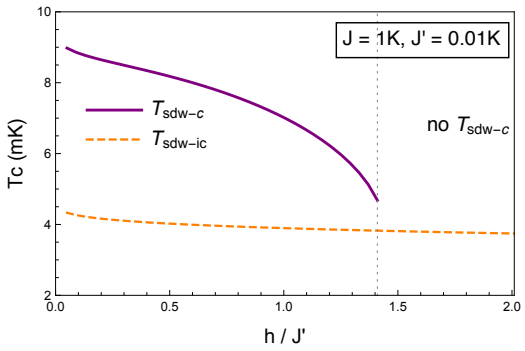

Figure B.2. Ordering temperatures of commensurate SDW ($T_{\mathrm{sdw-c}}$, purple solid line), and incommensurate SDW ($T_{\mathrm{sdw-ic}}$, orange dashed line) versus h/J'. Here $J = 1$ K, and $J' = 0.01$ K. Around $h/J' \sim 1.4$, longitudinal SDW order changes from the commensurate to the incommensurate one.

where the susceptibility is given by Eq. (B.6). The ordering temperature of the incommensurate(IC) SDW is

$$T_{\mathrm{sdw-ic}} = \frac{v}{2\pi}\left(\frac{\eta_2 \frac{\Gamma(1-\Delta_2)\Gamma(\Delta_2/2)^2}{\Gamma(\Delta_2)\Gamma(1-\Delta_2/2)^2}}{1+\eta_2 \frac{\Gamma(\Delta_2-1/2)}{\sqrt{\pi}(1-\Delta_2)\Gamma(\Delta_2)}}\right)^{1/(2-2\Delta_2)}. \tag{B.21}$$

where $\eta_2 = \pi c_2/v = \pi J' A_1^2/2v$. As explained below (B.6), the term in the denominator of the expression inside the brackets in this equation removes the divergence of the numerator in the $\Delta_2 \to 1$ limit (high-field limit).

Since the critical field $h_{\mathrm{c-ic}} \approx 1.4J'$ is sufficiently small, we focus on the IC-SDW order when studying the phase transition between it and the coneNN phase in Sec. 2.2.3. Plots of the SDW's T_{sdw} are shown as orange curves in **Figure 2.11**, **Figure 2.12**, and **Figure 2.13**.

B.1.3 ConeNN order

When it comes to the coneNN state, the calculations are straightforward:

$$\begin{aligned} \mathcal{H}_{\mathrm{NN}} &= -c_3 \sum_y \int \mathrm{d}x \cos\left[\beta(\tilde{\theta}_y - \tilde{\theta}_{y+2})\right], \\ c_3 &= \frac{\pi}{4}\frac{J'^2}{D} A_3^4 t_\theta^{2\Delta-1} \frac{\Gamma(1-\Delta_1)}{\Gamma(\Delta_1)}. \end{aligned} \tag{B.22}$$

Note that coupling constant c_3 should be considered an estimate, valid up to a numerical prefactor of order 1, since it is calculated via perturbative RG; see Appendix 2.2.6.

The ordering temperature has a simple form, due to the fact that $\mathcal{H}_{\rm NN}$ is free from oscillation and $T_{\rm coneNN}$ is free from divergence ($\Delta_1 \leq 1/2$),

$$T_{\rm coneNN} = \frac{v}{2\pi}\Big[\eta_3 \frac{\Gamma(1-\Delta_1)\Gamma(\Delta_1/2)^2}{\Gamma(\Delta_1)\Gamma(1-\Delta_1/2)^2}\Big]^{1/(2-2\Delta_1)}, \tag{B.23}$$

where $\eta_3 = \pi c_3/v$. The plot of $T_{\rm coneNN}$ is shown as the blue curve in **Figure 2.13** for the strong DM interaction.

B.2 Mean-field treatment of the C-IC transition

The commensurate-incommensurate transition (CIT) appears several times in our work, both in connection with the DM-induced CIT in the cone state and with the magnetic–field-induced CIT in the SDW state; see discussions in Secs. 2.2.2.2 and 2.2.2.3, and calculations in Appendix B. Here we sketch an approximate mean-field treatment of this transition at zero temperature.

As an example, let us consider $\mathcal{H}_{\rm cone}$ in Eq. (B.10) for a particular chain y, and suppose y is even. Then, removing all ˜ and ˇ symbols which do not play any role in this discussion, we need to consider a single-chain Hamiltonian

$$\begin{aligned} H_{\rm cit} &= \int {\rm d}x \Big(\frac{1}{2v}(\partial_x \varphi_y)^2 + \frac{v}{2}(\partial_x \theta_y)^2 - \frac{D}{\sqrt{2\pi}}\partial_x \theta_y \\ &\quad -\lambda \cos(\beta\theta_y)\Big), \end{aligned} \tag{B.24}$$

where $\lambda = 2c_1\Psi \sim J'\Psi$ depends on the self-consistently determined value of the order parameter $\Psi = \langle \cos(\beta\theta_y)\rangle$.

According to Ref.[130] (Appendix A.2), the critical value D_c, above which the ground state becomes incommensurate, scales as

$$D_c \sim \sqrt{\lambda v}\Big(\frac{\lambda}{v}\Big)^{\Delta/(4-2\Delta)}, \tag{B.25}$$

where $\Delta = \beta^2/(4\pi)$ is the scaling dimension of the cosine operator in $H_{\rm cit}$. At the same time, according to Ref.[97] (Appendix D.5), in the commensurate phase the order parameter scales as

$$\Psi \sim \Big(\frac{J'}{v}\Big)^{\Delta/(2-2\Delta)}. \tag{B.26}$$

Combining the last two equation we derive that

$$\frac{D_c}{J'} \sim \Big(\frac{v}{J'}\Big)^{(1-2\Delta)/(2-2\Delta)}. \tag{B.27}$$

We observe that D_c is function of magnetization M, via the dependence of $\Delta(M)$ on it. Since $\Delta(M)$ is a decreasing function of magnetization, $\Delta(M=0)=1/2$ while $\Delta(M=1/2)=1/4$, critical D_c is smallest at $M=0$: at this point $D_c/J' \sim 1$, in agreement with our comparison of critical temperatures in Appendix B. As $\Delta \to 1/4$, which corresponds to the high-field limit, the critical ratio increases to $(v/J')^{1/3} \gg 1$.

Put differently, our estimate of $D_c \approx 1.9J'$, obtained in Appendix B.1.1, provides the lower bound of the DM interaction magnitude D required to destroy the commensurate-cone state. If material is characterized by $D < D_c(M=0)$, the commensurate-cone phase is stable in the whole range of magnetization $0 \leq M \leq 1/2$.

B.3 Estimate of the interchain exchange J'

A variety of experimental techniques has been employed to characterize the parameters of $K_2CuSO_4Cl_2$ and $K_2CuSO_4Br_2$.[12,45] The dominant intrachain exchange J has been estimated using the empirical fitting function of Ref.[156] to fit the uniform magnetic susceptibility data as well as by fitting the inelastic neutron scattering continuum, a unique feature of the Heisenberg spin-1/2 chain, to the Müller ansatz.[157] DM vector $\boldsymbol{D}$ has been measured by electron spin resonance (ESR) as described in the Sec. 1.4.2. However the interchain exchange interaction J' has been estimated from the chain mean-field theory fit based on Monte Carlo improved study in Ref.[109] This fit, however, completely neglects DM interactions crucial for understanding these materials and, moreover, assumes that spin chains form simple nonfrustrated cubic structure. The second assumption is not justified as well. Inelastic neutron scattering data show that the interchain exchange between spin chains in the $a-b$ plane is at least an order of magnitude stronger than that along the c-axis, connecting different $a-b$ planes. As a result, it is more appropriate to consider the current problem as two-dimensional whereby spin chains, running along the a-axis, interact weakly via $J' \ll J$ directed along the b-axis. This is the geometry assumed in the present work.

The interchain J' is estimated from the value of the zero-field critical temperature T_c, which is calculated with the help of the chain mean-field (CMF) approximation in Appendix B. At $h=0$, and using $\Delta_1 = 1/2$ and $A_3 = 1/2$, Eq. (B.12) predicts

$$J' = (4\pi)^2 T_{\rm cone}^{h=0} / [|\Gamma(1/4 + iD/(4\pi T_{\rm cone}^{h=0}))|^4 \cosh(D/2T_{\rm cone}^{h=0})]. \tag{B.28}$$

Here $T_{\rm cone}^{h=0}$ =77 mK is the experimentally determined transition temperature of $K_2CuSO_4Cl_2$ at zero magnetic field and $D = 0.11$ K. We obtain $J'_{\rm Cl} = 0.083$ K.

Figure B.3 shows $T_{\rm cone}$ and $T_{\rm sdw}$ for $K_2CuSO_4Cl_2$ as a function of magnetization M. It compares well to Fig. 14 in Ref.[45] As expected, the cone phase is the ground state of this two-dimensional system at all M. The (approximately) factor of 2 difference between our result and the previous estimate in Ref.[45] is caused by the two-dimensional geometry of the system that we assume and by the finite value of $D/J' = 1.3$ for this system, which slightly frustrates transverse interchain exchange.

For $K_2CuSO_4Br_2$, which is characterized by strong DM interaction, the value of the interchain exchange J' can be estimated by identifying the zero-field ordering temperature $T_{\rm exp} = 0.1$ K[45] with that of the commensurate longitudinal SDW order, Eq.(B.18). For $h = 0$ this gives $T_{\rm sdw-c} = A_1^2\Gamma(1/4)^4 J'/(2\pi)^2 = 1.094J'$, so that $J' \approx 0.091$ K.

The most important outcome of these calculations consists of finding significantly different estimates of the D/J' ratio for the two materials; see **Table B.1**. $K_2CuSO_4Cl_2$ is characterized by $D/J' = 1.3$, which is below the critical value of 1.9 that destroys the cone phase at $M = 0$. As a result, the phase diagram of $K_2CuSO_4Cl_2$ consists of a single cone phase.

To the contrary, $K_2CuSO_4Br_2$ has a roughly two times greater value, $D/J' = 3.1$, which results in a much more complex sequence of transitions with increasing M, as **Figure B.4** shows. The ground state at smallest $M \leq 0.0006$ is the commensurate SDW which changes

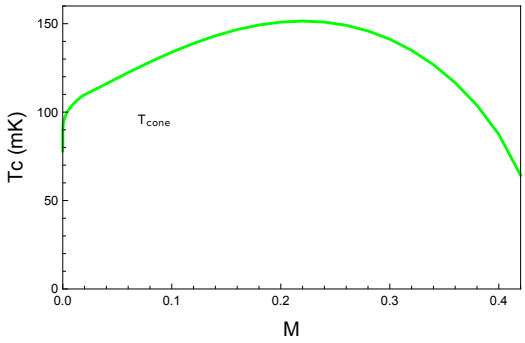

Figure B.3. Critical temperatures of cone ($T_{\rm cone}$, green solid) as a function of magnetization M for $K_2CuSO_4Cl_2$, with $J_{\rm Cl} = 3.1$ K, $D_{\rm Cl} = 0.11$ K and $J'_{\rm Cl} = 0.083$ K from Eq. (B.12) by setting $T_{\rm cone}^{h=0}$ to 77 mK. Here the phase diagram consists of a single cone phase.

Table B.1. Exchange constants for $K_2CuSO_4Cl_2$ and $K_2CuSO_4Br_2$: intrachain exchange J; magnitude of DM interaction D; interchain exchange J'_{exp} from Ref.[45] (it is obtained by fitting experimental T_c data[45]); to the $d = 3$ Heisenberg-exchange-only theory of Ref.;[109] interchain exchange J' in the fifth column is obtained by fitting experimental T_c data to our CMF calculations.

	$J(K)$	$D(K)$	$J'_{exp}(K)$	$J'(K)$ by CMF	D/J'
$K_2CuSO_4Cl_2$	3.1	0.11	0.031	0.083	1.3
$K_2CuSO_4Br_2$	20.5	0.28	0.034	0.091	3.1

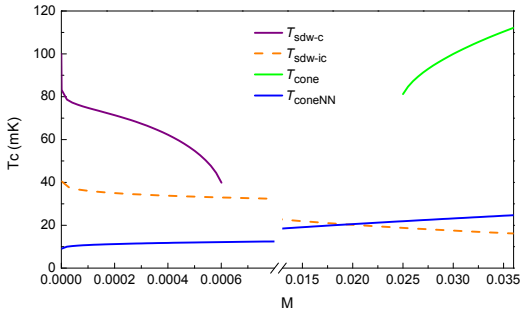

Figure B.4. Critical temperatures of commensurate SDW (T_{sdew-c}; purple solid line), incommensurate SDW ($T_{sdew-ic}$; orange dashed line), commensurate cone (T_{cone}; green solid line) and coneNN (T_{coneNN}; blue solid line) as a function of magnetization M, with $J = 20.5$ K, $J' = 0.091$ K and $D = 0.28$ K. Transition between SDW(IC) and coneNN happens at $M \sim 0.018$. Solution of T_{cone} appears discontinuously at $M \simeq 0.025$. Note that in order to accommodate all phases in the single graph the horizontal axis is broken into two regions.

into an incommensurate SDW order for $0.0006 \leq M \leq 0.018$. In the very narrow window $0.018 \leq M \leq 0.025$ the coneNN order takes over but then is replaced, again discontinuously, by the commensurate-cone order. Within the CMF description the coneNN-cone transition is discontinuous. The discontinuity in T_c is significant; its value increases by a factor of about 2. This feature is not seen in the experiment and most likely indicates that actual ratios of D/J' and J'/J for this interesting material are somewhat different from the values estimated by us here.

Importantly, that difference can be quite small. We find that the region of parameters with $D \approx 3J'$ is very tricky; small changes in D/J' change the outcome completely. For example, hypothetical material with a slightly greater DM interaction, $D = 0.4$ K so that

$D/J' = 4.4$, turns out to be strongly DM frustrated and does not support the cone phase at any magnetization, as **Figure B.5** shows. Such a material would show two different transitions: first, at tiny magnetization of the order of $M = 0.0007$, the commensurate SDW order changes to the incommensurate one. Then, at much higher magnetization of about $M = 0.09$, there is a first-order transition from the incommensurate-SDW to the coneNN phase. This time there is no discontinuity in the $T_c(M)$ but the derivative dT_c/dM is discontinuous still.

The multitude of possible behaviors is summarized by phase diagrams in **Figure 2.20**, which focuses on the small-M range, and **Figure B.6**, in which the full range of M is explored. In numerically calculating T_c for these diagrams we set $J = 20.5$ K and $J' \simeq 0.0045J = 0.09$ K. Being restricted to small values of M, **Figure 2.20** is calculated by keeping parameters v and $A_{1,3}$ at their $M = 0$ values but taking the variation of the scaling dimensions with M via Eq.(B.14). The commensurate-incommensurate transition between the two SDW phases happens at very small magnetization, as has already been seen in **Figure B.4**. The "triple point" where three phases intersect is at $M \simeq 0.02$ and $D/J' \simeq 3$.

Figure B.6 accounts for the M dependence of all parameters that appear in the expressions for various T_c. This is done with the help of numerical data from Ref.[98] in which the smallest magnetization value is 0.02. This, as our discussion above shows, is too big a magnetization for the commensurate-SDW state which therefore is absent from **Figure B.6**.

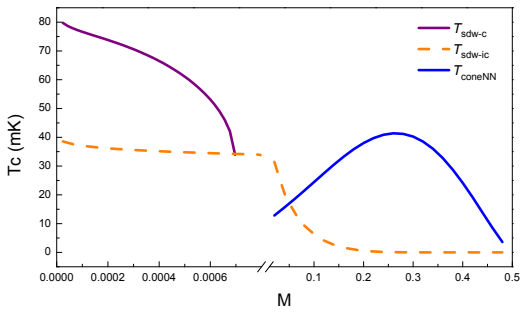

Figure B.5. Critical temperatures of commensurate SDW ($T_{\text{sdew}-c}$; purple solid line), incommensurate SDW (T_{sdw}; orange dashed line), and coneNN (T_{coneNN}; blue solid line) as a function of magnetization M, with $J = 20.5$ K, $J' = 0.091$ K, and $D = 0.4$ K. Here D is large enough to destroy the cone state in the full magnetization range. Note that in order to accommodate all three phases in the single graph the horizontal axis is broken into two regions.

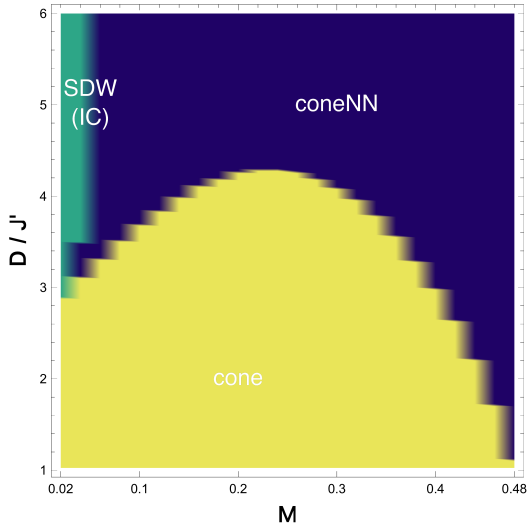

Figure B.6. $M - D$ phase diagram for the case of $\boldsymbol{h} \parallel \boldsymbol{D}$, obtained by the CMF calculation. Here $J = 20.5$ K, $J' = 0.0045J$. Cone phase is suppressed by large D/J', and large field/magnetization.

As discussed previously, the cone order is first enhanced by M, due to the decrease of the corresponding scaling dimension, and then gets suppressed at large magnetization, basically due to the Zeeman effect. It should be noted that our one-dimensional CMF calculations are not valid near the satuation, $M \to 0.5$, where the velocity v of the chain spin excitations vanishes to zero. This shortcoming has already been discussed in Ref.[97]

Once again, **Figure B.6** shows that the SDW phase is restricted to low magnetization values. The DM interaction staggered between chains is effective in suppressing the commensurate-cone phase for all M. For material with a strong DM interaction such as $D/J' > 4.2$ (for example the $D = 0.4$ K material in **Figure B.5**), the commensurate-cone phase is entirely avoided as one increases M from zero to saturation.

REFERENCES

[1] S. Blundell, *Magnetism in Condensed Matter* (Oxford University Press, New York, 2014).

[2] L. Balents, https://spinsandelectrons.files.wordpress.com/2016/04/cifar2016.pdf.

[3] R. Moessner and A. P. Ramirez, Physics Today **59**, 24 (2006).

[4] L. Balents, Nature **464**, 199 (2010).

[5] A. I. Smirnov et al., Phys. Rev. B **75**, 134412 (2007).

[6] D. Cabra, A. Honecker, and P. Pujol, The European Physical Journal B - Condensed Matter and Complex Systems **13**, 55 (2000).

[7] K. Okunishi and T. Tonegawa, Journal of the Physical Society of Japan **72**, 479 (2003).

[8] A. Honecker, J. Schulenburg, and J. Richter, Journal of Physics: Condensed Matter **16**, S749 (2004).

[9] F. D. M. Haldane, Phys. Rev. Lett. **50**, 1153 (1983).

[10] L. Faddeev and L. Takhtajan, Physics Letters A **85**, 375 (1981).

[11] M. Mourigal et al., Nat Phys **9**, 435 (2013).

[12] A. I. Smirnov et al., Phys. Rev. B **92**, 134417 (2015).

[13] M. Takigawa and F. Mila, in: *Introduction to Frustrated Magnetism: Materials, Experiments, Theory*, edited by C. Lacroix, P. Mendels, and F. Mila (Springer, Berlin, 2011), pp. 241-267.

[14] T. Hikihara, T. Momoi, A. Furusaki, and H. Kawamura, Phys. Rev. B **81**, 224433 (2010).

[15] O. A. Starykh, Reports on Progress in Physics **78**, 052502 (2015).

[16] O. A. Starykh and L. Balents, Phys. Rev. B **89**, 104407 (2014).

[17] S. Kimura et al., Phys. Rev. Lett. **101**, 207201 (2008).

[18] K. Penc and A. M. Läuchli, in: *Introduction to Frustrated Magnetism: Materials, Experiments, Theory*, edited by C. Lacroix, P. Mendels, and F. Mila (Springer, Berlin, 2011), pp. 331-362.

[19] A. V. Chubukov and O. A. Starykh, Phys. Rev. Lett. **110**, 217210 (2013).

[20] M. Mourigal et al., Phys. Rev. Lett. **109**, 027203 (2012).

[21] N. Büttgen et al., Phys. Rev. B **90**, 134401 (2014).

[22] Z. Wang et al., arXiv:1708.02980 (2017).

[23] B. Willenberg et al., Phys. Rev. Lett. **116**, 047202 (2016).

[24] L. Savary and L. Balents, Reports on Progress in Physics **80**, 016502 (2017).

[25] L. Savary, Ph.D. dissertation, University of California, 2014.

[26] P. W. Anderson, Science **235**, 1196 (1987).

[27] M. Tamura, A. Nakao, and R. Kato, Journal of the Physical Society of Japan **75**, 093701 (2006).

[28] C. Lhuillier and G. Misguich, in: *Introduction to Frustrated Magnetism: Materials, Experiments, Theory*, edited by C. Lacroix, P. Mendels, and F. Mila (Springer, Berlin, 2011), pp. 23-41.

[29] V. Kalmeyer and R. B. Laughlin, Phys. Rev. Lett. **59**, 2095 (1987).

[30] J. P. Eisenstein and H. L. Stormer, Science **248**, 1510 (1990).

[31] E. Witten, Comm. Math. Phys. **121**, 351 (1989).

[32] X.-G. Wen, arXiv:1610.03911 (2016).

[33] H. Yao and S. A. Kivelson, Phys. Rev. Lett. **99**, 247203 (2007).

[34] S.-S. Gong, W. Zhu, L. Balents, and D. N. Sheng, Phys. Rev. B **91**, 075112 (2015).

[35] Y.-C. He and Y. Chen, Phys. Rev. Lett. **114**, 037201 (2015).

[36] T. Meng, T. Neupert, M. Greiter, and R. Thomale, Phys. Rev. B **91**, 241106 (2015).

[37] C. L. Kane, R. Mukhopadhyay, and T. C. Lubensky, Phys. Rev. Lett. **88**, 036401 (2002).

[38] C. Castelnovo, R. Moessner, and S. L. Sondhi, Nature **451**, 42 (2008).

[39] M. J. P. Gingras and P. A. McClarty, Reports on Progress in Physics **77**, 056501 (2014).

[40] P. A. M. Dirac, Proceedings of the Royal Society of London A: Mathematical, Physical and Engineering Sciences **123**, 714 (1929).

[41] P. W. Anderson, Solid State Physics **14**, 99 (1963).

[42] I. Dzyaloshinsky, Journal of Physics and Chemistry of Solids **4**, 241 (1958).

[43] T. Moriya, Phys. Rev. **120**, 91 (1960).

[44] V. E. Dmitrienko et al., Nat Phys **10**, 202 (2014).

[45] M. Hälg et al., Phys. Rev. B **90**, 174413 (2014).

[46] K. Y. Povarov, A. I. Smirnov, O. A. Starykh, S. V. Petrov, and A. Y. Shapiro, Phys. Rev. Lett. **107**, 037204 (2011).

[47] H. Karimi and I. Affleck, Phys. Rev. B **84**, 174420 (2011).

[48] S. C. Furuya, Phys. Rev. B **95**, 014416 (2017).

[49] A. I. Smirnov and T. A. Soldatov, private communication, 2016.

[50] A. O. Gogolin, A. A. Nersesian, and A. M. Tsvelik, *Bosonization and Strongly Correlated Systems* (Cambridge University Press, Cambridge, 2004).

[51] G. D. Mahan, *Many-Particle Physics*, 3rd ed. (Plenum, New York, 2000).

[52] T. Giamarchi, *Quantum Physics in One Dimension*, 2nd ed. (Clarendon Press, Oxford, 2004).

[53] E. Fradkin, *Field Theories of Condensed Matter Physics* (Cambridge University Press, 2013).

[54] I. Garate and I. Affleck, Phys. Rev. B **81**, 144419 (2010).

[55] T. Holstein and H. Primakoff, Phys. Rev. **58**, 1098 (1940).

[56] A. Auerbach, *Interacting Electrons and Quantum Magnetism* (Springer, 1994).

[57] Z. Li, *Solid State Theory* (2009).

[58] M. I. Kaganov and A. V. Chubukov, Soviet Physics Uspekhi **30**, 1015 (1987).

[59] J. A. M. Paddison et al., Nat Phys **13**, 117 (2017).

[60] R. Coldea, D. A. Tennant, and Z. Tylczynski, Phys. Rev. B **68**, 134424 (2003).

[61] T. Ono et al., Progress of Theoretical Physics Supplement **159**, 217 (2005).

[62] N. A. Fortune et al., Phys. Rev. Lett. **102**, 257201 (2009).

[63] B. Willenberg et al., Phys. Rev. Lett. **116**, 047202 (2016).

[64] K. Y. Povarov, Y. Feng, and A. Zheludev, Phys. Rev. B **94**, 214409 (2016).

[65] Y.-H. Chan, W. Jin, H.-C. Jiang, and O. A. Starykh, Phys. Rev. B **96**, 214441 (2017).

[66] J. Alicea, Reports on Progress in Physics **75**, 076501 (2012).

[67] A. Manchon, H. C. Koo, J. Nitta, S. M. Frolov, and R. A. Duine, Nat. Mater. **14**, 871 (2015).

[68] A. Y. Kitaev, Physics-Uspekhi **44**, 131 (2001).

[69] A. Kitaev, Annals of Physics **321**, 2 (2006).

[70] I. E. Dzyaloshinskii, Journal of Physics and Chemistry of Solids **4**, 241 (1958).

[71] T. Moriya, Phys. Rev. **120**, 91 (1960).

[72] I. E. Dzyaloshinskii, Sov. Phys. - JETP **20**, 665 (1965).

[73] A. Zheludev et al., Phys. Rev. B **57**, 2968 (1998).

[74] Y. Togawa et al., Phys. Rev. Lett. **108**, 107202 (2012).

[75] S.-W. Cheong and M. Mostovoy, Nat. Mater. **6**, 13 (2007).

[76] J. Kishine and A. Ovchinnikov, Solid State Physics **66**, 1 (2015).

[77] K. Y. Povarov, A. I. Smirnov, O. A. Starykh, S. V. Petrov, and A. Y. Shapiro, Phys. Rev. Lett. **107**, 037204 (2011).

[78] A. I. Smirnov et al., Phys. Rev. B **92**, 134417 (2015).

[79] S. Gangadharaiah, J. Sun, and O. A. Starykh, Phys. Rev. B **78**, 054436 (2008).

[80] C. Sun and V. L. Pokrovsky, Phys. Rev. B **91**, 161305 (2015).

[81] A. P. Schnyder, O. A. Starykh, and L. Balents, Phys. Rev. B **78**, 174420 (2008).

[82] O. A. Starykh, in: *Handbook of Nanophysics: Nanotubes and Nanowires*, edited by K.D. Sattler (CRC Press, 2010), chp. 30.

[83] O. A. Starykh, A. Furusaki, and L. Balents, Phys. Rev. B **72**, 094416 (2005).

[84] W. Jin and O. A. Starykh, Phys. Rev. B **95**, 214404 (2017).

[85] D. V. Dmitriev, V. Y. Krivnov, and A. A. Ovchinnikov, Phys. Rev. B **65**, 172409 (2002).

[86] S. Lukyanov and A. Zamolodchikov, Nuclear Physics B **493**, 571 (1997).

[87] T. Hikihara and A. Furusaki, Phys. Rev. B **58**, R583 (1998).

[88] T. Hikihara and A. Furusaki, Phys. Rev. B **69**, 064427 (2004).

[89] T. Hikihara, A. Furusaki, and S. Lukyanov, arXiv:1706.02538 (2017).

[90] M. Hälg, Ph.D. dissertation, ETH-Zurich, 2015.

[91] V. N. Glazkov et al., Phys. Rev. B **92**, 184403 (2015).

[92] D. C. Dender, P. R. Hammar, D. H. Reich, C. Broholm, and G. Aeppli, Phys. Rev. Lett. **79**, 1750 (1997).

[93] I. Affleck and M. Oshikawa, Phys. Rev. B **60**, 1038 (1999).

[94] M. Sato and M. Oshikawa, Phys. Rev. B **69**, 054406 (2004).

[95] H. J. Schulz, Phys. Rev. Lett. **77**, 2790 (1996).

[96] O. A. Starykh and L. Balents, Phys. Rev. Lett. **98**, 077205 (2007).

[97] O. A. Starykh, H. Katsura, and L. Balents, Phys. Rev. B **82**, 014421 (2010).

[98] F. H. L. Essler, A. Furusaki, and T. Hikihara, Phys. Rev. B **68**, 064410 (2003).

[99] T. Hikihara and A. Furusaki, Phys. Rev. B **69**, 064427 (2004).

[100] W. Jin and O. A. Starykh, Journal of Physics: Conference Series **828**, 012019 (2017).

[101] S. Eggert, Phys. Rev. B **54**, R9612 (1996).

[102] W. Witczak-Krempa, G. Chen, Y. B. Kim, and L. Balents, Annual Review of Condensed Matter Physics **5**, 57 (2014).

[103] Z. Nussinov and J. van den Brink, Rev. Mod. Phys. **87**, 1 (2015).

[104] L. Savary and L. Balents, Reports on Progress in Physics **80**, 016502 (2017).

[105] S. M. Winter, K. Riedl, and R. Valenti, arXiv:1610.05468 (2016).

[106] I. Kimchi, R. Coldea, and A. Vishwanath, Phys. Rev. B **91**, 245134 (2015).

[107] I. Kimchi and R. Coldea, Phys. Rev. B **94**, 201110 (2016).

[108] A. W. Sandvik, Phys. Rev. Lett. **83**, 3069 (1999).

[109] C. Yasuda et al., Phys. Rev. Lett. **94**, 217201 (2005).

[110] T. Neupert, C. Chamon, C. Mudry, and R. Thomale, Phys. Rev. B **90**, 205101 (2014).

[111] G. Gorohovsky, R. G. Pereira, and E. Sela, Phys. Rev. B **91**, 245139 (2015).

[112] G. Gorohovsky, R. G. Pereira, and E. Sela, Phys. Rev. B **91**, 245139 (2015).

[113] P. Lecheminant and A. M. Tsvelik, arXiv:1608.05977 (2016).

[114] L. Messio, S. Bieri, C. Lhuillier, and B. Bernu, arXiv:1701.01243 (2017).

[115] J. C. Y. Teo and C. L. Kane, Phys. Rev. B **89**, 085101 (2014).

[116] L. F. Chibotaru and L. Ungur, Phys. Rev. Lett. **109**, 246403 (2012).

[117] L.-K. Lim, A. Hemmerich, and C. M. Smith, Phys. Rev. A **81**, 023404 (2010).

[118] O. A. Starykh, W. Jin, and A. V. Chubukov, Phys. Rev. Lett. **113**, 087204 (2014).

[119] R. Coldea et al., Phys. Rev. Lett. **88**, 137203 (2002).

[120] Y. Tokiwa et al., Phys. Rev. B **73**, 134414 (2006).

[121] S. A. Zvyagin et al., Phys. Rev. Lett. **112**, 077206 (2014).

[122] T. Ono et al., Journal of the Physical Society of Japan **74**, 135 (2005).

[123] Y. Shirata, H. Tanaka, A. Matsuo, and K. Kindo, Phys. Rev. Lett. **108**, 057205 (2012).

[124] T. Susuki et al., Phys. Rev. Lett. **110**, 267201 (2013).

[125] G. Koutroulakis et al., Phys. Rev. B **91**, 024410 (2015).

[126] A. V. Chubokov and D. I. Golosov, Journal of Physics: Condensed Matter **3**, 69 (1991).

[127] T. Nikuni and H. Shiba, Journal of the Physical Society of Japan **62**, 3268 (1993).

[128] C. Griset, S. Head, J. Alicea, and O. A. Starykh, Phys. Rev. B **84**, 245108 (2011).

[129] H. T. Ueda and K. Totsuka, Phys. Rev. B **80**, 014417 (2009).

[130] R. Chen, H. Ju, H.-C. Jiang, O. A. Starykh, and L. Balents, Phys. Rev. B **87**, 165123 (2013).

[131] Y. Kamiya and C. D. Batista, Phys. Rev. X **4**, 011023 (2014).

[132] D. Yamamoto, G. Marmorini, and I. Danshita, Phys. Rev. Lett. **112**, 127203 (2014).

[133] R. S. Gekht and I. N. Bondarenko, Journal of Experimental and Theoretical Physics **84**, 345 (1997).

[134] V. N. Popov, *Functional Integrals and Collective Excitations*, 2nd ed. (Cambridge University Press, Cambridge, 1987).

[135] T. Momoi and N. Shannon, Progress of Theoretical Physics Supplement **159**, 72 (2005).

[136] N. Shannon, T. Momoi, and P. Sindzingre, Phys. Rev. Lett. **96**, 027213 (2006).

[137] T. Vekua, A. Honecker, H.-J. Mikeska, and F. Heidrich-Meisner, Phys. Rev. B **76**, 174420 (2007).

[138] E. Parker and L. Balents, Phys. Rev. B **95**, 104411 (2017).

[139] A. V. Chubukov, Phys. Rev. B **44**, 4693 (1991).

[140] C. K. Majumdar and D. K. Ghosh, Journal of Mathematical Physics **10**, 1399 (1969).

[141] C. K. Majumdar and D. K. Ghosh, Journal of Mathematical Physics **10**, 1388 (1969).

[142] F. Heidrich-Meisner, I. A. Sergienko, A. E. Feiguin, and E. R. Dagotto, Phys. Rev. B **75**, 064413 (2007).

[143] H. Kikuchi, M. Chiba, and T. Kubo, Canadian Journal of Physics **79**, 1551 (2001).

[144] S. Guitarra, A. Caneiro, and D. Niebieskikwiat, Journal of Magnetism and Magnetic Materials **392**, 63 (2015).

[145] O. Pieper et al., Phys. Rev. B **79**, 180409 (2009).

[146] X. Zong et al., Phys. Rev. B **77**, 014412 (2008).

[147] P. Carretta, M. Filibian, R. Nath, C. Geibel, and P. J. C. King, Phys. Rev. B **79**, 224432 (2009).

[148] S.-S. Gong, W. Zhu, D. N. Sheng, and K. Yang, Phys. Rev. B **95**, 205132 (2017).

[149] J. Alicea, A. V. Chubukov, and O. A. Starykh, Phys. Rev. Lett. **102**, 137201 (2009).

[150] F. Heidrich-Meisner, I. A. Sergienko, A. E. Feiguin, and E. R. Dagotto, Phys. Rev. B **75**, 064413 (2007).

[151] T. Oguchi, Phys. Rev. **117**, 117 (1960).

[152] J. R. Schrieffer, *Theory of Superconductivity* (Frontiers in Physics, Charlottesville, 1964).

[153] D. Zwillinger, V. Moll, I. Gradshteyn, and I. Ryzhik, *Table of Integrals, Series, and Products*, 8th ed. (Academic Press, Boston, 2014).

[154] A. Orlova et al., Phys. Rev. Lett. **118**, 247201 (2017).

[155] N. Büttgen et al., Phys. Rev. B **90**, 134401 (2014).

[156] D. C. Johnston et al., Phys. Rev. B **61**, 9558 (2000).

[157] G. Müller, H. Thomas, H. Beck, and J. C. Bonner, Phys. Rev. B **24**, 1429 (1981).